Scuola Internazionale Superiore
di Studi Avanzati

Trieste, Academic year 2018/2019

Nonequilibrium phenomena in quantum many-body systems with long-range interactions

Candidate:
Alessio Lerose

Supervisors:
Prof. Andrea Gambassi
Prof. Alessandro Silva

A thesis submitted in fulfillment of the requirements for the degree of Doctor of Philosophy (Ph.D.)

in

Statistical Physics

SISSA

Invitation

The research work presented in this thesis concerns collective phenomena occurring in isolated quantum many-body systems driven away from thermodynamic equilibrium. The study of nonequilibrium dynamics plays a crucial role in the foundations of statistical mechanics, since it provides the microscopic basis for the description of equilibrium states with statistical ensembles, and hence for the effectiveness of macroscopic thermodynamics.

At the same time, and even more interestingly, it paves the way for understanding the limitations of this description: A number of physical ingredients have been discovered, which may prevent a system from quickly approaching thermal equilibrium, including quantumness, criticality, hidden symmetries, strong interactions and disorder. In these cases, a system may dynamically attain and linger in peculiar states which fail to be described by conventional statistical mechanics. The physics of nonequilibrium systems is largely undiscovered to present date, and its understanding constitutes one the central goals of contemporary theoretical physics.

Isolated quantum many-body systems out of equilibrium lie at the core of future quantum technologies. The development of the latter currently witness a huge and widespread effort due to the potential disruptive step forward in computational capabilities to which they could lead. Any conceivable platform to be exploited for quantum computation has to be a scalable system composed of a number of elementary units accessible and manipulable at the quantum scale, and well isolated from the external environment, such that its evolution maintains quantum coherence during the relevant time scale.

The focus of this thesis work is on the role of long-range interactions in the nonequilibrium coherent quantum dynamics. I have explored a number of settings in which long-range interactions allow for phenomena which do not possess a counterpart in equilibrium. The results contained in this thesis contribute to establish long-range interactions as a source of anomalous nonthermal behavior in quantum many-particle systems. In particular, the two parts of the thesis discuss two relative underlying mechanisms, which involve long-range interactions in different ways.

Systems with all-to-all interactions among their elementary constituents are so cooperative that in many respects they may behave as a single, collective object, in which internal fluctuations are locked. In such a limiting situation, the collective out-of-equilibrium dynamics is extremely simple, and approach

to thermal equilibrium is strictly ruled out. This leaves room for a wealth of genuinely nonequilibrium phenomena, and it is natural to ask whether and how these phenomena may survive when interactions have a long but finite range, which allows for the buildup of inter-particle fluctuations. This is the general philosophy of Part I of the thesis. In Chap. 2, the nonequilibrium dynamics of collective models will be reviewed, and in Chap. 3, I will introduce a general method to address the robustness of collective dynamical phenomena to fluctuations. Using this method, I will show in Chap. 4, that nonequilibrium fluctuations may give rise to pseudo-aleatory behavior in the collective dynamics near critical points, and in Chap. 5, that dynamically stabilized collective configurations via periodic drives may be robust to nonequilibrium fluctuations. Both these phenomena cannot occur in equilibrium and with short-range interactions. Finally, in Chap. 6, I will discuss how long-range interactions may counter-intuitively slow down the dynamical growth of quantum entanglement.

In Part II of the thesis I will discuss a radically different instance of long-range interactions, namely effective confining potentials between elementary excitations in quantum systems with local interactions. This occurrence is well known in particle physics, where it arises in the low-energy limit of the theory of fundamental interactions, and is relevant in low-dimensional condensed-matter physics, as well. In Chap. 7, I will review the physics of confinement in one-dimensional systems and establish a direct and precise bridge between its occurrence in lattice gauge theories and in condensed-matter models. Hence, in Chap. 8, I will show that quantum confinement provides a mechanism to stabilize nonthermal behavior and quasilocalization of excitations.

List of publications

Part I of the thesis is based on the following publications:

[1] **A. Lerose**, J. Marino, B. Žunkovič, A. Gambassi, A. Silva
Chaotic dynamical ferromagnetic phase induced by nonequilibrium quantum fluctuations
Phys. Rev. Lett. **120**, 130603 (2018)

[2] **A. Lerose**, B. Žunkovič, J. Marino, A. Gambassi, A. Silva
Impact of nonequilibrium fluctuations on pre-thermal dynamical phase transitions in long-range interacting spin chains
Phys. Rev. B **99**, 045128 (2019)

[3] **A. Lerose**, J. Marino, A. Gambassi, A. Silva
Prethermal quantum many-body Kapitza phases of periodically driven spin systems
Phys. Rev. B **100**, 104306 (2019) (*Editor's suggestion*)

[4] **A. Lerose**, S. Pappalardi
Origin of the slow entanglement growth in long-range interacting systems
arXiv:**1811.05505** (2018)

The content of the following publications is discussed in Part II of the thesis:

[5] P. P. Mazza, G. Perfetto, **A. Lerose**, M. Collura, A. Gambassi
Suppression of transport in nondisordered quantum spin chains due to confined excitations
Phys. Rev. B **99**, 180302 (2019) (*Rapid communication*)

[6] **A. Lerose**, B. Žunkovič, A. Silva, A. Gambassi
Quasilocalized excitations induced by long-range interactions in translationally-invariant quantum spin chains
Phys. Rev. B **99**, 121112 (2019) (*Rapid communication*)

[7] F. M. Surace, P. P. Mazza, G. Giudici, **A. Lerose**, A. Gambassi, M. Dalmonte
Lattice gauge theories and string dynamics in Rydberg-atom quantum simulators
arXiv:**1902.09551** (2019)

Forthcoming publications based on research involved in this thesis:

- **A. Lerose**, P. P. Mazza, G. Perfetto, F. M. Surace, M. Collura, A. Gambassi
  Slow dynamics by quantum confinement of excitations
  in preparation

- **A. Lerose**, S. Pappalardi
  Entanglement and chaos in collective quantum systems
  in preparation

Other articles published during the Ph.D. course:

[8] V. K. Varma, **A. Lerose**, F. Pietracaprina, J. Goold, A. Scardicchio
Energy diffusion in the ergodic phase of a many body localizable spin chain
J. Stat. Mech. **053101** (2017)

Contents

Invitation i

List of publications iii

1 Nonequilibrium behavior of quantum matter 1
1.1 Quantum statistical physics out of equilibrium 1
1.1.1 Quantum thermalization 2
1.1.2 Nonthermal stationary states and prethermalization . . . 7
1.1.3 Dynamical phase transitions 11
1.1.4 Nonequilibrium phases of periodically driven systems . . 12
1.1.5 Entanglement growth 14
1.2 Long-range interactions in quantum systems 18
1.2.1 Algebraically-decaying interactions in ultracold gases . . 19
1.2.2 Effective confining forces 22
1.3 Nonequilibrium physics with long-range interactions 23

I Impact of quantum fluctuations on mean-field nonequilibrium phenomena 28

2 Nonequilibrium dynamics of collective models 29
2.1 Mapping to semiclassical models 29
2.1.1 Permutational invariance 29
2.1.2 Fully-connected spin models 32
2.2 Equilibrium and out-of-equilibrium criticality 35
2.3 Driven dynamics: Kapitza phases 40
2.3.1 Phenomenology of driven dynamics 40
2.3.2 Theory: Effective Hamiltonian for fast driving 42
2.4 Finite-size (quantum) effects 45
2.4.1 Ground state and elementary excitations 46
2.4.2 Spectral properties 49
2.4.3 Relaxation and tunneling 50

3 Nonequilibrium spin-wave theory 54
3.1 Perturbative corrections to the equilibrium transition 54

3.2 Impact of dynamically excited spin waves on the collective spin dynamics . . . 61
3.3 Time-independent approach to nonequilibrium dynamics . . . 64

4 Collective pseudorandom behavior induced by quantum fluctuations 67
4.1 Effects of spin waves on mean-field dynamical criticality . . . 67
4.2 Generality of the chaotic dynamical phase . . . 72
4.3 Strong interactions: MPS-TDVP simulations . . . 74
4.4 Dynamical correlations of the local order parameter . . . 78
4.4.1 Modulated light-cone effect . . . 78
4.4.2 Dynamical correlations in the chaotic dynamical phase . . . 82
4.5 Effets of a variable quench rate . . . 82
4.6 Finite-size effects: Schrödinger cats . . . 84

5 Periodically driven dynamics: Quantum many-body Kapitza phases 88
5.1 Variable-range interactions . . . 88
5.2 Dynamically stabilized many-body phases . . . 91
5.3 Prethermalization and heating . . . 96
5.4 Quantum simulations with trapped ions . . . 98

6 Theory of entanglement dynamics 100
6.1 Entanglement entropy in infinite-range spin systems . . . 101
6.1.1 Two-boson formalism . . . 102
6.1.2 Ground-state correlations . . . 103
6.1.3 Entanglement entropy and spin squeezing . . . 105
6.2 Out-of-equilibrium growth of entanglement entropy . . . 106
6.2.1 Dynamical excitation of collective spin fluctuations . . . 108
6.2.2 Slow squeezing after generic quenches . . . 110
6.2.3 Fast squeezing at dynamical critical points . . . 111
6.2.4 Saturation of entanglement entropy . . . 112
6.3 Spatially-decaying interactions . . . 112
6.4 Numerical results for long-range quantum Ising chains . . . 114

II Slow dynamics by quantum confinement of excitations 122

7 Effective confining potentials in one-dimensional quantum systems 123
7.1 One-dimensional lattice gauge theories . . . 124
7.1.1 Lattice formulation of the Schwinger model . . . 124
7.1.2 U(1)-quantum link models . . . 127
7.1.3 Elimination of gauge degrees of freedom . . . 128
7.1.4 Elimination of matter degrees of freedom . . . 130
7.2 Confinement in one-dimensional condensed-matter systems . . . 132
7.2.1 Confinement in the quantum Ising chain . . . 133
7.2.2 Spectrum of mesonic excitations . . . 134
7.2.3 Equivalence to $1+1$-d lattice gauge theories . . . 136
7.3 "Confinement" in systems with long-range interactions . . . 139

7.3.1 Nonlinear confining potential between domain-walls . . 139
7.3.2 Residual attraction between "mesons" 142

8 Dynamical signatures of confinement 144
8.1 Confinement and slowdown of thermalization 145
8.2 Suppression of string breaking and lifetime of unstable mesons . 148
8.3 Slow diffusion of mesons 151
8.4 Continuum limit and the Schwinger effect 154
8.5 Quasilocalization of dilute particles 155
8.5.1 Suppression of energy transport in quantum Ising chains 156
8.5.2 Domain-wall localization in long-range quantum Ising chains 160
8.5.3 Particle localization in the lattice Schwinger model 166

A Broken permutational invariance 169

B Gaussian states 171

C Floquet Hamiltonian and high-frequency expansion 176

D Nonequilibrium spin-wave theory with weak disorder 177

E Semiclassical expansion for the dynamics of the Dicke model 182

F Fourier transform of $1/r^{\alpha}$ 185

G Bloch oscillations 189

Bibliography 193

Chapter 1

Nonequilibrium behavior of quantum matter

In this Introduction, we review the dynamical theory of isolated quantum many-body systems, and briefly outline the original results obtained in the doctoral research presented in this thesis.

1.1 Quantum statistical physics out of equilibrium

The textbook paradigm of statistical physics is represented by systems, the microscopic elementary constituents of which interact with their local surroundings by means of short-range forces. Most of the theory has been developed for such systems, due to their easier tractability and to their relevance in many domains of Physics. With the aim of better appreciating the extent to which long-range interactions give rise to qualitatively different phenomena, we shall begin by briefly reviewing the nonequilibrium statistical physics of quantum systems with short-range interactions. Emphasis on dynamical phenomena in isolated systems is motivated by the focus of the original work presented in this thesis.

Essentially all the results discussed in this thesis apply to quite general classes of quantum many-body systems, and we shall describe their expected generality throughout. However, for the sake of definiteness, simplicity, comparison with previous theoretical studies, and connection with a number of experiments, we shall often consider models of Ising-type magnets, with quantum spins-s on a lattice, interacting via ferromagnetic couplings $J_{\mathbf{r},\mathbf{r}'}$, and subject to magnetic fields. This class of models is defined by the Hamiltonian

$$\hat{H} = -\sum_{\mathbf{r},\mathbf{r}'} J_{\mathbf{r},\mathbf{r}'}\, \hat{\sigma}^x_{\mathbf{r}} \hat{\sigma}^x_{\mathbf{r}'} - h \sum_{\mathbf{r}} \hat{\sigma}^x_{\mathbf{r}} - g \sum_{\mathbf{r}} \hat{\sigma}^z_{\mathbf{r}}, \tag{1.1}$$

where the sums run over the sites of a lattice, and $\hat{\sigma}^\alpha_{\mathbf{r}} = \hat{s}^\alpha_{\mathbf{r}}/s$ are the operators corresponding to the normalized spin components in the $\alpha = x, y, z$ direction, acting on site $\mathbf{r}$. This represents a generalization of the case of spins one-half, where $s = 1/2$ and the $\hat{\sigma}^\alpha_{\mathbf{r}}$ reduce to the standard Pauli matrices. Such a

normalization allows us to keep track of the impact of quantum fluctuations, which is suppressed in the classical limit $s \to \infty$. The couplings $J_{\mathbf{r},\mathbf{r}'} \equiv J_r$ depend on the distance $r = |\mathbf{r} - \mathbf{r}'|$ between the two involved sites, and may have short or long range. The parameters g and h represent the transverse and longitudinal magnetic field intensity, respectively.

In a transverse field, i.e., for $g \neq 0$ and $h = 0$, and for generic ferromagnetic interactions $J_r \geqslant 0$, the system has an equilibrium zero-temperature phase transition upon reducing $|g|$, associated with a spontaneous breaking of its $\mathbb{Z}_2$ symmetry upon inverting the x-components of all spins. The longitudinal magnetization $\langle \hat{\sigma}^x_{\mathbf{r}} \rangle$ witnesses an abrupt change from a unique paramagnetic ground state with $\langle \hat{\sigma}^x_{\mathbf{r}} \rangle = 0$ for $|g| \geqslant g_{cr}$ to a pair of ferromagnetic ground states with $\langle \hat{\sigma}^x_{\mathbf{r}} \rangle_{\pm} = \pm m \neq 0$ for $|g| < g_{cr}$. The universality class of this quantum phase transition is the same as that of the $d+1$-dimensional classical Ising model [9]. Since this model has a dynamical critical exponent $z = 1$, the large-scale structure of the system in the vicinity of its critical point (scaling region) is captured by a relativistic field theory, and its universal properties are described by conformal field theory [10].

The possible emergence of a nonvanishing order parameter at a finite energy density above the ground state depends on the dimensionality d and on the range of the interactions. In particular, this occurs for $d \geqslant 2$ when the range is short. In this case, the universality class of the thermal phase transition is the same as that of the d-dimensional classical Ising model [9]. One-dimensional systems cannot support ordering in excited states [9, 11], unless interactions have a sufficiently long range (see below for discussion of this).

1.1.1 Quantum thermalization

Studies on nonequilibrium dynamics and thermalization of *isolated* quantum many-body systems are motivated both by the very foundations of quantum statistical mechanics [12, 13], and by recent experiments with ultracold matter. This versatile experimental platform currently represents one of the fundamental means of investigation in quantum physics: Experimentalists are able to cool down atoms, ions and molecules to very low temperatures, isolate them from the external environment to a high degree of accuracy, tune their interaction parameters, manipulate their configuration, and observe their time-evolution with remarkable resolution [14–21]. Such an unprecedented access to the equilibrium and real-time behavior of nearly-isolated quantum many-body systems has vigorously revived the interest in the theoretical foundations of their thermodynamical description, i.e., how thermal equilibrium is approached within Hamiltonian dynamics, and more generally in the theoretical characterization of their nonequilibrium dynamics, including the possible existence of nonthermal stationary or quasistationary states.

The theoretical foundations of classical statistical mechanics in its standard formulation, rely on concepts of ergodic and chaos theory [22, 23]. However, due to unitarity of time-evolution, strict mathematical analogs of such classical concepts are absent in quantum mechanics. Despite research in this field started

in the early days of quantum mechanics [12], the characterization of ergodic and chaotic behavior of quantum systems still presents controversial aspects and unresolved issues. Several studies have clarified that the correspondence with classical counterparts of ergodicity and chaos occurs through the evolution of observables rather than of states — see, e.g., the pioneering investigation in Ref. [24], and the recent Refs. [25–28]. In particular, the correspondence principle in the classical limit requires that the quantum expectation values of relevant observables in energy eigenstates must reproduce classical infinite-time-averages at the same energy. In this view, quantum ergodic systems can be defined as those which reproduce microcanonical averages within each single energy eigenstate. The central idea that single energy eigenstates describe ensemble behavior has been carried over to quantum many-body systems and extended to systems without a natural classical limit. The resulting statement that quantum averages of local observables in every single energy eigenstate $|E_i\rangle$ coincide with thermal averages at the corresponding temperature $\beta = \beta(E_i)$ is known as the eigenstate thermalization hypothesis (ETH) [29–31]. Thanks to both its theoretical consistency and strong numerical evidence, ETH is currently regarded as the fundamental characterization of thermalization in quantum physics.

In its more refined version, the ETH is an ansatz for matrix elements of local observables. If $\{|E_i\rangle\}_i$ is the energy eigenbasis of a quantum many-body Hamiltonian $\hat{H}$, and $\hat{A}$ is a local observable of the system, the ETH asserts that, in each symmetry sector of $\hat{H}$,[1] one can write

$$\langle E_i|\hat{A}|E_j\rangle = \mathcal{A}(\bar{E})\delta_{i,j} + e^{-S(\bar{E})/2} f_A(\bar{E},\omega) R_{i,j} \tag{1.2}$$

where $\bar{E} = (E_i + E_j)/2$, $\omega = E_i - E_j$, and $S(E)$ is the thermodynamic entropy function (i.e., the logarithm of the number of eigenstates at energy density E/N). The content of ETH is that the functions $\mathcal{A}$ and f_A depend *smoothly* on their arguments in the thermodynamic limit, and $R_{i,j}$ is a random variable with vanishing mean and unit variance. See Fig. 1.1 for an illustration. Provided ETH is satisfied, for any initial state $|\Psi_0\rangle$ in a microcanonical energy shell at energy $\bar{E}$, any local observable $\hat{A}$ thermalize to $\mathcal{A}(\bar{E})$, meaning that the dynamical expectation value $\langle\Psi_0|\hat{A}(t)|\Psi_0\rangle$ of $\hat{A}$ spends most of the time close to $\mathcal{A}(\bar{E})$ in the long run [27,28].

Nonequilibrium dynamics can be studied by preparing a system in a state which is not a stationary state of its Hamiltonian $\hat{H}$. Thermalization is usually studied in the framework of quantum quenches. A quantum quench is a simple protocol to drive a system out of equilibrium, which consists in preparing it in the ground state $|\Psi_0\rangle$ of its Hamiltonian $\hat{H}_0$, and hence changing the system Hamiltonian to a different one, $\hat{H} \neq \hat{H}_0$, which governs the subsequent time-evolution $|\Psi(t)\rangle = e^{-i\hat{H}t}|\Psi_0\rangle$. Unless $\hat{H}$ commutes with $\hat{H}_0$, the resulting evolution is generally nontrivial, meaning that local observables and their quantum correlations change in time as the state of the system evolves. One

[1] for example, the translation-invariant parity symmetric sector for a translation- and reflection-symmetric Hamiltonian

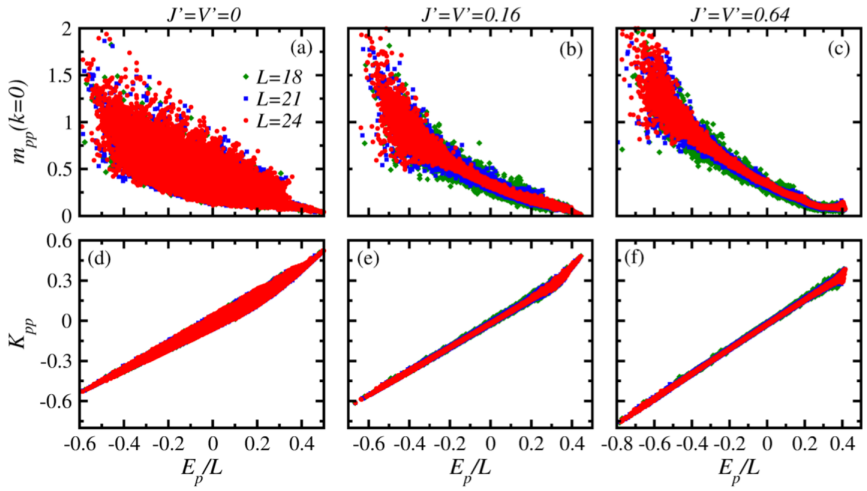

Figure 1.1: Numerical illustration of the validity of the eigenstate thermalization hypothesis, taken from Ref. [31]. The plots show expectation values of some relevant physical observables in energy eigenstates, as a function of energy density E_p/L, for a chain of interacting hardcore bosons. The parameters J' and V' are coefficients of integrability-breaking interactions in the Hamiltonian. In panels (b), (c), the "cloud" of eigenstate expectation values shrinks to a limiting curve in the thermodynamic limit, meaning that observables become smooth functions of energy, in agreement with the ETH.

speaks of a global and sudden quantum quench, when the protocol consists in modifying a parameter uniformly in the system and "instantaneously" — i.e., much faster than the system's dynamical time scales. A simple example is to prepare the quantum Ising magnet in Eq. (1.1) in the ground state (or one of its ground states) with a certain transverse magnetic field g_0, and then quenching the field to a different value $g_0 \to g$ at time $t = 0$. Generalizations of this protocol include inhomogeneous and local quenches, in which two subsystems in separate equilibrium states are suddenly joined together, or local impurities are suddenly created. Moreover, time-dependent ramps may be considered, in which the final Hamiltonian $\hat{H} = \hat{H}(t = \tau)$ is reached continuously from $\hat{H}_0 = \hat{H}(t = 0)$ through a continuous variation of parameters in $\hat{H}(t)$ between times 0 and τ: For $\tau \to 0$ one recovers sudden quenches, whereas for $\tau \to \infty$ one may approach the ideal adiabatic limit.

Protocols described above and variations thereof provide physically meaningful procedures to initialize a quantum many-body system in a nonequilibrium state. It should be noted that not all wavefunctions represent physically meaningful states which can be prepared by operative protocols. For example, consider the state $|\chi\rangle = (|E_n\rangle + |E_m\rangle)/\sqrt{2}$, a superposition of only two energy eigenstates with macroscopically separated energy values: there is no operative procedure to generate the state $|\chi\rangle$ in practice. In fact, it is known that meaningful initial states, under general conditions, have to satisfy a set of strict physical properties. In particular, they obey the so-called *cluster decomposition principle*,[2] which states that arbitrary connected quantum correlations decay upon increasing the

[2] this is a basic principle (axiom) in relativistic quantum field theories [32]

distance: If $\hat{O}_{\mathbf{r}_i}$, with $i = 1, 2, \ldots$, are localized observables in a finite region of space surrounding the point $\mathbf{r}_i$,

$$\langle \hat{O}_{\mathbf{r}_1} \hat{O}_{\mathbf{r}_2} \ldots \hat{O}_{\mathbf{r}_p} \rangle \quad \to \quad \langle \hat{O}_{\mathbf{r}_1} \rangle \langle \hat{O}_{\mathbf{r}_2} \rangle \ldots \langle \hat{O}_{\mathbf{r}_p} \rangle \qquad \text{as } |\mathbf{r}_i - \mathbf{r}_j| \to \infty \text{ for all } i \neq j \tag{1.3}$$

for any integer p. As a consequence, the distribution of collective local observables of the form $\hat{A} = \sum_i \hat{A}_i$ in physical initial states (the sum runs over the degrees of freedom), has to be peaked around an extensive value $A = \langle \hat{A} \rangle \propto N$, where N is the number of degrees freedom, with subextensive fluctuations $\Delta A \equiv \sqrt{\langle \hat{A}^2 \rangle - \langle \hat{A} \rangle^2} \propto N^\gamma$, with $\gamma < 1$. It is straightforward to see that the state $|\chi\rangle$ above violates both properties if $E_n - E_m = \mathcal{O}(N)$: In fact, taking $\hat{A} = \hat{H} = \sum_i \hat{H}_i$, one finds $\Delta H \propto N$ and, by this very equation, $\langle \hat{H}^2 \rangle - \langle \hat{H} \rangle^2 = \mathcal{O}(N^2)$, whence, assuming translation invariance for simplicity, $|\langle \hat{H}_i \hat{H}_j \rangle - \langle \hat{H}_i \rangle \langle \hat{H}_j \rangle| \geqslant \text{const} > 0$ for sufficiently far apart points i and j.

In a global quantum quench, a finite amount of energy density above the ground state is injected into each local degree of freedom of the system, as the Hamiltonian is suddenly changed everywhere in space. The total post-quench energy $E = \langle \Psi_0 | \hat{H} | \Psi_0 \rangle$ is related to the work performed by the external drive, and is determined by the depth of the quench (in the example above, the quantity $g - g_0$). The corresponding temperature increases from zero for vanishing quench depth, to typically large values for deep quenches, in a continuous fashion. As remarked above, the energy distribution of generic post-quench states in the thermodynamic limit is peaked around E with subextensive fluctuations. In other words, nonequilibrium states generated by quenches live in microcanonical energy shells corresponding to a uniquely defined temperature.

The primary quantities of interest in the post-quench nonequilibrium dynamics are local observables $\mathcal{O}(\mathbf{r}, t) = \langle \hat{O}_{\mathbf{r}}(t) \rangle$, which are directly relevant for thermalization, as they are expected to approach the thermal value determined by the initial energy only. Indeed, in the context of global quenches, quantum thermalization can be formalized as the convergence in time of the expectation values of all local observables to their thermal values at a temperature $1/\beta_E$ determined by the energy $E = \langle \Psi_0 | \hat{H} | \Psi_0 \rangle$ of the initial state, i.e.,

$$\lim_{t \to \infty} \lim_{N \to \infty} \langle \Psi_0 | e^{it\hat{H}} \hat{O}_{\mathbf{r}} e^{-it\hat{H}} | \Psi_0 \rangle = \mathrm{Tr} \left(\hat{O}_{\mathbf{r}} \frac{e^{-\beta_E \hat{H}}}{Z} \right), \tag{1.4}$$

with β_E determined by the equation

$$\langle \Psi_0 | \hat{H} | \Psi_0 \rangle = E = \mathrm{Tr} \left(\hat{H} \frac{e^{-\beta_E \hat{H}}}{Z} \right). \tag{1.5}$$

We remark that taking the thermodynamic limit $N \to \infty$ first is crucial for the existence of the long-time limit: In a finite system, recurrences occur over exponentially long times in the system size [33], and one must resort to time-averages in order to properly define thermalization, as mentioned above [27]. The collection of expectation values $\langle \Psi | \hat{O}_A | \Psi \rangle$ of local observables $\hat{O}_A$ with

support in a given finite region A, is encoded in the reduced density matrix $\hat{\rho}_A \equiv \mathrm{Tr}_{\bar{A}} |\Psi\rangle\langle\Psi|$, where $\bar{A}$ denotes the spatial complement (i.e., the exterior) of the region A, and the partial trace $\mathrm{Tr}_{\bar{A}}$ is performed over the Hilbert space of degrees of freedom in $\bar{A}$ only. This assertion follows from the identity $\langle\Psi|\hat{O}_A|\Psi\rangle = \mathrm{Tr}_A(\hat{\rho}_A \hat{O}_A)$. Due to the arbitrariness of the local observable $\hat{O}_{\mathbf{r}}$ in Eq. (1.4), the above characterization of quantum thermalization is equivalent to the convergence in time of local reduced density matrices of the system to the thermal state, i.e.,

$$\lim_{t\to\infty} \lim_{N\to\infty} \rho_A(t) = \mathrm{Tr}_{\bar{A}} \left(\frac{e^{-\beta_E \hat{H}}}{Z} \right). \tag{1.6}$$

Equation (1.6) highlights that quantum thermalization raises an apparent information paradox. In fact, on the one side, the global time-evolution $|\Psi_0\rangle \mapsto |\Psi(t)\rangle$ is unitary in Hilbert space, and thus it preserves in time all possible information. On the other side, thermalization implies that the asymptotic values of all relevant observables is encoded in the thermal state $e^{-\beta_E \hat{H}}/Z$, which depends on the initial state through a single number only, namely, the initial energy E that determines β_E. Accordingly, time-evolution is equivalent to performing a coarse-graining in the space of initial wavefunctions, associated with a drastic information erasure: All possible wavefunctions $|\Psi_0\rangle$ with initial energy E evolve into states described by the same density matrix $e^{-\beta_E \hat{H}}/Z$.

Similarly to the classical version of the irreversibility paradox, the resolution lies in the class of observables considered in the thermalization process, which is a restricted class of accessible observables of interest, usually *local* observables. Although the global wavefunction evolves unitarily, the reduced state of each subsystem with a finite spatial extent approaches a thermal state during time-evolution. The information originally encoded in nonthermal values of local observables is not irreversibly erased, but becomes *nonlocal*, i.e., gets spread to distant degrees of freedom.

This occurrence may be visualized via spatiotemporal diagrams of quantum correlation spreading after a quench. Equal-time correlation functions $\mathcal{C}(\mathbf{r}, \mathbf{r}', t) = \langle \hat{O}_{\mathbf{r}}(t) \hat{O}_{\mathbf{r}'}(t') \rangle$ give information on instantaneous quantum correlations existing between degrees of freedom far apart in the system. The spatiotemporal dependence of equal-time two-body correlations gives important insights on the propagation and "scrambling" of local quantum information encoded in the initial wavefunction. A typical example of such a diagram is reported in Fig. 1.2. Its most prominent aspect is the light-cone structure [35], which reflects the so-called Lieb-Robinson bound [36]. This rigorous result states that in quantum systems on a lattice, the support of an operator $\hat{O}_{\mathbf{r}_0}$, initially localized in a finite region around the site $\mathbf{r}_0$ and time-evolving (in Heisenberg picture) with a local Hamiltonian $\hat{H}$, spreads in space with a finite maximal velocity v_{LR}, meaning that the weight of the time-evolved operator outside the region $|\mathbf{r} - \mathbf{r}_0| \leqslant v_{LR} t$ is exponentially suppressed as $|\mathbf{r} - \mathbf{r}_0| - v_{LR} t \to \infty$. It is possible to derive that quantum correlation spreading after a quench is exponentially confined within a light-cone spacetime region characterized by a velocity

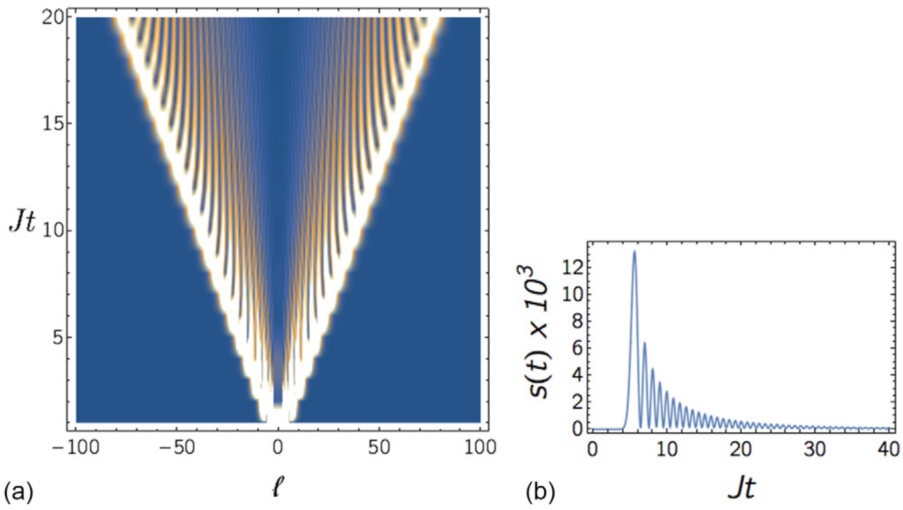

Figure 1.2: Illustration of the light-cone spreading of quantum correlations in quench dynamics, from Ref. [34]. The plot shows the space and time dependence of equal-time density-density connected correlation function after a homogeneous quench in a chain with free fermionic quasiparticles. The stationary part has been subtracted. The space slice on the right shows the arrival of the wavefront followed by relaxation to the GGE prediction (see Sec. 1.1.2 below).

v_{max} bounded above by the Lieb-Robinson velocity v_{LR} [34,37–39]. In strongly chaotic quantum systems, ballistic spatial spreading of equal-time quantum correlations does take place, which provides us with an intuitive picture on the resolution of the quantum thermalization "paradox" mentioned above. However, it is important to emphasize the fact that the occurrence of correlation spreading is *not* a sufficient condition for quantum thermalization, as explained below.

1.1.2 Nonthermal stationary states and prethermalization

As suggested above, approach to thermal equilibrium may be described as nonlocal scrambling of quantum information during the nonequilibrium evolution. As it is well known, the Gibbs state $\hat{\rho}_{GE} = \exp(-\beta\hat{H})/Z$ is the maximal entropy state compatible with a given energy density $e(\beta)$, i.e., "the most random" state that a system may locally attain while conserving energy. In this sense, a thermalizing system loses all the original local information encoded in its wavefunction, except the only piece that it is constrained to retain, i.e., how much energy density it has. Since locality plays a crucial role in this description, it should be clear that local conservation laws affect the thermalization process. In particular, if $\hat{Q}_1, \hat{Q}_2, \ldots$ are additional local conserved quantities, then the asymptotic state reached by the system must retain memory of their values. Hence, it is natural to conjecture that the asymptotic state is described by a generalized Gibbs state of the form

$$\hat{\rho}_{GGE} = \exp\Big(-\sum_j \lambda_j \hat{Q}_j\Big)/Z, \tag{1.7}$$

where we define for convenience $\hat{Q}_0 \equiv H$. The Lagrange multipliers λ_j are uniquely fixed by the expectation values of the conserved quantities $\hat{Q}_j$ in the initial state. Such a state is "the most random" state compatible with all local conservation laws.

Usually, local conservation laws are associated with global symmetries of the Hamiltonian, such as rotational symmetry in magnetic systems, or the conservation of the number of particles in nonrelativistic gases. In this case, the modified Gibbs state above is known as the grand-canonical state in standard thermodynamics. However, certain systems may possess a large set of nontrivial conservation laws. By analogy with classical mechanics, a quantum system is called *integrable* when conserved quantities commute with each other and their number equals the number of degrees of freedom.[3] While the investigation of the nonequilibrium dynamics of generic quantum many-body systems is usually restricted to numerical computations, integrable systems often offer viable analytical techniques to determine the dynamics of local observables and correlation functions.

The simplest case of integrability is given by systems of noninteracting particles, and by models which can be mapped to quadratic Hamiltonians. Such systems constitute excellent approximations for a variety of physical situations. A primary example in condensed matter is provided by mechanical vibrations of crystal lattices, which may often be treated as noninteracting bosons (phonons). A less trivial example is given by one-dimensional quantum magnets described by the transverse-field quantum Ising chain

$$\hat{H} = -J \sum_{i=1}^{L} \hat{\sigma}_i^x \hat{\sigma}_{i+1}^x - g \sum_{i=1}^{L} \hat{\sigma}_i^z. \tag{1.8}$$

In this case, it has been shown [41] that the model can be mapped to the Hamiltonian of free fermionic quasiparticles,

$$\hat{H} = E_{GS} + \sum_k \varepsilon_k \hat{\gamma}_k^\dagger \hat{\gamma}_k \tag{1.9}$$

with $\{\gamma_k^\dagger, \gamma_{k'}^\dagger\} = \delta_{k,k'}$ fermionic modes labelled by quasimomenta $k = 2\pi n/L$, with $n = 0, 1, \ldots, L-1$, and $\varepsilon_k = 2\sqrt{J^2 + g^2 - 2gJ\cos k}$. Interestingly enough, the free fermionic quasiparticles of this system have a different nature in the ordered ($|g| < J$) and disordered ($|g| > J$) phases: In the former case, they represent domain-wall excitations separating two magnetically ordered regions, whereas in the latter they represent spin waves, i.e., propagating local distortions of the paramagnetic spin alignment.

The conserved quantities in this class of systems are combinations of the occupation number in the normal modes which diagonalize the Hamiltonian. In translation-invariant systems, such modes are Fourier modes (for example, in the quantum Ising chain in Eq. (1.8) above, $\hat{n}_k \equiv \hat{\gamma}_k^\dagger \hat{\gamma}_k$). While Fourier modes are individually nonlocal, it can be shown that suitable linear combinations of

[3] Note that the notion of quantum integrability is not unambiguously defined, see Ref. [40].

such modes — essentially, their spatial Fourier transform — provides one with local conservation laws (see, e.g., Ref. [34]).

Beyond systems with free quasiparticles, there exist a number of *interacting* integrable one-dimensional quantum systems. Such systems typically have strictly local or fine-tuned interactions, and are amenable to beautiful analytical (Bethe-ansatz solution) and algebraic (Yang-Baxter theory) descriptions, which are, however, beyond the scope of this Introduction [42].

The stationary state attained by an integrable system driven out of equilibrium must retain memory of its infinite set of local conservation laws. Such a state may be written in the form (1.7) and is referred to as the generalized Gibbs ensemble (GGE) [11,43–55]. Note that the approach to the GGE still represents a dramatic erasure of local information: In fact, one has one conservation law per degree of freedom, while the complexity of the initial many-body wavefunction is exponential in the number of degrees of freedom. For this reason, one speaks of *generalized thermalization* for integrable systems. Also, it should be emphasized that local conserved quantities may be labelled according to the increasing extent of the support of their local densities. In order to describe the local asymptotic state of a finite region, one typically needs to include in the GGE only a finite number of conserved quantities, of the order of the size of the region [34].

To summarize what we have discussed so far, after a quantum quench, "generic" quantum many-body systems are expected to approach the maximal entropy Gibbs state, while systems with nontrivial local conservation laws are expected to approach a generalized Gibbs state with lower thermodynamic entropy. An illustrative picture for this distinction is presented in Fig. 1.3, where GGEs are represented as a smooth manifold in the space of reduced density matrices, spanned by the Lagrange multipliers, and thermal Gibbs states are represented by a one-dimensional curve on this manifold. Such a manifold is thus an attractor for the dissipative dynamics of local reduced density matrices.

Thermalization and generalized thermalization are believed to be generically "fast", i.e., to take place over a time scale given by the inverse of the typical energy scale of the system. However, interesting phenomena may arise when two or more competing energy scales are present in the system. A paradigmatic situation is given by a weakly-perturbed Hamiltonian,

$$\hat{H}' = \hat{H} + \epsilon \hat{V}, \tag{1.10}$$

where $\hat{H}$ is integrable (has a number of local conservation laws) and $\hat{V}$ breaks integrability (violates the conservation laws). The dimensionless parameter $\epsilon \ll 1$ is such that the energy scale of the perturbation is small compared to the unperturbed Hamiltonian. In this case, the time-evolution after a quench (from the ground state of a different Hamiltonian $\hat{H}_0$) will feel the effect of the perturbation $\hat{V}$ only over a parametrically long time scale in $1/\epsilon$, which may be much larger than the generalized thermalization time of that initial state evolved with $\hat{H}$. Accordingly, one expects that the system will first quickly *prethermalize* to a generalized Gibbs state defined by the unperturbed Hamiltonian $\hat{H}$, and that such a state will subsequently slowly approach the final Gibbs state of $\hat{H}'$

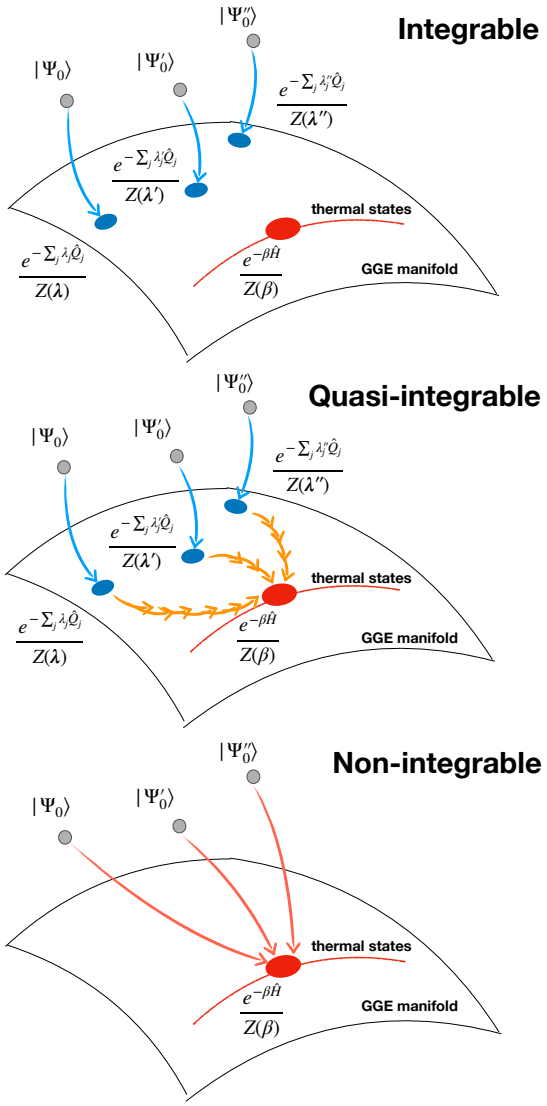

Figure 1.3: Cartoon illustration of the relaxation dynamics after a homogeneous quench (generalized thermalization, prethermalization and conventional thermalization). The cartoons show the system evolution starting from three different pre-quench initial states with equal post-quench energy density. In agreement with the theory of quantum thermalization (see the main text), evolution should be imagined in the space of reduced density matrices of finite subsystems. (Accordingly, in all state labels, partial trace over the complement of the subsystem should be understood.) The surface depicted in each cartoon represent the submanifold of GGE density matrices. The red curve represents thermal (Gibbs) density matrices. Top panel: Integrable systems [$\varepsilon = 0$ in Eq. (1.10)] relax to stationary states described by generalized Gibbs ensembles, which account for all their local conservation laws (*generalized thermalization*). Middle panel: quasiintegrable systems [as in Eq. (1.10) with $\varepsilon \ll 1$] first relax to quasistationary states described by generalized Gibbs ensembles associated with the nearby integrable Hamiltonian (*prethermalization*). Hence, such states are expected to slowly drift towards the asymptotic thermal state with a speed regulated by ε and vanishing in the integrable limit $\varepsilon \to 0$. Bottom panel: Generic (i.e., nonintegrable) systems [e.g., $\varepsilon \sim 1$ in Eq. (1.10)] relax to thermal stationary states described by the Gibbs ensemble (*conventional thermalization*).

on a longer time scale.

This phenomenon may be pictured as a slow drift along the GGE manifold, as illustrated in Fig. 1.3, whereby the Lagrange multipliers $\boldsymbol{\lambda} = (\lambda_0, \lambda_1, \lambda_2, \dots)$ evolve with a parametrically small speed in ϵ towards the point $(\beta, 0, 0, \dots)$. Such a prethermalization scenario has been suggested and studied with methods of field theory and quantum many-body theory [56–66]. However, the generality of its occurrence and its quantitative features are not yet fully understood to present date [67–75].

1.1.3 Dynamical phase transitions

The fate of long-range order in quench dynamics represents a source of interesting phenomena. Consider an interacting quantum many-body system in an equilibrium, low temperature, ordered phase [e.g., a ferromagnet as in Eq. (1.1) with $g_0 = h_0 = 0$], and drive it out of equilibrium by quenching a control parameter (e.g., the transverse magnetic field, $g_0 = 0 \to g \neq 0$). The initial long-range ordering is destabilized, and it is natural to investigate the fate of the order parameter in the nonequilibrium dynamics following the quench. If fast thermalization takes place as described in Sec. 1.1.1 above, the order parameter will show a behavior consistent with its equilibrium finite-temperature phase diagram. On the other hand, if the system shows metastable or quasisteady behavior over intermediate time scales before thermalization, genuinely nonequilibrium phenomena may occur. This scenario, which focuses on prethermal dynamics, typically occurs in systems close to integrability, as described in Sec. 1.1.2. In particular, the system lingers close to a state in which conventional equilibrium statistical mechanics does not apply, making the onset of novel types of phases of matter and critical behavior possible.

Quantum quenches from a broken-symmetry equilibrium state such as those proposed above, give rise to an interesting instance of nonequilibrium critical phenomena. These dynamical phase transitions (DPTs) [76–94] are characterized by a nonequilibrium order parameter exhibiting a finite or vanishing long-time temporal average, depending on whether the quantum model under consideration is quenched below or above an associated dynamical critical point separating the dynamical ordered phase from the dynamical disordered one. The behavior at the transition is believed to be universal, and its properties are generally different from those of the equilibrium counterpart [83, 84, 87]. In addition, in systems with local interactions, the scaling of dynamical correlation and response functions can distinguish the different phases [90, 95, 96], while quenching across dynamical critical points imprints a scaling behavior reminiscent of dynamical coarsening [97–100]. A recent experiment [101] has shown that these dynamical phase transitions can be realized with ultracold trapped ions which simulate long-range interacting Ising ferromagnets (see also Sec. 1.2.1 below).

A second notion of DPT, proposed in Ref. [102], has been recently studied experimentally in Ref. [103]. This notion, however, is not directly related to the existence of a local order parameter characterizing the various dynamical

phases, but rather to a nonanalytic behavior in the time dependence of the return probability amplitude [104]. Considering, for example, global quenches of the transverse field in the one-dimensional quantum Ising chain, a quench across the equilibrium critical point, starting from the ground state of the ferromagnetic phase and ending into the paramagnetic one, will induce a sequence of cusps in the time-resolved return probability amplitude [102, 105]. These two notions of dynamical phase transition are in general distinct, and therefore they may even not occur concomitantly in the same model. However, a connection has been pointed out whenever both DPTs are present [106] (see also Refs. [107, 108]).

The study of the two instances of DPTs is typically restricted to either integrable or mean-field models, or to numerical works, while Gaussian fluctuations have been accounted for in a limited number of cases [86, 87, 90, 97–100]. In Chap. 4, we shall study DPTs in nonintegrable models that, despite possessing nontrivial fluctuations and a nonvanishing order parameter, are amenable to an analytical approach, which we preliminarily present in Chap. 3.

1.1.4 Nonequilibrium phases of periodically driven systems

We have reviewed above the theory of extended quantum systems driven away from equilibrium and then let to evolve in isolation from external sources or work and heat. A complementary topic of great interest is constituted by persistent driving in time, and in particular by cyclically repeated driving.

This occurrence is ubiquitous in natural phenomena and in applications, ranging from electronics to condensed matter physics [109–111]. Understanding driven systems is of paramount importance in the context of quantum technologies, since they can both realize peculiar phases of matter and help manipulating quantum information [112, 113]. In fact, time-periodic protocols have been theoretically proposed and experimentally realized with ultracold gases to engineer a variety of systems, including topological phases [114, 115], time crystals [116–120], exotic Bose-Einstein condensates [121–124]. All of them have no equilibrium counterparts, i.e., they do not exist in the absence of driving. For instance, a gas of bosons may condense in a nonuniform, π-quasimomentum state in the presence of a rapidly varying electric field or of a shaken lattice [121–124]. Similarly, while invariance under time-translations cannot be broken at equilibrium, the formation of discrete time crystals under the effect of AC-driving has been theoretically proposed [116–118] and experimentally observed [119, 120]. Employing suitable periodic drives for designing and realizing exotic phases of matter is known in the literature as *Floquet-engineering*.

In systems with few degrees of freedom, a periodic drive might have spectacular effects, such as the stabilization of a pendulum upside down. A theory of this phenomenon was formulated by P. Kapitza in 1951 [125], and has found several experimental applications, e.g. in particle synchrotrons [126] and in Paul traps [127] (see also Sec. 1.2.1). More recently, it has been applied to quantum many-body physics out of equilibrium, for instance in order to stabilize Bose-Einstein condensate clouds in two and three spatial dimensions [128, 129], to prevent spin mixing in spinor condensates [130, 131], and to stabilize π-modes

in driven bosonic Josephson junctions [132, 133].

External drives perform work on a system, and hence driven systems exchange energy with their driving agents. The dynamics of the internal energy represents one of the most natural and interesting questions in the theory and applications of driven systems. According to the second principle of thermodynamics, in generic conditions the internal energy increases indefinitely upon continuously driving.

Fine-tuned exceptions to this generic behavior are possible. The most important one is constituted by few-body systems, such as the ones described above in connection with dynamical stabilization. In this case, the system typically has a finite set of characteristic frequencies associated with certain states. Consequently, a nonresonant drive — characterized by a frequency incommensurate with the system's eigenfrequencies — might induce a nonequilibrium stationary state at a finite energy density, with a stable periodic energy exchange between the system and the drive. In the many-body context, this occurrence naturally extends to systems with free stable quasiparticles, such as the quantum Ising chain in a transverse field, cf. Eq. (1.8). This system can be mapped to an ensemble of decoupled two-level systems, i.e., the free fermionic quasiparticles of the model. These excitations have a finite bandwidth. If the driving respects this integrable structure, being, for instance, a periodic modulation of the transverse field $g(t) = g_0 + \delta g \cos(\Omega t)$, then the system reduces to an ensemble of single-body driven systems,

$$\hat{H}(t) = -\sum_k \Big[J \cos k - g(t) \Big] \Big(\hat{c}_k^\dagger \hat{c}_k - \hat{c}_{-k} \hat{c}_{-k}^\dagger \Big) + i\, J \sin k \Big(\hat{c}_k^\dagger \hat{c}_k^\dagger + \hat{c}_{-k} \hat{c}_{-k} \Big), \tag{1.11}$$

and the drive induces nontrivial nonequilibrium stationary states [134–136].

However, this situation is hardly realized in quantum many-body systems. Upon repeated driving, generic systems are expected to heat up at long times to infinite-temperature states, indistinguishable from featureless random states in Hilbert space. This has been numerically shown to occur even in rather small systems of $\gtrsim 20$ interacting elementary units, whereby the long-time behavior is described by random-matrix theory [137]. Heating thus represents the most important issue in the realization of nontrivial, dynamically stabilized *phases* of driven quantum many-particle systems. In this respect, there is presently no evidence that heating can be circumvented, beyond the above mentioned fine-tuned integrable driven systems.

While heating is hard to overcome, it has been recently recognized that it is actually easy to dramatically slow it down [138–141]. In fact, fast driving at a frequency Ω much larger than the *single-particle* energy scale (bandwidth) J of the system, results in an exponentially suppressed heating rate.

$$\left| \frac{d \langle \hat{H}(t) \rangle}{dt} \right| \leqslant \exp\left(- \text{const} \times \frac{\Omega}{J} \right). \tag{1.12}$$

According to this scenario, dubbed *Floquet-prethermalization*, the time-evolved

system at stroboscopic times (integer multiples of the driving period) preliminarily prethermalizes to a Gibbs state $e^{-\beta_{\rm eff}\hat{H}_{\rm eff}}/Z$ of an effective static Hamiltonian $\hat{H}_{\rm eff}$, close to the time-averaged driving Hamiltonian,

$$\hat{H}_{\rm eff} = \frac{1}{T}\int_0^T dt\, \hat{H}(t) \quad + \mathcal{O}\left(J^2/\Omega\right) \tag{1.13}$$

with $T \equiv 2\pi/\Omega$. Hence, such a quasistationary state slowly drifts towards infinite-temperature over an exponentially long time scale $t^* \sim \exp(\text{const} \times \Omega/J)$ in the ratio between the driving frequency and the single-particle bandwidth. The first signatures of this occurrence have been put forward in Ref. [138]. The general theory has been fully detailed and made rigorous independently by two groups in Refs. [139–141]. This result constitutes the theoretical basis for the realization of Floquet-engineered phases of matter, which are expected to be stable for parametrically long temporal stages in generic interacting driven systems. Numerical validation of the above Floquet-prethermalization scenario has been studied in Ref. [142], see Fig. 1.4.

The following argument based on standard perturbation theory offers an intuitive picture of the exponential slowdown of heating in high-frequency driven systems [139–141]. A periodically modulated perturbation $\hat{V}(t+T) \equiv \hat{V}(t)$ at frequency $\Omega \equiv 2\pi/T$ to a static Hamiltonian $\hat{H}_0$, may be thought as a source of "photons" at frequency Ω, which induce transition between proper energy levels E_i, E_j of $\hat{H}_0$, with $E_i - E_j \approx \pm\Omega, \pm 2\Omega, \ldots$ (recall $\hbar = 1$ in our units). The spectrum of a quantum many-body system is dense and extensive in the thermodynamic limit, which allows the drive to mix states at arbitrary energy scales and heat up the system. However, the elementary transitions induced by the perturbation $\hat{V}$ at first order, involves only energy changes of the order of the single-particle energy bandwidth J, because the drive induces a configurational change of few particles only in each transition. Consequently, if $\Omega \gg J$, all first-order transitions are far off-resonant, and they will result in small energy fluctuations. Energy "delocalization" by resonant processes requires a number of elementary transitions n^* such that $\Delta E \sim n^* J \approx \Omega$. This occurs only to high order $n^* \sim \Omega/J \gg 1$ in perturbation theory. Therefore, heating takes a long time to take place. This argument represents the core intuition underlying the formal analysis in Refs. [139–141].

1.1.5 Entanglement growth

The problems addressed in the previous Sections represent the quantum counterpart of corresponding ones in classical many-body dynamics. The nature of quantum systems often allows one to pose simpler and more natural questions than their classical counterpart. It is also interesting to investigate quantum phenomena which, at least superficially, do not possess a classical analog. One important example in this class is provided by entanglement dynamics.

Entanglement is one the key concepts in quantum mechanics and its understanding at the deepest level constitutes one of the major efforts of contemporary

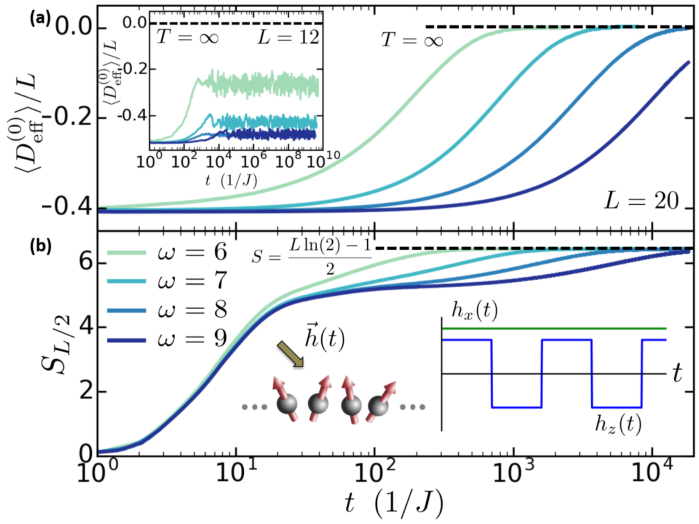

Figure 1.4: Numerical illustration of slow heating in periodically driven quantum many-body systems at high frequency (from Ref. [142]). According to the theory in Refs. [140,141], the system is predicted to linger in a quasistationary Gibbs ensemble of an effective static Hamiltonian for times which grow exponentially upon increasing the driving frequency, before eventually reaching their infinite-temperature value. Top panel: stroboscopic time-dependence of the average energy density of a quantum Ising chain with a periodically-varying external field (see the quoted article for details). For increasing values of the driving frequency (curves from left to right), heating to infinite-temperature moves exponentially fast to later times. Bottom panel: stroboscopic time-dependence of the bipartite entanglement entropy. After a plateau corresponding to the thermal entropy of the quasistationary state, entropy approaches the random-state value characteristic of infinite temperatures (see also Sec. 1.1.5).

physics. It has been proven extremely valuable to probe fundamental properties of intriguing quantum phases of matter, to quantify the loss of information in black holes, to characterize the efficiency of quantum-computation algorithms, and it is regarded as a crucial resource for future quantum technologies. Such multiple far-reaching facets of entanglement has motivated an enormous interest and ample cross-fertilization among diverse fields, ranging from condensed matter theory to quantum optics and high-energy physics.

It is by now well established that a large body of information about the nonequilibrium dynamics of quantum many-body systems, their thermalization properties, and the complexity of their numerical simulations, can be inferred from the evolution of their entanglement [143–153]. A paradigm for these studies is represented by the growth of bipartite entanglement entropy $S(t)$ after a quantum quench.

Bipartite entanglement entropy is defined as the von Neumann entropy of the reduced density matrix of a subsystem. Specifically, one considers an extended quantum many-body system, whose Hilbert space $\mathcal{H} = \otimes_i \mathcal{H}_i$ is the tensor product of the local Hilbert spaces $\mathcal{H}_i$ associated with local degrees of freedom. In order to quantify quantum entanglement between spatially separated degrees of freedom, one may subdivide the system into two complementary regions A and B, e.g., a finite domain in space and its complement. The global Hilbert space is thus the tensor product of the subspaces associated with the two subsystems $\mathcal{H} = \mathcal{H}_A \otimes \mathcal{H}_B$ with $\mathcal{H}_{A[B]} = \otimes_{i \in A[B]} \mathcal{H}_i$. We consider a (normalized) pure state $|\Psi\rangle \in \mathcal{H}$. Reduced states of subsystems A and B are defined by the partial traces

$$\hat{\rho}_A = \mathrm{Tr}_B \, |\Psi\rangle \langle\Psi| , \qquad \hat{\rho}_B = \mathrm{Tr}_A \, |\Psi\rangle \langle\Psi| . \tag{1.14}$$

Then, bipartite entanglement entropy is defined as the von Neumann entropy of the reduced state, i.e.,

$$S_A = -\mathrm{Tr}_A \, \hat{\rho}_A \log \hat{\rho}_A , \qquad S_B = -\mathrm{Tr}_B \, \hat{\rho}_B \log \hat{\rho}_B . \tag{1.15}$$

One can show that $S_A = S_B$, so that entanglement entropy is associated with the bipartition only. This quantity is a measure of entanglement according to the axioms of quantum information theory (see, e.g., Ref. [154]). In fact, if the state $|\Psi\rangle$ can be factored into two states $|\Psi_A\rangle \otimes |\Psi_B\rangle$ of subsystems A and B, then the reduced density matrices $\hat{\rho}_{A[B]} = \left|\Psi_{A[B]}\right\rangle \left\langle\Psi_{A[B]}\right|$ are pure, and hence $S = 0$. Otherwise, $S > 0$ and the state is entangled with respect to the considered bipartition.

The dynamics of the entanglement entropy $S(t)$ of two spatial regions after a quantum quench measures how fast nonlocal quantum correlations build up in the nonequilibrium dynamics of extended interacting systems. However, access to this quantity requires knowledge of the many-body wavefunction, which notably represents a difficulty. Significant progress has been made for systems with local interactions, characterized by a finite speed of correlation spreading [36], see Sec. 1.1.1. In this case $S(t)$ is generically expected to saturate to an extensive value ("volume law") after a linear increase in time

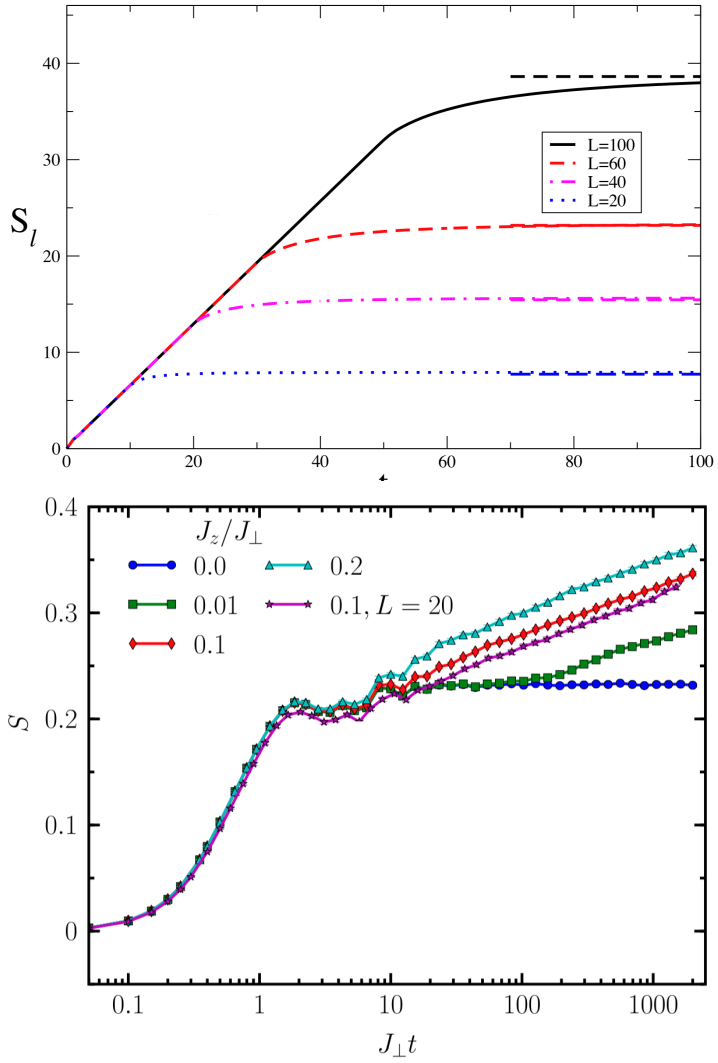

Figure 1.5: Illustration of the main paradigms of entanglement entropy growth after a quench. Top panel: linear growth of bipartite entanglement entropy of a finite interval with the rest of the system after a quench in the transverse-field quantum Ising chain (from Ref. [155]). The saturation value attained at long times increases linearly upon increasing the length ℓ of the interval. For critical quenches, the slope is related to the central charge of the underlying conformal field theory, as discovered by P. Calabrese and J. Cardy (see the quoted article). Bottom panel: logarithmic growth of half-system entanglement entropy in a many-body interacting Anderson model (from Ref. [156]). In the noninteracting limit ($J_z = 0$), all excitations are localized by disorder [157], and, consequently, entanglement is bounded. Its growth is activated by many-body interactions, whose strength is controlled by the parameter J_z. Theoretical understanding of this phenomenon in terms of the *dephasing* of localized excitations has been given in Ref. [148]. This shows that entanglement growth is not necessarily associated with transport of energy and matter, which is completely suppressed in localized systems.

[158, 159], see the top panel of Fig. 1.5 for an illustration. As it results from the discussion of thermalization in Sec. 1.1.1, the long-time saturation value of the entanglement entropy is expected to be the value in the thermal ensemble, i.e., the thermodynamic entropy. In fact, denoting by N_A and N the size of the region A and of the whole system, respectively, using the convergence of the reduced density matrix to the thermal ensemble in Eq. (1.6), one finds

$$\lim_{t\to\infty} \lim_{N\to\infty} \frac{S_A(t)}{N_A} \approx s(\beta_E), \tag{1.16}$$

where

$$s(\beta) = -\lim_{N\to\infty} \frac{1}{N} \mathrm{Tr}\left(\frac{e^{-\beta \hat{H}}}{Z} \log \frac{e^{-\beta \hat{H}}}{Z} \right) = \beta \left[e(\beta) - f(\beta) \right]. \tag{1.17}$$

In Eq. (1.16), β_E is determined by the energy E of the initial state, and s, e, f are the densities of entropy, energy and free energy. Equality in Eq. (1.16) holds for large subsystems $N_A \to \infty$; for finite subsystems, one has subleading boundary contributions to entropy. This observation provides a remarkable bridge between quantum entanglement and standard thermodynamics, and identifies the process of thermalization of a subsystem with the accumulation in time of quantum entanglement between the subsystem and the rest of the system. In integrable systems, the asymptotic saturation value of entanglement entropy corresponds to the "thermodynamic" GGE entropy, and the linear growth in time can be attributed to the ballistic spreading of infinitely long-lived quasiparticles [144–146, 160].

Conversely, the existence of (exact or approximate) spatially localized conserved operators results in a dramatically slower increase of entanglement entropy, as occurs in the presence of strong disorder [148, 161, 162] or sufficiently complex and strong interactions [163–168]. In these cases, a distinct logarithmic growth of $S(t)$ characterizes many-body localized (MBL) or quasilocalized dynamics [157, 169–173], see the bottom panel of Fig. 1.5 for an illustration. Systems exhibiting (quasi)localizated excitations at finite energy density, escape the conventional paradigm of quantum thermalization discussed above, and remain out of equilibrium as long as they can be considered isolated from the external environment. The finding above remarkably shows that entanglement growth is not necessarily associated with transport of energy and matter, which is completely suppressed in localized systems. In fact, its theoretical understanding is based on the *dephasing* of localized excitations [148] rather than their delocalization. Although we do not delve into this very interesting topic in this thesis, we shall show in Chap. 8 that *confinement* of excitations may result in qualitatively similar effects, despite the absence of quenched disorder.

1.2 Long-range interactions in quantum systems

In this Section, we discuss the theoretical and experimental motivations for studying quantum statistical physics of long-range interacting systems,

which constitute the main playground of this thesis. We further review the current status of the theoretical analysis of their nonequilibrium behavior, mainly developed in the last years, placing the focus on the most relevant aspects for the work presented in subsequent Chapters.

Classical long-range interacting systems are relevant to a number of important subjects in Physics, such as, e.g., galaxies [174], plasma [175], ionic crystals [176]. From the viewpoint of statistical mechanics, they present a wealth of distinguished properties, such as nonadditivity of energy, inequivalence of statistical ensembles, slow relaxation, and ergodicity breaking (see, e.g., Refs. [177, 178]).

Recently, long-range interactions have become the focus of a great attention even in the quantum domain, primarily motivated by remarkable experimental platforms in atomic, molecular and optical (AMO) physics, which allow the tunable and controlled study of coherent quantum dynamics for long times.

1.2.1 Algebraically-decaying interactions in ultracold gases

Algebraically-decaying interactions are ubiquitous in quantum experiments. For instance, they are relevant in the model description of Rydberg atoms [179–181], trapped ions [182–191], polar molecules [192, 193], and magnetic atoms [194, 195]. A particularly rich and exciting research direction based on AMO physics aims at developing quantum simulators and quantum computers, i.e., machines capable of performing manipulations on an assembly of physical entities by exploiting their quantum nature. Among the outstanding recently developed platforms for pioneering this enterprise, systems of ultracold ions in magneto-optical traps and arrays of optical tweezers hosting Rydberg atoms represent some of the most promising attempts, due to scalability and an unprecedented degree of controllability and highly-resolved addressability.

In view of the strong connections between these two experimental platforms and the theoretical work and results presented in Part I and Part II of the thesis, respectively, we shall briefly describe these setups below.

Trapped ions

Ion traps consist of an arrangement of electromagnetic fields designed to confine charged particles in a given region of space. By Earnshaw's theorem, stable mechanical equilibrium cannot be realized with electrostatic fields in the vacuum. Hence, in order to trap charged particles, one needs to combine electrostatic fields either with magnetic fields, or with time-dependent electric fields. The first option is realized in Penning traps, whereby an electrostatic field confines ions in one dimension, and a strong magnetic field in the same direction pins the ions in the transverse plane. The second option is realized in Paul traps, whereby an effective stable equilibrium is generated by means of an additional ac electric field, using the principle of dynamical stabilization first discovered for the Kapitza pendulum (see also Sec. 2.3 and Chap. 5). Ions can be trapped in a vacuum chamber by sublimating a solid sample by Joule effect,

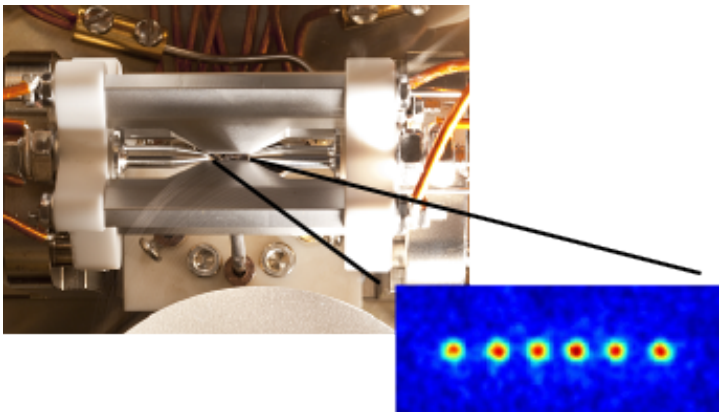

Figure 1.6: Picture of an ion trap in the Innsbruck IQOQI laboratory of R. Blatt. The inset shows a snapshot of a one-dimensional crystal of six trapped ions.

ionizing the atoms with suitable lasers, accelerating the atomic beam towards the trap, and cooling the cloud with standard techniques such as Doppler and Raman cooling — see, e.g., Ref. [185].

If the trap confinement is weak in one or two spatial directions, the ultracold ions arrange themselves in a one- or two-dimensional crystal, defined by the mechanical equilibrium configuration which balances attraction towards the trap center and inter-ion Coulomb repulsion (see Fig. 1.6). It has been recognized that the internal hyperfine levels of the trapped ions may be exploited for quantum-computing and quantum-simulation purposes. In fact, the system represents a well-isolated array of quantum few-level units (qubits if only two hyperfine levels are involved in operations, as it is usually the case). As a consequence of the large and regular spacing between the ions, individual units may be manipulated by tightly focussed lasers and observed by stimulated fluorescence. Most importantly, effective interactions between these qubits may be engineered and tuned. Typically, such interactions are generated by means of double stimulated Raman transitions involving a virtual hyperfine level and the absorption/emission of a phonon. The detuning of the laser frequencies from the virtual level and the shape and spectrum of the mechanical vibrations of the crystal determine the effective interaction between pairs of qubits. A typical effective Hamiltonian which is routinely realized along these lines is the long-range quantum Ising chain of the form [cf. Eq. (1.1)]

$$\hat{H} = -\sum_{i\neq j}^{N} J_{ij}\,\hat{\sigma}_i^x\hat{\sigma}_j^x - g\sum_{i=1}^{N}\hat{\sigma}_i^z. \tag{1.18}$$

where the sum runs over the ions, and $\hat{\sigma}$ are Pauli matrices describing the dynamics of hyperfine levels. The experimental Ising couplings J_{ij} describe a correlated hyperfine transition of the i-th and the j-th ion mediated by the exchange of a virtual phonon. They may often be approximated by algebraically-

decaying couplings as

$$J_{ij} \approx \frac{J}{|i-j|^{\alpha}}. \tag{1.19}$$

The effective power-law exponent α depends on the experimental setup. With Penning traps, spin-spin interactions are usually mediated most strongly by the collective center-of-mass vibrational mode, which couples uniformly to all effective spins. This results in a very small value of $\alpha = 0.02 \div 0.2$. On the other hand, with Paul traps one can in principle tune α between 0 and 3, and it has been found that $\alpha \approx 1$ provides a good fit for typical arrangements. See also Sec. 5.4.

Rydberg atom arrays

The setup we are interested in consists of arrays of optical traps, each of them hosting a single Rydberg atom. For simplicity, we focus here on a one-dimensional chain of L optical traps, as implemented in the recent experiment reported in Ref. [181] and schematically illustrated in Fig. 5.4. Higher-dimensional arrays have also been implemented [196]. The atoms represented in the figure are trapped in their electronic ground state (black circle), denoted by $|\downarrow\rangle_j$, where j numbers the trap. These ground states are quasiresonantly coupled by suitable lasers to a single Rydberg state, i.e., a highly-excited electronic level, denoted by $|\uparrow\rangle_j$. The coherent dynamics of this chain of qubits is governed by the following Hamiltonian [197, 198]:

$$\hat{H} = \sum_{j=1}^{L} \left(\Omega\, \hat{\sigma}_j^x + \delta\, \hat{\sigma}_j^z\right) + \sum_{j<\ell} V_{j,\ell}\, \hat{n}_j \hat{n}_\ell, \tag{1.20}$$

where $\hat{\sigma}_j^{\alpha}$ are Pauli matrices at site j, the operator $\hat{n}_j = (\hat{\sigma}_j^z + 1)/2$ signals the presence of a Rydberg excitation at site j, 2Ω and 2δ are the Rabi frequency and the detuning of the laser excitation scheme, respectively, and $V_{j,\ell}$ describes the interactions between atoms in their Rydberg states at sites (j, ℓ). This Hamiltonian is again of the Ising type encountered in Eqs. (1.1) and (1.18). The effective spin-spin interactions $V_{j,\ell}$ have dipolar nature, and hence they decay as a power-law of the distance, upon increasing it, with an exponent $\alpha = 6$.

For the cases of interest in Chap. 7, these interactions are strong at short distances and decay as $1/|j-\ell|^6$ at large distances. The dynamics described by $\hat{H}$ have been realized in several experiments, utilizing either optical lattices or optical tweezers [181, 199, 200]. In particular, Ref. [181] investigated the regime where $V_{j,j+1}$ is much larger than all other energy scales of the system, resulting in the so-called Rydberg *blockade effect*: atoms on neighboring sites cannot be simultaneously excited to the Rydberg state. This is modeled via the hard constraint $\hat{n}_j \hat{n}_{j+1} \equiv 0$.

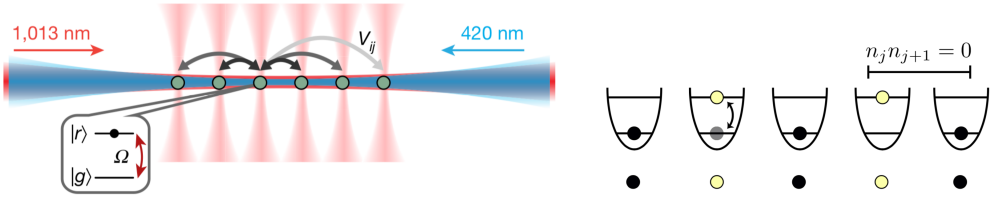

Figure 1.7: Schematic illustration of the experimental setup with interacting Rydberg atom arrays (left, from Ref. [181]), and of the Rydberg blockade effect (right, from Ref. [7]). In this picture, $|g\rangle \equiv |\downarrow\rangle$ and $|r\rangle \equiv |\uparrow\rangle$ represent the ground and excited Rydberg state, respectively.

In this regime, the resulting Hamiltonian is

$$\hat{H}_{\text{eff}} = \sum_{j=1}^{L} \left(\Omega \, \hat{P}^{\downarrow}_{j-1} \hat{\sigma}^{x}_{j} \hat{P}^{\downarrow}_{j+1} + 2\delta \, \hat{n}_{j} \right), \tag{1.21}$$

where we neglect longer-range terms which do not affect qualitatively the dynamics. $\hat{H}_{\text{eff}}$ acts on the constrained Hilbert space without double occupancies on nearest-neighbor sites, as illustrated in Fig. 5.4. This effective Hamiltonian was first introduced by S. Sachdev and collaborators [201], to describe the effective dynamics in a different class of experiments with Mott insulators in tilted optical lattices [15].

1.2.2 Effective confining forces

A second, radically different type of long-range interactions may emerge in quantum many-body systems with local interactions, namely, confining potentials between elementary excitations, which grow proportionally to their spatial separation. Such an occurrence may result from frustrating the configuration of all degrees of freedom between the two quasiparticles, as a consequence of local constraints. This mechanism is usually ascribed to an underlying gauge symmetry of interactions.

The above ideas appear in high-energy physics. In this field, gauge theories were first proposed, and it was shown that the nonperturbative phenomenon of confinement may take place [202, 203]. In fact, elementary particles such as quarks cannot exist individually as isolated entities, but experience spatial confinement into composite particles due to forces acting at arbitrary distances, mediated by gauge fields.

Various aspects of confinement in relevant gauge theories in high-energy physics are still unclear and subject to intense investigations. This problem is one the most challenging of contemporary physics, due to the lack of suitable analytical and numerical techniques. For example, there is presently no evidence of a successful method to study the real-time dynamics of nonAbelian $\mathrm{SU}(3)$ gauge theories, relevant, e.g., for heavy-ion collision experiments and for quark-gluon plasma dynamics in early-Universe cosmology.

For this purpose, recent years have witnessed a substantial interest in *quantum simulations* of gauge theories with ultracold atomic setups. To present date,

only some preliminary steps have been taken in this enterprise, involving lattice formulations of Abelian gauge theories in one spatial dimension. The primary example in this class is quantum electrodynamics (QED) in $1+1$ spacetime dimensions, formulated in terms of the so-called Schwinger model [204] or variants of it. From the theoretical viewpoint, in this simplified setup one can count on a number of analytical and numerical techniques [204–214]. In spite of a large number of experimental proposals [215–221], the current state-of-the-art in the field is represented by a proof-of-principle simulation of the lattice Schwinger model with only four trapped ions [222]. While the complexity of these models is significantly lower compared to the ultimate goal of nonAbelian $\mathrm{SU}(3)$ gauge theories in $3+1$ dimensional spacetime, they nonetheless share with the latter the occurrence of interesting and nontrivial phenomena such as confinement.

As we shall discuss in detail in Chap. 7, an analogous effect of confinement of elementary excitations can also be found in one-dimensional statistical physics and condensed matter models [223–228]. In fact, a pair of kink excitations separating two degenerate symmetric ground-state configurations of a quantum chain, experience a linearly-growing confining potential as soon as the degeneracy is lifted, which may occur by external symmetry-breaking fields or residual mean-field interactions [229–232]. Signatures of quantized excitation spectra due to confinement have been studied in a number of quasi1d magnetic insulators, beautifully confirming the theoretical predictions [233, 234]. We refer the reader to Chap. 7, in which the physics of confinement in one dimension will be extensively reviewed. In particular, we shall show in Sec. 7.2.3 that an interpretation of confinement in terms of an underlying gauge-invariance is always possible in one-dimensional quantum systems.

1.3 Nonequilibrium physics with long-range interactions

Stimulated by the development of the above experimental platforms, long-range interactions have recently become the focus of intense investigations in quantum many-body theory [142, 235–267]. Below, we give an overview of recent theory developments, and briefly outline the original contributions of the doctoral research presented in this thesis.

A preliminary, natural, and long-standing question concerns universal behavior, i.e., if and how long-range interactions modify the universality class of equilibrium criticality. Such a problem has been investigated both in classical and quantum statistical field theories. The most prominent qualitative result is that a long-range interacting system may be equivalent to a short-range interacting one with a modified (increased) effective dimensionality [268–270]. The correspondence has been suggested via renormalization-group techniques for the equilibrium phase diagram and the universal equilibrium critical properties of both quantum and classical systems.

Concerning the quantum Ising model in Eq. (1.1) on a d-dimensional lattice and with algebraically-decaying couplings $J_{\mathbf{r},\mathbf{r}'} \sim |\mathbf{r}-\mathbf{r}'|^{-\alpha}$, there exist two values $\alpha^{\pm} = \alpha^{\pm}(d)$, with $d \leqslant \alpha^{-}(d) \leqslant \alpha^{+}(d) \leqslant d+2$ such that for $\alpha < \alpha^{-}(d)$

the universal behavior is described by mean-field theory, and for $\alpha > \alpha^+(d)$ the universality class is that of the short-range models in the same spatial dimensionality d. If the actual dimensionality d is smaller than the upper-critical dimensionality d_{uc} of the short-range model, by tuning α between $\alpha^+(d)$ and $\alpha^-(d)$ one obtains a d-dimensional model with the properties of a d_{eff}-dimensional short-range interacting model, where the effective dimensionality d_{eff} varies continuously with α in the range $d < d_{eff}(\alpha) < d_{uc}$. A similar scenario is valid for more general systems which have been considered, such as $O(N)$ models.

A nontrivial consequence of the increased effective dimensionality consists in the stabilization of long-range order at finite temperature in low-dimensional systems. In fact, when $d = 1$ and $\alpha \leqslant 3$, according to the above mapping the system is equivalent to a short-range interacting system in $2/(\alpha-1)$ dimensions. In particular, for $\alpha \leqslant 2$, the effective dimension increases above $d_{eff} = 2$, which is the lower critical dimension for the existence of an ordered phase at finite temperature.

The possible existence of long-range order for $\alpha \leqslant 2$ in one-dimensional quantum chains at finite temperature, may be understood in more elementary terms by considering the Landau argument [271], as illustrated in Fig. 1.8. This argument asserts that long-range order in (classical or quantum) finite-temperature one-dimensional systems is prevented because of domain-wall excitations. Consider a chain in a long-range ordered state. When interactions act on a finite range, an isolated domain-wall excitation which separate two large long-range ordered regions has a finite configurational energy cost. Therefore, the creation and expansion of bubbles delimited by domain-walls within an initially long-range ordered state is an entropically favorable process that leads to a meltdown of long-range order. However, by increasing the range of interactions, one realizes that the energy cost of an isolated domain-wall configuration becomes correspondingly large. A simple computation shows that this energy cost can be estimated as

$$\Delta E_{dw} \sim \sum_{i \leqslant n} \sum_{j > n} J_{ij}, \tag{1.22}$$

where the domain-wall is located between sites n and $n+1$ and J_{ij} is the interaction strength between degrees of freedom at sites i and j along the chain. Considering algebraically-decaying interactions $J_{ij} \sim J\,|i-j|^{-\alpha}$, the computation shows that

$$\Delta E_{dw} \sim \sum_{r>0} \frac{J}{r^{\alpha-1}}. \tag{1.23}$$

One sees that for $\alpha > 2$ this energy is finite. As a result, a finite density of domain-walls will populate the chain at finite temperature, preventing the possibility of forming long-range order. In other words, interactions decaying faster than r^{-2} are qualitatively similar to short-range interactions as long as universal properties are concerned, in agreement with the formal result above. On the other hand, domain-walls become energetically inaccessible for $\alpha \leqslant 2$,

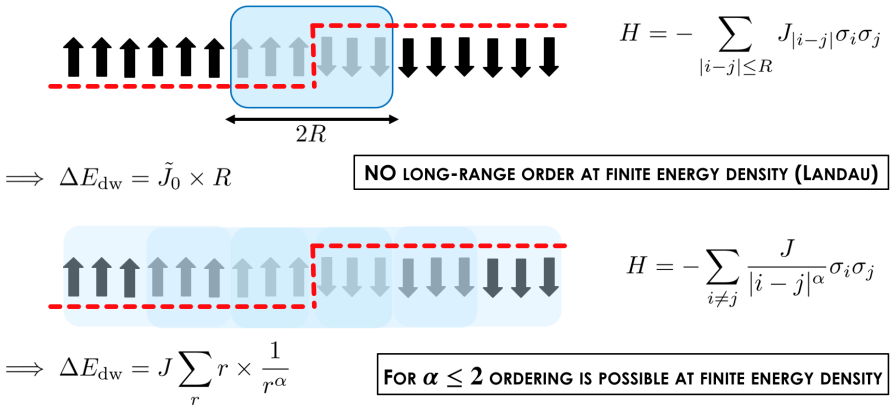

Figure 1.8: Schematic illustration of the generalized Landau argument for long-range interacting chains. The energy of an isolated domain-wall is finite with short-range interacting and infinite for algebraically-decaying interactions with exponent $\alpha \leqslant 2$.

giving rise to competition between energy and entropy and hence opening up the possibility of stable long-range ordered states at finite temperature [272–274].

The existence of long-range order in highly-excited states represents one of the distinctive properties of long-range interacting quantum chains. On the one hand, their low dimensionality makes them accessible to experimental quantum simulations with highly-controllable platforms such as ion traps and to numerical classical simulations with advanced computational techniques such as tensor networks. On the other hand, the long-range nature of their interactions allows one to explore characteristic phenomena of the physics of higher-dimensional systems. In fact, stable long-range order in highly-excited states is particularly relevant in nonequilibrium conditions, as it paves the way to the realization of dynamical phases without equilibrium counterparts, such as dynamically stabilized Floquet-prethermal phases and time-crystalline phases. This will play a crucial role in the results presented in Chap. 5.

In the work presented in Part I of this thesis, an additional interesting issue motivated by long-range interactions will play a major role, namely quasiintegrability, and the associated prethermal dynamical phases and dynamical phase transitions. It has been recalled in Sec. 1.1.2 above that parametric closeness of the Hamiltonian to an integrable point leads to a long temporal stage during which the system dynamics displays features dictated by integrability. Long-range interacting systems have a natural "integrable" limit, namely the limit $\alpha \to 0$ of infinite-range interactions. In this case, the mean-field analysis becomes exact, and the dynamics can be solved in terms of few semiclassical collective variables. This will be reviewed in detail in Chap. 2. It is presently unclear whether, in what sense, and the extent to which the limit $\alpha \to 0$ is singular as far as finite-size dynamical properties are concerned. Mean-field behavior is exactly recovered in the thermodynamic limit in the whole range $0 \leqslant \alpha \leqslant d$. In Part I of the thesis, we shall often think of the range of interactions as a parameter which controls the impact of many-body quantum fluctuations on the semiclassical collective dynamics which characterizes the infinite-range (mean-field) limit. In

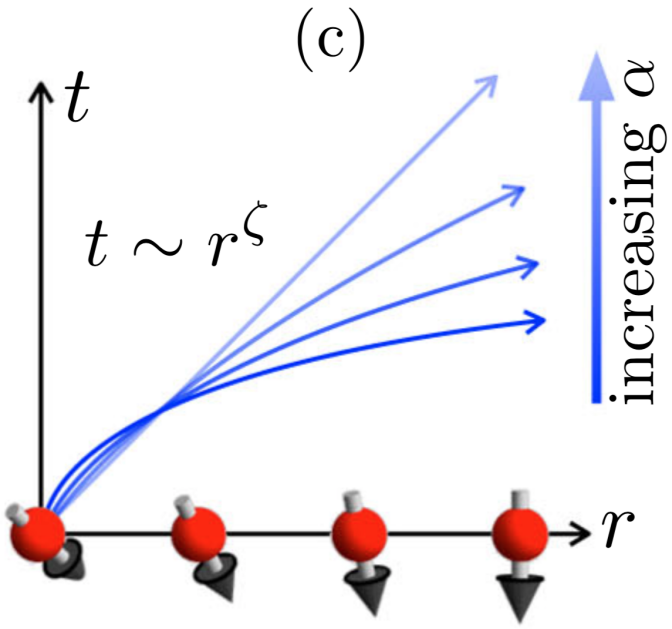

Figure 1.9: Schematic illustration of nonlinear light-cone spreading of quantum correlations in quantum chains with long-range interactions (from Ref. [277]). The cartoon shows the behavior of the light-cone edge $r = f(t)$, such that the dynamical quantum correlations are significantly different from zero only for distances $r < f(t)$, upon decreasing the range of interactions (i.e., increasing α). For sufficiently large α, one recovers the familiar linear light-cone spreading, cf. Fig. 1.2. For smaller α, the light-cone edge bends down, due to the long-range nature of interactions.

particular, we shall explore the consequences of quasiintegrability on dynamical critical behavior in Chap. 4, and on entanglement dynamics in Chap. 6.

In Sec. 1.1.4 we have reviewed the rigorous theory of slow heating in periodically driven short-range interacting systems. Generalizations of these results for long-range interacting systems have been published during the completion of this thesis [275, 276]. In Chap. 5 we shall present nonrigorous work along a similar direction, which agrees and extends the mentioned results. In particular, it is shown that dynamically stabilized quantum phases akin to the classical Kapitza pendulum do occur in driven interacting quantum many-body systems, despite the fluctuations of extensively many degrees of freedom.

A very interesting research direction concerns how long-range interactions affect the speed of quantum correlation spreading and entanglement growth. In fact, they pose a conceptually different and challenging problem. On the one hand, their nonlocal interactions allow quantum correlations between distant degrees of freedom to build up very quickly, resulting in unbounded quasiparticle speed, violations of the Lieb-Robinson bound, and nonlinear light-cone spreading of quantum correlations [277–285], see Fig. 1.9 for an illustration. On the other hand, numerical simulations have shown that the entanglement entropy growth after a quench features a dramatic counterintuitive slowdown as the range of interactions is increased. In particular, it becomes as slow as logarithmic when the couplings decay algebraically upon increasing the distances r_{ij} as $r_{ij}^{-\alpha}$, with α smaller than the spatial dimensionality d, even in the absence of

disorder [286–288]. The counterintuitive concurrence of fast correlation spreading and slow entanglement growth has been partially reconciled in Refs. [287] and [285] in terms of the change in the quasiparticle dispersion relation as the range of interaction increases. In Chap. 6, we shall discuss a qualitative change in the mechanism of entanglement growth when $\alpha \leqslant d$, whereby the standard quasiparticle contribution gets suppressed and nonlinear collective squeezing becomes the leading contribution.

Confinement of excitations via effective linearly-growing interactions, previously introduced in Sec. 1.2.2, also raise a set of basic questions concerning the nonequilibrium dynamics of local observables and quantum correlations. A recent pioneering investigation on this point is Ref. [289]. In this work, it has been suggested that confinement is at the root of a dramatic slowdown of quantum information spreading. This study will be extensively reviewed in Chap. 8, where a theoretical framework for the unconventional dynamical signatures of confinement will be proposed, and additional numerical work in support of the theory will be presented and discussed.

Part I

Impact of quantum fluctuations on mean-field nonequilibrium phenomena

Chapter 2

Nonequilibrium dynamics of collective models

In this introductory Chapter of Part I, we give a detailed review of the nonequilibrium dynamics of quantum many-body systems with collective interactions, i.e., in which all degrees of freedom interact with all the other ones with equal strength. The purpose of this Chapter is pedagogical, since most of the material presented below belongs to a well-understood and established topic in quantum physics. In particular, Secs. 2.1 and 2.4 serve as an introduction to the methodological core of Part I of the thesis contained in Chap. 3 and represent the starting point of the theoretical study of entanglement dynamics in Chap. 6. Section 2.2 serves as an introduction to the study of dynamical phase transitions in Chap. 4. The content of Sec. 2.3 is itself part of the original contributions published in Ref. [3], the main results of which will be presented in Chap. 5.

2.1 Mapping to semiclassical models

In the limiting situation of infinite-range interactions, one expects mean-field theory to become exact in the thermodynamic limit. The description of the quantum dynamics is enormously simplified by exploiting the symmetry of the Hamiltonian under arbitrary permutations of its elementary degrees of freedom. This occurrence allows for exactly mapping such models to systems of few variables characterized by an effective Planck constant $\hbar_{\text{eff}} \sim \hbar/N$, where N is the number of the original degrees of freedom. In this Section, we shall first describe the general theory formulated by B. Sciolla and G. Biroli [83] for systems with full permutational invariance in states belonging to the totally-symmetric sector. (Generalizations for both Hamiltonians and states are briefly discussed in App. A.) Hence, we shall specialize the discussion to spin models, on which we shall mostly concentrate in the rest of the thesis.

2.1.1 Permutational invariance

We consider an interacting ensemble of N identical q-level quantum systems. When interactions are endowed with a notion of locality (i.e., closer units

interact more strongly), the nonequilibrium dynamics is generally quite complex. Analytical solutions are limited to very few special cases, and numerical solutions are limited to very small systems, as the Hilbert space dimension grows exponentially with the system size as q^N. On the other hand, a drastic simplification occurs when the system is invariant under permutations of its elementary units, as we shall now describe.

A basis of the many-body Hilbert space may be constructed as a tensor product of identical single-unit bases. We denote $\{|\alpha\rangle\}$ one such basis, where $\alpha = 1, \ldots, q$ labels the states of each q-level system. A general many-body state may be expressed as a superposition of

$$|\Psi\rangle = \sum_{\alpha_1,\ldots,\alpha_N=1,\ldots,q} \psi_{\alpha_1,\ldots,\alpha_N} |\alpha_1, \ldots, \alpha_N\rangle . \tag{2.1}$$

Binary permutation operators are unitary transformations which exchange a pair of units in the system. Their action is defined by

$$\hat{P}_{ij} \left|\alpha_1, \ldots, \alpha_i, \ldots, \alpha_j, \ldots, \alpha_N\right\rangle = \left|\alpha_1, \ldots, \alpha_j, \ldots, \alpha_i, \ldots, \alpha_N\right\rangle \tag{2.2}$$

for all pairs of units $i < j$. General permutations can be expressed as a combination of binary permutations. A system has full permutational invariance if its Hamiltonian $\hat{H}$ commutes with all permutation operators.

Although permutation operators do not all commute with each other, it is possible to find a nontrivial subspace of the many-body Hilbert space which is simultaneously invariant under all permutations. We shall call this subspace the totally-symmetric subspace (TSS). A basis for such a subspace can be constructed in a straightforward manner by symmetrizing each many-body configuration $|\alpha_1, \ldots, \alpha_N\rangle$ with respect to all possible permutations, and normalizing the result. The resulting basis can be labelled by the numbers $N_1, \ldots, N_q$ of units occupying each level $\alpha = 1, \ldots, q$ (with $\sum_{\alpha=1}^{q} N_\alpha = N$), because two configurations with the same set of occupation numbers differ only by a permutation. One may understand this by identifying the single-body states $|1\rangle, \ldots, |q\rangle$ with a set of quantum orbitals, and a many-body basis state in the TSS with a configuration of N bosons in such orbitals. In terms of the original unsymmetrized basis states, one has

$$|N_1, \ldots, N_q\rangle = \sqrt{\frac{\prod_{\alpha=1}^{q} N_\alpha!}{N!}} \sum_{(\alpha_1,\ldots,\alpha_N)\in[N_1,\ldots,N_q]} |\alpha_1, \ldots, \alpha_N\rangle , \tag{2.3}$$

where we denoted by $[N_1, \ldots, N_q]$ the set of all configurations with N_1 units in state α_1, ..., N_q units in state α_q. The normalization factor is determined by the exchange degeneracy of each configuration. The dimension of the TSS is equal to the number of partitions of N into q nonnegative integers:

$$\dim \text{TSS} = \binom{N+q-1}{q-1} \underset{N\to\infty}{\sim} \frac{N^{q-1}}{(q-1)!}. \tag{2.4}$$

In the presence of permutational invariance, the time-evolution of totally-symmetric initial states is confined within the TSS. This causes a huge reduction of the complexity of quantum dynamics, because the dimension of the TSS is only polynomial in the system size. Typically, such initial states in the TSS may be simple tensor products of identical single-body states (e.g., $|\alpha_1, \alpha_1, \ldots, \alpha_1\rangle$), or ground states (unless permutational symmetry is spontaneously broken). This is the relevant situation in quantum quench experiments, see Sec. 1.1.1.

Following Ref. [83], we shall now show that the dynamics of intensive observables within the TSS is semiclassical in the thermodynamic limit. The underlying idea is that the matrix representation of a permutationally-invariant Hamiltonian in the TSS will look like a smooth inhomogeneous hopping problem. In order to show this, we first observe that transitions in the TSS basis above,

$$|N_1, \ldots, N_q\rangle \to |N_1 + m_1, \ldots, N_q + m_q\rangle\,, \qquad \mathbf{m} = (m_1, \ldots, m_q) \in \mathbb{Z}^q, \quad (2.5)$$

are uniquely identified by a set of integers $m_1, \ldots, m_q$. We turn the occupation numbers N_α into fractions $x_\alpha \equiv N_\alpha/N$, with $0 \leqslant x_\alpha \leqslant 1$ and $\sum_{\alpha=1}^{q} x_\alpha = 1$. We denote a state within the TSS by $|\mathbf{x}\rangle$, where $\mathbf{x} = (x_1, \ldots, x_q)$, and write the matrix elements of $\hat{H}$ as

$$H_{\mathbf{x},\mathbf{x}'} \equiv \langle \mathbf{x}|\hat{H}|\mathbf{x}'\rangle = V(\mathbf{x})\,\delta_{\mathbf{x},\mathbf{x}'} - \sum_{\mathbf{m}\neq\mathbf{0}} T_{\mathbf{m}}(\mathbf{x})\delta_{\mathbf{x},\mathbf{x}'+\mathbf{m}/N}. \quad (2.6)$$

The two terms represent the diagonal and off-diagonal parts, respectively. For simplicity, we assume time-reversal invariance, which results in real matrix elements $T_{\mathbf{m}}(\mathbf{x}) \in \mathbb{R}$. We observe that terms in the Hamiltonian $\hat{H}$ involving up to k bodies, change the state of up to k elementary units, and therefore changes the fractions x_α by one unit step $\Delta m_\alpha = 1$ up to $2k$ times, i.e., $|\mathbf{m}| \equiv \sum_\alpha m_\alpha \leqslant 2k$. The off-diagonal transitions in the TSS induced by a Hamiltonian with few-body interactions are thus *local*. The next crucial observation is that both the functions $V(\mathbf{x})$ and $T_{\mathbf{m}}(\mathbf{x})$ are extensive,

$$V(\mathbf{x}) \sim N\,v(\mathbf{x}), \qquad T_{\mathbf{m}}(\mathbf{x}) \sim N\,t_{\mathbf{m}}(\mathbf{x}), \quad (2.7)$$

which is a consequence of the extensivity of the Hamiltonian $\hat{H}$. The Hamiltonian densities v and t are smooth functions of $\mathbf{x}$, as they generally result from combinatoric factors of the occupation numbers which are insensitive to small changes $N_\alpha \mapsto N_\alpha \pm 1, 2, \ldots$ to leading order in the thermodynamic limit [83]. These properties allow us to rewrite the Schrödinger equation in the TSS as

$$i\frac{1}{N}\frac{\partial}{\partial t}\psi(\mathbf{x}, t) = \left\{v(\mathbf{x}) - \sum_{0<|\mathbf{m}|\leqslant 2k} t_{\mathbf{m}}(\mathbf{x}) \cosh\left(\frac{\mathbf{m}}{N}\cdot\frac{\partial}{\partial \mathbf{x}}\right)\right\}\psi(\mathbf{x}, t). \quad (2.8)$$

A technical remark: We have embedded the discrete lattice

$$x_\alpha = 0, \frac{1}{N}, \frac{2}{N}, \ldots, \frac{N-1}{N}, 1 \quad (2.9)$$

in a continuous space $x_\alpha \in [0,1]$, such that the continuous solution coincides with the lattice solution when restricted to the original lattice. In practice the distinction is negligible, because the Hamiltonian and the initial states are smooth functions of $\mathbf{x}$, and hence the solution $\psi(\mathbf{x},t)$ will also be smooth over a time scale which diverges as the discretization step $1/N$ is reduced, i.e., in the thermodynamic limit $N \to \infty$.

Equation (2.8) asserts that the evolution of the TSS wavefunction $\psi(\mathbf{x},t)$ is governed by an effective Hamiltonian

$$\mathcal{H}_{\rm eff}(\hat{\mathbf{q}},\hat{\mathbf{p}}) \equiv v(\hat{\mathbf{q}}) - \sum_{\mathbf{m}} t_{\mathbf{m}}(\hat{\mathbf{q}}) \cos(\mathbf{m}\cdot\hat{\mathbf{p}}) \tag{2.10}$$

and an effective Planck constant

$$\hbar_{\rm eff} \equiv \frac{1}{N} \qquad \text{(recall that } \hbar = 1 \text{ in our units)} \tag{2.11}$$

which approaches zero in the thermodynamic limit. In this correspondence, we have recognized the action of the operators

$$x_\alpha \mapsto \hat{q}_\alpha, \qquad -i\hbar_{\rm eff}\frac{\partial}{\partial x_\alpha} \mapsto \hat{p}_\alpha. \tag{2.12}$$

We observe that the exact constraint $\sum_\alpha x_\alpha \equiv 1$ may be easily solved explicitly, eliminating one degree of freedom. Thus, in general, Eq. (2.10) describes the semiclassical dynamics of $q-1$ collective degrees of freedom of the original system of all-to-all interacting q-level units.

It is not difficult to see that initial states in quench experiments generally correspond to narrow Gaussian wavepacket centered around a coordinate $\mathbf{x}_{\rm cl}(t=0)$ and an average momentum $\mathbf{p}_{\rm cl}(t=0) \equiv \langle\hat{\mathbf{p}}(t=0)\rangle$. According to standard semiclassical theory, for small $\hbar_{\rm eff}$ (i.e., large N), the wavepacket will remain Gaussian for a diverging time scale during the subsequent evolution. Its center will follow the classical orbit $\big(\mathbf{q}_{\rm cl}(t),\mathbf{p}_{\rm cl}(t)\big)$ governed by the classical Hamiltonian $\mathcal{H}_{\rm eff}(\mathbf{q},\mathbf{p})$ [cf. Eq. (2.10)] via the Hamilton equations $\dot{\mathbf{q}} = \partial\mathcal{H}_{\rm eff}/\partial p$, $\dot{\mathbf{p}} = -\partial\mathcal{H}_{\rm eff}/\partial q$. The quantum fluctuations around the classical trajectories evolve in the same way as initial classical displacements from the trajectory, and hence their distribution evolves in the same way as a classical Gaussian distribution, i.e., with the Liouville equation (see also Sec. 6.2 and App. B).

2.1.2 Fully-connected spin models

In the specific case of systems of interacting spins, the limiting semiclassical description can be formulated in a more direct and intuitive way. In order to illustrate this, we consider general spin models with arbitrary all-to-all multibody interactions, described by a Hamiltonian of the form

$$\hat{H} = -\sum_{p=1,2,\ldots}\left\{\sum_{\mu_1,\ldots,\mu_p=x,y,z}\frac{J_{\mu_1\ldots\mu_p}}{N^{p-1}}\sum_{j_1\neq\cdots\neq j_p}^{N}\hat{s}_{j_1}^{\mu_1}\ldots\hat{s}_{j_p}^{\mu_p}\right\} \tag{2.13}$$

where $\hat{\mathbf{s}}_i$, $i = 1, 2, \ldots, N$ are quantum spins-s. The rescaling factor $1/N^p$ is such that the energy contribution of all p-body interactions is extensive. These Hamiltonians can be written in terms of the collective spin of the system $\hat{\mathbf{S}} = \sum_{i=1}^{N} \hat{\mathbf{s}}_i$ as[1]

$$\begin{aligned}\frac{\hat{H}}{N} &= -\sum_{p\geqslant 1}\left\{\frac{1}{N^p}\sum_{\mu_1,\ldots,\mu_p=x,y,z} J_{\mu_1\ldots\mu_p}\,\hat{S}^{\mu_1}\ldots\hat{S}^{\mu_p}\right\}\\ &= -\sum_{\mu_1=x,y,z} J_{\mu_1}\frac{\hat{S}^{\mu_1}}{N}\\ &\quad -\sum_{\mu_1,\mu_2=x,y,z} J_{\mu_1\mu_2}\frac{\hat{S}^{\mu_1}}{N}\frac{\hat{S}^{\mu_2}}{N}\\ &\quad -\sum_{\mu_1,\mu_2,\mu_3=x,y,z} J_{\mu_1\mu_2\mu_3}\frac{\hat{S}^{\mu_1}}{N}\frac{\hat{S}^{\mu_2}}{N}\frac{\hat{S}^{\mu_3}}{N}\\ &\quad -\ldots\end{aligned} \tag{2.14}$$

where $\hat{S}^{\mu} \equiv \tilde{s}^{\mu}_{k=0} = \sum_i \hat{s}^{\mu}_i$ may be thought of as the Fourier spin mode with vanishing momentum $k = 0$. All the other degrees of freedom $\tilde{s}^{\mu}_{k\neq 0}$, corresponding to the spatial fluctuations of the spins with nonvanishing Fourier momentum $k \neq 0$, do not contribute to the dynamical properties of the model (2.13). (In this sense, infinite-range Hamiltonians have infinitely many conserved quantities, and may be referred to as "integrable".)

The collective spin's magnitude $|\hat{\mathbf{S}}| = \sqrt{S(S+1)}$ with $S = Ns, Ns-1, Ns-2, \ldots$ is extensive and conserved,

$$\left[|\hat{\mathbf{S}}|^2, \hat{H}\right] = 0. \tag{2.15}$$

The Hamiltonian $\hat{H}$ is thus separately diagonalizable in each total spin sector. Denoting $S = Ns - m$, the integer number $m = 0, 1, \ldots, Ns$ or $Ns - 1/2$ (depending on Ns being integer or half integer respectively) determines the maximal spin projection along a given quantization axis. When $N \to \infty$, these sectors can be labelled by a continuous variable,

$$1 - \frac{m}{Ns} \to \rho, \tag{2.16}$$

with $0 \leqslant \rho \leqslant 1$. In each sector, the total spin magnitude is

$$|\hat{\mathbf{S}}| = \sqrt{(Ns-m)(Ns-m+1)} \sim Ns\rho + \frac{1}{2}. \tag{2.17}$$

[1] In going from Eq. (2.13) to Eq. (2.14), one needs to add terms with equal indices in the sums. Such terms are immaterial for $s = 1/2$, while they provide corrections to the coefficients of order $1/N$ in higher-spin systems. This small modification does not alter the subsequent analysis and, accordingly, we will simply ignore it.

The maximal spin projection along a given axis in the same sector is

$$S = Ns - m = Ns\rho. \tag{2.18}$$

The finite subleading correction $1/2$ in Eq. (2.17) is inherently quantum-mechanical: It expresses the nonvanishing gap between the maximal spin projection and the spin length, as a consequence of quantum fluctuations of the transverse spin components. The ground state typically belongs to the maximal total spin sector, characterized by the maximal spin projection $S = Ns$ or $\rho = 1$ (see, e.g., Ref. [290]).

For such states with extensive spin (i.e., finite ρ), the thermodynamic limit $N \to \infty$ is equivalent to the semiclassical limit, or, in loose terms, to a classical, continuous spin $\langle \hat{\mathbf{S}} \rangle / N$ of (conserved) length $\rho s + 1/(2N) \approx \rho s$. In fact, these reduced spin variables satisfy a commutation relation of the form

$$\left[\frac{\hat{S}^\mu}{N}, \frac{\hat{S}^\nu}{N} \right] = i \frac{1}{N} \epsilon_{\mu\nu\rho} \frac{\hat{S}^\rho}{N}, \tag{2.19}$$

whence one sees that Eq. (2.14) defines a semiclassical system with an effective Planck constant $\hbar_{\text{eff}} \equiv 1/N$ which vanishes in the thermodynamic limit $N \to \infty$. The limiting classical Hamiltonian $\hat{H}/N \to \mathcal{H}_{\text{cl}}$ thus reads

$$\mathcal{H}_{\text{cl}}(\vec{\mathcal{S}}) = -\sum_{\mu_1} J_{\mu_1} \mathcal{S}^{\mu_1} - \sum_{\mu_1,\mu_2} J_{\mu_1\mu_2} \mathcal{S}^{\mu_1}\mathcal{S}^{\mu_2} - \dots , \tag{2.20}$$

where now $\hat{\mathbf{S}}/N \to \vec{\mathcal{S}}$ represents a classical spin on the two-dimensional sphere of radius ρs. The rigorous meaning of this statement is that, as $N \to \infty$, the ground state expectation values $\langle \hat{\mathbf{S}} \rangle_{\text{GS}} / N$ of the spin components converge to the minimum point $\vec{\mathcal{S}}^*$ of the classical Hamiltonian $\mathcal{H}_{\text{cl}}$ on the sphere, with vanishingly small quantum fluctuations, and their nonequilibrium evolution $\langle \hat{\mathbf{S}}(t) \rangle / N$ upon varying in time some parameter $J = J(t)$ in the Hamiltonian is described by the classical trajectory $\vec{\mathcal{S}}(t)$ on the sphere governed by $\mathcal{H}_{\text{cl}}$, i.e.,

$$\dot{\vec{\mathcal{S}}} = \{ \vec{\mathcal{S}}, \mathcal{H}_{\text{cl}} \}, \tag{2.21}$$

with the Poisson brackets $\{\mathcal{S}^\mu, \mathcal{S}^\nu\} = \epsilon_{\mu\nu\rho}\mathcal{S}^\rho$. Both these occurrences will be extensively discussed in the specific case of the quantum Ising model in the next Section.

We remark that in the above derivation we have assumed that the Hamiltonian (2.13) has no finite "self-interaction" terms with $j_1 = j_2$, i.e., of the form

$$\hat{H}_{\text{s-i}} = D \sum_{j=1}^{N} (\hat{s}_j^z)^2. \tag{2.22}$$

Such terms are immaterial in the case of a spin-1/2 system: In fact, for these systems the TSS is identical with the Dicke sector of maximal collective spin, and the description of Sec. 2.1.1 is fully equivalent to that presented above.

On the contrary, in higher-spin systems they play crucial role, because they break the conservation of the collective spin magnitude, while retaining the permutational invariance. In this case the TSS is $(N+1)(N+2)/2$-dimensional, while the Dicke manifold is only $N+1$-dimensional: the effective semiclassical model may be formulated via the general mapping of Sec. 2.1.1, and consists of *two* degrees of freedom rather than a single collective spin. Correspondingly, the effective classical dynamics need not be integrable, and may be chaotic and ergodic. For a study of this, see Ref. [291]. A natural context where higher-spin systems occur is given by spinor Bose-Einstein condensates. In these systems, an ensemble of bosonic atoms with spin s approximately occupy the same uniform wavefunction, and hence the spin interactions are permutationally invariant. In this case, terms of the form of Eq. (2.22) may arise from the quadratic Zeeman effect [292].

2.2 Equilibrium and out-of-equilibrium criticality

Here and in the rest of this Chapter, we will consider the mean-field limit of the Hamiltonian (1.1) with a purely transverse field ($h = 0$), i.e., the infinite-range quantum Ising model with uniform spin-spin couplings $J_r = \lambda/N$

$$H = -\frac{\lambda}{N}\sum_{i,j=1}^{N}\hat{\sigma}_i^x\hat{\sigma}_j^x - g\sum_{i=1}^{N}\hat{\sigma}_i^z. \tag{2.23}$$

For later purposes, it is convenient to follow the conventions of the Introduction, in which individual spins $\hat{\boldsymbol{\sigma}}_i \equiv \hat{\mathbf{s}}_i/s$ are normalized by their magnitude s. The spectrum of the σ operators extends from -1 to 1. For $s = 1/2$, this notation reduces to the standard Pauli matrices. Model (2.23) is equivalent to the Lipkin-Meshkov-Glick model [293], originally introduced in nuclear physics. It belongs to the class of fully-connected spin Hamiltonians (2.13) discussed in Sec. 2.1.2, and, as such, it may be rewritten in terms of the collective spin components only, which we denote here $\tilde{\sigma}^\alpha_{k=0} \equiv \sum_i \hat{\sigma}^\alpha_i$, as

$$H = -\frac{\lambda}{N}\left(\tilde{\sigma}^x_{k=0}\right)^2 - g\,\tilde{\sigma}^z_{k=0}. \tag{2.24}$$

As discussed in Sec. 2.1.2, the static and dynamical properties of a fully-connected spin system are completely determined by the classical Hamiltonian [294]

$$\mathcal{H}_{cl}(\vec{\sigma}) = -\lambda(\sigma^x)^2 - g\sigma^z, \tag{2.25}$$

corresponding to the quantity H/N, where $\tilde{\boldsymbol{\sigma}}_{k=0}/N \equiv \sum_i \hat{\boldsymbol{\sigma}}_i/N \to \vec{\sigma}$ is now a classical spin, its phase space being the surface of a sphere of radius $0 < \rho \leqslant 1$. For a given ρ, the classical Hamiltonian (2.25) has a single minimum for large enough g with $\sigma^x = \sigma^y = 0$, $\sigma^z = \rho$, corresponding to a paramagnetic phase. As the strength of the field decreases below the critical value

$$g_{cr} \equiv 2\lambda\rho, \tag{2.26}$$

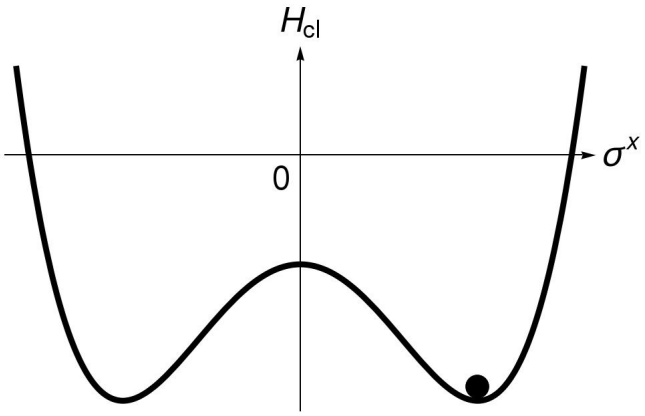

Figure 2.1: Classical energy landscape (2.25) of the collective spin $\vec{\sigma}$ of the LMG model along the plane $\sigma^y \equiv 0$ as a function of the magnetization σ^x, in the ferromagnetic phase $0 < g < g_{cr} \equiv 2\lambda\rho$. The location of the two symmetric minima is determined by Eq. (2.27). In the thermodynamic limit, the degenerate ground state wavefunctions of the collective spin are localized at the two classical minima respectively, and $\vec{\sigma}$ behaves like a classical particle at rest at the bottom of one of the two wells (e.g., black dot in the figure). At finite size, however, quantum tunneling induced by the presence of the other well occurs over an exponentially long time scale, see Sec. 2.4.

that minimum bifurcates into a pair of minima characterized by nonvanishing, opposite magnetization σ^x along the x-direction, located on the xz-plane and symmetrically with respect to the inversion of the x-axis [i.e., connected by the $\mathbb{Z}_2$ symmetry of the Hamiltonian (2.23)]. The corresponding double-well energy landscape is represented in Fig. 2.1. Parameterizing $\vec{\sigma}$ with spherical angles (θ, ϕ), i.e., as $\vec{\sigma} = \rho(\sin\theta\cos\phi, \sin\theta\sin\phi, \cos\theta)$, the two ferromagnetic minima are given by $(\theta^*, 0)$ and (θ^*, π), with

$$\cos\theta^* = \frac{g}{g_{cr}}. \tag{2.27}$$

Accordingly, the value of order parameter is

$$\sigma^x = \pm\rho\sin\theta^* = \pm\rho\sqrt{1-(g/g_{cr})^2} \tag{2.28}$$

(see the left panel of Fig. 2.2).

Let us now focus on the nonequilibrium dynamics. Suppose that the system is prepared at time $t = 0$ in a ferromagnetic ground state of the Hamiltonian (2.23) with a transverse field $g_0 < g_{cr} = 2\lambda$. As discussed in Sec. 2.1.2, this state is spin-polarized in the direction $(\theta^*, 0)$ or (θ^*, π) with $\cos\theta^* = g/g_{cr}$, see Eq. (2.27). At time $t = 0$, the external field is suddenly increased to $g > g_0$, performing a so-called quantum quench. The spins will initiate a collective precession, described in the thermodynamic limit by the classical trajectory of the post-quench Hamiltonian $\mathcal{H}_{cl}(g)$, with the initial condition corresponding to the minimum of the pre-quench Hamiltonian $\mathcal{H}_{cl}(g_0)$, see Eq. (2.25).

Depending on the strength $g - g_0$ of the quench $g_0 \to g$ of the transverse field, starting from a ferromagnetic pre-quench Hamiltonian, the resulting dynamics display qualitatively different orbits [83, 84, 295], as shown in Figs. 2.3 and 2.4:

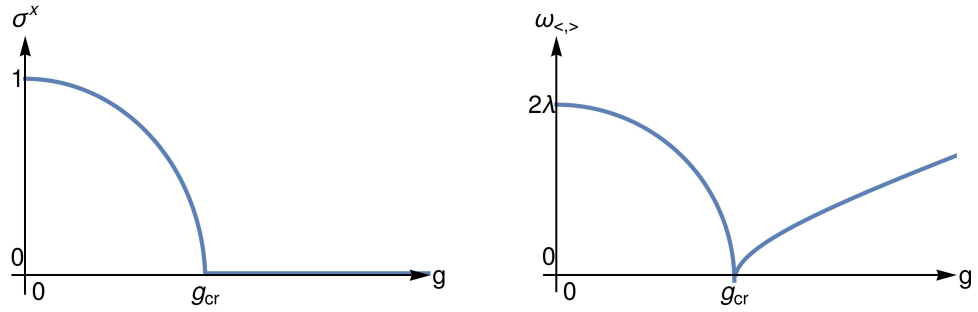

Figure 2.2: Left panel: Equilibrium order parameter σ^x of the infinite-range Ising model at zero-temperature as a function of the external field g, determined by Eq. (2.27). Right panel: Frequency $\omega_{<,>}$ of small oscillations of the collective spin around the minimum, see Eqs. (2.44) and (2.49), equal to the energy gap above the ground state. In both cases, the critical behavior is characterized by a square-root singularity.

1. For a shallow quench [$g < g_{dyn} \equiv (g_0 + g_{cr})/2$], the post-quench energy remains below the top of the barrier that separates the two ferromagnetic sectors. Correspondingly, the collective spin precesses within the starting ferromagnetic sector (blue lines in Figs. 2.3 and 2.4).

2. As the strength of the quench increases, the precession period $T_{cl} = 2\pi/\Omega_{cl}$ (which depends on both g_0 and g) increases, until for $g \nearrow g_{dyn}$ it takes an infinite time to complete one cycle, and the unstable point at the top of the energy barrier is approached exponentially fast along the classical separatrix (red lines in Figs. 2.3 and 2.4).

3. For deep quenches above this threshold $g > g_{dyn}$, the corresponding post-quench energy is larger than the barrier and the orbit of the collective spin on the sphere encircles both minima, such that the $\mathbb{Z}_2$ symmetry is *dynamically* restored after taking time-averages.

In fact, the time-average

$$\overline{\sigma^x} = \lim_{T\to\infty} \frac{1}{T} \int_0^T dt\, \sigma^x(t) \tag{2.29}$$

of the equilibrium order parameter σ^x as a function of the quench strength, vanishes abruptly at the dynamical critical value g_{dyn} of the transverse field which depends also on the initial condition. This dynamical critical point separates a *dynamical ferromagnetic phase* with $\overline{\sigma^x} \neq 0$ from a *dynamical paramagnetic phase* with $\overline{\sigma^x} = 0$.

The vanishing of an order parameter and the divergence of a characteristic time scale such as those reported in Fig. 2.5 are usually associated with critical phenomena. However, the system under consideration is clearly out of thermal equilibrium, as all microscopic spins perform a coherent, undamped precession. For this reason the above phenomenology can be described as *dynamical criticality*. In order to reinforce the idea that this behavior is distinct from the corresponding equilibrium phase transition, we emphasize that the equilibrium singularity of

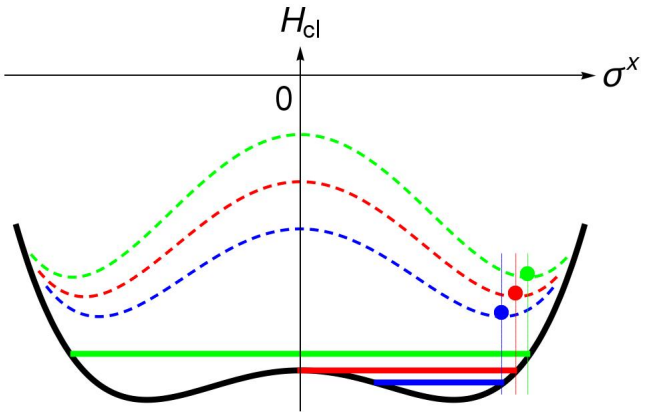

Figure 2.3: Classical energy landscapes (2.25) of the collective spin $\vec{\sigma}$ of the LMG model in the plane $\sigma^y \equiv 0$ as a function of the magnetization σ^x in the ferromagnetic phase, with a post-quench value g such that $0 < g < g_{cr}$ (black solid line) and several possible pre-quench values g_0 such that $0 < g_0 < g$ (blue, red and green dashed lines) of the transverse magnetic field. If the system is prepared in a ground state, e.g., with positive magnetization as illustrated by the blue, red, and green dots for decreasing values of g_0, and the magnetic field is suddenly quenched to a larger value $g_0 < g < g_{cr}$, then depending on the strength $g - g_0$ of the quench, the resulting nonequilibrium evolution may display dynamical ferromagnetic or paramagnetic behavior, exemplified by the blue and green line, respectively, separated by a critical trajectory with a diverging period, corresponding to the red line and associated with the *dynamical critical point* $g = g_{dyn}$. In contrast to Fig. 2.4, here the various resulting evolutions correspond to varying the pre-quench parameter g_0, with a fixed post-quench value g.

the order parameter upon approaching a critical point has a critical exponent $1/2$, see Fig. 2.2, whereas the nonequilibrium order parameter $\overline{\sigma^x}$ actually displays a *logarithmic* singularity, see Fig. 2.5. Indeed, the divergence of the period of the classical oscillations as $g \nearrow g_{dyn}$ is of the same form as that of a classical pendulum as the initial position approaches the upper configuration, with vanishing initial velocity [296], and therefore the time average $\overline{\sigma^x}$ inherits the same type of singularity: Denoting $q_{1,2}$ the extremal values of the coordinate q for a classical trajectory with energy E, and $v(q)$ the velocity as a function of q, one computes the singular behavior as

$$T_{cl} = 2\int_{q_1}^{q_2} \frac{dq}{v(q)} \sim \int_0^{\Delta} \frac{dq}{\sqrt{a(g-g_{cr}) + bq^2}} \sim \int_0^{\Delta'/\sqrt{g-g_{cr}}} \frac{d\eta}{\sqrt{1+\eta^2}} \sim \log \frac{\Delta}{\sqrt{g-g_{cr}}}, \quad (2.30)$$

and hence

$$\frac{1}{T}\int_0^T dt\, \sigma^x(t) \underset{T\to\infty}{\sim} \frac{c}{T_{cl}} \sim \frac{c'}{\log(g-g_{cr})}. \quad (2.31)$$

We conclude this summary of the nonequilibrium dynamics of the infinite-range quantum Ising model by observing that dynamical criticality discussed above is not peculiar of the Ising ferromagnets considered here or of sudden quenches. Rather, it is a general feature of mean-field models driven away from equilibrium [83, 84]. If the driving is chosen to be a slow ramp of the value of

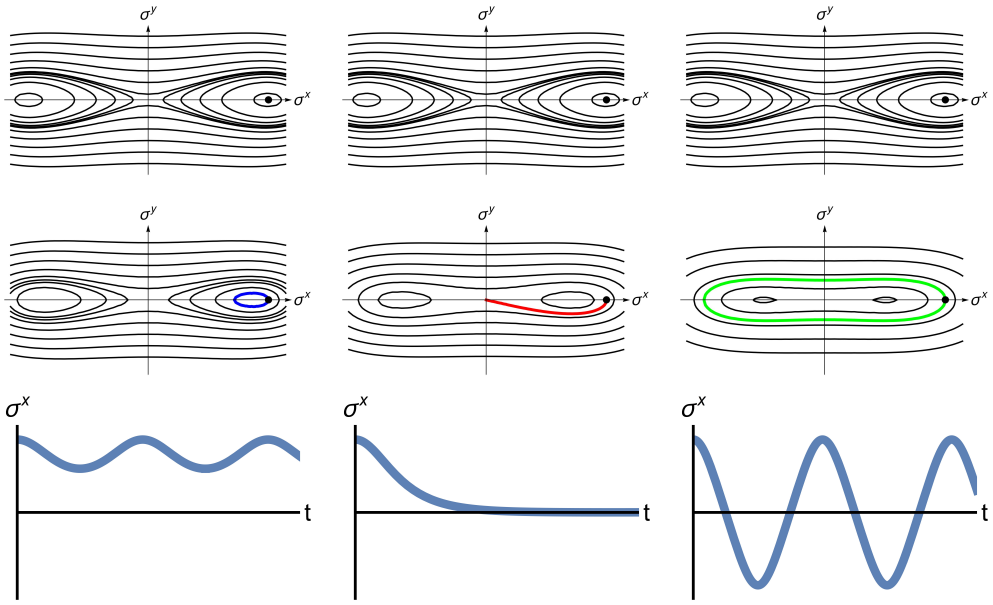

Figure 2.4: Nonequilibrium dynamics of the LMG model (2.23) in the thermodynamic limit, after a sudden quench $g_0 \to g$ of the transverse magnetic field starting from a ferromagnetic ground state of $H(g_0)$. The first row shows the semiclassical phase portrait of the pre-quench Hamiltonian $\mathcal{H}_{\rm cl}(g_0)$, where the initial state is represented by one of the two minima. The second row shows the semiclassical phase portrait of the post-quench Hamiltonian $\mathcal{H}_{\rm cl}(g)$, where the initial state is no longer a stationary point but moves along a nontrivial nonequilibrium trajectory, in the three qualitatively different cases corresponding to $g < g_{\rm dyn}$, $g = g_{\rm dyn}$ and $g > g_{\rm dyn}$ in the first, second and third column, respectively. The third row shows the dynamics of the order parameter as a function of time for the three cases. First column: for a weak quench, the dynamics remain trapped within the starting ferromagnetic sector; second column: for the critical quench, the initial state lies on a separatrix of the post-quench Hamiltonian and its subsequent evolution approaches the unstable equilibrium point at infinite time; third column: for a strong quench, the semiclassical orbit encircles both ferromagnetic minima, hence the symmetry is dynamically restored and the time-averaged order parameter is zero. In contrast to Fig. 2.3, here the different trajectories correspond to a varying post-quench parameter g, with a fixed pre-quench value g_0.

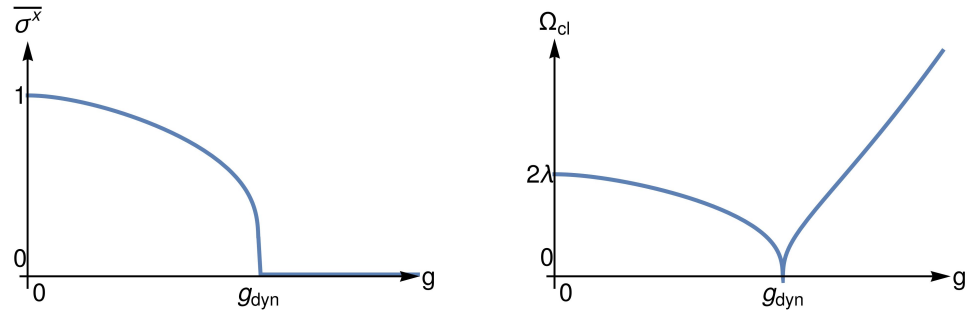

Figure 2.5: Left panel: nonequilibrium order parameter $\overline{\sigma^x}$, defined in Eq. (2.29), of the infinite-range Ising model (2.23) after a quench of the external magnetic field starting from a ferromagnetic ground state with $g_0 = 0$ and positive magnetization, as a function of the post-quench field g. Right panel: Classical frequency $\Omega_{\rm cl}$ of the mean-field dynamical trajectory, which represents the characteristic time scale of the nonequilibrium evolution, as a function of the post-quench field g. For both quantities, the nature of the singular behavior at the dynamical critical point $g = g_{\rm dyn}$ is logarithmic, as explained in the text. These plots can be compared with the analogous ones in equilibrium conditions in Fig. 2.2.

g instead of a sudden quench, the dynamical critical point retains its nature, although it gets shifted towards the equilibrium critical point, until it merges with the latter in the limit of adiabatic variation.

2.3 Driven dynamics: Kapitza phases

In this Section, we consider the nonequilibrium dynamics of fully-connected spin systems subject to an external periodic drive. In view of our later discussion of dynamically stabilized Kapitza phases in models describing quantum simulators with trapped ions, we discuss the infinite-range limit $\alpha \to 0$ of the long-range quantum Ising Hamiltonian in Eq. (1.18), i.e.,

$$\hat{H}_{\alpha=0}(t) = -J \sum_{i,j=1}^{N} \hat{\sigma}_i^x \hat{\sigma}_j^x - g(t) \sum_{i=1}^{N} \hat{\sigma}_i^z, \tag{2.32}$$

where the coupling scales as $J \sim \tilde{J}_0/N$ in the thermodynamic limit. This coincides with the model in Eq. (2.23) discussed in the previous Section in the context of quench dynamics, upon identifying $\lambda \leftrightarrow \tilde{J}_0$. For simplicity, we shall consider a monochromatic drive in the transverse field,

$$g(t) = g_0 + \delta g \cos(\Omega t), \tag{2.33}$$

with amplitude δg and frequency Ω. As discussed in the previous Sections, in the thermodynamic limit $N \to \infty$, the nonequilibrium dynamics starting from polarized spin states is governed by the classical limit $\mathcal{H}_{cl}(t)$ of the rescaled Hamiltonian $\hat{H}/N$,

$$\mathcal{H}_{cl}(t) = -\tilde{J}_0 \, (\sigma^x)^2 - g(t)\sigma^z. \tag{2.34}$$

as a function of the classical spin $\sum_i \hat{\boldsymbol{\sigma}}_i/N \to \vec{\sigma}$ on the Bloch sphere of radius $\rho = 1$.

2.3.1 Phenomenology of driven dynamics

When $g(t) = g_0$ is static, the nonequilibrium dynamics has been discussed in Sec. 2.2. For $|g_0| < 2\tilde{J}_0$, the system supports the ferromagnetic state indicated by the arrow in Fig. 2.6(a), $\vec{\sigma}(t)$ follows one of the trajectories represented on the Bloch sphere in panel (a), selected by the initial condition $\vec{\sigma}(0)$ (for definiteness, we will assume $g_0 \geqslant 0$ throughout). Two families of them are characterized by a ferromagnetic-like, symmetry-breaking periodic evolution with opposite signs of the nonvanishing time-averaged order parameter $\overline{\sigma^x}$. A trajectory (red) passing through the equilibrium unstable paramagnetic point (red star) separates these two families from the paramagnetic-like orbits with $\overline{\sigma^x} = 0$. See Sec. 2.2 for more details.

Turning on the modulation as in Eq. (5.2), representative samples of discrete stroboscopic trajectories $\{\vec{\sigma}(t_n)\}$, where $t_n = 2\pi n/\Omega$, with $n = 0, 1, 2, \ldots$ of the semiclassical collective spin are reported in Fig. 2.6(b), (c), and (d). When the

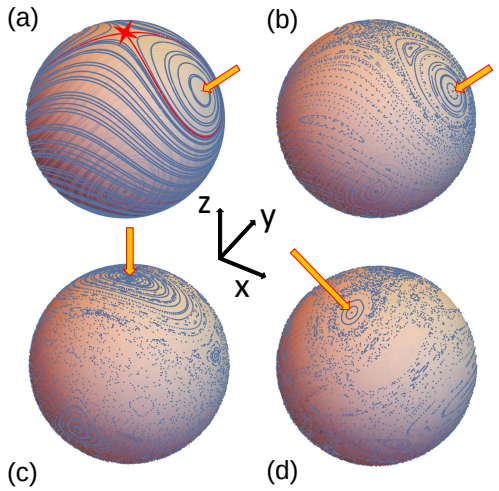

Figure 2.6: Dynamics on the Bloch sphere of the infinite-range Ising ferromagnet in the thermodynamic limit. (a) Semiclassical phase space trajectories of the static Hamiltonian with $g/\tilde{J}_0 = 1.2$. (b), (c), (d): Stroboscopic trajectories $\{\vec{\sigma}(t_n)\}$, with $t_n = 2\pi n/\Omega$, $n = 0, 1, 2, \ldots$ of the semiclassical collective spin on the Bloch sphere with driving frequency $\Omega/\tilde{J}_0 = 5$ and increasing amplitude $\delta g/\tilde{J}_0 = 0.01$ (b), 3.3 (c), and 5 (d), with $g_0/\tilde{J}_0 = 1.2$. Panel (b) shows the presence of a possible ferromagnetic dynamical ordering, corresponding to the evolution occurring within a single ferromagnetic sector $\sigma^x > 0$, with a special synchronized trajectory (appearing as a single point under stroboscopic observations), together with the onset of chaotic behavior around the unstable paramagnetic point [297]. Panel (c) shows the appearance of a dynamically stabilized phase, akin to the well-known stabilization of the inverted driven Kapitza pendulum [125, 301]. Panel (d) shows that for larger driving frequencies, an unconventional dynamical ferromagnetic ordering appears, where the direction of the magnetization is orthogonal to the direction x of the actual ferromagnetic interactions. "Islands" with stable stroboscopic trajectories are indicated by the arrows.

modulation δg is small [see panel (b)], the ferromagnetic states leave room to periodic trajectories of the collective spin within the corresponding ferromagnetic sector *synchronized* with the drive (and hence appearing as a single point under stroboscopic observations). Conversely, initial states in a neighborhood of the unstable paramagnetic point [red star in panel (a)] display chaotic motion as soon as $\delta g \neq 0$ [297, 298]. As δg increases, this chaotic region invades an increasingly large portion of the sphere [297]. This behavior can be understood on the basis of classical KAM and chaos theory [23, 299]. Related phenomena have been experimentally observed with Bose-Einstein condensates [300]. Upon further increasing the modulation [see panel (c)], a region in the parameter space emerges where *dynamical stabilization* of the unstable paramagnetic point occurs, thereby opening up a stability region around it. This phenomenon is analogous to the stabilization of the inverted pendulum discovered by Kapitza [125, 301]. In addition to this Kapitza-like stabilization, as δg increases with $g_0 \approx \tilde{J}_0$ [see panel (d)], an unconventional regime appears, characterized by dynamical ferromagnetic ordering in the yz-plane, orthogonal to the direction x of the actual ferromagnetic interactions.

2.3.2 Theory: Effective Hamiltonian for fast driving

The origin of the numerical phenomenology described above may be understood analytically by studying the regime of fast-driving limit $\Omega \to \infty$ as a function of the rescaled amplitude $\zeta = \delta g/\Omega$. In fact, in this case the effective Floquet Hamiltonian (see App. C) governing the stroboscopic evolution [302] may be determined exactly.

When the system is driven rapidly enough at finite driving amplitude, the effective evolution is governed by the time-averaged Hamiltonian [cf. Eq. (C.4)], since the system has no time to react to variations of external parameters much faster than its characteristic dynamical time scales. Nevertheless, if the modulation amplitude δg is simultaneously increased with the frequency, keeping a finite ratio $\zeta \equiv \delta g/\Omega$, the effective dynamics may become qualitatively different from those governed by the static Hamiltonian. Such qualitative changes involve a partial resummation of the high-frequency expansion (C.3) of the Floquet Hamiltonian [110], which is in general an intractable problem. However, analytic solutions in closed form may be obtained in some cases, by performing a convenient time-periodic transformation [110]. In our case, this strategy is implemented by moving to a rotating frame in order to effectively eliminate the oscillating magnetic field, i.e.,

$$\begin{pmatrix} \hat{\sigma}_i^x \\ \hat{\sigma}_i^y \\ \hat{\sigma}_i^z \end{pmatrix} = \begin{pmatrix} \cos\big(2\zeta\sin(\Omega t)\big)\,\hat{\sigma}_i'^x + \sin\big(2\zeta\sin(\Omega t)\big)\,\hat{\sigma}_i'^y \\ -\sin\big(2\zeta\sin(\Omega t)\big)\,\hat{\sigma}_i'^x + \cos\big(2\zeta\sin(\Omega t)\big)\,\hat{\sigma}_i'^y \\ \hat{\sigma}_i'^z \end{pmatrix}. \tag{2.35}$$

The equations of motion for $\vec{\sigma}'$ are affected by the *inertial* forces, described by the transformed generator $\widetilde{H}(t)$ of time-evolution. This is given by the static part of the Hamiltonian alone, which takes the same form as Eq. (5.1) with $\hat{\sigma}_i^x\hat{\sigma}_j^x$ replaced by

$$\begin{aligned} &\cos^2\big(2\zeta\sin(\Omega t)\big)\,\hat{\sigma}_i'^x\hat{\sigma}_j'^x + \sin^2\big(2\zeta\sin(\Omega t)\big)\,\hat{\sigma}_i'^y\hat{\sigma}_j'^y \\ &+\cos\big(2\zeta\sin(\Omega t)\big)\,\sin\big(2\zeta\sin(\Omega t)\big)\big(\hat{\sigma}_i'^x\hat{\sigma}_j'^y + \hat{\sigma}_i'^y\hat{\sigma}_j'^x\big). \end{aligned} \tag{2.36}$$

Crucially, the modulation δg now intervenes only via the finite combination ζ. Hence, a standard high-frequency expansion for the new time-periodic Hamiltonian $\widetilde{H}(t)$ will reproduce the correct high-frequency effective Hamiltonian $\hat{H}_{\rm eff}$ in a nonperturbative fashion. To lowest order, time-averaging and taking the classical limit yields

$$\mathcal{H}_{\rm eff} = -\tilde{J}_0\left(\frac{1+\gamma(\zeta)}{2}(\sigma^x)^2 + \frac{1-\gamma(\zeta)}{2}(\sigma^y)^2\right) - B_0\,\sigma_z, \tag{2.37}$$

i.e., an XY-model with an engineered anisotropy parameter

$$\gamma = \gamma(\zeta) = \mathcal{J}_0(4\zeta), \tag{2.38}$$

where $\mathcal{J}_0$ is the standard Bessel function of the first kind.

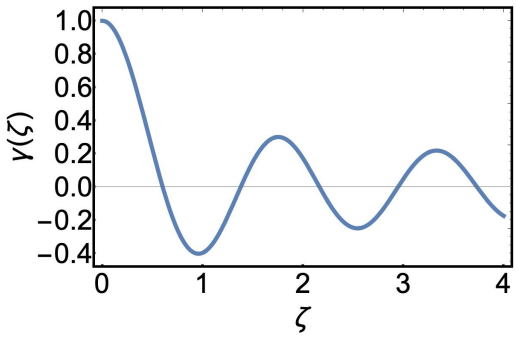

Figure 2.7: Plot of the anisotropy γ in the effective fast-driving Floquet Hamiltonian, as a function of the rescaled driving amplitude ζ, given by Eq. (2.38).

We see that the net effect of the driving is to redistribute the ferromagnetic coupling strength along the directions x and y. The behavior of the effective anisotropy γ as a function of the rescaled driving strength ζ is shown in Fig. 2.7. As ζ increases from zero, the effective ferromagnetic interaction along x weakens, which makes it possible to dynamically stabilize the paramagnetic configuration. The exact boundary $g_0 = g_{cr}(\zeta) \equiv \tilde{J}_0\,(1 + |\mathcal{J}_0(4\zeta)|)$ of the Kapitza phase K is reported in Fig. 2.8. Note that this region is continuously connected with the paramagnetic one P in the phase diagram, see Fig. 2.8, similarly to the region of dynamical stabilization of the Kapitza pendulum, which is continuously connected with the parameter region with a reversed direction of gravity, in which stability is trivial [301].

As ζ increases further, due to the oscillations of $\mathcal{J}_0$ around zero, intervals with a negative anisotropy γ appear, making ferromagnetic ordering along the direction y become favored. The mechanism is thus elucidated for the occurrence of the unconventional dynamical phases with ferromagnetic ordering in the yz-plane, orthogonal to the direction x of the actual ferromagnetic interaction, which builds up whenever $\gamma < 0$, $g_0 < \tilde{J}_0\,(1-\gamma)$, i.e., within the regions denoted by $F_\perp$ in Fig. 2.8.

The numerical results reported in Fig. 2.6 show that these nonequilibrium phases persist even at smaller driving frequencies, comparable to the characteristic energy scale $\tilde{J}_0$ of the system. Indeed, when the driving frequency Ω is large but finite, the effective Floquet Hamiltonian (2.37) receives perturbative corrections in an expansion in inverse powers of Ω. The first term beyond Eq. (2.37) is reported below in Eq. (2.39) and it causes small quantitative modifications of the boundaries in Fig. 2.8.

A second Kapitza phase coexists with $F_{\parallel,\perp}$ for $g_0 < \tilde{J}_0\,(1 - |\mathcal{J}_0(4\zeta)|)$ In fact, for $g_0 < \tilde{J}_0\,(1 - |\gamma(\zeta)|)$ (i.e., within the shaded region in Fig. 2.8), the effective Hamiltonian (2.37) has a *maximum* at the paramagnetic point in addition to the two ferromagnetic minima in the xz- or yz-plane, depending on γ being positive or negative, respectively. The corresponding phase portraits are shown in Fig. 2.9. In particular, in correspondence of the values $\zeta_1, \zeta_2, \ldots$ such that $\gamma = 0$ (related to the zeros of the Bessel function $\mathcal{J}_0$), the effective Hamiltonian has continuous $O(2)$ symmetry. In this case, stable trajectories exist around the

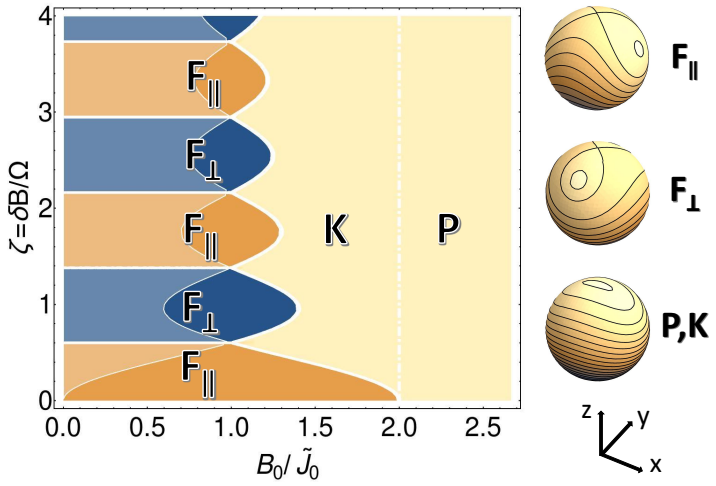

Figure 2.8: Left: Fast-driving nonequilibrium phase diagram of the periodically driven infinite-range Ising model defined by Eqs. (2.32) and (5.2), from Ref. [3] (notation: $B \to g$). Upon varying the average magnetic field g_0 and the rescaled modulation amplitude $\zeta = \delta g/\Omega$, a dynamical paramagnetic phase P, a dynamically stabilized Kapitza paramagnetic phase K, a conventional dynamical ferromagnetic phase $F_{\parallel}$ and an unconventional dynamical ferromagnetic phase $F_{\perp}$ with orthogonal magnetization emerge. The axis $\zeta = 0$ corresponds to the equilibrium phase diagram, where a ferromagnetic $F_{\parallel}$ and a paramagnetic P phase are present. The diagram shows the exact phase boundaries of the infinite-range system with $\alpha = 0$. (Note that the dashed line separating K and P does not correspond to an actual phase transition.) Within the shaded region on the left, a second Kapitza phase coexists with $F_{\parallel,\perp}$. Right: Schematic phase portraits on the Bloch sphere of the effective high-frequency Hamiltonians governing the evolution of the collective spin of the system, highlighting the various phases.

direction of both the ferromagnetic minima and the paramagnetic configuration, which would be unstable in the absence of the driving.

We report the corrections of order Ω^{-1} to the effective Hamiltonian (2.37) within the Magnus expansion in the oscillating frame (see App. C). By using Eq. (C.5), a straightforward calculation yields

$$\begin{aligned}\mathcal{H}^{(1)}_{\rm eff} =& \frac{8\pi \tilde{J}_0^2}{\Omega}\Big[\kappa_{x^2,y^2}(\zeta)\, S_x S_y S_z - \kappa_{xy,x^2}(\zeta)\, S_x^2 S_z \\ &+ \kappa_{xy,y^2}(\zeta)\, S_y^2 S_z + \frac{B_0}{2\tilde{J}_0}\kappa_{z,xy}(\zeta)\,(S_y^2 - S_x^2)\Big],\end{aligned} \tag{2.39}$$

in terms of the dimensionless coefficients κ

$$\begin{aligned}\kappa_{x^2,y^2}(\zeta) &= \int_0^{2\pi} \frac{d\xi}{2\pi}\,(\dot{A}B - \dot{B}A),\\ \kappa_{xy,x^2}(\zeta) &= \int_0^{2\pi} \frac{d\xi}{2\pi}\,(\dot{C}A - \dot{A}C),\\ \kappa_{xy,y^2}(\zeta) &= \int_0^{2\pi} \frac{d\xi}{2\pi}\,(\dot{C}B - \dot{B}C),\\ \kappa_{z,xy}(\zeta) &= \int_0^{2\pi} \frac{d\xi}{2\pi}\,C,\end{aligned} \tag{2.40}$$

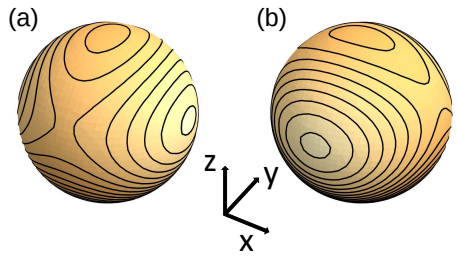

Figure 2.9: Schematic phase portraits of the effective Hamiltonian $\mathcal{H}_{\rm eff}$ in Eq. (2.37) on the sphere, with parameters belonging to the shaded region of the nonequilibrium phase diagram in Fig. 2.8, corresponding to the coexistence of a dynamically stabilized Kapitza phase and the ferromagnetic phase $F_{\parallel}$ [(a), shaded blue in Fig. 2.8], or $F_{\perp}$ [(b), shaded orange in Fig. 2.8]. We emphasize that the paramagnetic configuration is here associated with a *maximum* of $\mathcal{H}_{\rm eff}$.

where the dots stand for derivatives with respect to the argument ξ, and

$$\begin{aligned} A(\xi) &\equiv \int_0^{\xi} \frac{d\eta}{2\pi} \cos^2(2\zeta \sin\eta), \\ B(\xi) &\equiv \int_0^{\xi} \frac{d\eta}{2\pi} \sin^2(2\zeta \sin\eta) = \frac{\xi}{2\pi} - A(\xi), \\ C(\xi) &\equiv \int_0^{\xi} \frac{d\eta}{2\pi} \cos(2\zeta \sin\eta) \sin(2\zeta \sin\eta). \end{aligned} \tag{2.41}$$

The classical Hamiltonian $\mathcal{H}_{\rm eff}^{(0)} + \mathcal{H}_{\rm eff}^{(1)}$, with $\mathcal{H}_{\rm eff}^{(0)}$ given by Eq. (2.37) and $\mathcal{H}_{\rm eff}^{(1)}$ by Eq. (2.39), defines phase space trajectories on the Bloch sphere which better approximate the stroboscopic evolution of the collective spin at finite driving frequency Ω compared to the high-frequency limit (2.37). In particular, it is possible to determine the shift of the boundaries in Fig. 2.8 to order Ω^{-1}. We note that although the Magnus expansion is divergent [110], its truncations provide an increasingly accurate approximation of the regular orbits (KAM tori) in phase space, and hence of the dynamically stabilized phases.

In Chap. 5 below, we will demonstrate that most dynamically stabilized phases discussed above are robust to the impact of many-body effects induced by a space dependence in the spin-spin couplings.

2.4 Finite-size (quantum) effects

In this Section, we discuss the finite-size effects in the nonequilibrium dynamics of the fully-connected spin systems. As discussed in Sec. 2.1.2, the role of the system size is to modify the effective Planck constant $\hbar_{\rm eff} = 1/N$. For this reason, finite-size effects represent quantum corrections to the limiting classical behavior.

As usual, for the sake of definiteness, we focus here on the quantum Ising model in Eq. (2.23), which is equivalent to the Lipkin-Meshkov-Glick model [293]. (In Chap. 6 we shall generalize part of the following discussion to generic fully-connected spin systems.) It is worth mentioning that this model

is actually solvable by Bethe-ansatz for all N (see Ref. [303]). In principle, this occurrence allows one to analytically compute the ground-state as well as the nonequilibrium properties. However, a semiclassical approach turns out to be simpler and more powerful for large N.

2.4.1 Ground state and elementary excitations

Let us now compute the low-energy spectrum of the system defined by Eq. (2.23). Within each sector with fixed value of the total spin magnitude, labelled by ρ, the quantum mechanics of the collective spin is equivalent to that of a quantum particle in an energy landscape whose depth grows proportionally to N. In the thermodynamic limit, the lowest excitations of this particle are harmonic, and can be determined by a quadratic expansion of the classical Hamiltonian around its energy minimum(a). However, we may obtain the low-lying spectrum without explicitly resorting to the classical limit, via a Holstein-Primakoff transformation [304], as we discuss below.

For infinitely strong field $g \gg \lambda$, the ground state approaches the fully polarized state in the positive z-direction, and the elementary excitations above it coincide with the tower of spin-flip excitations, characterized by the eigenvalues $Ns-1, Ns-2, \dots$ of the collective spin projection along this direction. As the ratio g/λ decreases, this structure gets modified by the ferromagnetic interactions. This is best captured by mapping the transverse (x and y) spin components to canonical bosonic variables. In a classical description, this corresponds to approximating the surface of the Bloch sphere by its tangent plane at the North pole: as $N \to \infty$, the classical phase space coarse-graining by discrete quantum states becomes increasingly thin, making the approximation asymptotically exact. Such a transformation can be expressed via a Holstein-Primakoff mapping truncated to lowest order, i.e.,

$$\begin{cases} s\,\tilde{\sigma}^{z}_{k=0} = Ns\rho - \hat{n} = Ns\rho - \dfrac{\hat{q}^2+\hat{p}^2-1}{2}, \\ s\,\tilde{\sigma}^{x}_{k=0} \approx \sqrt{Ns\rho}\;\hat{q}, \\ s\,\tilde{\sigma}^{y}_{k=0} \approx \sqrt{Ns\rho}\;\hat{p}, \end{cases} \tag{2.42}$$

where the bosonic variables $\hat{q}, \hat{p}$ satisfy $[\hat{q},\hat{p}] = i$; one can check that the spin commutation relations $[\tilde{\sigma}^{\alpha}_{k=0}, \tilde{\sigma}^{\beta}_{k=0}] = (i/s)\epsilon^{\alpha\beta\gamma}\tilde{\sigma}^{\gamma}_{k=0}$ are satisfied to lowest order by the r.h.s. of Eqs. (2.42). The quantum number $n = 0, 1, 2, \dots$ labels the quantized spin projection along the direction z of the classical minimum. Using Eqs. (2.42), the Hamiltonian (2.23) can be approximated by neglecting terms of order $1/N$, and hence easily diagonalized,

$$\begin{aligned} \hat{H}_{>} &= -Ng\rho + \frac{g}{s}\frac{\hat{q}^2+\hat{p}^2-1}{2} - \frac{\lambda}{s}\hat{q}^2 = \\ &= -Ng\rho + \frac{1}{s}\left(\frac{\omega_{>}-\omega_{>}^{(0)}}{2}\right) + \frac{1}{s}\omega_{>}\,\hat{n}', \end{aligned} \tag{2.43}$$

where

$$\omega_> = \sqrt{g(g-g_{cr})}, \qquad \omega_>^{(0)} = g. \tag{2.44}$$

The first term in the last line of Eq. (2.43) represents the classical energy [compare with Eq. (2.25)], the second one is the variation of the quantum zero-point energy contribution, i.e., the energy increase due to the quantum fluctuations of the spin around the classical minimum configuration, while the last one is the energy of the elementary (harmonic) excitations, with $n' = 0, 1, 2, \ldots$.

For $g > g_{cr}$, the number $\langle \hat{n} \rangle = \langle \hat{q}^2 + \hat{p}^2 - 1 \rangle / 2$ of spin excitations in the ground state is finite, and diverges as $g \searrow g_{cr}$ [305]. On the other hand, for $g < g_{cr}$, the frequency $\omega_>$ becomes imaginary, which signals a failure of the expansion. In fact, at $g = g_{cr}$ the ground state undergoes a discontinuous change (quantum phase transition [9]), associated with the spontaneous breaking of the $\mathbb{Z}_2$ (x-inversion) symmetry of the model, as already discussed above at classical level. This phenomenon may be thought as a *condensation*, which can be characterized by the sudden buildup of a macroscopically large occupation of the collective quantum mode $\langle \hat{n} \rangle \sim N$.

In order to determine the ground state and the elementary excitations in the broken-symmetry phase, it is convenient to introduce now a procedure which will lend itself to powerful generalizations in the following chapters. We rewrite the components of the collective spin in a rotated frame denoted by capital letters $(\mathbf{X}, \mathbf{Y}, \mathbf{Z})$,

$$\tilde{\boldsymbol{\sigma}}_{k=0} = \mathbf{X}\, \hat{\sigma}^X_{k=0} + \mathbf{Y}\, \hat{\sigma}^Y_{k=0} + \mathbf{Z}\, \hat{\sigma}^Z_{k=0}, \tag{2.45}$$

obtained by rotating the axes by an angle θ in the xz-plane

$$\mathbf{X} \equiv \begin{pmatrix} \cos\theta \\ 0 \\ -\sin\theta \end{pmatrix}, \quad \mathbf{Y} \equiv \begin{pmatrix} 0 \\ 1 \\ 0 \end{pmatrix}, \quad \mathbf{Z} \equiv \begin{pmatrix} \sin\theta \\ 0 \\ \cos\theta \end{pmatrix}. \tag{2.46}$$

Hence, we perform a Holstein-Primakoff transformation [cf. Eq. (2.42)] along the rotated Z-axis and neglect terms of order $1/N$. As a result, we get

$$\begin{aligned} \hat{H}_< = & -N\Big(g\rho\cos\theta + \lambda\rho^2\sin^2\theta\Big) \\ & - \sqrt{\frac{\rho N}{s}}\sin\theta\Big(g - 2\lambda\rho\cos\theta\Big)\hat{q} \\ & + \frac{1}{s}\left[(2\lambda\rho\sin^2\theta + g\cos\theta)\frac{\hat{q}^2+\hat{p}^2-1}{2} - \lambda\rho\cos^2\theta\,\hat{q}^2\right]. \end{aligned} \tag{2.47}$$

In order for the bosonic variables to describe low-energy excitations above the ground state, it is necessary to fix the frame in such a way that linear terms in the second line vanish. This condition leads to the equation (2.27) for the classical minima, identified by the angle θ^*. The resulting quadratic Hamiltonian can then be easily diagonalized, obtaining

$$\hat{H}_< = -N\left(\frac{g^2}{4\lambda} + \lambda\rho^2\right) + \frac{1}{s}\left(\frac{\omega_< - \omega_<^{(0)}}{2}\right) + \frac{1}{s}\omega_<\,\hat{n}', \tag{2.48}$$

where

$$\omega_< = \sqrt{g_{cr}^2 - g^2}, \qquad \omega_<^{(0)} = g_{cr}. \tag{2.49}$$

Analogously to Eq. (2.43), the first term in the last line of Eq. (2.48) represents the classical energy [compare with Eq. (2.25)], the second one expresses the shift in the quantum zero-point energy contribution, i.e., the energy increase due to the quantum fluctuations of the spin around the classical minimum configuration, while the last one is the energy of the elementary (harmonic) excitations, with $n' = 0, 1, 2, \ldots$.

We observe that the results (2.43) and (2.48) are asymptotically exact for all finite n' as $N \to \infty$, and *nonperturbative* in the ratio λ/g. They could be obtained at the same level of accuracy by resorting to semiclassical considerations only. Systematic improvements in higher powers of n'/N have been nicely worked out by J. Vidal and collaborators with a more refined analysis [305]. We observe that the energy gap above the ground state closes at the equilibrium critical point $g = g_{cr}$, with a mean-field critical exponent 1/2 (see Fig. 2.2).

Even though spin excitations with finite wavelength $k \neq 0$ (spin waves) are dynamically decoupled from the collective spin in infinite-range systems, they could be excited in the presence of an external thermal bath at finite temperature T. It is straightforward to obtain their spectrum, as the effect of each such spin excitation is just to lower the collective spin magnitude by one unit. If $n_{sw} = 0, 1, 2, \ldots$ is the total occupation number of the spin-wave modes with $k \neq 0$, one has $\left|\tilde{s}_{k=0}\right|^2 = (Ns - n_{sw})(Ns - n_{sw} + 1)$, i.e.,

$$\rho = 1 - \frac{n_{sw}}{Ns}. \tag{2.50}$$

By substituting this equation into Eqs. (2.44) and (2.49), one finally obtains the complete spectrum of excitations above the ground state, in the thermodynamic limit and to leading order in n'/N and n_{sw}/N:

$$\begin{aligned} H_> &= -Ng + \frac{\omega_> - \omega_>^{(0)}}{2s} + \frac{1}{s}\left(g\,\hat{n}_{sw} + \omega_>\,\hat{n}'\right), \\ H_< &= -N\left(\frac{g^2}{4\lambda} + \lambda\right) + \frac{\omega_< - \omega_<^{(0)}}{2s} + \frac{1}{s}\left(2\lambda\,\hat{n}_{sw} + \omega_<\,\hat{n}'\right), \end{aligned} \tag{2.51}$$

valid for $g > 2\lambda$ and $g < 2\lambda$, respectively. All the spin wave excitations introduced above have a finite gap, g/s or $2\lambda/s$, and a flat dispersion relation independent of the wavevector $k \neq 0$, because the fully-connected interactions carry no information on spatial scales, hence cannot resolve finite wavelengths. As a consequence, the presence of a finite low temperature T leads to exponentially small corrections to the order parameter, with a shift of the critical point that can be computed [294] by minimizing the mean-field classical Hamiltonian (2.25) with

$$\rho(T) = 1 - \frac{1}{s}\,\frac{1}{e^{\frac{2\lambda/s}{T}} - 1}, \tag{2.52}$$

determined by the thermal (Bose-Einstein) occupation of spin-wave modes.

2.4.2 Spectral properties

Semiclassical arguments may be exploited to derive the critical scaling properties of infinite-range interacting systems both in and out of equilibrium.

For a system with a single degree of freedom, the spectrum obtained via the semiclassical quantization rule consists of classical trajectories with energy E_n such as to enclose an area $S_{cl}(E_n)$ in phase space equal to an integer multiple of Planck's constant $\hbar$, i.e.,

$$S_{cl}(E_n) = n\hbar, \quad n \text{ integer}, \tag{2.53}$$

where $S_{cl}(E)$ corresponds to the classical action. This quantization rule, together with the well-known relation between the action S_{cl} and the classical period of a trajectory (see, e.g., Ref. [296])

$$\frac{dS_{cl}(E)}{dE} = T_{cl}(E) \equiv \frac{2\pi}{\Omega_{cl}(E)} \tag{2.54}$$

yields the semiclassical level spacing

$$E_{n+1} - E_n \sim \frac{dE_n}{dn} = \hbar\,\Omega_{cl}(E_n). \tag{2.55}$$

This equation may be seen as a generalization of the relation valid for the spectrum of a harmonic oscillator to nonlinear dynamics, in which the oscillations are not isochronous and thus the quantum energy spectrum is not equispaced. The semiclassical density of states $\rho(E)$ is given by the inverse level spacing.

We can use the above semiclassical relation to elucidate the spectral properties of the fully-connected quantum Ising model. For $g > g_{cr}$, taking the low-energy limit (n finite and $N \to \infty$) of Eq. (2.55), one recovers the harmonic tower of excitations of Eq. (2.43), with $\Omega_{cl}(E_n) \sim \omega_>/s$. At the quantum critical point $g = g_{cr}$, the energy gap of the elementary excitations above the ground state vanishes in the thermodynamic limit. The classical counterpart of this phenomenon is the vanishing of the classical frequency of small oscillations, which occurs because the minimum of $\mathcal{H}_{cl}$ at criticality is quartic rather than quadratic. The critical scaling of the energy gap as $N \to \infty$ may be extracted via semiclassical considerations, as $\hbar_{eff} \sim 1/N$. Retaining the quartic terms of order $1/N$ neglected in Eq. (2.43), and applying the semiclassical quantization rule in Eq.(2.53), one finds the low-energy asymptotics of quantized energy levels as

$$E_n - E_0 \underset{\substack{n \text{ finite} \\ N\to\infty}}{\sim} c\,\frac{n^{4/3}}{N^{1/3}}, \tag{2.56}$$

which shows that the critical gap above the ground state for $g = g_{cr}$ scales as $N^{-1/3}$ for large N. For a more thorough analysis, see, e.g., Ref. [305].

As g is decreased below the quantum critical point g_{cr}, the classical landscape presents two symmetric minima, as discussed above and illustrated in Fig. 2.1. Below the energy $E_{dyn} \equiv \mathcal{H}_{cl}(\theta = 0)$ of the classical separatrix, two symmetric

families of classical trajectories fill the two energy wells. In the thermodynamic limit, this corresponds to two towers of pairwise degenerate energy levels, associated with wavefunctions localized in the two wells and hence distinguished by the sign of the order parameter. However, such a spontaneous symmetry breaking has to be smoothed out in finite systems, where no singularity may occur.[2] In fact, at finite size N, the actual energy eigenstates below the critical energy are nondegenerate and alternately even and odd with respect to the $\mathbb{Z}_2$ symmetry of the Hamiltonian. For large N, they approach even and odd superpositions of the localized wavefunctions. The energy splitting between each pair of quasidegenerate eigenstates is proportional to the quantum tunneling amplitude across the energy barrier, and hence it is exponentially small in the height of the barrier itself, which grows proportionally to the system size N (see e.g. Ref. [306]). Therefore, tunneling between the two broken-symmetry sectors is practically suppressed even for moderate system sizes, and one may consider the two towers of symmetry-breaking excited states independently of each other, as we did in Sec. 2.4.1. In addition, it should be noted that tunneling at the ground state level is extremely fragile to tiny symmetry-breaking perturbations, such as longitudinal magnetic fields.

Equation (2.55) asserts that, for large system size N, the spectral density of states $\rho(E)$ is proportional to the period $T_{cl}(E)$ of the classical trajectory with energy E. As discussed in Sec. 2.2 above, within the ferromagnetic phase $g < g_{cr}$, the classical period diverges logarithmically at the classical separatrix [cf. Eq. (2.30)], corresponding to the dynamical critical phenomenon. This singularity affects highly-excited states, and signals a phase transition at finite energy density. However, this transition cannot be identified with a standard thermal phase transition, as the system is confined in a small portion of the many-body Hilbert space, protected by the conservation of the collective spin magnitude. In fact, the universal properties of this critical phenomenon are described by the *dynamical* critical point rather than by the thermal equilibrium one. In the literature, this spectral transition has been studied separately, and is referred to as *excited state quantum phase transition* (ESQPT) [307].

2.4.3 Relaxation and tunneling

Let us now discuss the nonequilibrium dynamics within the semiclassical approximation [308,309]. The first quantum correction to the classical evolution starting from a spin-coherent state is equivalent to treating the corresponding Gaussian Wigner function in phase space as a probability distribution and considering its classical (Liouville) evolution. To this level of approximation, known as the truncated Wigner approximation (TWA), the role of quantum mechanics amounts to providing a degree of uncertainty to the classical phase space point which represents the initial state of the system [310]. The amount of uncertainty is quantified by the phase space extension of the wavepacket, which covers an area equal to Planck's constant $\hbar$, corresponding to the maximal phase

[2] By general arguments, the spectrum of a finite matrix depends smoothly on its parameters.

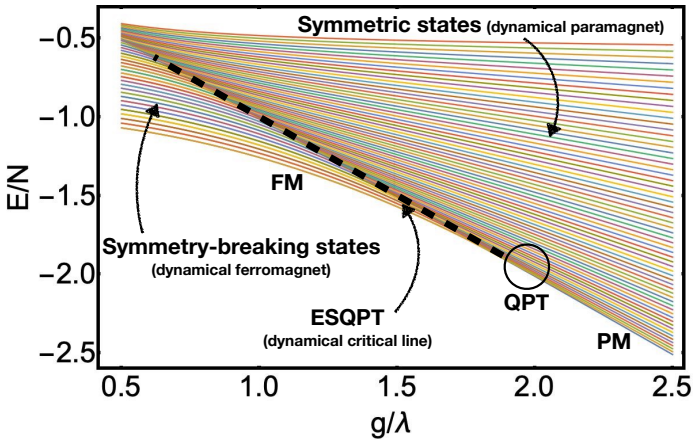

Figure 2.10: Spectrum of the fully-connected quantum Ising model in Eq. (2.23). The energy density E/N of the lowest 64 energy levels is shown on varying the transverse field g in the window $[0.5\lambda, 2.5\lambda]$ around the quantum critical point $g_{cr} = 2\lambda$ (QPT), in a system of $N = 100$ spins. One identifies the quantum critical point where the energy gap above the ground state shrinks to zero in the thermodynamic limit. The excited-state quantum phase transition (ESQPT) separates energy eigenstates with ferromagnetic and paramagnetic character, and the density of states is singular around it. Its counterpart in quench dynamics is the dynamical phase transition discussed in Sec. 2.2.

space resolution allowed by the Heisenberg uncertainty relation.

In the dynamics governed by a nonquadratic Hamiltonian, like the one in Eq. (2.25), closeby points in phase space separate *linearly* in time, due to their different periods. The sole exception is represented by the critical trajectory (separatrix), around which two points separate *exponentially* fast in time. Since the linear extension of the initial wavepacket in phase space is $\sqrt{\hbar_{\rm eff}} \sim 1/\sqrt{N}$, after a time scale of order $\mathcal{O}(\sqrt{N})$ [or $\mathcal{O}(\log N)$ around the separatrix] (the so-called Ehrenfest time $T_{\rm Ehr}$) the wavepacket has spread over the whole classical trajectory, and the observables have correspondingly relaxed to their "microcanonical" average [83, 308, 309].

While the truncated Wigner approximation is effective in capturing relaxation of local observables, it is actually insensitive to deeply quantum effects such as tunneling, which cannot be reproduced via naive classical simulations. As discussed in the previous Section, all eigenstates below the critical energy $E_{\rm dyn}$ are almost pairwise degenerate, and correspond to even and odd superpositions of semiclassical eigenstates localized within the two symmetric energy wells. The energy splitting between the two is exponentially small in the height of the barrier, i.e., in the system size N. This implies that tunneling to the opposite side from an initial state localized on one side is exponentially slow, i.e., the associated time scale is $T_{\rm tun} = \mathcal{O}(e^{cN})$.

In the light of the above, the qualitative modifications of the classical dynamics discussed in the previous Sections due to finite-size effects can be summarized as follows:

1. a fully polarized spin-coherent initial state actually corresponds to a broad wavepacket of linear extension $\propto 1/\sqrt{N}$ on the Bloch sphere, rather than

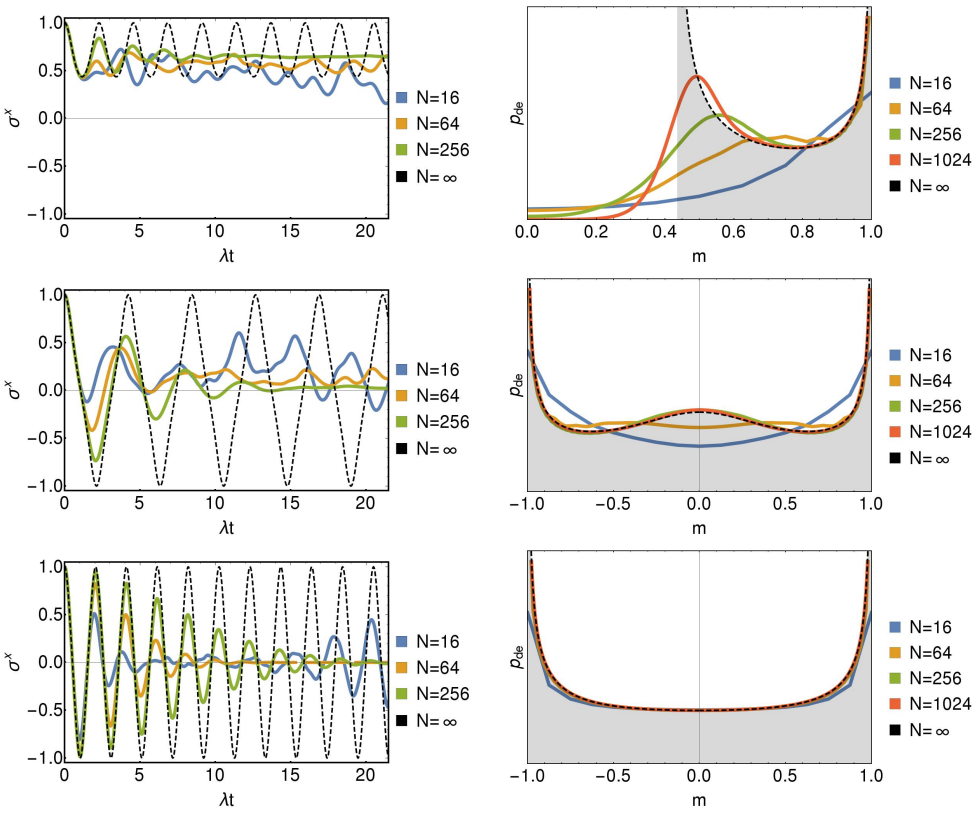

Figure 2.11: Convergence to the classical behavior in the thermodynamic limit $N \to \infty$ of the quantum dynamics governed by the Hamiltonian (2.23) with finite size N and with $s = 1/2$. This is studied via exact diagonalization in the maximal spin sector. Left panels: Evolution of the dynamical order parameter with $g/\lambda = 0.9$ (top), $g/\lambda = 1.1$ (center), $g/\lambda = 1.7$ (bottom), and increasing system size $N = 16, 64, 256$, starting from a fully polarized state along the x-direction, i.e., from a ground state with $g_0 = 0$. The classical limit is shown by the black dashed curve. Right panels: corresponding infinite-time average distribution of the order parameter, as obtained from the diagonal ensemble $p_{de}(m) = \overline{|\langle \Psi(t) | m \rangle|^2}$, where $|m\rangle$ is the state with magnetization m. The classical "microcanonical" distributions are shown by the black dashed curve. Note that the quantum evolution agrees with its classical limit over a time window that increases with N. After this time, quantum phenomena emerge. In all cases, damping of the classical oscillations takes place as a consequence of the quantum spreading of the wavepacket. Furthermore, for system sizes N as small as 16, additional quantum effects become observable. In the top left panel, quantum tunneling to the opposite well can be observed in the dynamical ferromagnetic phase at relatively small time, which scales as $T_{tun} = \mathcal{O}(e^{cN})$; note that the corresponding infinite-time distribution of the magnetization is suppressed in the classically forbidden region $m \approx 0$ as $N \to \infty$. In the center left panel, a remnant of ferromagnetic behavior can be observed in the dynamical paramagnetic phase, due to contributions to the wavepacket coming from ferromagnetic initial conditions (in order to visualize this, one should replace the small black dot in Fig. 2.4 with an extended circle of radius $1/\sqrt{N}$). In the bottom left panel, recurrences in the evolution of the order parameter emerge at relatively small time, due to wavepacket refocusing after spreading. All these three effects occur at larger times for $N = 64, 256$, and thus do not appear in the relative plots.

to a single point;

2. the center of the wavepacket initially performs classical oscillations;

3. wavepacket spreading along the classical trajectory occurs after the Ehrenfest time scale $T_{Ehr} \sim \mathcal{O}(\sqrt{N})$ [or $\mathcal{O}(\log N)$ around the dynamical critical point] ;

4. correspondingly, the persistent classical oscillations of observables are damped, and relaxation takes place towards to classical time-average;

5. the sharp dynamical phase transition highlighted in the previous section is smoothed out by quantum fluctuations, resulting in a crossover;

6. if the accessible phase space is classically disconnected, quantum tunneling may occur over a time scale T_{tun} that grows exponentially with N.

In particular, in order to observe the classical evolution described in Sec. 2.2, the thermodynamic limit must be taken first. In fact, the three relevant time scales $T_{cl} = \mathcal{O}(1)$, $T_{Ehr} = \mathcal{O}(\sqrt{N})$, $T_{tun} = \mathcal{O}(e^{cN})$ discussed above, are well separated in the thermodynamic limit, and the quantum phenomena (wavepacket spreading and quantum tunneling) set in at increasingly longer time. However, in small systems they all become important. In order to highlight the relevance and consequences of these finite-size effects, we report in Fig. 2.11 the time evolution of the order parameter σ^x as well as the infinite-time averaged distribution p_{de} of the magnetization for increasing system sizes N, as obtained from numerical diagonalization of the Hamiltonian (2.23) in the maximal spin sector.

Chapter 3

Nonequilibrium spin-wave theory

The lack of interaction between the collective spin and other spin excitations with finite wavelength (spin waves) is an artifact of the infinite-range interactions discussed in Chap. 2. In any realistic model with interactions depending on the spatial position of the spins, quantum fluctuations at all possible length scales participate in the dynamics. As a result, the system is expected to eventually thermalize. It is natural to investigate the possible persistence of instances of mean-field nonequilibrium phenomena such as those addressed in Chap. 2 — i.e, dynamical criticality and dynamical stabilization — in a *prethermal* stage of the dynamics, together with the possible onset of qualitatively new phenomena generated by these additional fluctuations. For this purpose, we present in this Chapter a method to systematically account for the effect of fluctuations on the dynamics of general interacting spin models.

The content of this Chapter represents the methodological core of Part I of the thesis. It has been originally announced in Ref. [1], and has been applied in subsequent work published in Refs. [2–4].

3.1 Perturbative corrections to the equilibrium transition

In order to understand the impact of quantum fluctuations on the physics of the fully-connected Ising ferromagnet in Eq. (2.23) in a conceptually clean way, it is convenient to consider toy models with *additional* finite-range interactions,

$$\hat{H} = -\frac{\lambda}{N}\sum_{\mathbf{r},\mathbf{r}'}\hat{\sigma}^x_{\mathbf{r}}\hat{\sigma}^x_{\mathbf{r}'} - g\sum_{\mathbf{r}}\hat{\sigma}^z_{\mathbf{r}} - \sum_{\mathbf{r},\mathbf{r}'}J_{\mathbf{r},\mathbf{r}'}\hat{\sigma}^x_{\mathbf{r}}\hat{\sigma}^x_{\mathbf{r}'}, \tag{3.1}$$

where $\mathbf{r},\mathbf{r}'$ run over a d-dimensional lattice with N sites, and the coupling $J_{\mathbf{r},\mathbf{r}'} \equiv J_r$ decays with the distance $r = |\mathbf{r}-\mathbf{r}'|$. For the purpose of later comparison with numerical simulations and with experiments, we shall focus on one-dimensional case $d = 1$, even though all of the results we find do not rely on this assumption, as will become clear in the following. Accordingly, we denote by $i, j = 1, \ldots, N$

the lattice sites. For technical simplicity, we shall consider periodic boundary conditions.

The perturbation makes the Hamiltonian a function not only of the spin Fourier component at $k = 0$ (as occurs for $J_r \equiv$ const), but of all the Fourier components with $k \neq 0$. When the perturbation is small, the degree of excitation in the modes with $k \neq 0$ is expected to be small, at least in a dynamical transient. Accordingly, it is reasonable to treat them perturbatively at the lowest nontrivial order, corresponding to a quadratic approximation. In order to do so, we introduce canonical variables describing small fluctuations around the mean-field spin-coherent states by using a Holstein-Primakoff transformation relative to the direction of the average collective spin vector $\langle \tilde{\boldsymbol{\sigma}}_{k=0} \rangle$. Let us start by expounding this approach in equilibrium. We first rewrite the Hamiltonian (3.1) in Fourier space,

$$\hat{H} = -\frac{\bar{\lambda}}{N} (\tilde{\sigma}^x_{k=0})^2 - g\, \tilde{\sigma}^z_{k=0} - \frac{1}{N} \sum_{k \neq 0} \tilde{J}_k\, \tilde{\sigma}^x_k \tilde{\sigma}^x_{-k}, \tag{3.2}$$

where $\tilde{J}_k \equiv \tilde{J}_{-k} = \sum_{r=0}^{N-1} e^{-ikr} J_r$ and $\tilde{\sigma}^\alpha_k = \sum_j e^{-ikj} \hat{\sigma}^\alpha_j$, with $k = 2\pi n/N$, for $n = 0, 1, \ldots, N-1$, and we have defined $\bar{\lambda} \equiv \lambda + \tilde{J}_0$. Let us now introduce a rotated reference frame $(\mathbf{X}, \mathbf{Y}, \mathbf{Z})$, whose components in the original fixed frame $(\mathbf{x}, \mathbf{y}, \mathbf{z})$ can be parameterized by the spherical angles θ and ϕ as

$$\mathbf{X} \equiv \begin{pmatrix} \cos\theta \cos\phi \\ \cos\theta \sin\phi \\ -\sin\theta \end{pmatrix}, \quad \mathbf{Y} \equiv \begin{pmatrix} -\sin\phi \\ \cos\phi \\ 0 \end{pmatrix}, \quad \mathbf{Z} \equiv \begin{pmatrix} \sin\theta \cos\phi \\ \sin\theta \sin\phi \\ \cos\theta \end{pmatrix}. \tag{3.3}$$

The spins can be decomposed on the rotated basis as

$$\hat{\boldsymbol{\sigma}}_j = \mathbf{X}\, \hat{\sigma}^X_j + \mathbf{Y}\, \hat{\sigma}^Y_j + \mathbf{Z}\, \hat{\sigma}^Z_j. \tag{3.4}$$

Accordingly, the Hamiltonian (3.2) can be rewritten in terms of the Fourier transforms $\tilde{\sigma}^{X,Y,Z}_k$ of $\hat{\sigma}^{X,Y,Z}_j$,

$$\begin{aligned} \frac{\hat{H}}{N} = &-\bar{\lambda} \left[(\mathbf{X}\cdot\mathbf{x}) \frac{\tilde{\sigma}^X_0}{N} + (\mathbf{Y}\cdot\mathbf{x}) \frac{\tilde{\sigma}^Y_0}{N} + (\mathbf{Z}\cdot\mathbf{x}) \frac{\tilde{\sigma}^Z_0}{N} \right]^2 \\ &- g \left[(\mathbf{X}\cdot\mathbf{z}) \frac{\tilde{\sigma}^X_0}{N} + (\mathbf{Y}\cdot\mathbf{z}) \frac{\tilde{\sigma}^Y_0}{N} + (\mathbf{Z}\cdot\mathbf{z}) \frac{\tilde{\sigma}^Z_0}{N} \right] \\ &- \sum_{k \neq 0} \tilde{J}_k \left[(\mathbf{X}\cdot\mathbf{x}) \frac{\tilde{\sigma}^X_k}{N} + (\mathbf{Y}\cdot\mathbf{x}) \frac{\tilde{\sigma}^Y_k}{N} + (\mathbf{Z}\cdot\mathbf{x}) \frac{\tilde{\sigma}^Z_k}{N} \right] \times \\ &\qquad \left[(\mathbf{X}\cdot\mathbf{x}) \frac{\tilde{\sigma}^X_{-k}}{N} + (\mathbf{Y}\cdot\mathbf{x}) \frac{\tilde{\sigma}^Y_{-k}}{N} + (\mathbf{Z}\cdot\mathbf{x}) \frac{\tilde{\sigma}^Z_{-k}}{N} \right]. \end{aligned} \tag{3.5}$$

In the rotated frame, we bosonize spin fluctuations via the Holstein–Primakoff

transformation [304], expanded to lowest order in $1/\sqrt{s}$, i.e.,

$$\begin{cases} \hat{\sigma}_j^X = \dfrac{\hat{q}_j}{\sqrt{s}} + \dots , \\ \hat{\sigma}_j^Y = \dfrac{\hat{p}_j}{\sqrt{s}} + \dots , \\ \hat{\sigma}_j^Z = 1 - \dfrac{\hat{n}_j}{s} \equiv 1 - \dfrac{\hat{q}_j^2 + \hat{p}_j^2 - 1}{2s}, \end{cases} \tag{3.6}$$

where $\hat{q}_j$ and $\hat{p}_j$ are conjugate canonical variables representing small deviations of the spin away from the **Z**-axis, and along the transverse directions **X** and **Y**, respectively. In our notation, the bosonic number operator is $\hat{n}_j = \hat{b}_j^\dagger \hat{b}_j$ where $\hat{b}_j = (\hat{q}_j + i\hat{p}_j)/\sqrt{2}$. Introducing the Fourier space representation $\tilde{q}_k = N^{-1/2} \sum_j e^{-ikj} \hat{q}_j$ and $\tilde{p}_k = N^{-1/2} \sum_j e^{-ikj} \hat{p}_j$, one has[1]

$$\begin{cases} \dfrac{\tilde{\sigma}_k^X}{N} = \dfrac{\tilde{q}_k}{\sqrt{Ns}} + \dots , \\ \dfrac{\tilde{\sigma}_k^Y}{N} = \dfrac{\tilde{p}_k}{\sqrt{Ns}} + \dots , \\ \dfrac{\tilde{\sigma}_k^Z}{N} = \delta_{k,0} - \displaystyle\sum_{k'} \dfrac{\tilde{q}_{k'} \tilde{q}_{k-k'} + \tilde{p}_{k'} \tilde{p}_{k-k'} - \delta_{k,0}}{2Ns}. \end{cases} \tag{3.7}$$

The Hamiltonian (3.5) written in terms of the canonical spin wave variables, can now be arranged in the form

$$\hat{H} = \hat{H}_0 + \hat{U}_2 + \hat{U}_3 + \hat{U}_4. \tag{3.8}$$

In Eq. (3.8), the term $\hat{H}_0$ describes the collective spin and its excitations,

$$\begin{aligned} \hat{H}_0 = & -\bar{\lambda} N (\mathbf{Z}\cdot\mathbf{x})^2 \left(1 - \frac{\hat{n}_0 + \hat{n}_{sw}}{Ns}\right)^2 - gN (\mathbf{Z}\cdot\mathbf{z}) \left(1 - \frac{\hat{n}_0 + \hat{n}_{sw}}{Ns}\right) \\ & - 2\bar{\lambda} \frac{\sqrt{N}}{\sqrt{s}} (\mathbf{Z}\cdot\mathbf{x}) \left(1 - \frac{\hat{n}_0 + \hat{n}_{sw}}{Ns}\right) [(\mathbf{X}\cdot\mathbf{x})\, \tilde{q}_0 + (\mathbf{Y}\cdot\mathbf{x})\, \tilde{p}_0] \\ & - g \frac{\sqrt{N}}{\sqrt{s}} [(\mathbf{X}\cdot\mathbf{z})\, \tilde{q}_0 + (\mathbf{Y}\cdot\mathbf{z})\, \tilde{p}_0] \\ & - \frac{\bar{\lambda}}{s} \left[(\mathbf{X}\cdot\mathbf{x})^2 \tilde{q}_0^2 + (\mathbf{Y}\cdot\mathbf{x})^2 \tilde{p}_0^2 + 2 (\mathbf{X}\cdot\mathbf{x}) (\mathbf{Y}\cdot\mathbf{x}) \frac{\tilde{q}_0\tilde{p}_0 + \tilde{p}_0\tilde{q}_0}{2} \right], \end{aligned} \tag{3.9}$$

while the remaining terms are proportional to $\tilde{J}_{k=0}$ and describe the $k \neq 0$

[1] Note that $\tilde{q}_k^\dagger \equiv \tilde{q}_{-k}$ and $\tilde{p}_k^\dagger \equiv \tilde{p}_{-k}$ are not real.

spin-wave excitations,

$$\begin{aligned}
\hat{U}_2 &= -\sum_{k\neq 0}\frac{\tilde{J}_k}{s}\Bigg[(\mathbf{X}\cdot\mathbf{x})^2\,\tilde{q}_k\tilde{q}_{-k}+(\mathbf{Y}\cdot\mathbf{x})^2\,\tilde{p}_k\tilde{p}_{-k}\\
&\qquad\qquad +2\,(\mathbf{X}\cdot\mathbf{x})\,(\mathbf{Y}\cdot\mathbf{x})\,\frac{\tilde{q}_k\tilde{p}_{-k}+\tilde{p}_k\tilde{q}_{-k}}{2}\Bigg],\\
\hat{U}_3 &= +\frac{1}{\sqrt{Ns}}\sum_{k\neq 0}\frac{\tilde{J}_k}{s}\,(\mathbf{Z}\cdot\mathbf{x})\\
&\qquad\times\Bigg\{(\mathbf{X}\cdot\mathbf{x})\left[\tilde{q}_k\sum_{k'}\frac{\tilde{q}_{k'}\tilde{q}_{-k-k'}+\tilde{p}_{k'}\tilde{p}_{-k-k'}}{2}+(k\leftrightarrow -k)\right]+\\
&\qquad+(\mathbf{Y}\cdot\mathbf{x})\left[\tilde{p}_k\sum_{k'}\frac{\tilde{q}_{k'}\tilde{q}_{-k-k'}+\tilde{p}_{k'}\tilde{p}_{-k-k'}}{2}+(k\leftrightarrow -k)\right]\Bigg\},\\
\hat{U}_4 &= -\frac{1}{Ns}\sum_{k\neq 0}\frac{\tilde{J}_k}{s}\,(\mathbf{Z}\cdot\mathbf{x})^2\sum_{k'}\frac{\tilde{q}_{k'}\tilde{q}_{k-k'}+\tilde{p}_{k'}\tilde{p}_{k-k'}}{2}\sum_{k''}\frac{\tilde{q}_{k''}\tilde{q}_{-k-k''}+\tilde{p}_{k''}\tilde{p}_{-k-k''}}{2}.
\end{aligned}\tag{3.10}$$

The three terms represent the quadratic, cubic, and quartic contributions in the spin waves, respectively. In Eq. (3.8), the quantity $\hat{n}_{sw}$ is the total number of bosonic spin-wave excitation, i.e.,

$$\hat{n}_{sw}=\sum_{k\neq 0}\hat{n}_k=\sum_{k\neq 0}\frac{\tilde{q}_k\tilde{q}_{-k}+\tilde{p}_k\tilde{p}_{-k}-1}{2}\tag{3.11}$$

[cf. Eq. (2.50)].

The truncation of the expansion in Eq. (3.8) is valid as long as the spin waves have a low density $\langle\hat{n}_0\rangle+\langle\hat{n}_{sw}\rangle\ll Ns$. An equivalent statement is that the collective spin magnitude is close to its maximal value Ns. In fact, each quantum of spin wave with $k\neq 0$ decreases the collective spin magnitude by one unit,

$$|\hat{\mathbf{S}}|^2=s^2\Big[\left(\tilde{\sigma}^X_{k=0}\right)^2+\left(\tilde{\sigma}^Y_{k=0}\right)^2+\left(\tilde{\sigma}^Z_{k=0}\right)^2\Big]\approx(Ns-\hat{n}_{sw})(Ns-\hat{n}_{sw}+1).\tag{3.12}$$

In this regime, spin waves behave as weakly-interacting bosonic excitations. Higher-order terms account for nonlinear scattering among the spin waves, and are expected to contribute significantly to the dynamics only at times parametrically long in the spin-wave density.

Our approach is equivalent to treating fluctuations within the Gaussian approximation, which is the lowest nontrivial order beyond mean-field. This is expected to be sufficiently accurate when the interaction $\tilde{J}_{k\neq 0}$ introduces a small perturbation to the mean-field dynamics, such that a small spin-wave density $\langle n_{sw}(t)\rangle/(Ns)$ is generated during the evolution. In this case, similarly to the well-known Bogolyubov theory of weakly-interacting Bose gases [311], excitation can be treated at the quadratic level, and the neglected nonlinear interactions are expected to drive the system at long times away from the prethermal regime

relevant for the nonequilibrium phenomena discussed in the rest of Part I of the thesis.

In the low-density regime considered here, the only relevant interaction is that between the collective mode $\tilde{q}_0, \tilde{p}_0$ and the spin waves, given by terms in $\hat{U}_3$ with $k' = 0, k, -k$, which describe scattering of the zero-momentum mode into a pair of spin waves with opposite momenta $(k, -k)$, and viceversa. Thereby, we arrive at the following form of the Hamiltonian (3.1), truncated to *linear* order in the collective $k = 0$ mode and to *quadratic* order in the spin-wave operators with $k \neq 0$,

$$
\begin{aligned}
\hat{H} \simeq & -\bar{\lambda} N (\mathbf{Z}\cdot\mathbf{x})^2 - gN(\mathbf{Z}\cdot\mathbf{z}) \\
& + \frac{1}{s}\sum_{k\neq 0}\left[2\bar{\lambda}(\mathbf{Z}\cdot\mathbf{x})^2 + g(\mathbf{Z}\cdot\mathbf{z})\right]\frac{\tilde{q}_k\tilde{q}_{-k}+\tilde{p}_k\tilde{p}_{-k}-1}{2} \\
& - \frac{1}{s}\sum_{k\neq 0}\tilde{J}_k\Bigg[(\mathbf{X}\cdot\mathbf{x})^2\,\tilde{q}_k\tilde{q}_{-k} + (\mathbf{Y}\cdot\mathbf{x})^2\,\tilde{p}_k\tilde{p}_{-k} \\
& \qquad + 2(\mathbf{X}\cdot\mathbf{x})(\mathbf{Y}\cdot\mathbf{x})\,\frac{\tilde{q}_k\tilde{p}_{-k}+\tilde{p}_k\tilde{q}_{-k}}{2}\Bigg] \\
& + \frac{\sqrt{N}}{\sqrt{s}}\tilde{q}_0\Bigg\{-2\bar{\lambda}\left(1-\frac{\hat{n}_{sw}}{Ns}\right)(\mathbf{Z}\cdot\mathbf{x})(\mathbf{X}\cdot\mathbf{x}) - g(\mathbf{X}\cdot\mathbf{z}) \\
& \qquad + 2(\mathbf{Z}\cdot\mathbf{x})\frac{1}{Ns}\sum_{k\neq 0}\tilde{J}_k\left[(\mathbf{X}\cdot\mathbf{x})\,\tilde{q}_k\tilde{q}_{-k} + (\mathbf{Y}\cdot\mathbf{x})\,\frac{\tilde{q}_k\tilde{p}_{-k}+\tilde{p}_k\tilde{q}_{-k}}{2}\right]\Bigg\} \\
& + \frac{\sqrt{N}}{\sqrt{s}}\tilde{p}_0\Bigg\{-2\bar{\lambda}\left(1-\frac{\hat{n}_{sw}}{Ns}\right)(\mathbf{Z}\cdot\mathbf{x})(\mathbf{Y}\cdot\mathbf{x}) - g(\mathbf{Y}\cdot\mathbf{z}) \\
& \qquad + 2(\mathbf{Z}\cdot\mathbf{x})\frac{1}{Ns}\sum_{k\neq 0}\tilde{J}_k\left[(\mathbf{Y}\cdot\mathbf{x})\,\tilde{p}_k\tilde{p}_{-k} + (\mathbf{X}\cdot\mathbf{x})\,\frac{\tilde{q}_k\tilde{p}_{-k}+\tilde{p}_k\tilde{q}_{-k}}{2}\right]\Bigg\},
\end{aligned}
\tag{3.13}
$$

where the explicit expressions of the various scalar products between versors in terms of the rotation angles θ and ϕ can be inferred from Eq. (3.3). The Hamiltonian (3.13) is our starting point for assessing the impact of fluctuations on equilibrium and nonequilibrium physics.

We first study the equilibrium behavior in the presence of fluctuations. The direction of the spin polarization in equilibrium can be determined at the Gaussian level by imposing vanishing expectation values of $\tilde{q}_0$ and $\tilde{p}_0$, i.e.,

$$
\langle \tilde{q}_0 \rangle = \langle \tilde{p}_0 \rangle = 0. \tag{3.14}
$$

Equation (3.7) with $k = 0$ shows that this is equivalent to requiring that the average collective spin $\langle \tilde{\boldsymbol{\sigma}}_{k=0} \rangle$ is aligned with the $\mathbf{Z}$-direction, identified by the spherical angles θ, ϕ. In the mean-field limit $\tilde{J}_{k\neq 0} = 0$, the spin waves are frozen in their vacuum state and the problem becomes equivalent to finding the ground state of the single classical spin $\vec{\sigma} = \langle \tilde{\boldsymbol{\sigma}}_{k=0} \rangle / N$ on the sphere, as detailed in Sec. 2.2. As soon as $\tilde{J}_{k\neq 0} \neq 0$, the spin waves are excited even in the ground state.

This occurrence is analogous to the depletion of the condensate fraction in a dilute Bose gas in the presence of weak interactions.

Equations (3.14) require to adjust the values of θ and ϕ in such a way that the equilibrium expectation values of the two curly brackets in Eq. (3.13) vanish. The second one does it if $\mathbf{Y}\cdot\mathbf{x} = \mathbf{Y}\cdot\mathbf{z} = 0$, and $\langle \tilde{q}_k \tilde{p}_{-k} + \tilde{p}_k \tilde{q}_{-k}\rangle = 0$, which implies that $\phi^* = 0$ or π. In other words, the equilibrium configuration of the collective spin is in the xz-plane, as could be anticipated based on symmetry arguments. The remaining equation determines the value of θ^*. In particular, $\theta^* = 0$ is always a solution: however, it is stable only for g large enough. For small g, stable solutions can be calculated as follows. First we diagonalize the quadratic part of the Hamiltonian [second and third sums on the r.h.s. of Eq. (3.13)] obtaining a spin wave dispersion relation ω_k/s which depend parametrically on θ, i.e.,

$$\omega_k = \sqrt{\left(2\bar{\lambda}\sin^2\theta + g\cos\theta\right)\left(2\bar{\lambda}\sin^2\theta + g\cos\theta - 2\tilde{J}_k\cos^2\theta\right)}. \tag{3.15}$$

Denoting by $\omega_k^{(0)}/s$ the "unperturbed" common frequency of the spin wave modes,

$$\omega_k^{(0)} = \lim_{\tilde{J}_{k\neq 0}\to 0} \omega_k = 2\bar{\lambda}\sin^2\theta + g\cos\theta, \tag{3.16}$$

the quantum fluctuations of spin modes can then be expressed as

$$\begin{cases} \langle \tilde{q}_k \tilde{q}_{-k}\rangle = \dfrac{1}{2}\dfrac{\omega_k^{(0)}}{\omega_k}, \\ \langle \tilde{p}_k \tilde{p}_{-k}\rangle = \dfrac{1}{2}\dfrac{\omega_k}{\omega_k^{(0)}}, \\ \left\langle \dfrac{\tilde{q}_k\tilde{p}_{-k} + \tilde{p}_k\tilde{q}_{-k}}{2}\right\rangle = 0. \end{cases} \tag{3.17}$$

Hence, the equation of state which determines θ^* reads

$$\sin\theta^* \times \left[-2\bar{\lambda}(1-\epsilon)\cos\theta^* + g + \cos\theta^* \frac{1}{Ns}\sum_{k\neq 0}\tilde{J}_k \sqrt{\frac{2\bar{\lambda}\sin^2\theta^* + g\cos\theta^*}{2\bar{\lambda}\sin^2\theta^* + g\cos\theta^* - 2\tilde{J}_k\cos^2\theta^*}}\right] = 0. \tag{3.18}$$

The total spin depletion ϵ is defined by the equation

$$\frac{\left|\langle \tilde{\sigma}_{k=0}\rangle\right|}{N} = 1 - \frac{\langle \hat{n}_{sw}\rangle}{Ns} \equiv 1 - \epsilon, \tag{3.19}$$

Combining Eqs. (3.11) and (3.17), we get an explicit expression for it, i.e.,

$$\epsilon \equiv \frac{\langle \hat{n}_{sw}\rangle}{Ns} = \frac{1}{2Ns}\sum_{k\neq 0}\left(\frac{1}{2}\frac{\omega_k^{(0)}}{\omega_k} + \frac{1}{2}\frac{\omega_k}{\omega_k^{(0)}} - 1\right)_{\theta=\theta^*}. \tag{3.20}$$

Note that the spin-wave density $\epsilon = \mathcal{O}\left(\tilde{J}^2_{k\neq 0}\right)$ vanishes in the limits $g \to 0$ and $g \to \infty$, in which the ground state is fully polarized along the x and z direction, respectively. It is arguably maximal at the critical point $g_{cr} = 2\bar{\lambda} - \mathcal{O}\left(\tilde{J}^2_{k\neq 0}\right)$ (see below).

As a check, in the mean-field case $\tilde{J}_{k\neq 0} \equiv 0$, Eqs. (3.15) and (3.18) imply $\omega^{(0)}_k = \omega_k$, $\epsilon = 0$, and $\cos\theta^* = g/2\lambda$ in the ferromagnetic phase $g < 2\lambda$, retrieving the mean-field equilibrium properties, determined in Sec. 2.2. As soon as finite-range interactions $\tilde{J}_{k\neq 0} \neq 0$ is turned on, quantum fluctuations modify the equilibrium state.

In the equilibrium paramagnetic phase $g > g_{cr}$, the ground state has $\theta^* = 0$, and from Eq. (3.15) we find

$$\omega_{k,>} = \sqrt{g(g - 2\tilde{J}_k)}. \tag{3.21}$$

Deep in the equilibrium ferromagnetic phase, with $g \to 0$, the system approaches instead full ferromagnetic ordering with $\theta^* \to \pi/2$, and the corresponding dispersion relation derived from Eq. (3.15) becomes independent of k, i.e., the band becomes flat,

$$\omega_{k,<} \underset{g\to 0}{\longrightarrow} 2\bar{\lambda}. \tag{3.22}$$

This could have been anticipated by observing that in the limit $g \to 0$ the spin Hamiltonian (3.1) becomes diagonal in the σ^x-basis in real space.

Let us determine now the perturbative corrections to position of the critical point, employing a variational approach. Criticality occurs at the value of g such that the paramagnetic configuration $\theta = 0$ becomes an unstable saddle-point of H. We compute the variational energy $\mathcal{E}(\theta) = \langle H\rangle_\theta$ as a function of θ (with fixed $\phi = 0$), by taking the average of $\hat{H}$ in Eq. (3.13) with $\langle\tilde{q}_0\rangle = \langle\tilde{p}_0\rangle = 0$ and $\langle\tilde{q}_k\tilde{q}_{-k}\rangle$ given by Eq. (3.17), thereby obtaining

$$\frac{\mathcal{E}(\theta)}{N} = -\bar{\lambda}\sin^2\theta - g\cos\theta + \frac{1}{Ns}\sum_{k\neq 0}\frac{\omega_k - \omega^{(0)}_k}{2}. \tag{3.23}$$

In order to determine the stability of the solution $\theta^* = 0$, we expand $\mathcal{E}(\theta)$ at small θ. We find

$$\begin{aligned}\frac{\mathcal{E}(\theta)}{N} \underset{\theta\to 0}{\sim} & -g + \frac{1}{Ns}\sum_{k\neq 0}\frac{1}{2}\left(\sqrt{g(g-2\tilde{J}_k)} - g\right) \\ & + \left\{ g - 2\bar{\lambda} + \frac{1}{Ns}\sum_{k\neq 0}\left[\sqrt{g(g-2\tilde{J}_k)}\frac{1}{2}\left(\frac{2\bar{\lambda} - g/2 + 2\tilde{J}_k}{g - 2\tilde{J}_k} + \frac{2\bar{\lambda} - g/2}{g}\right)\right.\right. \\ & \left.\left. - \left(2\bar{\lambda} - g/2\right)\right]\right\}\frac{\theta^2}{2} + \mathcal{O}(\theta^4).\end{aligned} \tag{3.24}$$

The critical point is then determined by the vanishing of the coefficient of the

quadratic term in curly bracket, which yields an equation for g_{cr}. The shift of g_{cr} away from the mean-field value $2\bar{\lambda}$ may be found perturbatively for small $\tilde{J}_{k\neq 0}$. We expand the solution $g = g_{cr}\left(\tilde{J}_{k\neq 0}\right)$ in powers of $\tilde{J}_{k\neq 0}$ and equate both sides order by order. The explicit calculation leads to a quadratic correction:

$$g_{cr} = 2\bar{\lambda}\left[1 - \frac{5}{16}\frac{1}{Ns}\sum_{k\neq 0}\left(\frac{\tilde{J}_k}{\bar{\lambda}}\right)^2\right] + \mathcal{O}\left(\tilde{J}^3_{k\neq 0}\right) \sim 2\bar{\lambda}\left[1 - \frac{5}{16s}\int_{-\pi}^{\pi}\frac{dk}{2\pi}\left(\frac{\tilde{J}_k}{\bar{\lambda}}\right)^2\right]. \tag{3.25}$$

As expected on physical grounds, the spin waves destabilize the ferromagnetic ordering and thereby lower the critical value g_{cr}.

The ground state equations discussed above can immediately be generalized to finite-temperature equilibrium states. In fact, it is sufficient to substitute in Eqs. (3.17) the prefactor $1/2$ with

$$\frac{1}{2} + \langle \hat{n}_k \rangle_T = \frac{1}{2} + \frac{1}{e^{\omega_k/T} - 1}, \tag{3.26}$$

where $\langle \hat{n}_k \rangle_T$ is the Bose-Einstein distribution of the excited spin waves and $T > 0$ is the temperature. The expression of ϵ in Eq. (3.20) and the equilibrium configuration determined by θ^* in the equation of state (3.18) are modified accordingly. As in the mean-field case, thermal corrections are exponentially suppressed at low temperature as long as the gap in the dispersion relation (3.15) with $\theta = \theta^*$ is nonvanishing.

In conclusion of the discussion on equilibrium physics, we emphasize that the validity of spin-wave theory has been rigorously established in the regime of low density in the recent work in Ref. [312].

3.2 Impact of dynamically excited spin waves on the collective spin dynamics

The nonequilibrium dynamics in the presence of weak fluctuations can be studied by generalizing the approach developed in the previous section to time-evolving states. The spin-wave expansion can be performed with respect to a time-dependent rotated frame, with the angles $\theta(t), \phi(t)$ co-moving with the average collective spin [1]. This is implemented by the unitary operator

$$\hat{V}(\theta(t), \phi(t)) = e^{-i\phi\, s \sum_j \hat{\sigma}^z_j}\, e^{-i\theta\, s \sum_j \hat{\sigma}^y_j}, \tag{3.27}$$

acting on the spins as a time-dependent global rotation:

$$\begin{cases} \hat{V}\hat{\sigma}^x_j\hat{V}^\dagger = \mathbf{X}\cdot\hat{\boldsymbol{\sigma}}_j \equiv \hat{\sigma}^X_j, \\ \hat{V}\hat{\sigma}^y_j\hat{V}^\dagger = \mathbf{Y}\cdot\hat{\boldsymbol{\sigma}}_j \equiv \hat{\sigma}^Y_j, \\ \hat{V}\hat{\sigma}^z_j\hat{V}^\dagger = \mathbf{Z}\cdot\hat{\boldsymbol{\sigma}}_j \equiv \hat{\sigma}^Z_j. \end{cases} \tag{3.28}$$

The Heisenberg equations of motion for $\hat{\sigma}_j^\alpha$ ($\alpha \in \{X, Y, Z\}$), in the mobile frame, read

$$\frac{d}{dt}\hat{\sigma}_j^\alpha = \frac{1}{i}\left[\hat{\sigma}_j^\alpha, \widetilde{H}\right], \quad \text{with } \widetilde{H} \equiv \hat{H} + i\hat{V}\dot{\hat{V}}^\dagger, \tag{3.29}$$

where the last term is the inertial force contribution equivalent to a generalized Larmor field [313]

$$i\hat{V}\dot{\hat{V}}^\dagger = -s\,\boldsymbol{\omega}(t)\cdot\sum_j \hat{\boldsymbol{\sigma}}_j = -s\,\boldsymbol{\omega}(t)\cdot\tilde{\boldsymbol{\sigma}}_{k=0}, \tag{3.30}$$

where we introduced the vector $\boldsymbol{\omega} = (\omega^X, \omega^Y, \omega^Z)$, with $\omega^X = \dot{\mathbf{Y}}\cdot\mathbf{Z}$, $\omega^Y = \dot{\mathbf{Z}}\cdot\mathbf{X}$, and $\omega^Z = \dot{\mathbf{X}}\cdot\mathbf{Y}$. With the standard choice of parameterization of the rotating frame in Eqs. (3.3), one has

$$\omega^X = \cos\theta\dot{\phi}\,, \qquad \omega^Y = \dot{\theta}\,, \qquad \omega^Z = -\sin\theta\dot{\phi}\,. \tag{3.31}$$

.

The resulting Hamiltonian $\widetilde{H}(t)$ is given by the expression in Eq. (3.13) for $\hat{H}$ with two changes: *i*) the frame $(\mathbf{X}(t), \mathbf{Y}(t), \mathbf{Z}(t))$ is time-dependent [i.e., the angles $\theta(t)$, $\phi(t)$ are time-dependent], and *ii*) the additional terms

$$\begin{aligned}
-s(\dot{\mathbf{X}}\cdot\mathbf{Y})\,\tilde{\sigma}_0^Z =& -s(\dot{\mathbf{X}}\cdot\mathbf{Y}) \\
&+\frac{1}{s}\sum_{k\neq 0}\left[s(\dot{\mathbf{X}}\cdot\mathbf{Y})\right]\frac{\tilde{q}_k\tilde{q}_{-k}+\tilde{p}_k\tilde{p}_{-k}-1}{2}, \\
-s(\dot{\mathbf{Y}}\cdot\mathbf{Z})\,\tilde{\sigma}_0^X =& \frac{\sqrt{N}}{\sqrt{s}}\tilde{q}_0\Big\{-s(\dot{\mathbf{Y}}\cdot\mathbf{Z})\Big\}, \\
-s(\dot{\mathbf{Z}}\cdot\mathbf{X})\,\tilde{\sigma}_0^Y =& \frac{\sqrt{N}}{\sqrt{s}}\tilde{p}_0\Big\{-s(\dot{\mathbf{Z}}\cdot\mathbf{X})\Big\},
\end{aligned} \tag{3.32}$$

appear in the second, fourth and fifth line of Eq. (3.13), respectively. This time-dependent Hamiltonian governs the self-consistent coupled equations of motion of the angles θ, ϕ and of the excitations $\tilde{q}_k, \tilde{p}_k$. The evolution of the angles is obtained by requiring that the condition (3.14) to hold at all times, which corresponds to setting the coefficients of $\tilde{q}_0$ and $\tilde{p}_0$ in $\widetilde{H}(t)$ equal to zero. This

procedure yields a pair of classical evolution equations for $\theta(t), \phi(t)$,

$$\begin{cases} s\dfrac{d}{dt}\theta = +2\bar{\lambda}[1-\epsilon(t)]\sin\theta\cos\phi\sin\phi \\ \qquad\qquad -2\Big(\dfrac{1}{Ns}\displaystyle\sum_{k\neq 0}\tilde{J}_k\Delta_k^{pp}(t)\Big)\sin\theta\cos\phi\sin\phi \\ \qquad\qquad +2\Big(\dfrac{1}{Ns}\displaystyle\sum_{k\neq 0}\tilde{J}_k\Delta_k^{qp}(t)\Big)\cos\theta\sin\theta\cos^2\phi, \\ s\dfrac{d}{dt}\phi = -g+2\bar{\lambda}[1-\epsilon(t)]\cos\theta\cos^2\phi \\ \qquad\qquad -2\Big(\dfrac{1}{Ns}\displaystyle\sum_{k\neq 0}\tilde{J}_k\Delta_k^{qq}(t)\Big)\cos\theta\cos^2\phi \\ \qquad\qquad +2\Big(\dfrac{1}{Ns}\displaystyle\sum_{k\neq 0}\tilde{J}_k\Delta_k^{qp}(t)\Big)\sin\phi\cos\phi, \end{cases} \tag{3.33}$$

where $\Delta_k^{qq}(t)$, $\Delta_k^{qp}(t)$, $\Delta_k^{qq}(t)$ are the equal-time correlation functions

$$\begin{cases} \Delta_k^{qq}(t) \equiv \langle \tilde{q}_k(t)\tilde{q}_{-k}(t)\rangle, \\ \Delta_k^{pp}(t) \equiv \langle \tilde{p}_k(t)\tilde{p}_{-k}(t)\rangle, \\ \Delta_k^{qp}(t) \equiv \dfrac{1}{2}\langle \tilde{q}_k(t)\tilde{p}_{-k}(t)+\tilde{p}_k(t)\tilde{q}_{-k}(t)\rangle, \end{cases} \tag{3.34}$$

and, as in Eq. (3.35), the nonequilibrium density $\epsilon(t)$ of spin waves reads

$$\epsilon(t) \equiv \frac{1}{Ns}\sum_{k\neq 0}\langle \hat{n}_k(t)\rangle = \frac{1}{Ns}\sum_{k\neq 0}\frac{\Delta_k^{qq}(t)+\Delta_k^{pp}(t)-1}{2}. \tag{3.35}$$

The evolution equations (3.33) for the collective spin orientation depend also on the instantaneous state of the spin waves via their correlation functions Δ's. The dynamical excitation of spin waves thereby affects the classical mean-field trajectory of the collective spin via "quantum feedback" terms, given by the second and third lines in both Eqs. (3.33). This effect is parametrically small in the strength $\tilde{J}_{k\neq 0}$ of the perturbation.

Concurrently, the change in time of the reference vacuum state $\theta(t), \phi(t)$ drives the nonequilibrium evolution of the spin excitations $\tilde{q}_k, \tilde{p}_k$. The equations of motion for the spin wave variables, $\frac{d}{dt}\tilde{q}_k = -i\big[\tilde{q}_k, \widetilde{H}(t)\big]$ and analogously for $\tilde{p}_k$, give

$$\begin{cases} s\dfrac{d}{dt}\tilde{q}_k = +2\bar{\lambda}\cos^2\phi\ \tilde{p}_k - 2\tilde{J}_k\sin^2\phi\ \tilde{p}_k + 2\tilde{J}_k\cos\theta\cos\phi\sin\phi\ \tilde{q}_k, \\ s\dfrac{d}{dt}\tilde{p}_k = -2\bar{\lambda}\cos^2\phi\ \tilde{q}_k + 2\tilde{J}_k\cos^2\theta\cos^2\phi\ \tilde{q}_k - 2\tilde{J}_k\cos\theta\cos\phi\sin\phi\ \tilde{p}_k. \end{cases} \tag{3.36}$$

Using these equations, one obtains the evolution of the parameters $\Delta_k^{qq}, \Delta_k^{qp}, \Delta_k^{pp}$,

$$\begin{cases} s\dfrac{d}{dt}\Delta_k^{qq} = 4\tilde{J}_k \cos\theta \cos\phi \sin\phi\, \Delta_k^{qq} + 4\left(\bar{\lambda}\cos^2\phi - \tilde{J}_k \sin^2\phi\right)\, \Delta_k^{qp}, \\ s\dfrac{d}{dt}\Delta_k^{qp} = -2\left(\bar{\lambda}\cos^2\phi - \tilde{J}_k \cos^2\theta\cos^2\phi\right)\Delta_k^{qq} + 2\left(\bar{\lambda}\cos^2\phi - \tilde{J}_k \sin^2\phi\right)\Delta_k^{pp}, \\ s\dfrac{d}{dt}\Delta_k^{pp} = -4\left(\bar{\lambda}\cos^2\phi - \tilde{J}_k \cos^2\theta\cos^2\phi\right)\Delta_k^{qp} - 4\tilde{J}_k \cos\theta\cos\phi\sin\phi\,\Delta_k^{pp}. \end{cases} \tag{3.37}$$

The equations of motion in Eq. (3.37) describe the dynamics of the Gaussian wavefunction of the spin waves. They are actually not independent, as the quantities $\Delta^{qq}, \Delta^{qp}, \Delta^{pp}$ are related by the condition

$$4\,(\Delta^{qp})^2 = 4\Delta^{qq}\Delta^{pp} - 1, \tag{3.38}$$

which is an exact property of Gaussian pure states (equivalent to having minimal quantum uncertainty), and which is then satisfied at all times and for all values of k. See App. B for a detailed discussion of this.

The dynamical problem is now fully specified by the system of coupled evolution equations (3.33) and (3.37), taking into account the constraints (3.38), together with suitable initial conditions, which may correspond to the ground state or to a thermal state of the pre-quench Hamiltonian. These equilibrium states, already determined in Sec. 3.1 via the equation of state (3.18) (and its generalization to thermal states), may be retrieved by looking for stationary solutions of the dynamical equations with the initial parameters $g_0, \lambda_0, \tilde{J}_{k,0}$. A variation in time of $g = g(t)$, corresponding to the driving protocol under consideration, yields the nonequilibrium evolution at Gaussian level according to the dynamical equations of motion derived above.

3.3 Time-independent approach to nonequilibrium dynamics

The system of coupled evolution equations for the collective spin and the spin waves discussed above can also be derived by using a time-independent approach. The original Hamiltonian $\hat{H}$ in Eq. (3.1) can be written in terms of two global canonical variables, the total spin projection $\hat{P}$ along the **z**-direction

$$\hat{P} = s\,\tilde{\sigma}^z_{k=0} = (Ns - \hat{n}_{sw})\cos\hat{\theta}, \tag{3.39}$$

and its conjugated angle

$$\hat{Q} = \hat{\phi}, \tag{3.40}$$

in addition to the canonical spin-wave variables $\tilde{q}_{k\neq 0}, \tilde{p}_{k\neq 0}$ analogous to the ones introduced in the previous section [cf. Eq. (3.7)]. An explicit calculation shows that these observables provide a complete set of 2N canonical variables

for the spin system, i.e.,

$$[\hat{Q}, \tilde{q}_k] = [\hat{Q}, \tilde{p}_k] = [\hat{P}, \tilde{q}_k] = [\hat{P}, \tilde{p}_k] = 0 \qquad \text{for all } k \neq 0. \tag{3.41}$$

Expanding $\hat{H}$ up to the quadratic order in the modes $\tilde{q}_k$ and $\tilde{p}_k$, while retaining the full nonlinearity in the collective spin coordinates $\hat{Q}$ and $\hat{P}$, one obtains[2]

$$\begin{aligned}\hat{H} \simeq -Ng\frac{\hat{P}}{Ns} - N\bar{\lambda}\left[\left(1-2\frac{\hat{n}_{sw}}{Ns}\right) - \frac{\hat{P}^2}{N^2s^2}\right]\cos^2\hat{Q} \\ - \sum_{k\neq 0}\frac{\tilde{J}_k}{s}\left[\frac{\hat{P}^2}{N^2s^2}\cos^2\hat{Q}\;\tilde{q}_k\tilde{q}_{-k} + \sin^2\hat{Q}\;\tilde{p}_k\tilde{p}_{-k}\right. \\ \left. - 2\frac{\hat{P}}{Ns}\cos\hat{Q}\sin\hat{Q}\;\frac{\tilde{q}_k\tilde{p}_{-k}+\tilde{p}_k\tilde{q}_{-k}}{2}\right],\end{aligned} \tag{3.42}$$

where $\hat{n}_{sw}$ is defined as in Eq. (3.11). Conceptually, this corresponds to promoting the rotated-frame angles θ and ϕ to proper dynamical variables, rather than treating them as external parameters to be self-consistently adjusted, as was the case in the time-dependent approach discussed in the previous Section. Accordingly, the variables $\tilde{q}_0, \tilde{p}_0$ do not appear in this case.

The equations of motion derived from the time-independent Hamiltonian (3.42) are

$$\begin{cases} s\,\dot{\hat{Q}} = -g + 2\bar{\lambda}\frac{\hat{P}}{Ns}\cos^2\hat{Q} - \frac{1}{Ns}\sum_{k\neq 0}2\tilde{J}_k\left[\frac{\hat{P}}{Ns}\cos^2\hat{Q}\,\Delta_k^{qq} - \cos\hat{Q}\sin\hat{Q}\,\Delta_k^{qp}\right], \\ s\frac{\dot{\hat{P}}}{Ns} = -2\bar{\lambda}\left[\left(1-2\frac{\hat{n}_{sw}}{Ns}\right) - \frac{\hat{P}^2}{N^2s^2}\right]\cos\hat{Q}\sin\hat{Q} \\ \qquad - \frac{1}{Ns}\sum_{k\neq 0}2\tilde{J}_k\left[\frac{\hat{P}^2}{N^2s^2}\cos\hat{Q}\sin\hat{Q}\,\Delta_k^{qq} - \cos\hat{Q}\sin\hat{Q}\,\Delta_k^{pp}\right. \\ \qquad\qquad \left. + \frac{\hat{P}}{Ns}\left(\cos^2\hat{Q} - \sin^2\hat{Q}\right)\Delta_k^{qp}\right], \\ s\,\dot{\tilde{q}}_k = +2\bar{\lambda}\cos^2\hat{Q}\;\tilde{p}_k - 2\tilde{J}_k\sin^2\hat{Q}\;\tilde{p}_k + 2\tilde{J}_k\frac{\hat{P}}{Ns}\cos\hat{Q}\sin\hat{Q}\;\tilde{q}_k, \\ s\,\dot{\tilde{p}}_k = -2\bar{\lambda}\cos^2\hat{Q}\;\tilde{q}_k + 2\tilde{J}_k\frac{\hat{P}^2}{N^2s^2}\cos^2\hat{Q}\;\tilde{q}_k - 2\tilde{J}_k\frac{\hat{P}}{Ns}\cos\hat{Q}\sin\hat{Q}\;\tilde{p}_k, \end{cases} \tag{3.43}$$

where the Δ_k's are defined as in Eq. (3.34).

Crucially, the quantum fluctuations of the collective operators $\hat{P}/N$ and $\hat{Q}$ in the initial state are of order $1/\sqrt{N}$, and hence they behave like uncertainty-free classical variables in the thermodynamic limit (see Sec. 2.4 for details on the convergence to the classical behavior). By identifying $\langle\hat{Q}\rangle = \phi$ and by changing variable from $\langle\hat{P}\rangle$ to θ via Eq. (3.39), after taking quantum averages

[2] The ordering of the operators $\hat{Q}$, $\hat{P}$ is actually immaterial, as differently ordered expressions differ by terms of higher order in $1/N$, suppressed in the thermodynamic limit. Indeed, as discussed in Chap. 2, when $N \to \infty$ the behavior of the collective mode is classical.

with $\langle \hat{n}_{sw} \rangle / (Ns) \equiv \epsilon$ [cf. Eq. (3.35)], one finds

$$\dot{\theta} = \frac{\frac{\langle \dot{\hat{P}} \rangle}{Ns} + \cos\theta \, \dot{\epsilon}}{-(1-\epsilon)\sin\theta},$$

and one verifies that the equations of motion (3.43) obtained here are equivalent to Eqs. (3.33) and (3.36) obtained within the time-dependent spin wave approach, to the quadratic order in quantum fluctuations.

Interestingly, the quadratic spin-wave expansion (3.42) of the Hamiltonian (3.1) suggests an insightful viewpoint on the system, which may alternatively be regarded as a macroscopic classical degree of freedom $(\hat{Q}, \hat{P})$ — the collective spin — interacting with an extensive ensemble of quantum oscillators $\{(\tilde{q}_k, \tilde{p}_k)\}_{k\neq 0}$ — the spin waves. This is reminiscent of Caldeira-Leggett models [314,315], although the bath of microscopic degrees of freedom is in our case self-generated by the many-body Hamiltonian dynamics of the spin system.

The formulation (3.42) of the Hamiltonian makes sense of the quasiintegrability of the model for small additional finite-range interaction. In fact, it is apparent in that expression, that in the mean-field limit $\tilde{J}_{k\neq 0} \to 0$, all spin-wave occupation numbers commute with the Hamiltonian,

$$\left[\hat{n}_k, \hat{H}\right] = 0. \tag{3.44}$$

Mean-field models have an extensive set of conserved quantities which prevent them from approaching thermal equilibrium, see the discussion in the Introduction and in Chap. 2. As a matter of fact, all degrees of freedom are frozen except the collective ones, which behave semiclassically in the thermodynamic limit. The formalism outlined in this Chapter allows us to tackle the questions on the impact of finite-range, integrability-breaking interactions on the peculiar mean-field nonequilibrium phenomena.

In the rest of Part I of the thesis, we shall apply the method described in the present one to study the impact of fluctuations on the mean-field nonequilibrium phenomena introduced in Chap. 2. Several extensions of the equations derived in this Chapter, and more generally of the formalism of nonequilibrium spin-wave theory, have been partly worked out and are reported further below in this thesis. In particular, in Sec. 4.2 and Chap. 5 we discuss the nonequilibrium dynamics of a variety of magnetic systems obtained by adapting the scheme above. In Chap. 6 we discuss the application of the formalism to study collective spin fluctuations and entanglement. In particular, this is extended in App. E to the Dicke model for atoms collectively interacting with cavity light. Moreover, in App. D, a nontrivial extension of the formalism is presented in order to take into account the possible presence of weak disorder. In conclusion, we remark that the discussion in Sec. 7.3 identify spin waves in a ferromagnetic phase with the lowest-energy bound state of a pair of domain-walls, referred to as a "meson" in the context of confinement physics. This provides us with a posteriori additional insights on the range of validity of the spin-wave expansion.

Chapter 4

Collective pseudorandom behavior induced by quantum fluctuations

In this Chapter, we discuss the fate of the mean-field dynamical criticality, discussed in Sec. 2.2, upon considering the effect of quantum fluctuations activated by finite-range interactions.

For the sake of definiteness, we shall first consider perturbations of the mean-field Hamiltonian in the form of nearest-neighbor interactions in one dimension. A similar analysis is then carried out — and similar results are obtained — in Sec. 4.2 for a much wider class of models. It is found that nonequilibrium fluctuations can significantly affect the critical dynamics, resulting in a pseudo-aleatory collective evolution, reminiscent of a classical particle in a multiple-well potential, with a large initial energy, and subject to (quantum) friction. The nonequilibrium phase diagram universally acquires the characteristics of a "coin toss" experiment. This result is confirmed by matrix-product-state numerical simulations away from the perturbative regime, discussed in Sec. 4.3. We further characterize the dynamics of quantum correlations (Sec. 4.4) and the effect of decreasing the quench rate in slower ramps (Sec. 4.5). We finally tackle the challenging question of finite-size effects in Sec. 4.6.

The content of this Chapter is constituted by the original results published in Refs. [1] and [2].

4.1 Effects of spin waves on mean-field dynamical criticality

We consider the Hamiltonian

$$\hat{H} = -\frac{\lambda}{N}\sum_{i,j=1}^{N}\hat{\sigma}_i^x\hat{\sigma}_j^x - g\sum_{i=1}^{N}\hat{\sigma}_i^z - J\sum_{i=1}^{N}\hat{\sigma}_i^x\hat{\sigma}_{i+1}^x, \tag{4.1}$$

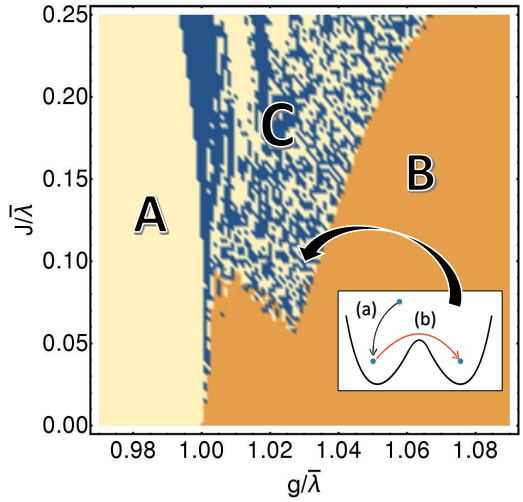

Figure 4.1: Dynamical phase diagram of the model in Eq. (4.1) after a quench of the transverse field $g_0 = 0 \to g$ starting from the fully polarized ground state with positive magnetization, as a function of g and J. As a reference scale for the transverse field, we choose the mean-field dynamical critical value $\bar{\lambda} \equiv \lambda + J$. The color of each point of the diagram is determined by the sign of the long-time average $\overline{\sigma^x}$ of $\sigma^x(t)$: light yellow for $\overline{\sigma^x} > 0$, orange for $\overline{\sigma^x} = 0$, and blue for $\overline{\sigma^x} < 0$. Regions A and B are perturbative extensions of the dynamical ferromagnetic and paramagnetic phases of the infinite-range model with $J = 0$, corresponding to the horizontal axis (see Fig. 4.2 for an illustration of the dynamics within A and B). Upon increasing J at fixed g, in a neighborhood of the mean-field critical point $g = \bar{\lambda}$, a new *chaotic dynamical ferromagnetic phase* C emerges, within which the magnetization $\sigma^x(t)$, after an initial dynamical paramagnetic behavior, gets trapped in one of the two symmetry-broken sectors with opposite signs of the collective magnetization [process (a) in the inset], in some cases followed by hopping between them [process (b) in the inset] (see Fig. 4.3 for an illustration of the dynamics within C). Here $N = 100$. The extent and features of the three phases A, B, C are stable as N is increased.

where the strength of the nearest-neighbor perturbation is controlled by the parameter J and periodic boundary conditions are understood. In the opposite limit $\lambda \to 0$ with finite J, the model reduces to the well-known quantum Ising chain in a transverse field, which is exactly solvable in terms of free Bogolyubov fermions [41]. In this case, however, dynamical criticality disappears, because the system does not support long-range order in excited states (see the Introduction).

In order to study the resulting dynamics, we will use Eqs. (3.33), (3.34), (3.35), (3.37), with $\tilde{J}_k = J \cos k$. We numerically integrate the evolution equations (3.33) and (3.37) for a range of post-quench values of g and J and starting from a fully polarized ferromagnetic initial state with $\langle \hat{\sigma}^x_j(t=0) \rangle = 1$ (i.e., the pre-quench Hamiltonian has $g_0 = 0$, and the value of J_0 is immaterial as long as $|J_0| < \lambda$). At each integration time, we compute the time-dependent components of the average collective spin $\vec{\sigma}$,

$$\vec{\sigma}(t) \equiv \frac{1}{N} \left\langle \tilde{\boldsymbol{\sigma}}_{k=0}(t) \right\rangle = \left[1 - \epsilon(t)\right] \begin{pmatrix} \sin\theta(t)\cos\phi(t) \\ \sin\theta(t)\sin\phi(t) \\ \cos\theta(t) \end{pmatrix}, \tag{4.2}$$

verifying that the nonequilibrium density $\epsilon(t)$ of spin waves [see Eq. (3.35)] remains small for considerably long times within the range of parameters con-

sidered. From this $\vec{\sigma}(t)$, we compute the long-time average of the magnetization along the ferromagnetic direction x, i.e., the dynamical order parameter $\overline{\sigma^x}$, and plot it for different values of J and g, coloring the corresponding point in light yellow if $\overline{\sigma^x} > 0$ (dynamical ferromagnetic ordering in the initial sector), in orange if $\overline{\sigma^x} = 0$ (dynamical paramagnetic behavior), and in blue if $\overline{\sigma^x} < 0$ (reversed dynamical ferromagnetic ordering). The result is the dynamical phase diagram reported in Fig. 4.1.

This figure shows that the dynamical ferromagnetic and paramagnetic phases A and B respectively, which touch each other at the dynamical critical point $g_{dyn} = \bar{\lambda}$ for $J = 0$, withstand the effects of the quantum fluctuations introduced by having $J \neq 0$, apart from getting separated by a new phase C around the line $g \simeq \bar{\lambda}$ (note the horizontal scale of Fig. 4.1). The robustness of phases A and B is further demonstrated in Fig. 4.2, which shows the time-evolution of the order parameter $\sigma^x(t)$ (first row) and of the spin wave density $\epsilon(t)$ (second row) within the dynamical ferromagnetic (first column) and paramagnetic (second column) phases, with $g/\bar{\lambda} = 0.9$ and $g/\bar{\lambda} = 1.5$ respectively. (Note that these values are well outside the range covered by Fig. 4.1.) The red solid and blue dashed lines correspond to increasing values of the coupling J with spin waves, which, as anticipated, do not alter significantly the qualitative features of the dynamics. Note that in both the dynamical phases A and B, $\epsilon(t)$ remains sufficiently small and therefore we expect the spin wave treatment developed in Sec. 3 to be accurate and these two phases to be robust.

Close to the mean-field dynamical transition point $g_{dyn} = \bar{\lambda}$, however, the system becomes extremely sensitive to nonequilibrium fluctuations, resulting in the peculiar phase C. In a typical point of this region, the dynamics of $\sigma^x(t)$ is driven by two processes, illustrated in the inset of Fig. 4.1: (a) the decay from a transient paramagnetic behavior to one of the two possible ferromagnetic sectors, and (b) the possible hopping between them. Heuristically, these phenomena occur when the energy of the macroscopic collective spin $\vec{\sigma}(t)$ is slightly above the barrier separating the two ferromagnetic minima. In this case the dynamical production of spin waves reduces the energy carried by $\vec{\sigma}$ and hence causes the dynamical trapping into one of the two ferromagnetic wells, accompanied by an increase of the spin wave density $\epsilon(t)$. The system is dynamically ferromagnetic, although it can occasionally hop to the opposite well, with a process assisted by the absorption of energy from the spin wave bath. The asymptotic sign of $\sigma^x(t)$, and therefore the sign of $\overline{\sigma^x}$, sensitively depends on the specific values of the parameters in a large portion of this novel dynamical ferromagnetic region (C in Fig. 4.1), with a collective pseudo-aleatory character of the dynamics, which is illustrated in Fig. 4.3. Due to this sensitive dependence on the post-quench values of the parameters, which actually implies the same for the choice of the initial state, this phase C is referred to as "chaotic".

This dynamical behavior, obtained on the basis of the time-dependent spin wave theory, persists up to large values $J = 2\lambda$ of the short-range coupling. In these conditions, the significant growth of $\epsilon(t)$ invalidates the low-density spin-wave expansion. In order to explore this strong coupling regime, we relied on a time-dependent variational principle developed on matrix product states,

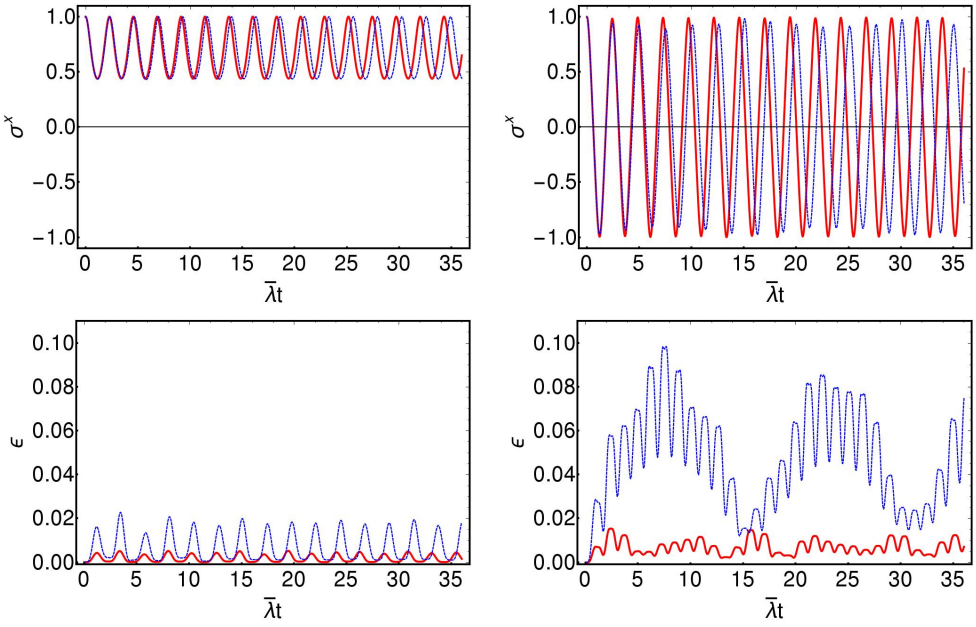

Figure 4.2: Dynamical behavior of the order parameter $\sigma^x(t)$ (first row) and of the spin wave density $\epsilon(t)$ (second row) of the fully-connected quantum Ising model with a nearest-neighbor perturbation of strength $J/\bar{\lambda} = 0.1$ (solid red line) and 0.2 (dashed blue), after a quench from a fully polarized ferromagnetic state ($g_0 = 0$), cf. Eq. (4.1). Left panels: dynamical ferromagnetic phase with $g/\bar{\lambda} = 0.9$. Right panels: dynamical paramagnetic phase with $g/\bar{\lambda} = 1.5$. These dynamical phases are characterized by the sign of the time-average of $\sigma^x(t)$, shown in the top panels. The quantity $\epsilon(t)$ shown in the bottom panels represents the total amount of spin wave excitations generated during the nonequilibrium evolution. This is the control parameter for the validity of the low-density expansion, which is consistent if $\epsilon \ll 1$, i.e., if the magnitude of the collective spin $|\vec{\sigma}(t)| = 1 - \epsilon(t)$ remains close to its maximal value. The presence of a short-range interaction, produces a perturbative modification of the mean-field evolution and, correspondingly, a small amount of spin waves. In particular, the classical, mean-field persistent oscillations are not damped by the self-generated bosonic "bath". In the plots, $N = 100$ and the mean-field dynamical critical point is $g_{dyn}/\bar{\lambda} = 1$.

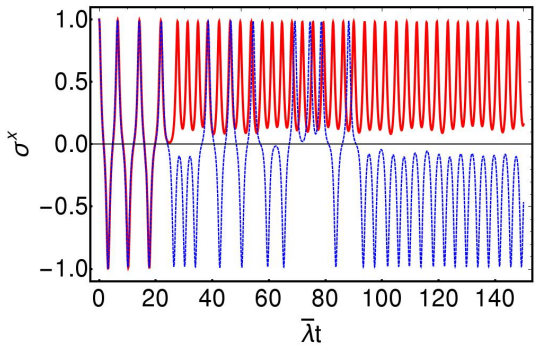

Figure 4.3: Evolution of the order parameter $\sigma^x(t)$ within the chaotic dynamical ferromagnetic phase C in Fig. 4.1, for $g/\bar{\lambda} = 1.03$ (solid red line) and 1.031 (dashed blue), and with $J/\bar{\lambda} = 0.1$. Here $N = 100$. The two lines are practically indistinguishable during the initial paramagnetic transient, but they have markedly distinct fates at the onset of the critical process denoted by (a) in the inset of Fig. 4.1 and they eventually end up into distinct wells. In both cases, $\epsilon(t)$ grows from $\epsilon(t = 0) = 0$ to values around 0.04. This extreme sensitivity on the value of g (and of J) is at the origin of the "mosaic" structure of region C in Fig. 4.1.

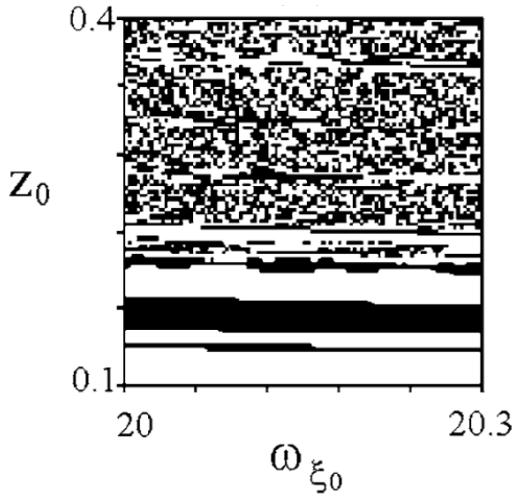

Figure 4.4: "Nonequilibrium phase diagram" of a coin toss, from Ref. [316]. The final outcome of the toss (heads or tails) is plotted as a function of the initial heigth Z_0 and angular momentum ω_{ξ_0} of the coin. The qualitative similarity with the chaotic dynamical ferromagnetic phase in Fig. 4.1 is striking. The "predictable" outcome for sufficiently small Z_0 appears in the form of a sequence of regular stripes, which correspond to the coin attaining the final configuration (heads of tails) after one, two, ..., turns. This is remarkably reminiscent of the regular stripes on the left side of region C in Fig. 4.1, which correspond the collective spin attaining the asymptotic magnetization sector (positive or negative) after one, two, ..., changes of sign. In both cases, as the initial energy increases (larger Z_0 and g, respectively), the outcome becomes increasingly sensitive to the initial condition, and "practically random" above a certain threshold. See also Ref. [317].

see Sec. 4.3.

The dynamics in the chaotic dynamical ferromagnetic region C may be understood qualitatively via a simple analogy: a coin toss. The toss corresponds to the sudden quench of the external field, where a macroscopic amount of energy is injected into the system in the form of regular motion of a macroscopic object. The coin repeatedly hitting the ground and exciting its phonons corresponds to the loss of energy of the collective spin in favor of the microscopic degrees of freedom, i.e., the spin waves. Finally, the coin settling into one of the two macroscopically distinct stable configurations (heads or tails) corresponds to the trapping into one of the two ferromagnetic sectors ($\overline{\sigma^x} > 0$ or $\overline{\sigma^x} < 0$). A diagram of the outcomes of the coin (heads or tails) as a function of the variables which parameterize the toss, results in a picture very similar to region C of Fig. 4.1, as indeed shown in Ref. [316] and reported in Fig. 4.4. Although the equations of motion in both cases are completely deterministic, the final outcome is extremely sensitive to the details of the dynamics and it can be considered as an *effectively random* process. We emphasize that we checked that the numerical results reported above in Fig. 4.1 and in the figures which follow are not affected as N is increased (up to $N = 400$). See also the subsequent Ref. [317] for a finer study of the properties of the chaotic dynamical ferromagnetic phase.

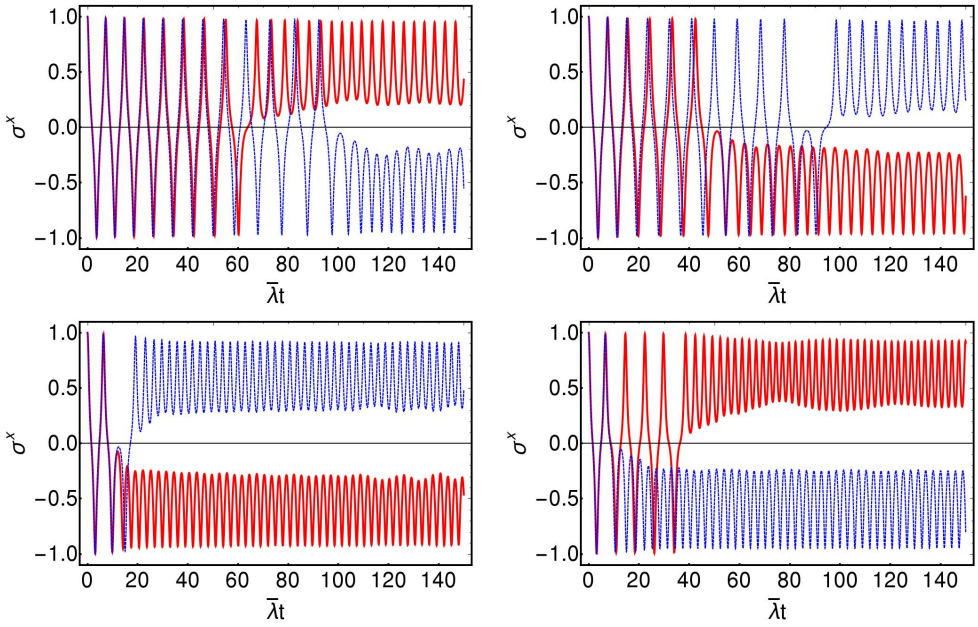

Figure 4.5: Evolution of the order parameter $\sigma^x(t)$ after a quench from a pure ferromagnetic state ($g_0 = 0$) in four different generalizations of the Ising Hamiltonian (3.1). Top left: XY spin chain with an infinite-range and a nearest-neighbor interaction, defined by Eq. (4.3) with $\alpha_y = 0.25$, $\alpha_z = 0$, $g/\bar{\lambda} = 1.03$ (solid red line) and 1.032 (dashed blue), with $J/\bar{\lambda} = 0.4$. Top right: XYZ spin chain with an infinite-range and a nearest-neighbor interaction, defined by Eq. (4.3) with $\alpha_y = 0.25$, $\alpha_z = 0.125$, $g/\bar{\lambda} = 0.9$ (solid red line) and 0.902 (dashed blue), with $J/\bar{\lambda} = 0.4$. Bottom left: Ising spin chain with an infinite-range and a next-to-nearest-neighbor interaction, defined by Eq. (4.4) with $v(r) = \delta_{r,1} + 0.5\delta_{r,2}$, $g/\bar{\lambda} = 1.03$ (solid red line) and 1.031 (dashed blue), with $J/\bar{\lambda} = 0.2$. Bottom right: Ising spin chain with an infinite-range and a power-law decaying interaction, defined by Eq. (4.4) with $v(r) = 1/r^2$, $g/\bar{\lambda} = 1.03$ (solid red) and 1.031 (dashed blue), with $J/\bar{\lambda} = 0.2$. In all simulations, $N = 100$. These trajectories have been obtained by numerically integrating the evolution equations given by the time-dependent spin wave theory, analogous to Eqs. (3.33), (3.37), derived for the generalized spin chains above through the same procedure as that explained in details in Sec. 3.2 for the Ising model.

4.2 Generality of the chaotic dynamical phase

We now show that the chaotic dynamical phase is not peculiar to the model in Eq. (4.1), but is actually expected to emerge in a rather general class of ferromagnetic spin systems, characterized by competition between long- and short-range interactions.

First of all, the occurrence of the chaotic dynamical phase discussed in the previous section does not depend on the particular initial state we have chosen, as long as it has sufficiently strong magnetic ordering. In particular, the direction of the initial magnetization $\mathrm{Tr}\left[\hat{\rho}(t=0)\hat{\boldsymbol{\sigma}}_j\right] \propto (\sin\theta_0, 0, \cos\theta_0)$ with $\theta_0 \neq 0$ is immaterial, and the initial state $\hat{\rho}(t=0)$ needs not be pure. This class encompasses all low-temperature equilibrium ordered states of $\hat{H}(g < g_{cr})$.

The chaotic dynamical phase occurs for arbitrary quantum spin magnitude s. A larger value of s amounts to rescaling the coupling strength J in Eqs. (3.33), and therefore to decreasing the overall effect of the feedback from quantum fluctuations on the evolution of the collective order parameter. In addition,

in the limit $s \to \infty$, quantum fluctuations in the pre-quench ground state are suppressed as a consequence of the individual spins approaching their classical limit. Accordingly, the extent of the chaotic dynamical phase progressively shrinks. However, thermal fluctuations can play a role similar to that of quantum fluctuations when initial states in equilibrium with a finite temperature $T > 0$ are considered, leading to a nonvanishing feedback and thus to an extended chaotic dynamical phase even in the classical limit $s \to \infty$.

We also expect that the phenomena discussed here for a spin chain with an interaction characterized by $\mathbb{Z}_2$ symmetry emerge also for other discrete symmetry groups. In the case of quenches from the ordered states of systems with a "clock" symmetry $\mathbb{Z}_n$, for instance, the dynamical order parameter is expected to get eventually trapped into one of the n distinct symmetry-breaking sectors, resulting in a multicolor version of the picture of Fig. 4.1 with different colors corresponding to the n possible sectors. In this case, the appropriate heuristic analogy would be that of a "roulette" rather than a coin.

Changing the sign of short-range spin-spin interaction term J from ferromagnetic to antiferromagnetic ($J < 0$) does not alter the structure of the phase diagram in Fig. 4.1. Indeed, the time-dependent spin wave theory evolution equations (3.33) do not change when $J \mapsto -J$, provided the substitution of the summation variable $k \mapsto \pi - k$ is performed.[1]

We now turn our attention to generalizations of the Ising Hamiltonian (4.1). The top panel of Fig. 4.5 shows the evolution of the order parameter $\sigma^x(t)$ for the XY (top left panel) and XYZ (top right) versions of the model with a nearest-neighbor anisotropic perturbation, defined by

$$\begin{aligned}\hat{H}_{XYZ} = &-\frac{\lambda}{N}\sum_{i,j=1}^{N}\left(\hat{\sigma}_i^x\hat{\sigma}_j^x + \alpha_y\hat{\sigma}_i^y\hat{\sigma}_j^y + \alpha_z\hat{\sigma}_i^z\hat{\sigma}_j^z\right)\\ &- g\sum_{i=1}^{N}\hat{\sigma}_i^z - J\sum_{i=1}^{N}\left(\hat{\sigma}_i^x\hat{\sigma}_{i+1}^x + \alpha_y\hat{\sigma}_i^y\hat{\sigma}_{i+1}^y + \alpha_z\hat{\sigma}_i^z\hat{\sigma}_{i+1}^z\right).\end{aligned} \tag{4.3}$$

with $\alpha_z = 0$ (XY model) or nonvanishing values of $\alpha_{y,z}$ (XYZ model), while they reduce to the standard Ising model in Eq. (4.1) for $\alpha_y = \alpha_z = 0$. Note that at the isotropic point $\alpha_y = 1$ the discrete $\mathbb{Z}_2$ symmetry turns into a continuous $O(2)$ symmetry, as σ^z is conserved. Consequently, the barrier separating the two ferromagnetic minima becomes increasingly shallow as this point is approached, which hinders the possibility for the collective order parameter to get trapped. Accordingly, the chaotic dynamical phase disappears in this limit.

The bottom panel of Fig. 4.5 shows the evolution of the order parameter $\sigma^x(t)$ for the fully-connected quantum Ising model with a next-to-nearest-neighbor

[1] Note, however, that completely different phenomena are expected in the presence of antiferromagnetic *long-range* interactions, i.e., when $\lambda < 0$. See, e.g., Ref. [318].

(bottom left) or algebraically-decaying (bottom right) perturbation, defined by

$$\hat{H}_{LR} = -\frac{\lambda}{N}\sum_{i,j=1}^{N}\hat{\sigma}_i^x\hat{\sigma}_j^x - g\sum_{i=1}^{N}\hat{\sigma}_i^z - J\sum_{i,r}^{N}v(r)\hat{\sigma}_i^x\hat{\sigma}_{i+r}^x, \tag{4.4}$$

where $v(r)$ decays to zero upon increasing the distance r between the two interacting spins. The qualitative similarity of all the panels in Fig. 4.5 with the evolution displayed in Fig. 4.3 demonstrates that the chaotic behavior observed in the latter case is actually a generic phenomenon which emerges also in the generalized models discussed above. In particular, the evolution of a certain initial state under the effect of two close post-quench Hamiltonians (red and blue curves) results into two markedly different asymptotic states. Although Fig. 4.5 refers to specific choices of the various parameters involved, we verified that this strong sensitivity of the dynamics to the values of the parameters of the post-quench Hamiltonian persists in a neighborhood of the points considered. We finally observe that the spatial dimensionality of the finite-range perturbation does not play an important role, as well.

We finally observe that the phenomenon discussed above is expected to be enhanced by the presence of further fluctuations in the system generated by possible other mechanisms, such as, e.g., weak quenched disorder. This issue can be studied by extending the formalism of Chap. 3, as discussed in App. D.

In summary, we have shown that the emergence of a chaotic dynamical phase is an ubiquitous phenomenon that requires essentially two sole physical ingredients, namely *i*) the spontaneous breaking of a discrete symmetry and *ii*) a mean-field model perturbed by an interaction term with a nontrivial spatial dependence, which introduces fluctuations.

4.3 Strong interactions: MPS-TDVP simulations

In order to check the robustness of the observed phenomena in the presence of a nearest-neighbor interaction strength J in Eq. (4.1) increased beyond the perturbative regime considered in the previous sections, we simulate numerically the evolution of the system by using the time-dependent variational principle developed in Refs. [319,320]. This formulation requires a matrix product operator (MPO) representation of the Hamiltonian. Since the interaction strength of the infinite-range part of the Hamiltonian (3.1) scales with the system size N, it is not possible to rewrite the thermodynamic limit of the Hamiltonian in the MPO form and hence to simulate the time evolution directly in the thermodynamic limit. Accordingly, we performed finite-size simulations of long chains, up to $N = 400$.

The reformulation of the Hamiltonian in the MPO form is done in two steps. First, we write an exact homogeneous MPO with a large bond dimension $D_{MPO} = N + 1$ and then use standard methods in order to find a compact inhomogeneous MPO representation with a bond dimension up to $D_{MPO} = 17$ and an error below 10^{-10}. In all simulations we used a time step of 0.02 (in units

of λ), a matrix product state bond dimension up to $D = 600$, and the second order single-site integrator proposed in Refs. [319,320].

We first verify that the sensitivity of the evolution and of the final state to the values of the quench parameters, observed in the perturbative regime of small spin wave density ϵ, carries over to a larger nearest-neighbor interaction strength J. By extensive numerical simulations, we show that the phenomenon persists in this region. In Fig. 4.6 we show the dependence of the long-time time-averaged value of the order parameter $\overline{\sigma^x}$ on the transverse field g for various values of J around $0.5\bar{\lambda}$, i.e., $J \approx \lambda$. In particular, depending on the value of J, the dynamical ferromagnetic phase with $\overline{\sigma^x} > 0$ at $g/\bar{\lambda} \lesssim 0.9$ turns into a dynamical paramagnetic phase with $\overline{\sigma^x} = 0$ at $g/\bar{\lambda} \gtrsim 1.3$ via an intermediate region in which the ferromagnetic ordering is reversed as compared to the initial one, i.e., $\overline{\sigma^x} < 0$. This is reminiscent of the "stripes" of reversed magnetization in Fig. 4.1 in the leftmost part of region C. We therefore expect a "chaotic" region to be present in between.

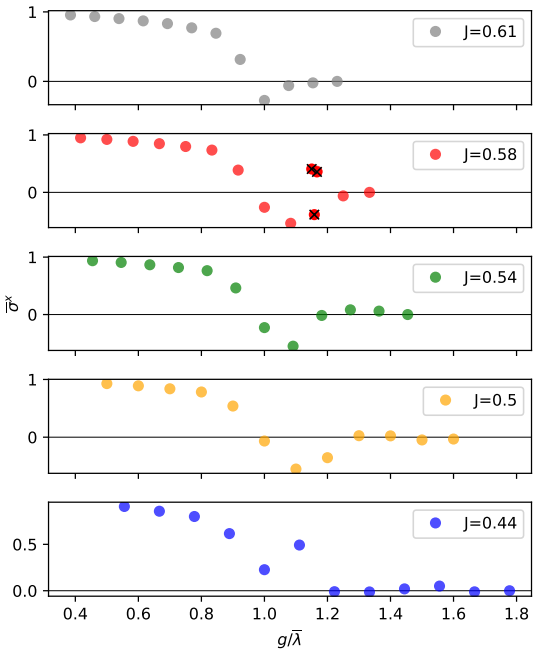

Figure 4.6: Time-averaged order parameter $\overline{\sigma^x}$ of the model of Eq. (4.1) as a function of the post-quench values g of the transverse field, for various values of the coupling J around $0.5\bar{\lambda}$. The black crosses ($J = 0.58$) correspond to a finer grid of values of g, with $\delta g = 0.008\bar{\lambda}$, which are shown in order to display the high sensitivity of the chaotic phase to post-quench parameters. These data show that the dynamically ferromagnetic and chaotic region persist also at strong nearest-neighbor interactions. The data is calculated for system size $N = 200$.

Far from the mean-field dynamical critical point $g_{\text{dyn}} = \bar{\lambda}$, the time evolution of the order parameter remains qualitatively similar to the mean-field case. As shown in Fig. 4.7, for $g/\bar{\lambda} = 0.5$ and $g/\bar{\lambda} = 1.5$ the ferromagnetic (red solid line) and paramagnetic (blue solid) trajectories are only slightly shifted with respect to the mean-field evolution ($J = 0$, dashed red and blue lines) despite the large interaction strength $J = 0.5\bar{\lambda} = \lambda$.

Upon getting closer to the mean-field dynamical critical point $g = \bar{\lambda}$ with

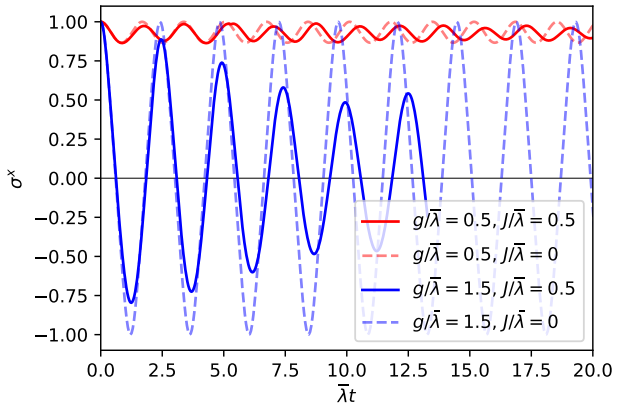

Figure 4.7: Comparison between the evolution of the order parameter σ^x at large J (solid lines) with those of the mean-field model with $J = 0$ (dashed lines) far from the critical region and for the same model as in Fig. 4.6. We observe that the evolution corresponding to both the ferromagnetic and paramagnetic phases are not altered qualitatively by the effects of quantum fluctuations. The decay of the oscillations amplitude upon increasing time is a finite-size effect. In these simulations $N = 400$ and $D = 300$.

$J \neq 0$ one observes, instead, significant qualitative changes in the time evolution of $\sigma^x(t)$ compared to the case $J = 0$, as shown in Figs. 4.8 and 4.9. In particular, in the region of parameters highlighted in Fig. 4.6, one observes that the eventual sign of $\sigma^x(t)$ is reversed compared to the initial value and that it is attained possibly after a number of sign changes, as in Fig. 4.8. This final sign reversal appears to be stable in longer simulations. The dynamics, however, become more complex when g approaches the dynamical paramagnetic phase: as expected, the associated instability significantly affects the resulting evolution of $\sigma^x(t)$ which is displayed in Fig. 4.9 and which is characterized by a sensitive dependence of the long-time magnetization on the quench parameter (magnetic field). Correspondingly, the time evolution of the order parameter looks irregular before it settles in one of the two sectors with a definite sign of σ^x. For some trajectories visible in both Figs. 4.8 and 4.9, the order parameter oscillates between them before it eventually reaches the final magnetization sector. In this case, the period of these oscillations progressively increases before the "trapping" occurs. Similarly to the case of the propagation of correlations at weak interactions discussed in Sec. 4.4, this change of the oscillation frequency corresponds to a transition from a dynamically paramagnetic to a dynamically ferromagnetic regime. Trajectories of Fig. 4.9 are marked in the phase diagram shown in Fig. 4.6 by black crosses.

In summary, the qualitative picture of the phases observed at small interactions persists also at large J. We emphasize the fact that for the values of J used in the simulations reported in this Section, the accuracy of the spin-wave approach is poor and no quantitative agreement between the two methods has to be expected. In turn, at smaller values of J and for the largest system sizes N reached in these simulations, the time scale over which the collective magnetization gets trapped into a ferromagnetic sector is larger than the Ehrenfest time scale $T_{Ehr} \lesssim \mathcal{O}(\sqrt{N})$ over which the motion of the collective magnetization

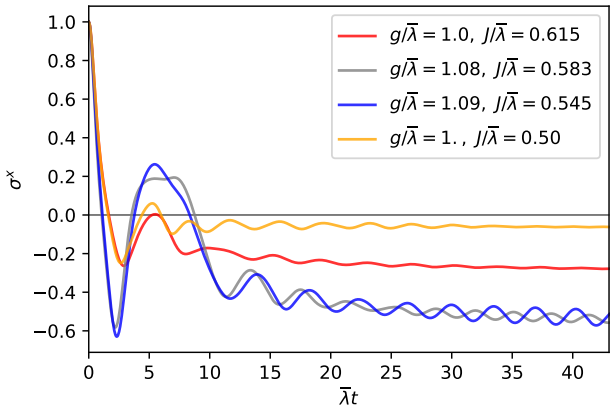

Figure 4.8: Stability of the flipped ferromagnetic region. We show several trajectories within a wide range of different quench parameters as a part of the same region with a flipped final magnetization. This demonstrates stability of the flipped ferromagnetic region at large nearest-neighbor interactions. Simulations were performed with N = 200, D = 200.

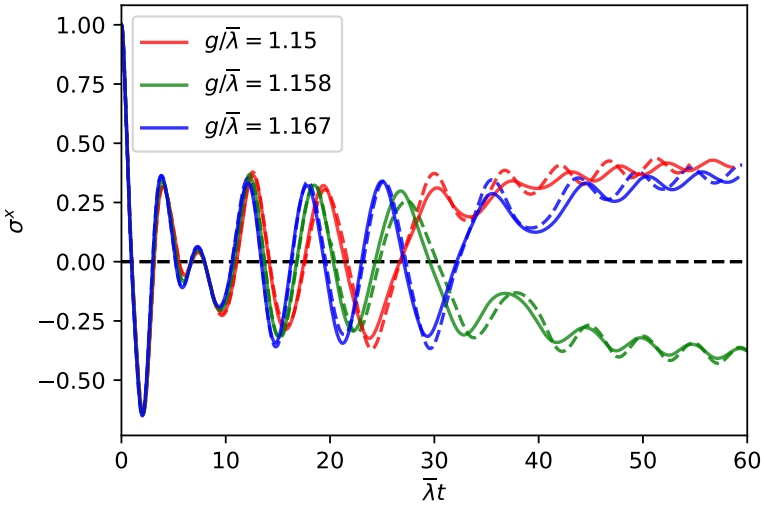

Figure 4.9: Evolution of the order parameter $\sigma^x(t)$ for a quench occurring close to the mean-field dynamical critical point within the chaotic phase. These curves at fixed $J/\bar{\lambda} = 0.583$ show a sensitive dependence on the value of g, and they may oscillate for a long time before settling eventually in a sector with definite positive or negative order parameter. By changing the quench parameter $g/\bar{\lambda}$ only slightly (approximately by 0.08) we observe a large change in the final magnetization which jumps from the positive to the negative sector and finally back to the positive sector. The curves in this plot correspond to the data points indicated by black crosses in Fig. 4.6. Simulations were performed with N = 200, and with D = 600 (full lines) and D = 500 (dashed lines).

is approximately classical (see Secs. 2.4 and 4.6). This fact makes it difficult to observe the chaotic dynamical phase in this regime with MPS-TDVP. For this reason, the two methods used in this paper effectively explore complementary regimes of the dynamics of the system and they cannot be quantitatively compared.

Finally, we remark that the convergence properties with respect to the bond dimension are better in the ferromagnetic and paramagnetic regions than in the chaotic region. Far from the critical point the simulations for the system size

$N = 400$ converged already with bond dimension $D = 300$. On the other hand, in the chaotic region we needed bond dimensions around $D = 600$. Therefore, we could perform simulations only up to the system size $N = 200$.

4.4 Dynamical correlations of the local order parameter

According to the picture presented above, the prethermal dynamics of the system can be understood in terms of the motion of a classical, macroscopic degree of freedom (the collective spin $\vec{\sigma}$) coupled to a weakly interacting many-body system (the bosonic "bath" of spin waves), which, in turn, is driven by the former: see Eqs. (3.42) and (3.43). This driving mechanism is determined by the persistent precession of the collective spin and can be highlighted by studying the time- and space-dependent equal-time correlation functions $\langle \hat{\sigma}^x_j(t)\hat{\sigma}^x_{j+r}(t)\rangle$, of the local order parameter $\langle \hat{\sigma}^x_j(t)\rangle$. Taking into account Eq. (3.4) and Eq. (3.7) at the leading order in the low-density expansion of Chap. 3, the connected correlation function $C^{xx}(r,t)$ can be expressed as

$$
\begin{aligned}
C^{xx}(r,t) \equiv & \langle \hat{\sigma}^x_j(t)\hat{\sigma}^x_{j+r}(t)\rangle - \langle \hat{\sigma}^x_j(t)\rangle\langle \hat{\sigma}^x_{j+r}(t)\rangle \\
= & (\mathbf{X}\cdot\mathbf{x})^2 \frac{1}{s}\langle \hat{q}_j(t)\hat{q}_{j+r}(t)\rangle + (\mathbf{Y}\cdot\mathbf{x})^2 \frac{1}{s}\langle \hat{p}_j(t)\hat{p}_{j+r}(t)\rangle \\
& + 2\,(\mathbf{X}\cdot\mathbf{x})\,(\mathbf{Y}\cdot\mathbf{x})\,\frac{1}{s}\left\langle \frac{\hat{q}_j(t)\hat{p}_{j+r}(t) + \hat{p}_j(t)\hat{q}_{j+r}(t)}{2}\right\rangle \\
= & \cos^2\theta(t)\cos^2\phi(t)\,\frac{1}{Ns}\sum_{k\neq 0}\cos(kr)\,\Delta^{qq}_k(t) \\
& \sin^2\phi(t)\,\frac{1}{Ns}\sum_{k\neq 0}\cos(kr)\,\Delta^{pp}_k(t) \\
& - 2\cos\theta(t)\cos\phi(t)\sin\phi(t)\,\frac{1}{Ns}\sum_{k\neq 0}\cos(kr)\,\Delta^{qp}_k(t).
\end{aligned}
\tag{4.5}
$$

Analogous expressions can be readily obtained for $C^{\alpha\beta}(r,t)$, with $\alpha,\beta = x,y,z$. In this section, for definiteness, we focus on the model in Eq. (4.1).

4.4.1 Modulated light-cone effect

Density plots of the equal-time correlation functions $C^{xx}(r,t)$ are shown in Fig. 4.10. They are obtained by integrating the equations of motion (3.33) and (3.37) with the same initial conditions as in the previous sections and by substituting their solution $\left(\theta(t),\phi(t),\{\Delta^{qq}_k(t),\Delta^{qp}_k(t),\Delta^{pp}_k(t)\}\right)$ into Eq. (4.5), with $s = 1/2$.

A light-cone effect [35] is present for all values of the parameters g and J, which is characterized by an exponentially fast decay in time of the correlation function for $|r| > 2v_{max}t$ with a certain v_{max}, see Ref. [36]. In fact, the infinite-

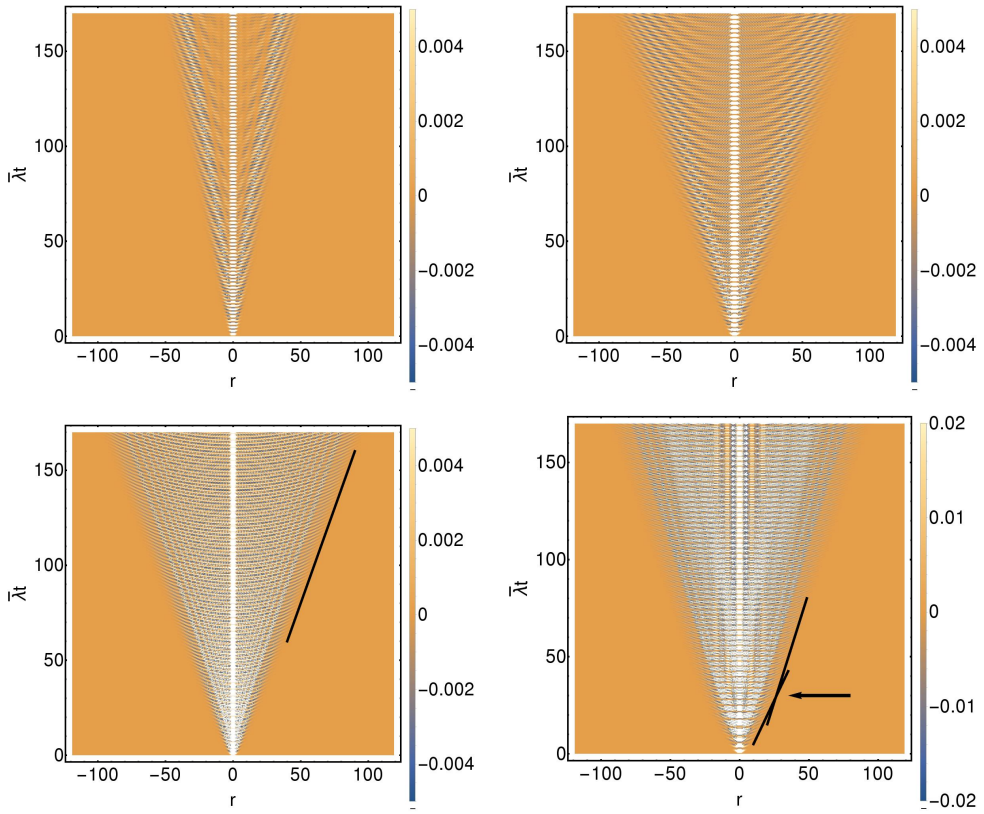

Figure 4.10: Space-time density plots of the dynamical correlation function $C^{xx}(r,t)$ [see Eq. (4.5)] after a quench of the magnetic field g from a fully polarized ferromagnetic state ($g_0 = 0$) to $g/\bar{\lambda} = 0.7, 0.9, 1.025, 3$, in clockwise order from top left. In all plots, $J/\bar{\lambda} = 0.25$, $N = 240$. For a small quench occurring deep in the ferromagnetic phase (top left), the overall amplitude of the correlation function is weak (few excitations are produced) and the light-cone is narrow due to an almost constant spin waves dispersion relation. The amplitude and the width become larger as the dynamical critical region is approached (top right). In the chaotic dynamical phase (bottom right), a "knee" is visible, marked by the black arrow, witnessing a change of the maximal velocity of propagation due to the trapping of the orbit, after a paramagnetic transient, into a ferromagnetic sector (notice the change of scale, highlighting a larger amplitude of the correlations). Finally, deep in the paramagnetic phase (bottom left), the maximal velocity approaches the value analytically predicted in Eq. (4.7), indicated by the black line. An approximately periodic modulation of the amplitude of $C^{xx}(r,t)$ is visible in all cases, which reflects the approximately periodically driven nature of the spin waves, induced by the precession of the collective spin.

range Hamiltonian generates a collective coherent precession of all the spins with no spatial structure, due to the full permutational symmetry of the spins. However, a nontrivial spatial dependence of the dynamical correlations arises in the presence of the additional short-range interaction term, which results in a light-cone effect.

A closer inspection of the figures reveals that a (seemingly) periodic modulation is superimposed to the amplitude of the correlations. The origin of this phenomenon can be explained in the following terms. Within the low-density expansion considered here, the quadratic bosonic Hamiltonian (3.13) governing the evolution of the spin waves has coefficients which depend parametrically on the angles $\theta(t), \phi(t)$. The latter evolve approximately periodically in time (cf.

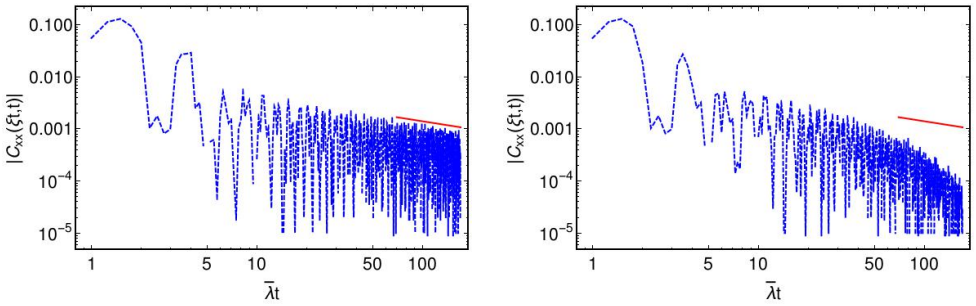

Figure 4.11: Long-time behavior of the correlation function $C(\xi,t,t)$ along two close spacetime rays with fixed $\xi = 0.5\bar{\lambda}$ (left) and $0.55\bar{\lambda}$ (right) in a log-log scale, after a quench of the magnetic field from a pure ferromagnetic state ($g_0 = 0$) to $g/\bar{\lambda} = 0.9$ with $J/\bar{\lambda} = 0.25$, $N = 240$, corresponding to the data of the top right panel of Fig. 4.10. Apart from an (approximately) periodic modulation, $C(\xi,t,t)$ decays, in the large spacetime limit, as a power-law (left) or as an exponential (right) as a function of time. The red line highlights the $t^{-1/2}$ decay suggested by the argument in the text, see Eq. (4.9). Data are consistent with a maximal velocity of propagation of the effective free quasiparticles between $0.25\bar{\lambda}$ and $0.275\bar{\lambda}$ in this specific numerical instance.

Fig. 4.2), resulting in an instantaneous dispersion relation of the spin waves with an approximately periodic time-dependence. The "stroboscopic" dynamics of the spin waves at integer multiples of the "period" of the collective precession can thus be argued to relax to a periodic or stroboscopic generalized Gibbs ensemble [321,322], which is known to occur in quadratic quantum many-body models subject to an *external* periodic driving. We emphasize, however, that here the "periodic" drive is determined by the dynamics of the system itself, i.e., it is self-generated by the autonomous Hamiltonian dynamics, without external actions: the collective motion of the classical spin $\vec{\sigma}(t)$ generates an effective "external" drive for the spin waves, see Eq. (5.3). In particular, the backreaction ("feedback") of the driven quasiparticles — i.e., the spin waves — on the drive — i.e., the collective spin — is controlled by J.

Let us now investigate the behavior of the slope of the light-cone edge as a function of the system's parameters. This quantity is known to be twice the maximal velocity v_{max} of propagation of the quasiparticles [34], which can be computed as the maximal slope of their effective dispersion relation $\omega_k^{(eff)}$ (see below). In the two limiting cases, $g \to 0$ and $g \to \infty$, this velocity v_{max} can be determined analytically.

For $g \ll \bar{\lambda}$, the classical spin performs small oscillations near the initial ferromagnetic configuration, hence $\theta(t) \approx \pi/2$ and $\phi(t) \approx 0$ (or π) for all times. The dispersion relation in such a near-equilibrium condition has already been determined in Eq. (3.22): in fact, it is asymptotically flat, $\omega_k^{(eff)} \to 2\bar{\lambda}$, as $g \to 0$, and hence v_{max} approaches zero in this limit. This is confirmed by numerical computations, as shown in the two top panels of Fig. 4.10 where the light-cone width shrinks as g decreases.

In the opposite limit $g \gg \bar{\lambda}$, the collective spin approximately rotates uniformly along the equator, $\theta(t) \approx \pi/2$, $\phi(t) \approx 2gt$, at frequency $2g$. The effective (Floquet) Hamiltonian (see App. C and Ref. [302]) of the spin waves is simply given by the time-averaged Hamiltonian to lowest order in the driving period

π/g. Thus, by averaging in time the coefficients of Eq. (3.42), we find the effective dispersion relation

$$\omega_k^{(\mathrm{eff})} = 4\sqrt{\bar{\lambda}(\bar{\lambda} - J\cos k)}, \tag{4.6}$$

and therefore, for small $J/\bar{\lambda}$, the maximal velocity of propagation is given by

$$v_{\max} = \max_k \left| \frac{\partial \omega_k^{(\mathrm{eff})}}{\partial k} \right| \sim J. \tag{4.7}$$

Visually comparing this prediction with the slope $2v_{\max}$ of the light-cone of correlations, we find excellent agreement with the data shown in the bottom left panel of Fig. 4.10.

A more precise quantitative determination of the light-cone edge from numerics requires some care. In order to address this, consider a quantum system composed by free quasiparticles with dispersion relation ω_k, and assume parity symmetry, i.e., $\omega_k = \omega_{-k}$. An equal-time, two-point correlation function can be generically expressed as (see, e.g., Ref. [323])

$$C(r,t) = \int_{-\pi}^{\pi} \frac{dk}{2\pi} f(k)\, e^{ikr - i2\omega_k t}, \tag{4.8}$$

where the function f depends on the model and on the quench. In the scaling limit of large r and t with fixed $r/t \equiv \xi$, $t \to \infty$, this correlation function shows a different asymptotic behavior along rays within or outside the causal region delimited by the light cone $|\xi| \leqslant 2v_{\max}$. Indeed, by straightforward saddle-point integration, one finds

$$C(\xi t, t) \underset{t\to\infty}{\sim} \begin{cases} \sum_{k^*} f(k^*(\xi)) \dfrac{\exp\left[i\left(k^*(\xi)\xi - 2\omega_{k^*(\xi)}\right)t\right]}{\sqrt{2\pi\omega''_{k^*(\xi)}\, t}}, & \text{for } |\xi| < 2v_{\max}, \\ A\exp\Big(-\delta(\xi)t\Big), & \text{for } |\xi| > 2v_{\max}, \end{cases} \tag{4.9}$$

where $k^*(\xi)$ is a solution to the equation $2\partial\omega_k/\partial k(k) = \xi$, which exists only if $|\xi| < 2v_{\max}$, and the sum runs over the set of such solutions. Accordingly, upon increasing the time t, the correlation function decays to zero as $t^{-1/2}$ along rays *within* the light-cone, whereas it decreases exponentially along rays *outside* the light-cone (the latter is a general fact valid for all systems with short-range interactions, as follows from the Lieb-Robinson bound [36] — see the discussion in the Introduction). The proper way of extracting $v_{\max}$, and thus of defining the light-cone edge from the numerical data, is therefore to inspect the decay of the correlation function along space-time rays and thereby discriminate power-law from exponential decay. The light-cone edge is the critical ray which separates the two behaviors. Figure 4.11 shows that the two scaling behaviors in Eq. (4.9) are indeed found in the the numerical data. This agrees with the picture of self-consistently periodically driven spin waves.

4.4.2 Dynamical correlations in the chaotic dynamical phase

The chaotic dynamical ferromagnetic phase C in Fig. 4.1 leaves detectable signatures on the dynamics of the local order parameter correlation functions. The self-consistent internal driving provided by the collective spin dynamics changes when the transient paramagnetic behavior turns into an evolution occurring eventually within one of the ferromagnetic sectors, as happens, e.g., in Fig 4.3. From the point of view of the spin waves, this can be seen as a change of their effective (Floquet) Hamiltonian, which, accordingly, results in a change of the associated "speed of light". Although the values of v_{max} before and after this change from dynamical paramagnet to dynamical ferromagnet, are not very different, a variation of slope in the light-cone is visible in some of the numerical computations, such as, e.g., those reported in the bottom right panel of Fig. 4.10. They correspond to the macroscopic, qualitative change in the internal driving provided by $\vec{\sigma}(t)$. This phenomenon is a consequence of the existence of a chaotic dynamical ferromagnetic phase, and it can be seen as a further, characteristic hallmark of its peculiar nature.

4.5 Effets of a variable quench rate

We now extend the analysis to a time-dependent ramp $g(t)$ of the transverse field, describing the crossover from the sudden quench (infinitely quick ramp) to the adiabatic evolution (infinitely slow ramp). We consider a linear time-dependence

$$g(t) = \begin{cases} g_0, & \text{for } t < 0, \\ g_0 + (g - g_0)\frac{t}{\tau}, & \text{for } 0 \leqslant t \leqslant \tau, \\ g, & \text{for } t > \tau. \end{cases} \tag{4.10}$$

The parameter τ controls the total duration of the ramp. The system is initialized in the ground state of $H(g_0)$ at $t_0 < 0$ and then evolves with the time-dependent Hamiltonian $H\big(g(t)\big)$ at later times. When $\bar{\lambda}\tau \ll 1$, the results approach those obtained for the quantum quench dynamics of the previous section, see Fig. 4.1. Upon increasing τ, we expect two effects. *i)* The final state for $t \geqslant \tau$, will be progressively closer to the adiabatic one (i.e., the ground state of the final Hamiltonian, since the system is initialized in a zero-temperature ground state). This implies that the dynamical critical point, separating nonequilibrium trajectories within one ferromagnetic well from the dynamically paramagnetic ones encircling both wells, will move towards the equilibrium critical point, which is asymptotically reached in the adiabatic limit $\tau \to \infty$. This phenomenon occurs also in the absence of spatial fluctuations, i.e., in infinite-range models. *ii)* In the presence of fluctuations, an increasingly slower protocol will deposit in the system a progressively smaller amount of energy in the form of spin wave excitations with $k \neq 0$. By inspecting the Hamiltonian (5.3) or the equations of motion, one notices that the driving $g(t)$ directly affects only the dynamics of the collective spin. This macroscopic precession, in turn, causes the production of spin waves. Near the dynamical transition, the self-generated "gas" of spin

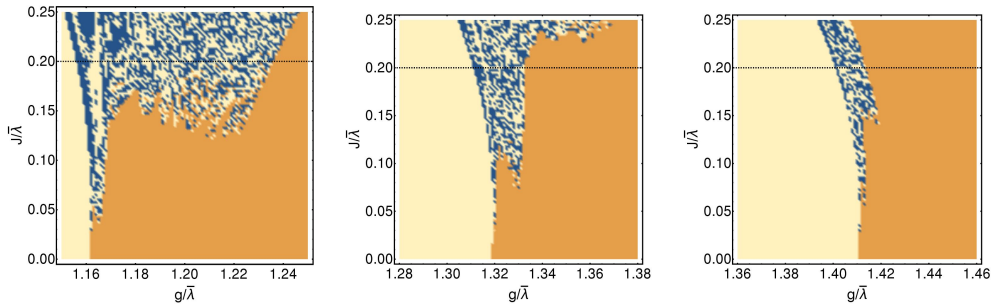

Figure 4.12: Dynamical phase diagrams for linear ramps [see Eq. (4.10)] of the transverse magnetic field for the model described by Eq. (3.1) starting from $g_0 = 0$ (fully polarized ferromagnetic state), in the plane of the dimensionless final magnetic field $g/\bar{\lambda}$ and short-range interaction strength $J/\bar{\lambda}$, analogous to Fig. 4.1. Here $N = 100$. The color of each point in the diagrams indicates the asymptotic sign of the time-averaged order parameter, with the same graphical conventions as in Fig. 4.1. The dimensionless duration $\bar{\lambda}\tau$ of the ramp is 0.7 (left), 1.00 (middle), 1.15 (right). As the driving becomes slower, the mean-field dynamical critical point for $J \to 0$ shifts from the sudden quench value $g_{dyn}/\lambda = 1$ towards that in the adiabatic limit, i.e., the equilibrium critical point $g_{cr}/\lambda = 2$ which is witnessed by the progressive shift rightwards along the horizontal axis of the border between the yellow and orange regions in the plot. Simultaneously, the chaotic dynamical ferromagnetic phase shrinks, due to the progressively smaller amount of nonequilibrium excitations produced by the increasingly slower ramp.

waves dissipates the energy of the classical spin, causing its trapping into either of the ferromagnetic wells. Accordingly, the smaller the amount of spin waves, the smaller the region of the parameter space within which the trapping phenomenon can occur. Consequently, we expect that the chaotic dynamical ferromagnetic phase C will shrink as τ increases.

This picture is confirmed by the numerical integration of the equations of motion, as one sees in Figs. 4.12 and 4.13. In particular, Fig. 4.12 shows how the dynamical phase diagram in Fig. 4.1 changes upon increasing, from left to right, the duration of the ramp τ in $g(t)$ which takes it from the initial value g_0 to the final value g. As expected, the chaotic region C in the parameter space shrinks with its two boundaries getting increasingly closer to each other, while region C as a whole moves towards the line at which the transition occurs in equilibrium, see Eq. (3.25).

In order to highlight this shift and the fate of the chaotic phase, the left panel of Fig. 4.13 shows a cut of the phase diagrams in Fig. 4.12 corresponding to a fixed value $J/\bar{\lambda} = 0.2$ along the horizontal axis, and how the corresponding phases as a function of $g/\bar{\lambda}$ change as $\bar{\lambda}\tau$ increases well beyond the values considered in Fig. 4.12. In order to assess the reliability of the spin wave approximation on which our analysis rely, the right panel of Fig. 4.13 shows with colorcode how fast the long-time averaged spin wave density $\epsilon(t)$ [see Eq. (3.35)] decreases upon increasing the ramp duration and as a function of $g/\bar{\lambda}$ for the same conditions as in the left panel.

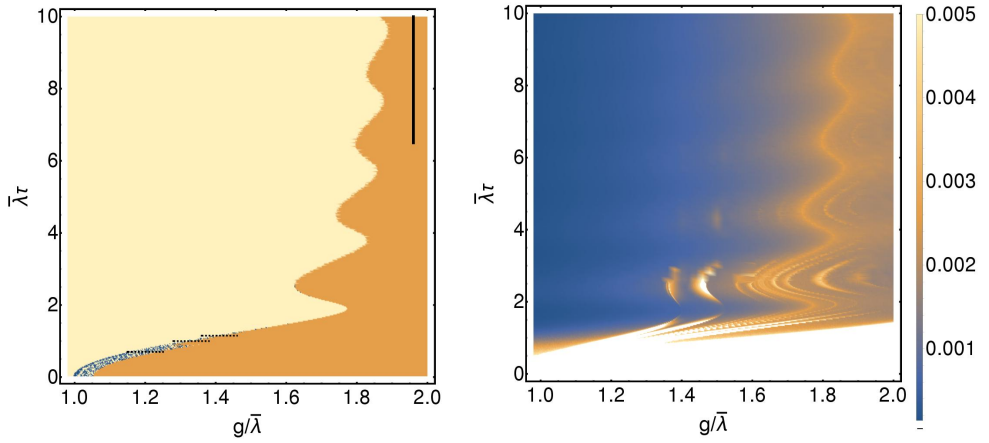

Figure 4.13: Left panel: Dynamical phase diagram for linear ramps of the magnetic field g of the same model as in Fig. 4.12, in the plane of the dimensionless final magnetic field $g/\bar{\lambda}$ and of the dimensionless ramp duration $\bar{\lambda}\tau$, but with fixed $J/\bar{\lambda} = 0.2$. The color of each point of the diagram is assigned as in Figs. 4.12 or 4.1, and the diagram corresponds to taking a horizontal cut of those in Fig. 4.12 at fixed $J/\bar{\lambda} = 0.2$ and varying τ continuously. As the ramp becomes slower, we notice two features: first, the two boundaries of the chaotic phase shift from the sudden quench position around $g_{dyn}/\bar{\lambda} = 1$ towards the equilibrium critical point $g_{cr}/\bar{\lambda} = 2 - (5/8)(J/\bar{\lambda})^2 + \mathcal{O}(J/\bar{\lambda})^3 \approx 1.975$ [see Eq. (3.25)] in the adiabatic limit, marked by the black vertical line. Second, the chaotic dynamical phase shrinks and practically disappears as τ is increased. Both these features are clearly visible in the picture. The "oscillatory" dependence of the phase boundary on τ is already present at the mean-field level. Right panel: long-time average of the density $\epsilon(t)$ of spin wave excitations generated in the nonequilibrium dynamics.

4.6 Finite-size effects: Schrödinger cats

In this last section, we discuss the relevance of the finite-size effects in the chaotic dynamical phase.

The first observation in order is that the spin-wave equations developed in Chap. 3 are rigorously valid only in the thermodynamic limit, where the collective spin can be treated as a classical degree of freedom, see Chap. 2. In infinite-range models, the spin-wave expansion of the Hamiltonian allows one to compute the finite-size modifications to the classical evolution equations due to the quantum fluctuations of the $k = 0$ mode in terms of $\Delta^{qq}_{k=0}$, $\Delta^{qp}_{k=0}$, $\Delta^{pp}_{k=0}$. These fluctuations are suppressed as N^{-1} [see also Chap. 6 below]. As discussed in Sec. 3, integrability-breaking perturbations with $\tilde{J}_{k\neq 0} \neq 0$ generate quantum feedback terms which involve all the spin waves modes with $k \neq 0$, expressed in Eq. (3.33) by terms of the form $\frac{1}{Ns}\sum_{k\neq 0}\tilde{J}_k\Delta^{qq}_k(t)$ and similar ones. In contrast to the feedback from the collective spin fluctuations, the latter terms have a finite limit as $N \to \infty$. For this reason, they have been properly taken into account in Chap. 3 and thereafter, while the feedback from the quantum fluctuations of the $k = 0$ mode has been neglected throughout.

In view of the above clarification, all the results based on the time-dependent spin-wave theory assume that the thermodynamic limit is taken at fixed time. The neglected finite-size effects typically set in at the (divergent) Ehrenfest time scale $T_{Ehr} \sim \mathcal{O}(\sqrt{N})$ discussed in Sec. 2.4. Accordingly, in Eqs. (3.33) and (3.37),

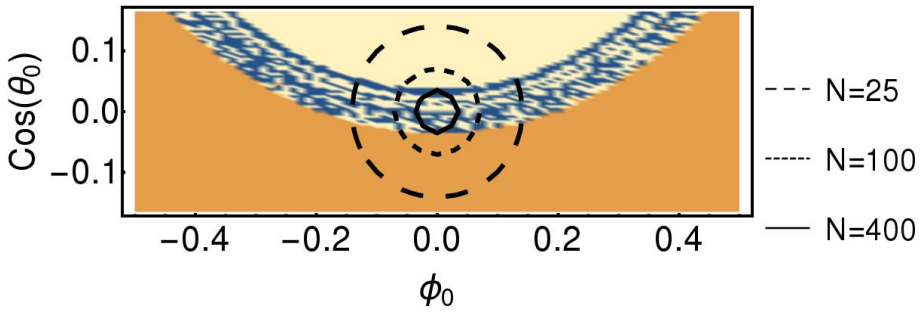

Figure 4.14: nonequilibrium phase diagram of the model (4.1) as a function of the polarization of the spin-coherent initial state on the Bloch sphere, parameterized by the canonically conjugated phase space coordinates ϕ_0 and $\cos\theta_0$ (cf. Sec. 3.3). Post-quench parameters $g/\bar{\lambda} = 1.03$, $J/\bar{\lambda} = 0.25$ are fixed. As in Fig. 4.1, this plot is obtained via numerically integrating the evolution equations of the time-dependent spin wave theory in the thermodynamic limit, with the same graphical conventions thereof. The lowest-order finite-size correction consists in replacing a classical, uncertainty-free initial condition, specified by a point $(\phi_0, \cos\theta_0)$, with a Gaussian distribution in phase space centered around it, with linear extension $\sqrt{\hbar_{\text{eff}}} = 1/\sqrt{Ns}$, which takes into account the quantum uncertainty at the lowest order in the semiclassical expansion, as discussed in Sec. 2.4. The circles superimposed to the diagram indicate the width of these Gaussian distributions centered around $(0,0)$ for various values of N, corresponding to quenches from a ground state of the pre-quench Hamiltonian with $g_0 = 0$ considered in all simulations reported in this Chapter. By considering this and analogous plots, the chaotic dynamical phase is expected to be blurred by quantum fluctuations for $N \lesssim 10^2$. This effect is more severe when N is in the range $\lesssim 16$ accessible to full exact diagonalization of the Hamiltonian (4.1), which makes it hard to observe signatures of the chaotic dynamical phase via this exact method. The latter is observed in MPS-TDVP simulations with N in the range $10^2 \div 10^3$ and stronger perturbation $J/\bar{\lambda} \approx 0.5$, as reported in Sec. 4.3, in correspondence of which the extension of the regions with a uniform sign of the asymptotic magnetization becomes sufficiently large compared to the coarse-graining scale $1/\sqrt{N}$.

as well as in their numerical integration, the parameter N plays the role of a discretization of the Brillouin zone integrals such as $\frac{1}{Ns}\sum_{k\neq 0}\tilde{J}_k\Delta_k^{qq}(t) \sim \int_{-\pi}^{\pi}\frac{dk}{2\pi s}\tilde{J}_k\Delta_k^{qq}(t)$, rather than properly accounting for actual finite-size effects.

The spin-wave analysis carried out in the previous sections predicts the occurrence of a chaotic dynamical phase in perturbed mean-field models in the thermodynamic limit $N \to \infty$, which corresponds to a transient paramagnetic evolution followed by localization of the collective spin within one of the two ferromagnetic wells. It is important to estimate how large N should be in practice for this phenomenon to occur. In order to do this, we resort both to semiclassical arguments (cf. Sec. 2.4) as well as to MPS-TDVP simulations (cf. Sec. 4.3).

As explained in Sec. 2.4, within the lowest-order semiclassical analysis or TWA [310], the quantum corrections to the classical motion amount to replacing the classical trajectory with the classical (Liouville) evolution of a Gaussian distribution in phase space centered around an initial condition θ_0, ϕ_0. The width of this distribution is given by the quantum uncertainty of the transverse components $\tilde{\sigma}^X_{k=0}/N$, $\tilde{\sigma}^Y_{k=0}/N$ of the rescaled collective spin. This is given by $\sqrt{\langle\tilde{q}_0^2\rangle}/\sqrt{Ns} = \sqrt{\Delta^{qq}_{k=0}}/\sqrt{Ns}$ and $\sqrt{\langle\tilde{p}_0^2\rangle}/\sqrt{Ns} = \sqrt{\Delta^{pp}_{k=0}}/\sqrt{Ns}$, respectively [see Eq. (3.7)], and hence are proportional to $1/\sqrt{N}$. The result of this approxima-

tion is visualized in Fig. 4.14, where the asymptotic magnetization is shown for quenches to $g/\bar{\lambda} = 1.03$, $J/\bar{\lambda} = 0.25$ as a function of the initial condition $(\phi_0, \cos\theta_0)$, with the same color conventions as in Fig. 4.1: The dynamical order parameter for a finite system of N spins corresponds to replacing the asymptotic magnetization of each point in this nonequilibrium phase diagram with its average over a Gaussian distribution centered at $(\phi_0 = 0, \cos\theta_0 = 0)$ with a width of order $1/\sqrt{N}$, pictorially represented by the circles in Fig. 4.14, corresponding to various values of N. This width can be viewed as a semiclassical phase space coarse-graining scale. In a finite system, within the chaotic dynamical phase, for small N, the distribution may encompass several initial conditions θ_0, ϕ_0 whose trajectories end up into distinct ferromagnetic sectors. This quantum superposition is expected to blur the critical region C in the diagram. Such blurring is dramatic for N of the order of tens, see Fig. 4.14. A classical-like behavior characterized by a nonvanishing average magnetization is expected to be visible only when the size of the initial wavepacket becomes smaller than the distance between the phase space boundaries of regions with a definite sign of the asymptotic magnetization, which happens for sufficiently large N. Estimates based on the spin wave approximation in Chap. 3 and in particular on the size of the largest spots of region C in Fig. 4.1 and in analogous diagrams for a range of parameters suggest that the *minimal* system size N required in order to observe localization of the wavepacket within a single sector should lie in the range $10^2 \div 10^3$. This agrees with the observed convergence of the MPS-TDVP simulations within this region upon raising the bond dimension, as shown in Sec. 4.3.

The above arguments suggest that the actual many-body wavefunction of a finite system is expected to realize after a transient a *quantum* superposition of two wavepackets localized in the two distinct ferromagnetic sectors, i.e., a so-called *cat state*. These cat states represent the remnant of the chaotic dynamical phase or small N. Their occurrence could in principle be detected by inspecting the evolution of the full statistics of the order parameter, rather than only of its the average. This study can actually be carried out via Exact numerical diagonalization of the Hamiltonian can be used to compute the time-evolving quantum distribution of the magnetization in systems of up to 16 spins. However, severe finite-size effects are predominant for such small sizes (cf. Fig. 2.11), which is understood within the semiclassical picture illustrated in Fig. 4.14. The order of magnitude $\mathcal{O}(1/\sqrt{N})$ of the phase-space uncertainty associated with a spin-coherent state is comparable with the global size $\mathcal{O}(1)$ of the whole Bloch sphere when $N = 16$. Hence, the evolution consists of a complicated superposition and interference of ferromagnetic, paramagnetic and "chaotic" classical trajectories. This prevents us from detecting clear signatures of the chaotic dynamical phase.

We remark that cat states violate the cluster decomposition principle, which is usually considered as a basic property of physical states, see the discussion in the Introduction. However, this needs not be the case when long-range interactions are present. This may be explicitly verified for the post-quench states in infinite-range models after the Ehrenfest time, whereby global observables acquire

extensive fluctuations, whereas the cluster decomposition principle would imply subextensive fluctuations.

It should be noted that by tuning continuously the parameters across one of the phase boundaries in Fig. 4.1, one should be able to observe cat states for arbitrarily large N: in fact, the evolution governed by a finite matrix has to depend smoothly on the parameters, and the time-evolved wavefunction cannot undergo "discontinuous" transitions at finite N, as is well-known from general theory. However, by the above semiclassical arguments, such cat states are expected to be confined within thin "layers" around the phase boundaries, whose width should shrink upon increasing N.

We conclude with two remarks on the crossover between quantum-mechanical behavior and its classical limit in the phenomena presented in this Chapter. First, we note that the scale $1/\sqrt{N}$, which is associated with the extension of the Wigner function of spin-coherent states, may be interpreted as the characteristic distance in phase space beyond which two spin-coherent states become effectively orthogonal in Hilbert space. In fact, two initial spin-coherent states whose polarization directions are separated by a smaller distance on the Bloch sphere, cannot localize in two distinct sectors after arbitrary times, because their overlap is nonvanishing and conserved by unitary quantum evolution. Accordingly, the "collective chaotic behavior" discussed in this Chapter can arise in quantum systems only when the phase space coarse-graining scale $1/\sqrt{N}$ provides a sufficiently fine resolution for resolving the different classical outcomes. There is no basic contradiction in the emergence of a classical-like chaos in a quantum system, as long as two nearby initial conditions, whose classical evolution undergoes exponentially fast separation, correspond to orthogonal initial vectors in Hilbert space. We have shown that this can occur in systems with competition of long- and short-range interactions driven close to a dynamical phase transition, provided the system size N is sufficiently large.

The second, related, remark is that, although the emergence of a classical-like collective chaotic behavior involves a subtle interplay between the thermodynamic limit and the time evolution, in practice a cat state and a classical sensitivity of the asymptotic magnetization with respect to the parameters of the system are essentially indistinguishable. In fact, in both cases, experimental measurements of the collective magnetization will result in a distribution characterized by two peaks, and understanding whether the origin of such a macroscopic superposition is quantum-coherent (as in a cat state) or classical-incoherent (as would result from unavoidable experimental errors) would actually be unfeasible, due to fast decoherence of the cat state (as for the original Schrödinger's cat!).

Chapter 5

Periodically driven dynamics: Quantum many-body Kapitza phases

The dynamically stabilized collective Kapitza phases discussed in Sec. 2.3 represent an interesting quantum realization of the classical Kapitza pendulum. In fact, as discussed in Sec. 2.1.2, the quantum dynamics of a spin system with all-to-all interactions reduce to the semiclassical dynamics of a single collective spin. With a suitable external driving, it is possible to stabilize configurations of the collective spin which have no counterpart in static conditions. This phenomenon is similar to the single-mode stabilization occurring in many instances of classical and quantum physics — see Sec. 1.1.4 in the Introduction.

However, it is a priori unclear whether such a Kapitza dynamical stabilization may occur in general quantum many-body systems. In fact, finite-range interactions give rise to fluctuations at all length scales. While dynamical stabilization of a collective degree of freedom is possible, the presence of extensively many fluctuating degrees of freedom may be expected to destabilize orderly structures. As discussed in the previous Chapter for quench dynamics, quantum fluctuations — unlike thermal ones — cannot be completely suppressed, and their effect may be dramatic.

In this Chapter, we show the existence of dynamically stabilized many-body Kapitza phases in a general class of quantum many-body systems in which fluctuations are not suppressed, and discuss their characteristics. This material has been published in Ref. [3].

5.1 Variable-range interactions

Although the results are general, we focus on experimentally relevant quantum Ising chains with algebraically-decaying interactions, described by the

Hamiltonian [cf. Eq. (1.18)]

$$\hat{H} = -\sum_{i\neq j}^{N} \frac{J}{|i-j|^{\alpha}} \hat{\sigma}_i^x \hat{\sigma}_j^x - g \sum_{i}^{N} \hat{\sigma}_i^z, \tag{5.1}$$

where σ's are Pauli matrices, $J > 0$ and $\alpha \leqslant 0$ controls the range of interactions. When $0 \leqslant \alpha < 1$, the rescaling $J \propto N^{\alpha-1}$ is necessary for a meaningful thermodynamic limit [324]. These systems accurately model the nonequilibrium dynamics of quantum simulators with trapped ions ($0 \leqslant \alpha \leqslant 3$) [101,185,187] or Rydberg atoms ($\alpha = 6$) [181,196], see Sec. 1.2.1 in the Introduction. For $\alpha \to 0$, Eq. (5.1) reduces to the driven infinite-range quantum Ising model discussed in Sec. 2.3.

As in Sec. 2.3, we shall consider a periodic modulation of the magnetic field,

$$g(t) = g_0 + \delta g \cos(\Omega t). \tag{5.2}$$

The phonomenology and theory of driven fully-connected systems have been discussed there. In this Chapter, we shall demonstrate that the dynamically stabilized phases discussed in Sec. 2.3, may persist over a parametrically large time scale in the general class of systems in Eq. (5.1) with $0 < \alpha \leqslant 2$, for which the many-body problem cannot be reduced to that of a single collective degree of freedom. These phases are actually more stable in higher-dimensional [187,196] and/or higher-spin [325] systems, where fluctuations are less effective.

As already discussed at length in Chapter 2, the collective behavior of infinite-range systems ($\alpha = 0$) can essentially be understood in terms of one-body physics. However, when interactions have a nontrivial spatial dependence ($\alpha > 0$), fluctuations at all length scales are activated. Although, their effect is parametrically reduced by decreasing α, the limit $\alpha \to 0$ might be singular due to integrability of the model, which protects the collective spin from exciting spin waves in the course of time-evolution (cf. discussion in Sec. 3.3).

When $\alpha > 0$, both the collective spin $\vec{\sigma}$, representing the $k = 0$ Fourier mode of the spin system, and all the spin excitations with $k \neq 0$, are affected by interactions. As discussed in Chap. 3, these excitations may be described as spin waves and their bound states. The nonequilibrium spin-wave theory presented in Chap. 3 can be used to study the coupled dynamics of the collective spin and of the spin waves dynamically generated on top of the reference time-dependent spin-coherent state aligned with $\vec{\sigma}(t) \equiv \langle \sum_i \hat{\sigma}_i \rangle / N$. As suggested in Sec. 3.3, this formalism offers an intuitive physical picture for the nonequilibrium dynamics. The system may be thought of as a macroscopic semiclassical spin $\vec{\sigma}(t)$, which "drags" an extensive set of quantum oscillators $(\tilde{q}_k, \tilde{p}_k)$'s, i.e., of microscopic degrees of freedom corresponding to the bosonic spin-wave excitations with quasimomentum $k \neq 0$.

We report below the expression of the variable-range Hamiltonian $\hat{H}(t)$ (5.1) in terms of the instantaneous configuration $\vec{\sigma}/|\vec{\sigma}| = (\sin\theta\cos\phi, \sin\theta\sin\phi, \cos\theta)$ of the collective spin, and of the spin-wave operators $\tilde{q}_k$'s, $\tilde{p}_k$'s to quadratic order. For simplicity, we consider periodic chains and correspondingly redefine

the distance in Eq. (5.1) as the minimal distance $||i-j||$ between two sites along a ring, i.e., $||r|| \to \mathrm{Min}\left(|r|, N-|r|\right)$. One has

$$\begin{aligned}\hat{H}(t) = -Ng(t)\left(1-\frac{\hat{n}_0+\hat{n}_{sw}}{N}\right)\cos\theta(t) \\ - N\tilde{J}_0\left[\left(1-\frac{\hat{n}_0+\hat{n}_{sw}}{N}\right)\sin\theta(t)\cos\phi(t)\right]^2 \\ - 4\sum_k \tilde{J}_k(\alpha)\Bigg(\cos^2\theta(t)\cos^2\phi(t)\ \frac{\tilde{q}_k\tilde{q}_{-k}}{2} + \sin^2\phi(t)\ \frac{\tilde{p}_k\tilde{p}_{-k}}{2} \\ - \cos\theta(t)\cos\phi(t)\sin\phi(t)\ \frac{\tilde{q}_k\tilde{p}_{-k}+\tilde{p}_k\tilde{q}_{-k}}{2}\Bigg),\end{aligned} \tag{5.3}$$

where the quasimomentum k runs over the set $\{2\pi n/N\}$ with $n = 0, 1, \ldots, N-1$, and $\tilde{J}_k(\alpha)$ is the Fourier transform of the interaction

$$\tilde{J}_k(\alpha) = \sum_{r=1}^{N-1} e^{-ikr}\frac{J}{|r|^\alpha} \equiv \tilde{J}_0\, f_{\alpha,k}. \tag{5.4}$$

The rescaling $J \sim N^{\alpha-1}$ for $\alpha < 1$ and $J \sim 1/\log N$ for $\alpha = 1$ (Kac normalization), anticipated below Eq. (5.1), is necessary to obtain a meaningful thermodynamic limit for $\alpha \leqslant 1$. We define it in such a way that the energy scale $\tilde{J}_0$ defined via Eq. (5.4) is finite and independent of α, and $f_{\alpha,k=0} \equiv 1$. The quantity $\hat{n}_0 = \left[(\tilde{q}_0)^2 + (\tilde{p}_0)^2 - 1\right]/2$ represents the number of collective spin excitations, and the total number of spin waves $\hat{n}_{sw} = \sum_{k\neq 0}\hat{n}_k = \sum_{k\neq 0}(\tilde{q}_k\tilde{q}_{-k} + \tilde{p}_k\tilde{p}_{-k} - 1)/2$ determines the depletion $\epsilon \equiv \langle \hat{n}_{sw}\rangle/(N/2)$ of the collective spin magnitude from its maximal value, i.e., $|\vec{\sigma}| = 1-\epsilon$. See Chap. 3 for more details.

The self-consistent evolution of the angles $\theta(t)$, $\phi(t)$ and of the spin waves can be straightforwardly adapted from Eqs. (3.33), (3.37), upon replacing $s = 1/2$, $\lambda = 0$ and $J_r = J/r^\alpha$. One finds

$$\begin{cases}\dfrac{d\theta}{dt} = 4\left[\tilde{J}_0(1-\epsilon(t)) - \delta^{pp}(t)\right]\sin\theta\cos\phi\sin\phi \\ \qquad\qquad + 4\,\delta^{qp}(t)\,\cos\theta\sin\theta\cos^2\phi, \\ \dfrac{d\phi}{dt} = -2g(t) + 4\left[\tilde{J}_0(1-\epsilon(t)) - \delta^{qq}(t)\right]\cos\theta\cos^2\phi \\ \qquad\qquad + 4\,\delta^{qp}(t)\,\sin\phi\cos\phi,\end{cases} \tag{5.5}$$

where $\delta^{\alpha\beta}(t) \equiv 2\sum_{k\neq 0}\tilde{J}_k(\alpha)\Delta_k^{\alpha\beta}/N$ with $\alpha, \beta \in \{p, q\}$ is the quantum "feedback" in terms of correlation functions of the spin waves, $\Delta_k^{qq}(t) = \langle\tilde{q}_k(t)\tilde{q}_{-k}(t)\rangle$ and analogously Δ_k^{qp}, Δ_k^{pp} [cf. Eqs. (3.34)]. The evolution of $\Delta_k^{\alpha\beta}$ is ruled by Eqs. (3.37) upon substituting $\bar{\lambda} \mapsto \tilde{J}_0$. The validity of the quadratic approximation is controlled by the density of spin waves and is discussed in Chap. 3.

It should be observed that the entire dependency on α is in the matrix element $\tilde{J}_k(\alpha) \equiv \tilde{J}_0\, f_{\alpha,k}$ associated with the excitation of a quasiparticle with momentum k. A thorough discussion of the behavior of the dimensionless $f_{\alpha,k}$

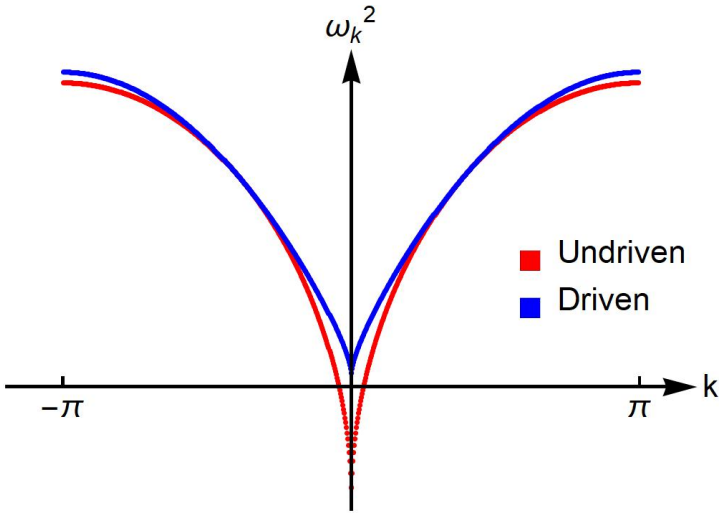

Figure 5.1: Stabilization of the *many-body* Kapitza phases. In the presence of a suitable periodic driving, the otherwise unstable spectrum of quantum excitations around the paramagnetic configuration gets simultaneously dynamically stabilized for all values of k. Here $\alpha = 1.5$, $N = 400$, and $g_0/\tilde{J}_0 = 1.35$. In the absence of the driving $\delta g = 0$, the system is in the ferromagnetic phase. The red points represent the (squared) frequency spectrum $\omega_k^2 = 4g_0(g_0 - 2\tilde{J}_k)$ of the spin-wave excitations, labeled by their wavevector k. An extended interval of long-wavelength modes are unstable (i.e., $\omega_k^2 < 0$ for k near 0). As the driving is turned on with a strength δg in a suitable range of values, not only the collective spin mode with $k = 0$ discussed in Sec. 2.3, but also the whole set of modes with $k \neq 0$ become *stable* (i.e., $\omega_k^2 > 0$ for all k). The blue points show the exact effective dispersion relation $\omega_k^2 = 4(B_0 - \tilde{J}_k)^2$ in the presence of a high-frequency driving $\Omega \to \infty$ with $\zeta = \delta g/\Omega = 0.6014$ (corresponding to $\gamma = 0$ in the effective Hamiltonian, see the text). When $\tilde{J}_0 \ll \Omega < \infty$, this effective dispersion relation receives perturbative corrections in inverse powers of Ω, and no qualitative changes occur as long as the system is in the prethermal regime (see Sec. 5.3 and references therein).

function on varying α and the system size N is presented in App. F.

5.2 Dynamically stabilized many-body phases

A many-body Kapitza phase consists of a simultaneous dynamical stabilization of the whole spectrum of quantum excitations around an unstable configuration. Intuition on this phenomenon can be obtained at the level of linear stability by expanding $\hat{H}(t)$ to quadratic order in the quantum fluctuations, as in Eq. (5.3), around the paramagnetic configuration with $\theta = 0$:

$$\hat{H}(t) = \mathcal{E}_{cl}(t) + 2\sum_k \left\{ \left[g(t) - 2\tilde{J}_k \right] \frac{\tilde{q}_k \tilde{q}_{-k}}{2} + g(t) \frac{\tilde{p}_k \tilde{p}_{-k}}{2} \right\}, \tag{5.6}$$

where $\mathcal{E}_{cl}(t) = -2Ng(t)$. In the absence of modulation in the ferromagnetic phase [i.e., $g(t) = g_0 < 2\tilde{J}_0$], an extended interval $[-k^*, k^*]$ around $k = 0$ in the spin-wave band is associated with unstable modes, as their corresponding frequency $\omega_k = 2[g_0(g_0 - 2\tilde{J}_k)]^{1/2}$ becomes imaginary for small enough k. However, upon introducing the modulation $g(t)$ as in Eq. (5.2) with $\delta g \neq 0$, the effective dispersion relation $\omega_{k,\mathrm{eff}}$ is modified. For a suitable choice of the

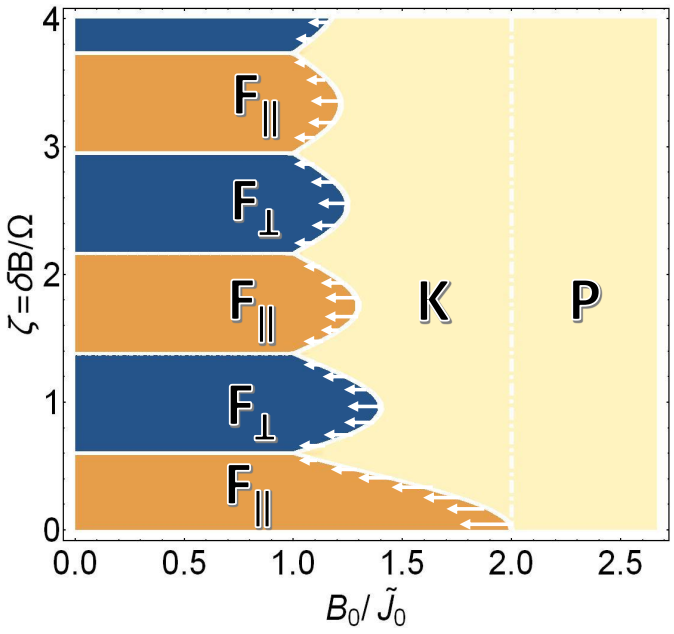

Figure 5.2: Fast-driving nonequilibrium phase diagram of the periodically driven long-range Ising chain defined by Eqs. (5.1) and (5.2), for $\alpha > 0$, from Ref. [3] (notation: $B \to g$). Compared to Fig. 2.8, the shaded region of coexistence of phase K with $F_{\|,\perp}$ has disappeared, and the left boundary of region K moves leftwards upon increasing α, as determined by Eq. (5.12) and indicated by the white arrows. This displacement is vanishingly small in the thermodynamic limit for $0 < \alpha \leqslant 1$, and finite for $\alpha > 1$. The amount indicated by the arrows corresponds to Eq. (5.12) with $\alpha = 1.5$ (it is magnified by a factor 2 for ease of visualization).

driving parameters, the frequencies ω_k may become real for all values of k. The occurrence of this nontrivial stabilization of an otherwise unstable phase of matter against all possible fluctuations of its degrees of freedom is illustrated in Fig. 5.1 and it represents a generalization of the Kapitza pendulum to a genuine many-body system.

In order to understand how all the degrees of freedom can get dynamically and simultaneously stabilized by driving a single modulated global field $g(t)$, we consider on the fast-driving limit $\Omega \to \infty$ as a function of the rescaled driving amplitude ζ, which can be studied analytically also for $\alpha \neq 0$. As discussed in Sec. 1.1.4 the Introduction, for a parametrically long time in the driving frequency Ω — a regime referred to as Floquet-prethermal in the literature, see Sec. 5.3 below — the stroboscopic evolution of the system at times $t_n = 2\pi n/\Omega$ with $n = 0, 1, 2, \ldots$ is governed by an effective static Hamiltonian $\hat{H}_{\text{eff}}$ obtained via a high-frequency expansion (see App. C). The computation of $\hat{H}_{\text{eff}}$ has been discussed in Sec. 2.3 for the infinite-range limit, and is independent of the particular dependence of the interactions on the distance. Consequently, it can be implemented using exactly the same steps. One obtains an effective long-range XY spin chain,

$$\hat{H}_{\text{eff}} = -\sum_{i\neq j}^{N} \frac{J}{\|i-j\|^{\alpha}} \left[\frac{1+\gamma(\zeta)}{2} \hat{\sigma}_i^x \hat{\sigma}_j^x + \frac{1-\gamma(\zeta)}{2} \hat{\sigma}_i^y \hat{\sigma}_j^y \right] - g_0 \sum_{i}^{N} \hat{\sigma}_i^z, \tag{5.7}$$

where the anisotropy parameter $\gamma(\zeta) = \mathcal{J}_0(4\zeta)$ is the same as in Eq. (2.37) and is plotted in Fig. 2.7.

Equation (5.7) allows us to discuss the modification of the nonequilibrium phase diagram in Fig. 2.8 for $\alpha > 0$ and large $\Omega/\tilde{J}_0 \to \infty$. The driven dynamics at stroboscopic times is equivalent to the *quench* dynamics governed by the effective Hamiltonian $\hat{H}_{\rm eff}$. For $\alpha = 0$, the effective Hamiltonian is integrable, and the dynamics consist of a semiclassical precession of the collective spin on the Bloch sphere, governed by the classical limit of $\hat{H}_{\rm eff}$ in Eq. (2.37). For $\alpha > 0$, the mean-field integrability is broken. As discussed in the Introduction, the thermalization properties of long-range interacting quantum systems have not yet been established in full generality. Two alternative scenarios may occur: *i*) transient integrable-like behavior, characterized by a long-lived precession of the collective spin or *ii*) quick stroboscopic prethermalization to a Gibbs state $e^{-\beta \hat{H}_{\rm eff}}/Z$ of the effective Hamiltonian. As shown below, the nonequilibrium spin-wave theory suggests the first occurrence for small α. However, in both possible scenarios, dynamically stabilized many-body ordered phases exist as long as $\hat{H}_{\rm eff}$ supports long-range order at finite energy density above the ground state. In this case, initializing the system in a state with a well-defined average polarization close to that characterizing an equilibrium state of $\hat{H}_{\rm eff}$, its stroboscopic polarization will be stable in the course of time-evolution.

As we discussed in Sec. 1.3 in the Introduction, it is known that long-range order at finite energy density in one-dimensional systems can be stabilized by long-range interactions with an exponent $\alpha \leqslant 2$ [272–274]. In this regime, one should expect the emergence of dynamically stabilized nonequilibrium ordering in quantum many-body systems. In the case under consideration, for small static field g_0, the character of the dynamical magnetic ordering of the system depends on driving amplitude ζ : When the effective anisotropy parameter $\gamma(\zeta)$ is negative, there appear dynamically stabilized unconventional ferromagnetic phases with magnetization in the yz-plane orthogonal to the direction of actual ferromagnetic interactions, which have no equilibrium counterpart in the Ising model.

Upon increasing α up to the value 2, quantum fluctuations modify the phase boundaries in the nonequilibrium phase diagram in Fig. 2.8. as shown in Fig. 5.2. The modification of the boundaries shown by the white arrows is determined in the following way. The left boundary of region K is given by the critical value $g_0 = g_{\rm cr}(\zeta)$ below which the high-frequency effective Hamiltonian (5.7) develops ferromagnetic ordering, either in the xz- or in the yz-plane depending on the anisotropy $\gamma(\zeta)$ being positive or negative, respectively. The sudden buildup of ordering in $\hat{H}_{\rm eff}$ is signalled by the occurrence that tilted spin configurations, with average orientation forming an angle $\theta \neq 0$ with the field direction z, acquire a lower energy $\langle \hat{H}_{\rm eff} \rangle$ than the paramagnetic states with $\theta = 0$. In the infinite-range case $\alpha = 0$, the critical line is $g_{\rm cr}(\zeta) = \tilde{J}_0 \left[1 + |\gamma(\zeta)|\right]$, in correspondence of which the energy landscape $\mathcal{E}_{\rm eff}(\theta) \equiv \langle H_{\rm eff} \rangle_{\theta,\phi^*}$ (with $\phi^* = 0$ or $\pi/2$ depending on $\gamma(\zeta) > 0$ or < 0, respectively) of the semiclassical collective spin $\vec{\sigma} = (\sin\theta\cos\phi, \sin\theta\sin\phi, \cos\theta)$ changes from a single well

for $B_0 > B_{cr}(\zeta)$, with a minimum at $\theta^* = 0$, to a symmetric double well for $B_0 < B_{cr}(\zeta)$, with two minima at $\theta^* = \pm\arccos(B_0/B_{cr}(\zeta))$. For $\alpha \neq 0$, the quantum fluctuations of all the spin degrees of freedom with Fourier wavevector $k \neq 0$ modify the effective energy landscape $\mathcal{E}_{\rm eff}(\theta)$ of the collective spin, thereby shifting the critical value of g_0 to $g_{cr}(\zeta) \equiv \tilde{J}_0\left[1+|\gamma(\zeta)|\right] + \Delta g_{cr}(\zeta)$. This effect is similar to that discussed in Sec. 3.1, and can be quantified by adapting the variational calculation therein to compute the shift $\Delta g_{cr}(\zeta)$ to lowest order in $\tilde{J}_{k\neq 0}$. In particular, one considers the expansion of $\hat{H}_{\rm eff}$ to quadratic order in the spin-wave operators around the direction in the xz- or yz-plane identified by the angle θ, resulting in Eq. (5.3) with $\phi = 0$ or $\pi/2$ respectively. Hence, one determines the energy landscape $\mathcal{E}_{\rm eff}(\theta) \equiv \min_\psi \langle \hat{H}_{\rm eff}\rangle_\psi$ by computing the spin-wave ground state energy, parametrically in θ. The result is

$$\frac{\mathcal{E}_{\rm eff}(\theta)}{N} = -\tilde{J}_0\frac{1+|\gamma|}{2}\sin^2\theta - B_0\cos\theta + \int_{-\pi}^{\pi}\frac{dk}{\pi}\,\frac{\omega_k - \omega_k^{(0)}}{2}, \tag{5.8}$$

where

$$\begin{aligned}\omega_k^2 =& 4\Big[\tilde{J}_0(1+|\gamma|)\sin^2\theta - \tilde{J}_k(1+|\gamma|)\cos^2\theta + B_0\cos\theta\Big] \\ &\times\Big[\tilde{J}_0(1+|\gamma|)\sin^2\theta - \tilde{J}_k(1-|\gamma|) + B_0\cos\theta\Big]\end{aligned} \tag{5.9}$$

and

$$\omega_k^{(0)} = 2\Big[\tilde{J}_0(1+|\gamma|)\sin^2\theta + B_0\cos\theta\Big] = \omega_k\Big|_{\tilde{J}_{k\neq 0}=0}. \tag{5.10}$$

The last term in Eq. (5.8) represents the zero-point contribution of quantum fluctuations. The energy landscape $\mathcal{E}_{\rm eff}(\theta)$ in Eq. (5.8) can be expanded at small θ as

$$\mathcal{E}_{\rm eff}(\theta) = \mathcal{E}_{\rm eff}(\theta=0) + r(g_0)\,\frac{\theta^2}{2} + \mathcal{O}(\theta^4), \tag{5.11}$$

and the critical value g_{cr} of g_0 is determined by the equation $r(g_0) = 0$, corresponding to the transition from a single- [$r(g_0) > 0$] to a double- [$r(g_0) < 0$] well landscape. The solution may be found by formally expanding g_0 in powers of $\tilde{J}_{k\neq 0}$ and equating both sides order by order. This procedure leads to the negative quadratic correction

$$g_{cr}(\zeta) \simeq \tilde{J}_0\,\left(1+|\gamma(\zeta)|\right)\,\left[1 - \kappa(\zeta)\int_{-\pi}^{\pi}\frac{dk}{\pi}\,\left(f_{\alpha,k}\right)^2\right], \tag{5.12}$$

with $\kappa(\zeta) \equiv [2\gamma(\zeta) + 3\gamma^2(\zeta)]/\{4[1+\gamma(\zeta)]^2\}$. As in Eq. (3.25), one sees that the quantum fluctuations tend to destabilize ferromagnetic ordering, as expected on physical grounds. Note that the shift Δg_{cr} of the critical value is maximal for $\gamma = 1$ and vanishes at isotropic points with $\gamma = 0$.

The leftwards shift of the phase boundary $g_0 = g_{cr}(\zeta)$ of region K, expressed by $\Delta g_{cr}(\zeta)$ in Eq. (5.12), depends on α via the integral of $(f_{\alpha,k})^2$. The behavior of the function $f_{\alpha,k}$ upon varying α and N is discussed in App. F and summarized in Fig. F.1 therein. In particular, one has $f_{\alpha,k\neq 0} \to 0$ when $0 < \alpha \leqslant 1$. In

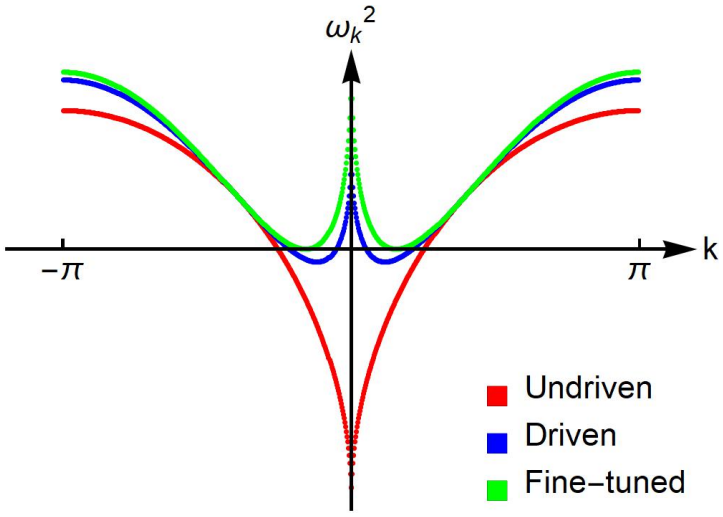

Figure 5.3: Effective spectrum of the quantum spin-wave excitations around the unstable paramagnetic configuration for $\alpha = 1.5$, $g_0/\tilde{J}_0 = 0.35$, in the presence of a high-frequency drive with $\delta g/\Omega = 0$ (red), 0.4023 (blue) and 0.6014 (green), corresponding to effective anisotropy parameters $\gamma = 1$, 0.45, and 0, respectively, in the effective Hamiltonian $\hat{H}_{\rm eff}$ in Eq. (5.7). The blue and green points correspond to parameters within the shaded region in Fig. 2.8, in which coexistence of Kapitza and ferromagnetic phases occurs in the infinite-range model. Although the collective $k = 0$ mode is dynamically stabilized, for $\alpha > 0$ an extended interval in the Brillouin zone appears with modes characterized by imaginary frequencies $\omega_k^2 < 0$, as shown, e.g., by the blue points. As shown by the green points, this instability disappears only at isolated points $\zeta_1, \zeta_2, \ldots$ for which $\gamma = 0$ [corresponding to the zeros of the Bessel function, see after Eq. (2.37)], i.e., characterized by an emergent $O(2)$ rotational symmetry.

this case, equilibrium fluctuations are suppressed as $N \to \infty$, and the system becomes equivalent to its mean-field limit. On the other hand, $f_{\alpha,k\neq 0}$ is finite for $1 < \alpha \leqslant 2$, with a cusp behavior $f_{\alpha,k} \sim 1 - c(\alpha)|k|^{\alpha-1}$ for small wavenumbers k. Therefore, the modification of the phase boundary in Fig. 2.8 due to quantum fluctuations is vanishingly small in the thermodynamic limit when $0 < \alpha \leqslant 1$ and is finite as $\alpha > 1$. It can be shown by an explicit calculation that

$$\Delta g_{\rm cr}(\zeta) \underset{\alpha \searrow 1}{\sim} -\bar{\kappa}(\zeta)\,(\alpha-1)^2 + \mathcal{O}\Big((\alpha-1)^3\Big) \tag{5.13}$$

with $\bar{\kappa}(\zeta) \propto \kappa(\zeta)$.

Quantum fluctuations have a further, dramatic effect of the nonequilibrium phase diagram. In fact, the second Kapitza phase which coexists with the ferromagnetic phases at mean-field level, indicated by the shaded region in Fig. 2.8, turns out to be unstable to many-body fluctuations at finite wavelength. Although the driving can stabilize the collective spin, there appears an extended interval of unstable spin modes in the Brillouin zone with finite wavelength $k \neq 0$, which are expected to prevent dynamical stabilization. In fact, within a linear stability analysis, the effective spectrum of excitations is given by

$$\omega_k^2 = 4\big\{B_0 - [1-\gamma(\zeta)]\,\tilde{J}_k\big\}\big\{B_0 - [1+\gamma(\zeta)]\,\tilde{J}_k\big\}, \tag{5.14}$$

as obtained by expanding Eq. (5.7) in spin-wave operators around the para-

magnetic configuration $\theta = 0$. The effective dispersion relation features a finite interval in the Brillouin zone characterized by with imaginary frequencies within the range of parameter values $B_0 < \tilde{J}_0 \left[1 - |\gamma(\zeta)|\right]$ under consideration, see Fig. 5.3. The amplitude of this interval shrinks to zero when the anisotropy $\gamma = \mathcal{J}_0(4\zeta)$ approaches 0, i.e., when the driving strength ζ equals one of the zeros ζ_n with $n = 1, 2, \ldots$ of the Bessel function. Away from this discrete set of values, the Kapitza phase coexisting with the ferromagnetic phases turns out to be destabilized by these finite-wavelength fluctuations, at least at the level of linear stability, in spite of the stabilization of the collective $k = 0$ mode.

We remark that when ζ is tuned to an isotropic point ζ_n, the many-body Kapitza phase discussed above becomes stable in the high-frequency limit $\Omega \to \infty$, and thus approximately stable for $\Omega \gg \tilde{J}_0$. The reason behind such stability may be easily traced back to the stroboscopic conservation of the collective spin projection σ^z along the field direction, due to the emergent $O(2)$ rotational symmetry. Indeed, if the system is initialized in a fully polarized state with a small displacement θ_0 away from the z-axis, the collective spin has to remain trapped in a neighborhood of the fully polarized configuration $\theta = 0$, because $\sigma^z(t_n) \approx 1 - \theta_0^2/2$ cannot decrease.

Let us finally comment on what happens for $\alpha > 2$. It is convenient to discuss first the limit $\alpha = \infty$, in which the system (5.1) reduces to the standard quantum Ising chain with nearest-neighbor interactions (which has been studied in Refs. [134–136]). In this case, the effective high-frequency Hamiltonian (5.7) describes the XY quantum spin chain, which is exactly solvable in terms of free fermions [41]. From the exact solution, we see that the quantum critical point $B_{cr} = \tilde{J}_0$ is independent of γ, and thus of the driving strength ζ. Accordingly, it is natural to conjecture that the left boundary of the Kapitza phase moves leftwards as α exceeds 1, as shown in Fig. 5.2, and eventually approaches the straight vertical line $g_{cr}(\zeta) = \tilde{J}_0$ when $\alpha \to \infty$.

However, ferromagnetic ordering in not stable at finite energy density for $\alpha > 2$. In the nonequilibrium dynamics starting from a polarized state, domain-wall excitations melt the original magnetic ordering if $\hat{H}_{eff}$ generates a fast thermalization. In this case the equilibrium (ground-state) phase diagram [135, 136] of the effective Hamiltonian does *not* allow an interpretation in terms of dynamically stabilized many-body Kapitza phases.

However, it should be noted that studies of quench dynamics in long-range interacting chains with $\alpha > 2$ have suggested that magnetic ordering surprisingly survives for long times in a prethermal regime [93, 106, 267, 326]. In such a prethermal regime, signatures of dynamically stabilized Kapitza phases are expected to emerge. We shall further discuss this from a different viewpoint in Sec. 7.3 in Part II of the thesis.

5.3 Prethermalization and heating

We address the footprint of the fast-driving nonequilibrium phase diagram on the finite-frequency dynamics, upon reducing Ω down to a scale comparable

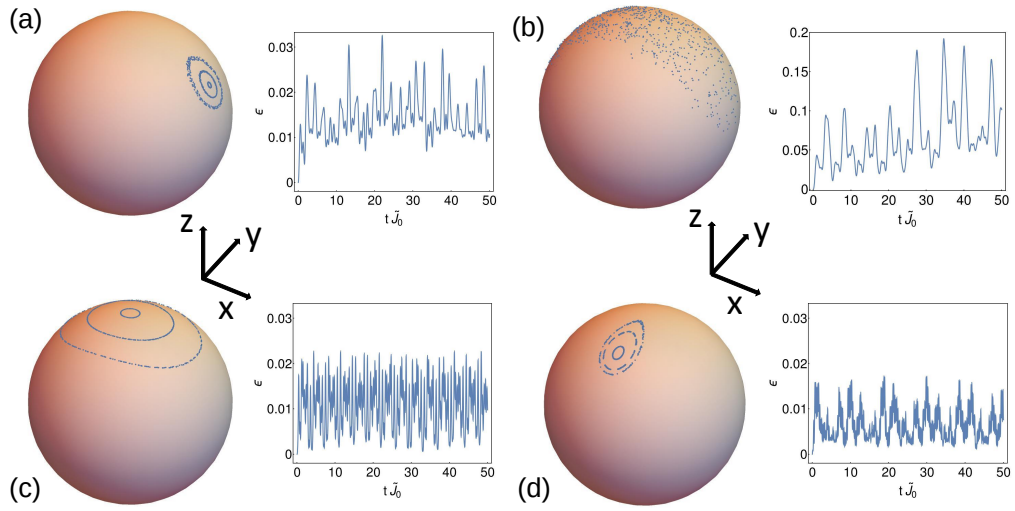

Figure 5.4: Persistence of the dynamically stabilized phases at finite driving frequency. Left in each panel: Stroboscopic time-evolution $\vec{\sigma}(t_n)$ of the collective spin of the long-range Ising chains in Eq. (5.1) with $\alpha \neq 0$, subject to the modulated magnetic field in Eq. (5.2). $\vec{\sigma}(t_n)$ is obtained by nonequilibrium spin-wave theory and, for simplicity of visualization, is projected onto the unit sphere. In all simulations, the static field is $g_0/\tilde{J}_0 = 1.2$, as in Fig. 2.6, the driving frequency is $\Omega/\tilde{J}_0 = 8$, and we used $N = 100$. The system is initialized in fully polarized states in the xz [panels (a), (b), (c)] and yz [panel (d)] planes. Right in each panel: relative departure $\epsilon(t)$ of the total spin from its maximal length $N/2$ [i.e., $\vec{\sigma}(t) = 1 - \epsilon(t)$], due to the dynamical generation of quantum spin-wave excitations, corresponding to the largest trajectory in each panel. In particular: (a) Dynamical ferromagnetic phase, with $\alpha = 1$ and $\delta g/\tilde{J}_0 = 0.05$. (b) Fast heating in the chaotic dynamical regime, with $\alpha = 0.8$, $\delta g/\tilde{J}_0 = 0.2$. (c) Dynamically stabilized Kapitza phase, with $\alpha = 1$, $\delta g/\tilde{J}_0 = 5.33$. (d) Dynamically stabilized ferromagnetic phase with magnetization in the yz-plane orthogonal to the direction x of the actual ferromagnetic interactions, with $\alpha = 1$, $\delta g/\tilde{J}_0 = 8$. Panels (a), (c), and (d) demonstrate that the dynamical phases $F_{\|}$, K, $F_{\perp}$ (see Fig. 2.8), respectively, continue to exist at finite driving frequency. The amount of excitations generated remains small and the total energy remains bounded across many cycles, qualifying these phases as *prethermal*. In panel (b), instead, heating is witnessed by the growth of $\epsilon(t)$ (notice the different vertical scale in the plot). The heating rate in this case increases upon increasing α.

with the single-particle energy scale $\tilde{J}_0$ of the system. In this case, one should expect the system to eventually absorb an ever-increasing amount of energy from the drive [137]. In order to address this point, we initialize the system in various fully polarized states parameterized by angles (θ_0, ϕ_0) on the Bloch sphere, and study the driven evolution for various values of $\alpha > 0$ and driving parameters $g_0, \delta g, \Omega$ by numerically integrating the dynamical equations of the time-dependent spin wave theory. In this formalism, the heating rate can be monitored through the depletion of the collective spin's magnitude from its maximal value. In fact, heating to infinite-temperature must be accompanied by a deterioration of magnetic ordering.

The results are illustrated in Fig. 5.4. Whenever the system is initialized in a stable or dynamically stabilized regime P/K or $F_{\|,\perp}$, and the frequency Ω is off-resonant with the spin-wave band, i.e., $\Omega \gg 4\tilde{J}_0$, as shown in Fig. 5.4(a),(c),(d) the evolution presents a long time interval during which the absorption of energy from the drive, as well as the amount of spin-wave excitations, is bounded. On the other hand, whenever the system is initialized in a chaotic dynamical

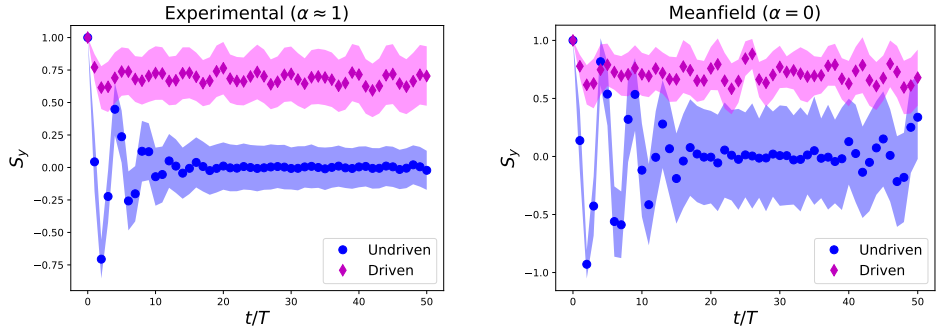

Figure 5.5: Illustration of the dynamical stabilization of the unconventional ferromagnetic phase $F_\perp$ in a realistic trapped-ion setup (left panel) and in the corresponding infinite-range system (right panel), from Ref. [3] (notation: $S_y \to \sigma^y$). The orthogonal magnetization $\sigma^y(t_n) \pm \Delta\sigma^y(t_n)$ (see the text) is plotted at stroboscopic times $t_n = nT$, with $T = 2\pi/\Omega$ and $n = 0, 1, 2, \ldots$, for undriven and driven systems of $N = 16$ spins, governed by the Hamiltonian in Eq. (1.18) with the actual space-dependent couplings J_{ij} which characterize a chain of trapped ions experimentally studied in Ref. [101], roughly described by Eq. (5.1) with $\alpha \approx 1$ and (5.2) (left panel). The system is initialized in a fully polarized state in the y-direction, and the driving parameters are $g_0/\tilde{J}_0 = 0.5$, $\zeta = 1$, and $\Omega/\tilde{J}_0 = 8$, corresponding to a point well inside a region $F_\perp$ in Fig. 5.2. For comparison, the corresponding simulation with J_{ij} replaced by all-to-all uniform interactions of equal average strength is shown in the right panel. Ferromagnetic ordering in the yz-plane is dynamically stabilized by the drive, and is found to be robust to finite driving frequency, finite-size effects and "imperfections" in the long-range couplings, realizing a prethermal quantum many-body Kapitza phase observable with trapped-ion quantum simulators.

regime as in Fig. 5.4(b), irrespective of the value of Ω and of α, the density $\epsilon(t)$ of dynamically generated spin-wave excitations increases at a finite rate, as well as the energy $\langle \hat{H}(t) \rangle$. This is a witness of heating, which has been extensively shown to be the generic response of a many-body system to an external periodic driving, in the absence of dissipative mechanisms [327]. In the dynamical regimes $F_{\parallel,\perp}$ of panels (a) and (d), the synchronized trajectories of the collective spin $\vec{\sigma}(t)$ act as an "internal" periodic driving at frequency Ω on the quantum oscillators $(\tilde{q}_k, \tilde{p}_k)$'s through the last interaction terms in the spin-wave Hamiltonian (5.3). As long as Ω is off-resonant (see above), the spin waves behave like a periodically driven system of quasifree particles, which relaxes to a periodic quasistationary state described by a stroboscopic generalized Gibbs ensemble [134, 328]. The presence of nonlinear spin-wave interactions cause the latter *prethermal* stage [138, 329–333, 333] to be ultimately followed by slow heating, after a parametrically long time τ which is expected to scale as $\tau \sim \exp(\text{const} \times \Omega/\tilde{J}_0)$ [139–142].

5.4 Quantum simulations with trapped ions

We finally address the robustness of the dynamically stabilized nonequilibrium phases to finite-size effects as well as their observability in the setup of quantum simulations with trapped ions. In particular, we computed the nonequilibrium evolution of small driven systems of $N = 16$ spins by numerically integrating the time-dependent many-body Schrödinger equation, and

demonstrate the occurrence of quantum many-body Kapitza phases for the long-range interacting chains in Eq. (5.1) as well as with the space-dependent spin-spin couplings J_{ij} which characterize a chain of trapped ions experimentally investigated in Ref. [101], roughly corresponding to model (5.1) with $\alpha \approx 1$ (cf. the discussion in Sec. 1.2.1 of the Introduction).

In Fig. 5.5 we report an illustration of the stabilization of the *ordered* phase $F_\perp$, which is of greater experimental relevance as it presents a type of magnetic ordering that is absent in the equilibrium phase diagram. In order to probe its occurrence, the driving parameters in Eq. (5.2) are chosen well inside the region $F_\perp$ of the nonequilibrium phase diagram in Fig. 5.2, and the system is initialized in a fully polarized state along the y-direction. In the top panel, the stroboscopic time-evolution of the orthogonal magnetization

$$\sigma^y(t_n) \equiv \frac{1}{N}\left\langle \sum_{i=1}^{N} \hat{\sigma}_i^y(t_n) \right\rangle, \tag{5.15}$$

with $t_n = nT$, $T = 2\pi/\Omega$ and $n = 0, 1, 2, \ldots$, is shown for the simulated trapped-ion system subject to the drive (magenta) as well as in the limit of vanishing driving strength (blue). In both cases, the shaded region around the symbols indicates the instantaneous quantum uncertainty of the magnetization

$$\Delta\sigma^y(t) \equiv \sqrt{\frac{1}{N}\left\langle \left\{ \sum_{i=1}^{N} \left[\hat{\sigma}_i^y(t_n) - \sigma^y(t_n)\right] \right\}^2 \right\rangle}. \tag{5.16}$$

As the plot clearly shows, the drive stabilizes a magnetic ordering that is not possible in static conditions, in agreement with the theory presented in this Chapter. We remark that the preparation of tilted fully polarized states, the implementation of the considered driving protocols and the measurements of the tilted magnetization can be achieved with standard experimental techniques, which makes it possible to actually observe this phenomenon with trapped ions.

In order to disentangle the finite-frequency and finite-size effects from the effects of having experimentally realistic interactions, we report in the bottom panel of Fig. 5.5 the outcome of analogous simulations in which the trapped-ion couplings have been replaced with uniform collective interactions $J_{ij} \equiv \tilde{J}_0/(N-1)$ with the same average strength. The qualitative appearance of the two plots is similar, in agreement with our theory. However, we observe that the strong many-body quantum fluctuations affecting data in the top panel have a visible effect in the transient relaxation dynamics: in fact, while the *single-body* collective spin oscillations in the bottom panel become increasingly long-lived in larger systems as the classical limit is approached, the *many-body* spatially-decaying interactions in the top panel cause damping and, correspondingly, are expected to lead to a Gibbs-type Floquet prethermal state in terms of the approximate high-frequency Floquet Hamiltonian [given by Eq. (5.7) with the couplings $J/|i-j|^\alpha$ replaced by the experimental ones J_{ij}] [138–142].

Chapter 6

Theory of entanglement dynamics

The phenomena discussed in the previous Chapters mainly concerned the nonequilibrium dynamics of single-body observables, such as the collective spin polarization. In the present one, we focus instead on the evolution of intrinsically many-body quantities, such as quantum correlations and entanglement between subsystems.

As briefly mentioned in the Introduction, translation-invariant extended quantum systems with short-range interactions are generically expected to exhibit a linear temporal growth after a quantum quench of the entanglement entropy associated with a spatial bipartition. On the other hand, long-range interacting systems pose a conceptually different and challenging problem. Despite their nonlocal interactions allow quantum correlations between distant degrees of freedom to build up very quickly [277–285], several numerical simulations have shown that entanglement growth after a quench features a dramatic counterintuitive slowdown as the range of interactions is increased. In particular, it may become as slow as logarithmic when the couplings decay algebraically with an exponent α smaller than the spatial dimensionality d [286–288].

Below, we discuss the origin of the qualitative change in the mechanism which governs the growth of entanglement in quantum spin systems as the interaction range is increased across the threshold $\alpha = d$. By using the nonequilibrium spin-wave theory presented in Chap. 3, we show that the standard quasiparticle contribution to the von Neumann entanglement entropy $S(t)$ is suppressed for $\alpha \leqslant d$ in a prethermal regime. The growth of $S(t)$ is determined by collective spin excitations, directly related to *spin squeezing* [334–340], as schematically illustrated in Fig. 6.1. In particular, the dynamical rate of spin squeezing after a quench generically leads to a universal logarithmic growth in time $S(t) \sim \log t$ as reported in previous numerical studies. Exceptions are represented by dynamical critical points, such as those discussed in Sec. 2.2, which are characterized by fast entanglement growth $S(t) \sim \lambda t$. In this case, the rate λ is given by the exponential divergence rate λ_{Lyap} of the underlying semiclassical trajectories, i.e., the Lyapunov exponent.

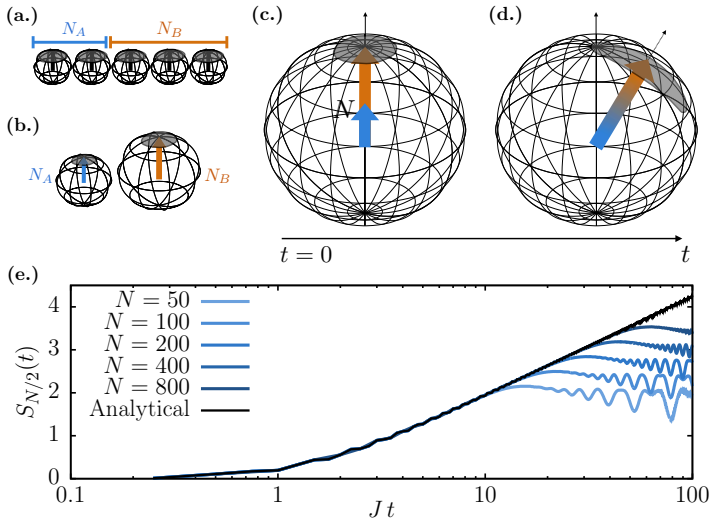

Figure 6.1: Entanglement dynamics and collective spin squeezing in long-range interacting quantum spin systems. (a) The system is partitioned into two blocks of N_A and N_B spins-1/2, initially fully polarized. (b) Collective spins of the two blocks on spheres of radii $N_A/2$ and $N_B/2$. The shaded area represents the quantum uncertainty of transverse components, of relative width $1/\sqrt{N_{A,B}}$ respectively. (c) Collective spin in the factorized initial state, represented on a sphere of radius $N/2$. (d) Nonlinear interactions give rise to dynamical spin squeezing, which makes the two blocks increasingly correlated (entangled). The slow rate of squeezing after noncritical quenches determines the slow growth of entanglement. (e) The general analytical formula derived in this work captures the growth of entanglement entropy until saturation in generic quantum spin systems with slowly-decaying interactions (here, quantum quench from the ferromagnetic to the paramagnetic phase of in a fully-connected quantum Ising model).

The content of this Chapter is constituted by original results published in Ref. [4].

6.1 Entanglement entropy in infinite-range spin systems

In order to isolate the contribution of collective spin fluctuations to entanglement growth in the cleanest way, it is convenient to start by analyzing infinite-range spin systems. In this Section, we shall revisit the two-boson formalism developed in Refs. [341, 342] (see also Ref. [343]) to understand entanglement entropy in collective models in equilibrium. We refer to the general fully-connected spin models introduced in Eq. (2.13) and discussed in Sec. 2.1.2, reported here

$$\hat{H} = -\sum_{p=1,2,\dots} \left\{ \sum_{\mu_1,\dots,\mu_p = x,y,z} \frac{J_{\mu_1\dots\mu_p}}{N^{p-1}} \sum_{j_1 \neq \dots \neq j_p}^{N} \hat{s}_{j_1}^{\mu_1} \dots \hat{s}_{j_p}^{\mu_p} \right\} \tag{6.1}$$

As discussed therein, in the presence of infinite-range interactions, the behavior of local spin observables is exactly captured by mean-field theory in the thermodynamic limit. In particular, the nonequilibrium dynamics is essentially classical, as the effective Planck constant $\hbar_{\text{eff}} = 1/N$ is vanishingly small. One might thus naively expect that quantum entanglement becomes vanishingly small, as well.

On the contrary, not only does entanglement have a finite limit as $\hbar_{\text{eff}} \to 0$, but also this limiting quantity lends itself to a clean classical interpretation.

We aim at understanding the entanglement properties of the class of spin systems in Eq. (2.13) in and out of equilibrium. For a composite system with Hilbert space $\mathcal{H} = \mathcal{H}_A \otimes \mathcal{H}_B$ in a pure state $\hat{\rho} = |\psi\rangle\langle\psi|$, the entanglement between subsystems A and B can be quantified by the Von Neumann entropy of the reduced density matrix $\hat{\rho}_A = \mathrm{Tr}_B\ \hat{\rho}$,

$$S_A = -\,\mathrm{Tr}\left[\hat{\rho}_A \log \hat{\rho}_A\right] . \tag{6.2}$$

See also Sec. 1.1.5 of the Introduction.

6.1.1 Two-boson formalism

We consider a bipartition of the system described by Eq. (6.1) into two subsets of spins A and B with N_A and $N_B = N - N_A$ spins, respectively. The collective spin $\hat{\mathbf{S}}$ in Eq. (2.14) can be decomposed as

$$\hat{\mathbf{S}} = \hat{\mathbf{S}}_A + \hat{\mathbf{S}}_B. \tag{6.3}$$

The quantum correlations between subsystems A and B can be understood by bosonizing the quantum fluctuations of the two spins $\hat{\mathbf{S}}_A$, $\hat{\mathbf{S}}_B$. For global quantum quenches, all spins have a common well-defined polarization $\langle\hat{\mathbf{S}}\rangle$. In analogy with previous Chapters, we introduce a rotated reference frame $(\mathbf{X}, \mathbf{Y}, \mathbf{Z})$ parameterized as in Eq. (3.3), such that $\mathbf{Z}$ is aligned with the collective spin polarization $\langle\hat{\mathbf{S}}\rangle$, both in and out of equilibrium. The expansion is obtained by means of Holstein-Primakoff transformations [cf. Eq. (2.42)],

$$\begin{cases} \hat{S}^X_{A,B} = \sqrt{N_{A,B}\, s}\ \ \hat{q}_{A,B}\ + \mathcal{O}\left(1/\sqrt{N_{A,B}}\right), \\ \hat{S}^Y_{A,B} = \sqrt{N_{A,B}\, s}\ \ \hat{p}_{A,B}\ + \mathcal{O}\left(1/\sqrt{N_{A,B}}\right), \\ \hat{S}^Z_{A,B} = N_{A,B}\, s - \hat{n}_{A,B} \equiv N_{A,B}\, s - \dfrac{\hat{q}^2_{A,B} + \hat{p}^2_{A,B} - 1}{2}, \end{cases} \tag{6.4}$$

where $s = 1/2$ here. The two bosonic modes $(\hat{q}_A, \hat{p}_A)$ and $(\hat{q}_B, \hat{p}_B)$ describe spin excitations localized in subsystem A and B, respectively. In terms of these two modes, the collective spin of the global system reads

$$\begin{cases} \hat{S}^X = \sqrt{N\, s}\left(\sqrt{f_A}\ \hat{q}_A + \sqrt{f_B}\ \hat{q}_B\right)\ + \mathcal{O}\left(1/\sqrt{N}\right), \\ \hat{S}^Y = \sqrt{N\, s}\left(\sqrt{f_A}\ \hat{p}_A + \sqrt{f_B}\ \hat{p}_B\right)\ + \mathcal{O}\left(1/\sqrt{N}\right), \\ \hat{S}^Z = N\, s - \hat{n}_A - \hat{n}_B, \end{cases} \tag{6.5}$$

where $f_{A,B} \equiv N_{A,B}/N$ represent the fraction of spins in subsystems A and B, respectively (so $f_A + f_B = 1$).

We can now express the Hamiltonian in Eq. (6.1) in terms of the collective spin components $\hat{S}^X$, $\hat{S}^Y$, $\hat{S}^Z$, and hence systematically expand in $(\hat{q}_A, \hat{p}_A)$,

$(\hat{q}_B, \hat{p}_B)$ via Eqs. (6.5). In this two-boson description, the entanglement between subsystems A and B is encoded by the entanglement between these two bosonic modes.

6.1.2 Ground-state correlations

It is convenient to work with the "collective" and "spin-wave" modes $(\hat{Q}, \hat{P})$ and $(\hat{q}, \hat{p})$ defined by

$$\begin{cases} \hat{Q} = +\sqrt{f_A}\ \hat{q}_A + \sqrt{f_B}\ \hat{q}_B \\ \hat{q} = -\sqrt{f_B}\ \hat{q}_A + \sqrt{f_A}\ \hat{q}_B \end{cases}, \tag{6.6}$$

$$\begin{cases} \hat{P} = +\sqrt{f_A}\ \hat{p}_A + \sqrt{f_B}\ \hat{p}_B \\ \hat{p} = -\sqrt{f_B}\ \hat{p}_A + \sqrt{f_A}\ \hat{p}_B \end{cases}, \tag{6.7}$$

i.e., a rotation by an angle $\zeta = \arctan\left(\sqrt{f_B/f_A}\right)$ in the $\hat{q}_A$-$\hat{q}_B$ and $\hat{p}_A$-$\hat{p}_B$ planes. By Eqs. (6.5), in terms of these bosonic modes, the collective spin reads

$$\begin{cases} \hat{S}^X = \sqrt{N\,s}\ \hat{Q}\ + \mathcal{O}\left(1/\sqrt{N}\right), \\ \hat{S}^Y = \sqrt{N\,s}\ \hat{P}\ + \mathcal{O}\left(1/\sqrt{N}\right), \\ \hat{S}^Z = N\,s - \dfrac{\hat{Q}^2 + \hat{P}^2 - 1}{2} - \dfrac{\hat{q}^2 + \hat{p}^2 - 1}{2} \\ \qquad\ \equiv N\,s - \hat{n}_{exc} - \hat{n}_{sw}, \end{cases} \tag{6.8}$$

The $(\hat{Q}, \hat{P})$ mode represents uniform collective spin excitations in the entire system, and, accordingly, does not affect the collective spin magnitude $|\hat{\mathbf{S}}|^2$. On the other hand, the $(\hat{q}, \hat{p})$ mode represents spatial fluctuations of the spins in subsystems A and B, which decrease the collective spin magnitude $|\hat{\mathbf{S}}|^2 = (N/2 - \hat{n}_{sw})(N/2 - \hat{n}_{sw} + 1)$ [cf. Eq. (3.12)]. In analogy with previous Chapters, we refer to these excitations as "spin waves". With reference to the notation of Chap. 3, we observe that $\hat{Q}, \hat{P} \equiv \tilde{q}_{k=0}, \tilde{p}_{k=0}$, while $\hat{q}, \hat{p}$ can be expressed in terms of a combination of the actual spin-wave Fourier modes $\tilde{q}_k, \tilde{p}_k$ with $k \neq 0$.

The Holstein-Primakoff expansion of the Hamiltonian (2.14) in terms of the above modes has the form

$$\begin{aligned} \hat{H} = &+ N\ \mathcal{E}_{cl}(\theta, \phi) \\ &+ \sqrt{N}\left[h_Q^{(1)}(\theta, \phi)\ \hat{Q} + h_P^{(1)}(\theta, \phi)\ \hat{P}\right] \\ &+ h_{QQ}^{(2)}(\theta, \phi)\ \frac{\hat{Q}^2}{2} + h_{PP}^{(2)}(\theta, \phi)\ \frac{\hat{P}^2}{2} + h_{QP}^{(2)}(\theta, \phi)\ \frac{\hat{Q}\hat{P} + \hat{P}\hat{Q}}{2} \\ &+ h_{sw}^{(2)}(\theta, \phi)\ \frac{\hat{q}^2 + \hat{p}^2 - 1}{2} \\ &+ \mathcal{O}\left(1/\sqrt{N}\right), \end{aligned} \tag{6.9}$$

where the explicit expression of the coefficients $\mathcal{E}_{cl}$, $h^{(1)}$, $h^{(2)}$ is determined

by the couplings J in the Hamiltonian (2.14) and by the spherical angles θ, ϕ which parameterize the rotated frame. By truncating this expansion to quadratic order in the bosonic excitations, it is possible to determine the ground-state correlations and their time-evolution after a quench, as shown below. This approximation is accurate for Gaussian states with a small number of collective excitations $\langle \hat{n}_{exc} \rangle \ll N$ compared to the system size. This condition is generically valid in ground states, even at quantum critical points, where one typically has $\langle \hat{n}_{exc} \rangle \sim N^{1/3}$ (cf. discussion in Sec. 2.4.2). The discussion below generalizes that presented in Sec. 2.4.1 for the infinite-range quantum Ising model.

In equilibrium, the angles θ and ϕ are fixed in such a way that the linear terms $h^{(1)}$ in Eq. (6.26) vanish. This yields the minimum point of the classical limit $\mathcal{H}_{cl}$ of $\hat{H}$ in Eq. (2.20). The mode $(\hat{q}, \hat{p})$ enters Eq. (6.26) only through the number of bosons $\hat{n}_{sw} = (\hat{q}^2 + \hat{p}^2 - 1)/2$, and, accordingly, these spin waves cannot be excited in the ground state (nor dynamically) in infinite-range systems, i.e.,

$$\langle \hat{n}_{sw} \rangle \equiv 0. \tag{6.10}$$

For the same reason one also has vanishing mixed correlations

$$\langle \hat{q}\hat{Q} \rangle = \langle \hat{p}\hat{P} \rangle = \langle \hat{q}\hat{P} \rangle = \langle \hat{p}\hat{Q} \rangle \equiv 0. \tag{6.11}$$

On the other hand, collective excitations $\hat{n}_{exc} = (\hat{Q}^2 + \hat{P}^2 - 1)/2$ are present in the ground state (and can be dynamically generated). The correlations of $\hat{Q}$ and $\hat{P}$ can be obtained by diagonalizing $\hat{H}$ with a generalized Bogolyubov transformation,

$$\begin{cases} \hat{Q} = +\, e^{\gamma} \cos\eta\ \hat{Q}' - e^{\gamma} \sin\eta\ \hat{P}', \\ \hat{P} = +\, e^{-\gamma} \sin\eta\ \hat{Q}' - e^{-\gamma} \cos\eta\ \hat{P}', \end{cases} \tag{6.12}$$

with

$$\begin{aligned} \tan(2\eta) &= \frac{h^{(2)}_{QP}}{h^{(2)}_{QQ} + h^{(2)}_{PP}}, \\ e^{2\gamma} &= \frac{h^{(2)}_{QQ} + h^{(2)}_{PP} - \delta}{h^{(2)}_{QQ} + h^{(2)}_{PP} + \delta}, \end{aligned} \tag{6.13}$$

where we have set $\delta \equiv (h^{(2)}_{QQ} - h^{(2)}_{PP}) \cos(2\eta) + 2h^{(2)}_{QP} \sin(2\eta)$. One finds

$$\begin{cases} \Delta^{QQ} \equiv \langle \hat{Q}^2 \rangle_{GS} = \frac{1}{2}\big[\cosh(2\gamma) + \sinh(2\gamma)\cos(2\eta)\big], \\ \Delta^{PP} \equiv \langle \hat{P}^2 \rangle_{GS} = \frac{1}{2}\big[\cosh(2\gamma) - \sinh(2\gamma)\cos(2\eta)\big], \\ \Delta^{QP} \equiv \frac{\langle \hat{Q}\hat{P} + \hat{P}\hat{Q} \rangle_{GS}}{2} = \frac{1}{2}\sinh(2\gamma)\sin(2\eta). \end{cases} \tag{6.14}$$

In particular,

$$\langle \hat{n}_{exc} \rangle_{GS} = \frac{\Delta^{QQ} + \Delta^{PP} - 1}{2} = \frac{\cosh(2\gamma) - 1}{2}. \tag{6.15}$$

See also App. B for a wide discussion of pure Gaussian states.

6.1.3 Entanglement entropy and spin squeezing

For a given (stationary or time-evolving) state of the system, we can compute the entanglement entropy between the two subsystems A and B within the two-boson formalism. This amounts to computing the entanglement entropy between the two bosonic modes $(\hat{q}_A, \hat{p}_A)$ and $(\hat{q}_B, \hat{p}_B)$. The reduced density matrix of subsystem A is a Gaussian state completely determined by the 2×2 correlation matrix

$$\Delta_A = \begin{pmatrix} \langle \hat{q}_A^2 \rangle & \frac{\langle \hat{q}_A \hat{p}_A + \hat{p}_A \hat{q}_A \rangle}{2} \\ \frac{\langle \hat{q}_A \hat{p}_A + \hat{p}_A \hat{q}_A \rangle}{2} & \langle \hat{p}_A^2 \rangle \end{pmatrix} \equiv \begin{pmatrix} \Delta^{q_A q_A} & \Delta^{q_A p_A} \\ \Delta^{q_A p_A} & \Delta^{p_A p_A} \end{pmatrix}. \tag{6.16}$$

The Von Neumann entropy (6.2) of such a Gaussian state can be expressed in terms of the determinant of Δ_A as [344]

$$S_A = 2\sqrt{\det \Delta_A}\, \operatorname{arccoth}\left(2\sqrt{\det \Delta_A}\right) + \frac{1}{2} \log\left(\det \Delta_A - \frac{1}{4}\right). \tag{6.17}$$

On the other hand, the matrix Δ_A can be easily related to the correlation matrix Δ of collective excitations (Q, P) in the system by inverting Eqs. (6.6)-(6.7). An explicit computation shows that its determinant amounts to

$$\det \Delta_A = \frac{1}{4} + \frac{1}{2} f_A f_B \operatorname{Tr}\left[\Delta - \frac{\mathbb{1}}{2}\right] \equiv \frac{1}{4} + f_A f_B \, \langle \hat{n}_{exc} \rangle. \tag{6.18}$$

Plugging this formula into Eq. (6.17), we arrive at the result

$$S_A = \sqrt{1 + 4 f_A f_B \, \langle \hat{n}_{exc} \rangle}\, \operatorname{arccoth}\left(\sqrt{1 + 4 f_A f_B \, \langle \hat{n}_{exc} \rangle}\right) + \frac{1}{2} \log\left(f_A f_B \, \langle \hat{n}_{exc} \rangle\right). \tag{6.19}$$

This function is plotted in the top panel of Fig. 6.2. Taking the limits of small or large $\langle \hat{n}_{exc} \rangle$ in Eqs. (6.19), (6.18), one finds

$$S_A \sim f_A f_B \, \langle \hat{n}_{exc} \rangle \, \log f_A f_B \langle \hat{n}_{exc} \rangle \qquad \text{for} \qquad \langle \hat{n}_{exc} \rangle \ll 1\,, \tag{6.20a}$$

$$S_A \sim 1 + \frac{1}{2} \log f_A f_B + \frac{1}{2} \log \langle \hat{n}_{exc} \rangle \qquad \text{for} \qquad \langle \hat{n}_{exc} \rangle \gg 1\,. \tag{6.20b}$$

Equations (6.19) and (6.18) are valid both in and out of equilibrium. They highlight that the reduced state of subsystems A and B is pure (i.e., $\det \Delta_A = 1/4$, cf. App. B) only in fully polarized states, in which no collective spin excitations are present in the system, i.e., $\langle \hat{n}_{exc} \rangle = 0$.

The above equations may be seen as a direct relation between bipartite entanglement entropy and collective spin squeezing, usually quantified by the

minimal transverse variance of collective spin fluctuations [345–347]

$$\xi^2 \equiv \frac{\mathrm{Min}_{|\mathbf{u}|=1,\mathbf{u}\perp\mathbf{Z}} \left\langle \left(\mathbf{u}\cdot\hat{\mathbf{S}}\right)^2 \right\rangle}{N/4} \,. \tag{6.21}$$

This squeezing parameter ξ is equal to 1 for fully polarized states, while $\xi < 1$ for squeezed states. The number of collective excitations $\langle \hat{n}_{exc} \rangle$ can be taken as a measure of collective spin squeezing for general Gaussian states: from Eqs. (6.14) and (6.15) one derives ξ as

$$\xi^2 = e^{-2|\gamma|} = 1 - 2\left(\sqrt{\langle \hat{n}_{exc}\rangle^2 + \langle \hat{n}_{exc}\rangle} - \langle \hat{n}_{exc}\rangle\right). \tag{6.22}$$

This relation is plotted in the middle panel of Fig. 6.2, and shows that the amount of collective excitations $\langle \hat{n}_{exc} \rangle$ increases from 0 to $\sim N$, as the collective spin state is squeezed from a fully polarized configuration with $\xi = 1$ towards massively squeezed configurations with $\xi \sim 1/\sqrt{N}$.

Besides the number of collective excitations $\langle \hat{n}_{exc} \rangle$ and the spin-squeezing parameter ξ, it is also possible to characterize entanglement entropy via yet another significant quantity, i.e., the *effective temperature* of the two subsystems. In fact, the reduced density matrices may be written as $\hat{\rho}_{A,B} = \exp(-\beta_{eff}\hat{H}_{A,B})/Z_{A,B}$, where the state-dependent quadratic operators $\hat{H}_{A,B}$ are usually termed *modular* or *entanglement Hamiltonian*. It is straightforward to derive a relation between the effective dimensionless temperature and the other quantities, i.e.,

$$T_{eff} = \frac{1}{2\,\mathrm{arctanh}\left(\frac{1}{\sqrt{1+4f_A f_B \langle \hat{n}_{exc}\rangle}}\right)}. \tag{6.23}$$

The dependency specified by this equation is plotted in the bottom panel of Fig. 6.2. It makes it explicitly clear that the growth of $\langle \hat{n}_{exc}(t) \rangle$ — which comes via collective spin squeezing — is responsible for "heating up" the two subsystems, i.e., for raising their effective temperature, thus continuously accumulating entanglement entropy in time.

6.2 Out-of-equilibrium growth of entanglement entropy

In a system of noninteracting spins subject to an external field, an initial spin-coherent state remains spin-coherent during time-evolution, as each spins perform an independent precession around the field and no correlations are dynamically generated. However, nonlinear collective interactions give rise to spin excitations in the form of spin squeezing, as quantitatively expressed by Eq. (6.22).

The rate of spin squeezing depends on the nature of the underlying classical dynamics, as illustrated in Fig. 6.3. In fact, the *quantum* evolution of spin fluctuations $(\hat{Q},\hat{P})$ around the classical trajectory of the collective spin, is equivalent to the *classical* evolution of small displacements away from it in the linear approxi-

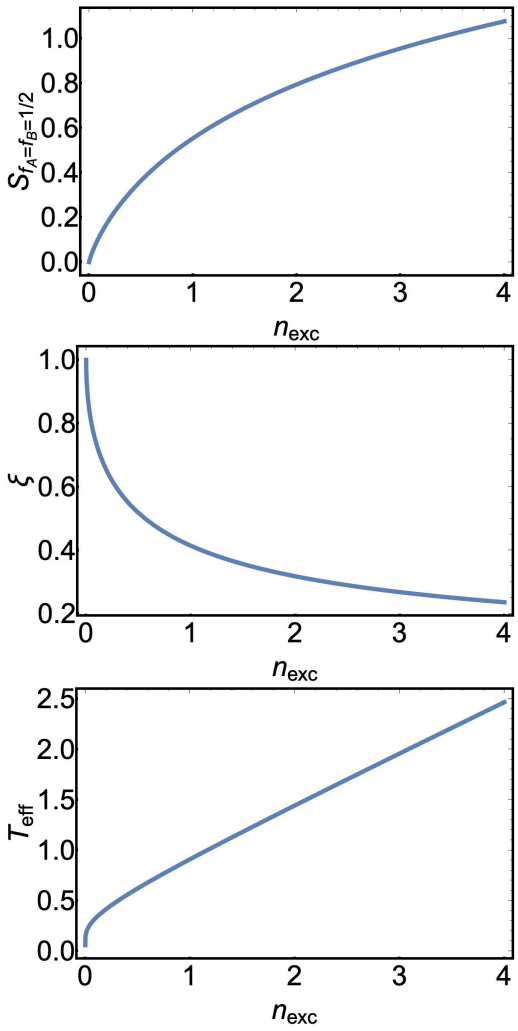

Figure 6.2: Plots of half-system bipartite entanglement entropy S (top), spin squeezing ξ (middle) and effective temperature T_{eff} (bottom) in pure Gaussian states as a function of the amount $n = \langle \hat{n}_{exc} \rangle$ of collective spin excitations in the system, given by Eqs. (6.19), (6.22) and (6.23), respectively.

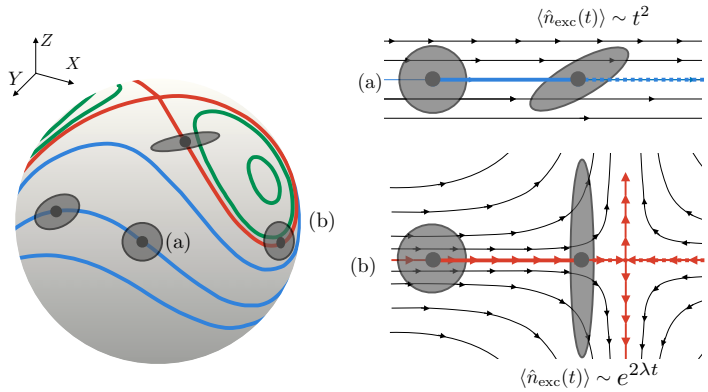

Figure 6.3: Schematic illustration of spin squeezing induced by the structure of the underlying semiclassical trajectories. In both panels, the arrows indicate the semiclassical flow in phase space (i.e., on the Bloch sphere of the collective spin), the dark green line represents a trajectory of the average collective spin, and the grey ellipses represent its quantum fluctuations around the classical average in a fully polarized configuration (left) and in its evolution after a certain time (right). The squeezing parameter $\xi(t)$ corresponds to the relative length of the minor semi-axis of the ellipse. (a) For generic quenches, closed trajectories separate linearly in time, leading to a t^2-growth of the amount of collective excitations $\langle \hat{n}_{\rm exc}(t) \rangle$ and thus to a logarithmic growth of entanglement entropy. (b) In the case of a quench to a dynamical critical point, the configuration of the collective spin lies on the stable manifold of an unstable fixed point in phase space. Nearby trajectories separate exponentially in time at a rate λ given by the largest eigenvalue of the linearized flow. Correspondingly, entanglement entropy grows as λt.

mation [308], see Fig. 6.3(a) for an illustration. In classical integrable systems such as the single classical spin in Eq. (2.20), trajectories originating from nearby initial conditions separate linearly in time, which implies $\hat{Q}(t), \hat{P}(t) \sim t$. Since $\hat{n}_{\rm exc}$ is quadratic in the spin fluctuations $\hat{Q}$,$\hat{P}$, the collective excitations grow polynomially in time $\langle \hat{n}_{\rm exc}(t) \rangle \sim t^2$ after a generic quench [83]. By Eq. (6.19), this leads to

$$S_A(t) \sim \log t. \tag{6.24}$$

On the other hand, for exceptional quenches to dynamical critical points, nearby trajectories separate exponentially fast, leading to a linear growth of entanglement entropy. Such a description is valid up to the Ehrenfest time scale $T_{\rm Ehr}(N)$, which diverges with the system size.

Below, we make the above arguments rigorous.

6.2.1 Dynamical excitation of collective spin fluctuations

Suppose we prepare the system in the ground state of a fully-connected Hamiltonian (6.1), characterized by a well-defined classical polarization and with quantum fluctuations described by Eqs. (6.14), and we then drive it out of equilibrium by varying in time some parameter $J(t)$ in the Hamiltonian. Both the direction of the collective spin configuration $\theta(t)$, $\phi(t)$ and its quantum fluctuations $\Delta^{QQ}(t)$, $\Delta^{QP}(t)$, $\Delta^{PP}(t)$ evolve in time. As discussed in Sec. 3.2, the evolution of the angles $\theta(t)$, $\phi(t)$ can be accounted for by adjusting the reference frame along the time-dependent direction of $\langle \hat{\mathbf{S}}(t) \rangle$. With the conventions introduced therein, the modified Hamiltonian in this time-dependent frame

includes inertial forces, and reads

$$\widetilde{H}(t) = \hat{H} - \boldsymbol{\omega}(t) \cdot \hat{\mathbf{S}}, \tag{6.25}$$

with $\omega^X = -\sin\theta\ \dot{\phi}$, $\omega^Y = \dot{\theta}$, and $\omega^Z = \cos\theta\ \dot{\phi}$ [cf. Eq. (3.31)]. The time-dependence of $\theta(t)$ and $\phi(t)$ is determined by the vanishing of the linear terms in $\hat{S}^X$ and $\hat{S}^Y$. In the infinite-range systems discussed here, the corrections ("feedback") by quantum fluctuations are vanishingly small, and one simply obtains the classical trajectory $\theta^*(t), \phi^*(t)$ governed by $\mathcal{H}_{cl}$ in Eq. (2.20). The resulting time-dependent quadratic Hamiltonian generalizes Eq. (6.26),

$$\begin{aligned}\widetilde{H}(t) = &+ N\ \widetilde{\mathcal{E}}_{cl}(t) + \\ &+ \widetilde{h}^{(2)}_{QQ}(t)\ \frac{\hat{Q}^2}{2} + h^{(2)}_{PP}(t)\ \frac{\hat{P}^2}{2} + \widetilde{h}^{(2)}_{QP}(t)\ \frac{\hat{Q}\hat{P} + \hat{P}\hat{Q}}{2} \\ &+ \widetilde{h}^{(2)}_{sw}(t)\ \frac{\hat{q}^2 + \hat{p}^2 - 1}{2} \\ &+ \mathcal{O}\left(1/\sqrt{N}\right),\end{aligned} \tag{6.26}$$

with

$$\begin{aligned}\widetilde{h}^{(2)}_{QQ,PP,sw}(t) &\equiv h^{(2)}_{QQ,PP,sw}\big(\theta^*(t), \phi^*(t)\big) - \cos\theta^*(t)\ \dot{\phi^*}(t), \\ \widetilde{h}^{(2)}_{QP}(t) &\equiv h^{(2)}_{QP}\big(\theta^*(t), \phi^*(t)\big).\end{aligned} \tag{6.27}$$

The quadratic part of $\widetilde{H}(t)$ determines the dynamical generation of collective bosonic excitations, which can be monitored through the time-evolving correlation functions $\Delta^{QQ}(t)$, $\Delta^{QP}(t)$, $\Delta^{PP}(t)$. They can be computed as in Chap. 3 and in App. B. One starts from the Heisenberg equations of motion

$$\begin{cases}\dot{\hat{Q}} = +\widetilde{h}^{(2)}_{QP}(t)\ \hat{Q} + \widetilde{h}^{(2)}_{PP}(t)\ \hat{P}, \\ \dot{\hat{P}} = -\widetilde{h}^{(2)}_{QQ}(t)\ \hat{Q} - \widetilde{h}^{(2)}_{QP}(t)\ \hat{P}.\end{cases} \tag{6.28}$$

Denoting the solution

$$\begin{pmatrix}\hat{Q}(t) \\ \hat{P}(t)\end{pmatrix} = U(t) \begin{pmatrix}\hat{Q}(0) \\ \hat{P}(0)\end{pmatrix}, \tag{6.29}$$

and collecting the dynamical correlations

$$\begin{cases}\Delta^{QQ}(t) \equiv \langle \hat{Q}^2(t) \rangle, \\ \Delta^{PP}(t) \equiv \langle \hat{P}^2(t) \rangle, \\ \Delta^{QP}(t) \equiv \dfrac{\langle \hat{Q}(t)\hat{P}(t) + \hat{P}(t)\hat{Q}(t) \rangle}{2},\end{cases} \tag{6.30}$$

in the matrix

$$\Delta(t) = \begin{pmatrix}\Delta^{QQ}(t) & \Delta^{QP}(t) \\ \Delta^{QP}(t) & \Delta^{PP}(t)\end{pmatrix} = U(t)\ \Delta\big(t=0\big)\ U^T(t), \tag{6.31}$$

the number of dynamically generated excitations can be expressed as

$$\langle \hat{n}_{exc}(t) \rangle = \frac{\Delta^{QQ}(t) + \Delta^{PP}(t) - 1}{2} = \frac{1}{2} \operatorname{Tr} \left[\Delta(t) - \frac{\mathbb{1}}{2} \right]. \tag{6.32}$$

Note that $\det \Delta(t) \equiv 1/4$, which is an exact property of *pure* Gaussian states [cf. Eq. (6.14)] preserved by the time-evolution. See App. B for more details.

6.2.2 Slow squeezing after generic quenches

A time-independent system with a single degree of freedom is integrable, due to the conservation of energy, and hence canonical action-angle variables $(\mathcal{A}, \varphi)$ can be introduced, where the action $\mathcal{A}$ is a constant of motion related to the area enclosed by a trajectory in phase space, and the angle φ periodically sweeps the range $[0, 2\pi]$ along the trajectory. In these variables, the (classical and quantum) evolution of the system is similar to that of a free particle,[1]

$$\begin{cases} \dot{\hat{\mathcal{A}}} = 0 \\ \dot{\hat{\varphi}} = \partial_{\mathcal{A}} \hat{H} \equiv \omega(\hat{\mathcal{A}}), \end{cases} \tag{6.33}$$

with the solution

$$\begin{cases} \hat{\mathcal{A}}(t) = \hat{\mathcal{A}}(0) \\ \hat{\varphi}(t) = \hat{\varphi}(0) + \omega\big(\hat{\mathcal{A}}(0)\big) t. \end{cases} \tag{6.34}$$

For a given classical trajectory characterized by a value of the action $\mathcal{A}_{cl}$, the evolution of quantum fluctuations around it,

$$\begin{aligned} \delta\hat{\mathcal{A}}(t) &\equiv \hat{\mathcal{A}}(t) - \mathcal{A}_{cl}, \\ \delta\hat{\varphi}(t) &\equiv \hat{\varphi}(t) - \varphi_{cl}(t), \end{aligned} \tag{6.35}$$

is described by

$$\begin{cases} \delta\hat{\mathcal{A}}(t) = \delta\hat{\mathcal{A}}(0) \\ \delta\hat{\varphi}(t) = \delta\hat{\varphi}(0) + \Big[\omega\big(\hat{\mathcal{A}}(0)\big) - \omega\big(\mathcal{A}_{cl}\big) \Big] t = \\ \qquad\quad = \delta\hat{\varphi}(0) + \partial_{\mathcal{A}} \omega\big|_{\mathcal{A}_{cl}} \delta\hat{\mathcal{A}}(0)\, t + \mathcal{O}\left(\frac{t}{N}\right). \end{cases} \tag{6.36}$$

The error term follows from the fact that the variables $(\hat{\mathcal{A}}, \hat{\varphi})$ parameterize the rescaled collective spin $\hat{\mathbf{S}}/N$, and hence their ground state quantum fluctuations are subextensive, i.e., $\big(\delta\hat{\mathcal{A}}(0)\big)^2 \sim 1/N$ (cf. Sec. 2.1.2). The time-dependence of

[1] where the role of the action is played by the momentum

correlations can then be derived from the above solution,

$$\begin{cases} \Delta^{\mathcal{A}\mathcal{A}}(t) \equiv \langle \delta\hat{\mathcal{A}}(t)\delta\hat{\mathcal{A}}(t)\rangle \\ \qquad\quad = \Delta^{\mathcal{A}\mathcal{A}}(0) \\ \Delta^{\mathcal{A}\varphi}(t) \equiv \frac{1}{2}\langle \delta\hat{\mathcal{A}}(t)\delta\hat{\varphi}(t) + \delta\hat{\varphi}(t)\delta\hat{\mathcal{A}}(t)\rangle \\ \qquad\quad = \Delta^{\mathcal{A}\varphi}(0) + \partial_{\mathcal{A}}\omega\big|_{\mathcal{A}_{cl}} \Delta^{\mathcal{A}\mathcal{A}}(0)\, t \\ \Delta^{\varphi\varphi}(t) \equiv \langle \delta\hat{\varphi}(t)\delta\hat{\varphi}(t)\rangle \\ \qquad\quad = \Delta^{\varphi\varphi}(0) + 2\partial_{\mathcal{A}}\omega\big|_{\mathcal{A}_{cl}} \Delta^{\mathcal{A}\varphi}(0)\, t \\ \qquad\qquad + \partial_{\mathcal{A}}\omega\big|^2_{\mathcal{A}_{cl}} \Delta^{\mathcal{A}\mathcal{A}}(0)\, t^2 + \mathcal{O}\left(\frac{t^2}{N}\right). \end{cases} \tag{6.37}$$

This t^2-growth of quantum fluctuations is analogous to the spreading of wavepackets of free quantum particles. Both $(\hat{Q}, \hat{P})$ and $(\delta\hat{\mathcal{A}}, \delta\hat{\varphi})$ describe quantum fluctuations of the collective spin, hence they must be related via a linear canonical transformation which depends on the instantaneous classical configuration, (θ, ϕ) or $(\mathcal{A}_{cl}, \varphi_{cl})$. For a general closed trajectory, the latter varies periodically in time, with a period $T_{cl} = 2\pi/\omega(\mathcal{A}_{cl})$. Thus, the correlations $\Delta^{QQ}(t)$, $\Delta^{QP}(t)$ and $\Delta^{PP}(t)$ are obtained from those in Eq. (6.37) by a time-periodic linear transformation.

We have proved that the time-dependence of correlations $\Delta^{QQ}(t)$, $\Delta^{QP}(t)$ and $\Delta^{PP}(t)$ generically shows a t^2-growth after a quench with a periodic modulation superimposed, the periodicity being that T_{cl} of the underlying classical trajectory. From Eqs. (6.37), we see that corrections to this behavior manifest over the Ehrenfest time scale $T_{Ehr} \sim \sqrt{N}$, which diverges in the thermodynamic limit. We emphasize that all the quantities above can in principle be computed analytically for any given fully-connected spin system, due to Liouville-integrability [296].

6.2.3 Fast squeezing at dynamical critical points

A remarkable exception to the behavior described above is represented by isolated trajectories in phase space known as *separatrices*, which traverse unstable fixed points and divide the Bloch sphere into topologically distinct disconnected regions. These trajectories have a divergent period and are related to the so-called mean-field dynamical phase transitions [83] discussed in Sec. 2.2.

For quenches to dynamical critical points, the growth of the number of collective excitations is exponential in time rather than polynomial, due to the exponential separation of classical trajectories originating from points near a separatrix. The rate of such an exponential separation is determined by the positive eigenvalue λ of the linearized flow around the unstable fixed point (see Fig. 6.3, bottom panel, for an illustration). In fact, exponential growth of quantum fluctuations is encoded by $U(t) \sim \exp(\lambda t)$ in Eq. (6.29) and hence by $\Delta(t) \sim \exp(2\lambda t)$ in Eq. (6.31), which directly leads to $S_A(t) \sim \lambda t$ by Eqs. (6.19) and (6.18), as claimed. The proof of this is essentially analogous to that presented

in the previous Section. This effect is similar to that discussed in Ref. [348].

6.2.4 Saturation of entanglement entropy

As remarked above, our approach to the nonequilibrium dynamics is adequate only before the *Ehrenfest time scale* defined by $\langle \hat{n}_{exc}(t = T_{Ehr}) \rangle \sim N$. In fact, in correspondence of T_{Ehr}, the quantum fluctuations of the collective spin become comparable with the magnitude of the collective spin itself, which makes the description inaccurate and thus sets the limit of validity of semiclassical analyses [349]. This time scale diverges with the system size in a way which depends on the nature of the underlying semiclassical trajectories: $T_{Ehr} \sim \sqrt{N}$ for generic quenches, and $T_{Ehr} \sim \log N$ for quenches to dynamical critical points. At this time scale, the number of excitations reaches its maximal value, implying through Eq. (6.20b) a saturation value of S_A proportional to the logarithm of the number of spins in subsystem A,

$$S_A \sim \frac{1}{2} \log N_A \, . \tag{6.38}$$

This is actually related to the usual volume-law scaling of entanglement out of equilibrium. In fact, the stationary states after a quantum quench explore all the allowed Hilbert space, and their entanglement is upper-bounded by $S_A \leqslant \log(\dim \mathcal{H}_A)$. For generic many-body systems, the dimension of $\mathcal{H}_A$ is exponentially large with the volume of the subsystem [e.g. $\dim(\mathcal{H}_A) = 2^{N_A}$ for spins-1/2], causing volume-law scaling. In the collective models under consideration here, however, the conservation of the collective spin magnitude $|\hat{\mathbf{S}}|^2$ reduces the dimension of the allowed Hilbert space to $\dim(\mathcal{H}_A) = N_A + 1$. Moreover, by conservation of energy, the dimension of the accessible Hilbert space in the eigenbasis of the Hamiltonian is further reduced to $\sim \sqrt{N_A}$, as an initial spin-coherent state typically overlaps with a subextensive energy shell centered around its average energy. This is consistent with Eq. (6.38).

6.3 Spatially-decaying interactions

We are now in a position to understand the effects of having slowly-decaying interactions on entanglement dynamics. For the sake of definiteness, we consider periodic d-dimensional cubic lattices of $N = L^d$ spins governed by a Hamiltonian of the form

$$\hat{H} = -\frac{1}{\mathcal{N}_{\alpha,N}} \sum_{\mu,\nu=x,y,z} J_{\mu\nu} \sum_{i\neq j}^{N} \frac{\hat{s}_i^\mu \hat{s}_j^\nu}{\|\mathbf{r}_i - \mathbf{r}_j\|^\alpha} - \sum_{\mu=x,y,z} J_\mu \sum_i^N \hat{s}_i^\mu \, , \tag{6.39}$$

where the exponent $\alpha \geqslant 0$ characterizes the algebraic decay of spin-spin interactions. The distance $\|\mathbf{r}_i - \mathbf{r}_j\|$ between two sites on the periodic lattice is taken

as

$$\|\mathbf{r}_i - \mathbf{r}_j\| = \sqrt{\sum_{\mu=1}^{d} \left[\mathrm{Min}(|r_i^\mu - r_j^\mu|, L - |r_i^\mu - r_j^\mu|)\right]^2}. \tag{6.40}$$

As in Chap. 5, a Kac rescaling factor $1/\mathcal{N}_{\alpha,N}$ with $\mathcal{N}_{\alpha,N} = \sum_{i\neq j}|\mathbf{r}_i - \mathbf{r}_j|^{-\alpha}/N$ replaces the $1/N^{p-1}$ factor in Eq. (6.1) for $p = 2$-body interactions, ensuring the extensivity of the Hamiltonian for $\alpha \leqslant d$ and fixing an α-independent energy scale [324]. The fully-connected limit is recovered by letting $\alpha \to 0$.

For $\alpha > 0$, the full permutational symmetry of the infinite-range Hamiltonian (2.13) is broken and all the noncollective (i.e., finite-wavelength) spin modes participate in the dynamics. These excitations now allow the system to explore the full Hilbert space beyond the Dicke manifold, i.e., "inside the Bloch sphere", and the system may be expected to thermalize by accumulating extensive entanglement entropy [147]. However, we show that there exists a long prethermal temporal regime in which these quasiparticle excitations are suppressed, so that collective quantum fluctuations represent the dominant contribution to entanglement entropy growth.

The two-boson approach to entanglement dynamics described above was strictly based on the conservation of the collective spin magnitude. In this case, we need to resort to the nonequilibrium spin-wave theory presented in Chap. 3. The resulting rotating frame Hamiltonian reads

$$\widetilde{H}(t) = \widetilde{H}_0(t) - \sum_{\mathbf{k}\neq 0} \widetilde{f}_{\alpha,\mathbf{k}} \Bigg[J_{qq}(\theta,\phi)\, \frac{\tilde{q}_{\mathbf{k}}\tilde{q}_{-\mathbf{k}}}{2} + J_{pp}(\theta,\phi)\, \frac{\tilde{p}_{\mathbf{k}}\tilde{p}_{-\mathbf{k}}}{2} + J_{qp}(\theta,\phi)\, \frac{\tilde{q}_{\mathbf{k}}\tilde{p}_{-\mathbf{k}} + \tilde{p}_{\mathbf{k}}\tilde{q}_{-\mathbf{k}}}{2} \Bigg] + \mathcal{O}\left(\frac{1}{\sqrt{N}}\right), \tag{6.41}$$

where J's are coefficients depending on the angles $\theta(t)$ and $\phi(t)$ and, as in Eq. (5.4)

$$f_{\alpha,\mathbf{k}} = \frac{1}{\mathcal{N}_{\alpha,N}} \sum_{j(\neq i)}^{N} \frac{e^{-i\mathbf{k}\cdot(\mathbf{r}_j - \mathbf{r}_i)}}{|\mathbf{r}_j - \mathbf{r}_i|^\alpha}. \tag{6.42}$$

In Eq. (6.41) we have defined the collective-mode Hamiltonian

$$\widetilde{H}_0(t) = N\,\mathcal{E}_{cl}(\theta,\phi) - \left[J_{qq}(\theta,\phi)\frac{\hat{Q}^2}{2} + J_{pp}(\theta,\phi)\frac{\hat{P}^2}{2} + J_{qp}(\theta,\phi)\frac{\hat{Q}\hat{P} + \hat{P}\hat{Q}}{2} \right] + \widetilde{h}_{sw}^{(2)} \sum_{\mathbf{k}} \hat{n}_{\mathbf{k}} + \mathcal{O}\left(\frac{1}{\sqrt{N}}\right), \tag{6.43}$$

which accounts for the α-*independent* infinite-range part $f_{\alpha,0}\,\delta_{\mathbf{k},0} \equiv \delta_{\mathbf{k},0}$ of the interaction $f_{\alpha,\mathbf{k}}$. In other words, $\widetilde{H}_0(t)$ describes the dynamics of the collective spin fluctuations, parameterized by $\hat{Q} \equiv \tilde{q}_0$ and $\hat{P} \equiv \tilde{p}_0$, but conserves the bosonic occupation numbers of all the other spin-wave modes at finite wavelength,

$\hat{n}_{\mathbf{k}\neq\mathbf{0}} \equiv (\tilde{q}_{\mathbf{k}}\tilde{q}_{-\mathbf{k}} + \tilde{p}_{\mathbf{k}}\tilde{p}_{-\mathbf{k}} - 1)/2$ as

$$\left[\hat{n}_{\mathbf{k}}, \widetilde{H}_0\right] = 0 \qquad \text{for all } \mathbf{k} \neq 0 \tag{6.44}$$

(note that this is rigorously true to all orders in the Holstein-Primakoff expansion). Just as in previous Chapters, in the above equations, it is assumed that the evolution of the angles $\theta(t)$ and $\phi(t)$ is fixed in such a way that linear terms in the collective quantum fluctuations $Q \equiv \tilde{q}_{\mathbf{0}}$ and $P \equiv \tilde{p}_{\mathbf{0}}$ vanish, which is equivalent to the self-consistency requirement $\langle \hat{S}^X(t)\rangle \equiv \langle \hat{S}^Y(t)\rangle \equiv 0$. In the present case with $\alpha > 0$, the dynamical generation of spin waves can modify the classical trajectory of the collective spin (6.48), due to the feedback from quantum fluctuations.

In view of the above discussion, the corrections due to weak spatial decay of interactions $\alpha > 0$ to entanglement dynamics associated with collective spin excitations, discussed in Sec. 6.2 above, are encoded in the analytic structure of the couplings $f_{\alpha,\mathbf{k}}$. These couplings are vanishing in the infinite-range model with $\alpha = 0$. For $0 < \alpha \leqslant d$ these couplings are suppressed in the thermodynamic limit $N \to \infty$: in App. F, we rigorously derive the following bounds

$$\left|f_{\alpha,\mathbf{k}\neq\mathbf{0}}\right| \leqslant \begin{cases} \text{const} \times \dfrac{1}{(|\mathbf{k}|L)^{\frac{d+1}{2}}} & \text{for } \alpha \leqslant \dfrac{d-1}{2}, \\ \text{const} \times \dfrac{1}{(|\mathbf{k}|L)^{d-\alpha}} & \text{for } \dfrac{d-1}{2} < \alpha < d, \\ \text{const} \times \dfrac{\left|\log|\mathbf{k}| + \tilde{F}(|\mathbf{k}|)\right|}{\log L} & \text{for } \alpha = d. \end{cases} \tag{6.45}$$

By virtue of these bounds, there exists a long time scale, during which the dynamical excitation of spin waves with finite wavelengths is suppressed. A simple lower bound is given by the inverse coupling, i.e., $T_{sw} \sim N^{\beta/d}$, with $\beta \equiv \text{Min}\left(d-\alpha, (d+1)/2\right)$.

6.4 Numerical results for long-range quantum Ising chains

In this Section, we test our analytical understanding of entanglement dynamics in paradigmatic one-dimensional long-range quantum Ising chains. Here we conform with the notation of the original paper, Ref. [4]. The Hamiltonian reads

$$\hat{H} = -\frac{J}{2\mathcal{N}_{\alpha,N}} \sum_{i\neq j}^{N} \frac{\hat{\sigma}_i^x \hat{\sigma}_j^x}{|i-j|^\alpha} - h \sum_i^N \hat{\sigma}_i^z, \tag{6.46}$$

where $i, j = 1, \ldots, N$, $\hat{\sigma}_i^{x,z}$ are Pauli matrices, h is a global transverse magnetic field, $\mathcal{N}_{\alpha,N}$ is the Kač rescaling factor introduced above, and periodic boundary conditions are assumed.

The entanglement entropy contribution due to collective spin squeezing is α-independent as long as neglecting the feedback of quantum fluctuations on the

evolution of the collective spin is justified. As discussed in the previous Section, for $\alpha < d$ the dynamically generated density of spin waves is suppressed in the thermodynamic limit, which results in a negligible feedback on the mean-field dynamics. (We could anyhow take it into account.) The spin-squeezing contribution to entanglement entropy is expressed by Eq. (6.19) and is computed explicitly as follows. The expansion (6.26) of the Hamiltonian (6.46) under consideration in the rotating frame, via Eqs. (6.25) and (6.27), reads

$$\widetilde{\mathcal{E}}_{cl} = -h\,\cos\theta - \frac{1}{2}\cos\theta\dot{\phi} - \frac{J}{2}\sin^2\theta\cos^2\phi\,, \tag{6.47a}$$

$$\widetilde{h}^{(1)}_{Q} = h\,\sin\theta + \frac{1}{2}\sin\theta\,\dot{\phi} - J\cos\theta\sin\theta\cos^2\phi\,, \tag{6.47b}$$

$$\widetilde{h}^{(1)}_{P} = -\frac{1}{2}\,\dot{\theta} + J\sin\theta\,\sin\phi\cos\phi\,, \tag{6.47c}$$

$$\widetilde{h}^{(2)}_{QQ} = J\sin^2\theta\cos^2\phi\,, \tag{6.47d}$$

$$\widetilde{h}^{(2)}_{PP} = J\cos 2\phi\,, \tag{6.47e}$$

$$\widetilde{h}^{(2)}_{QP} = J\cos\theta\sin\phi\cos\phi\,, \tag{6.47f}$$

$$\widetilde{h}^{(2)}_{sw} = J\cos^2\phi\,. \tag{6.47g}$$

By setting to zero the linear terms $\widetilde{h}^{(1)}$, the classical equations of motion [294] are obtained

$$\begin{cases} \dot{\theta} = 2J\sin\theta\cos\phi\sin\phi\,, \\ \dot{\phi} = -2h + 2J\cos\theta\cos^2\phi\,, \end{cases} \tag{6.48}$$

while the dynamical correlations of collective spin fluctuations in Eq. (6.30) evolve according to

$$\begin{cases} \dot{\Delta}^{QQ} = 4J\cos\theta\sin\phi\cos\phi\,\Delta^{QQ} + 4J\cos 2\phi\,\Delta^{QP}, \\ \dot{\Delta}^{PP} = -4J\cos\theta\sin\phi\cos\phi\,\Delta^{PP} - 4J\cos^2\phi\sin^2\theta\,\Delta^{QP}, \\ \dot{\Delta}^{QP} = -2J\cos^2\phi\sin^2\theta\,\Delta^{QQ} + 2J\cos 2\phi\,\Delta^{PP}, \end{cases} \tag{6.49}$$

with $\theta = \theta(t)$ and $\phi = \phi(t)$ determined by Eq. (6.48). Equations (6.49) are a set of linear time-dependent differential equations and their numerical integration with the appropriate initial conditions [given by Eq. (6.14) for a general quench], determines the time-evolution of the number of collective excitations $\langle\hat{n}_{exc}(t)\rangle$ in Eq. (6.32) after a quantum quench.

We first focus here on quenches from a ferromagnetic initial state $|\psi_0\rangle = |{\rightarrow}{\rightarrow}\cdots{\rightarrow}\rangle$, i.e., quenches in the transverse field from $h_0 = 0$ to h_f. This corresponds to the initial conditions $\theta_0 = \pi/2$, $\phi_0 = 0$, $\Delta^{QP}(t=0) = 0$ and $\Delta^{QQ}(t=0) = \Delta^{PP}(t=0) = 1/2$ in Eqs. (6.48), (6.49). In the infinite-range limit $\alpha \to 0$, our approach is exact in the thermodynamic limit and the finite-size

exact diagonalization (ED) results are perfectly reproduced by our analytical calculation up to saturation at the Ehrenfest time $T_{Ehr} \sim \sqrt{N}$. Figures 6.1 (bottom) and 6.4(a),(b) show this for the quenches $h_0 = 0 \to h_f = 2J$, $h_f = 0.2J$ and $h_f = 0.5J$, i.e., above, below and at the critical dynamical point $h_c = J/2$ respectively. For quenches above and below h_c, one sees that entanglement entropy increases logarithmically $S_A \sim \log t$ before $T_{Ehr} \sim \sqrt{N}$, in agreement with the theory presented in this Chapter. For the critical quench, due to the exponential growth of the collective spin excitations, it increases linearly in time as $S_A \sim \lambda_{h_c} t$ before $T_{Ehr} \sim \log N$. For this Hamiltonian, the eigenvalue of the instability matrix of the unstable fixed point $\theta = 0$ is

$$\lambda_{h_c} = 2\sqrt{h_c(J - h_c)}. \tag{6.50}$$

The first and third quench qualitatively correspond the blue (a) and red (b) lines in the illustrative figure 6.3.

At finite N, the entanglement entropy is bounded and thus always saturates to a finite value, as in Eq. (6.38). The saturation value scales as $\log\sqrt{N}$, as shown in the inset of Fig. 6.5. In Fig. 6.7, we compare the time-dependent spin-squeezing-induced entanglement entropy with the exact numerical results at fixed size N for various bipartitions f_A. The agreement is excellent until saturation to $\sim 1/2 \log N_A$ at time T_{Ehr}, see the inset.

Let us now discuss the opposite case of a quantum quench from a paramagnetic initial state, i.e., the ground state of Hamiltonian with $h_0 = \infty$

$$|\phi_0\rangle = |\uparrow\uparrow \ldots \uparrow\rangle, \tag{6.51}$$

which corresponds to the initial conditions $\theta_0 = 0$, $\Delta^{QP}(t = 0) = 0$ and $\Delta^{QQ}(t = 0) = \Delta^{PP}(t = 0) = 1/2$ in Eqs. (6.48), (6.49) (due to the singularity of spherical coordinates, the value of ϕ_0 is immaterial in this case). For $h_f < J$, the initial state lies on top of the unstable trajectory at $\theta = 0$, hence the collective quantum fluctuations grow exponentially in time. The theory then predicts a linear increase $S_A \sim \lambda_{h_f} t$ of entanglement before T_{Ehr}, with λ_{h_f} given in Eq. (6.50), see Fig. 6.8 (left). Conversely, for $h_f > J$, the quantum fluctuations of the initial state undergo oscillations with period T_{cl}, which leads to a periodic dynamics of entanglement entropy as in Fig. 6.8 (right), with a simple semiclassical interpretation in terms of periodic squeezing of the collective spin.

For spatially-decaying interactions with $0 < \alpha < 1$, we numerically compute entanglement dynamics employing the MPS-TDVP technique [350, 351]. The accuracy of this technique is controlled over the whole relevant time window of the simulations by monitoring the convergence with respect to increasing the MPS bond dimension. We consider open boundary conditions and approximate the long-range matrix-product-operator (MPO) with a sum of exponentials, as detailed in Ref. [352], with a relative tolerance of 10^{-11}. Then, for fixed system size, we increase the MPS bond dimension D up to convergence, as shown in Fig. 6.9. We emphasize that convergence of entanglement entropy provides us with rigorous control on the validity of the results, contrary to the convergence

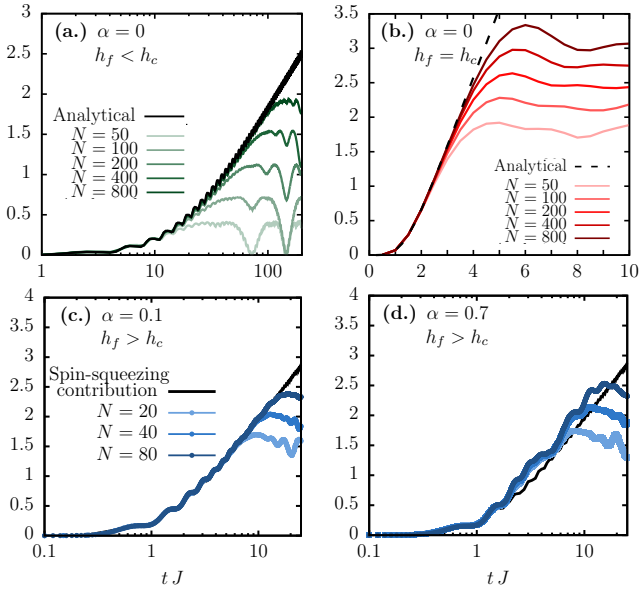

Figure 6.4: Theory and numerical results for long-range quantum Ising chains. Quenches in the transverse field $h_0 = 0 \to h_f > 0$ are considered, and the evolution of the half-system entanglement entropy $S_{N/2}(t)$ is shown. Top: Fully-connected limit with $\alpha = 0$. Analytical results (black lines) are compared with ED data for increasing system sizes $N = 20 \div 800$. (a.) For a noncritical quench $h_0 = 0 \to h_f = 0.2J$, the growth of $S_{N/2}(t)$ is logarithmic up to saturation around $1/2 \log N$ at $t_{Ehr} \sim \sqrt{N}$ (b.) For the critical quench $h_f = h_c = J/2$, the growth of $S_{N/2}(t)$ is linear until $t_{Ehr} \sim \log N$, with a slope $\lambda_{h_c} = J$. Bottom: Deep quench with $h_f = 2J$ in long-range interacting chains with $0 < \alpha \leqslant 1$. The contribution due to collective spin squeezing, Eq. (6.19), is compared with MPS-TDVP data for $N = 20 \div 80$ converged with bond dimension $D = 128$, for $\alpha = 0.1$ (c.) and $\alpha = 0.7$ (d). As α increases, small additional entanglement entropy contributions due to long-wavelength spin waves appear on top of the dominant logarithmic growth.

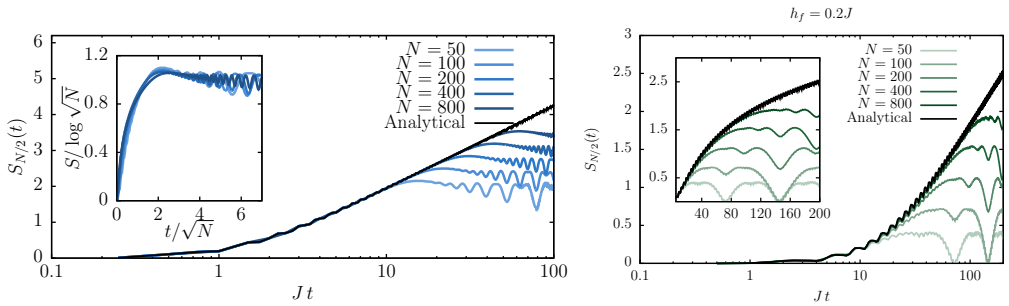

Figure 6.5: Logarithmic growth in time of the half-system entanglement entropy $S_{N/2}$ after a quantum quench above (top) and below (bottom) the dynamical critical point. We compare our general formula (6.19) with the exact numerical computation for increasing system sizes $N = 50 \div 800$. The exact diagonalization results follow the logarithmic growth up to $T_{Ehr} \sim \sqrt{N}$, where they saturate to $S_{N/2} \sim \log N$. The inset shows the same data with $S_{N/2}$ rescaled by $\log N$ and time by $\sqrt{N}$.

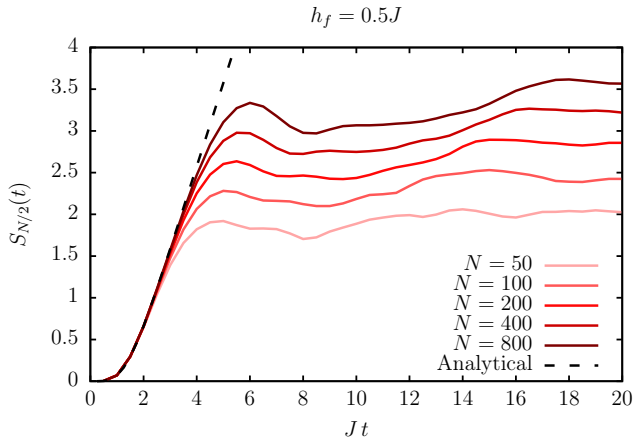

Figure 6.6: Linear growth in time of the half-system entanglement entropy $S_{N/2}$ at the dynamical critical point. We compare our general formula (6.19) with the exact numerical computation for increasing system sizes $N = 50 \div 400$. Before the Ehrenfest time $T_{Ehr} \sim \log N$, numerical data for $S_{N/2}$ are accurately reproduced by the analytical result (6.19) marked by the dotted line with a slope $\lambda_{h_c} = J$ [cf. Eq. (6.50)]. This linear regime is followed by saturation to a value $\sim \log N$.

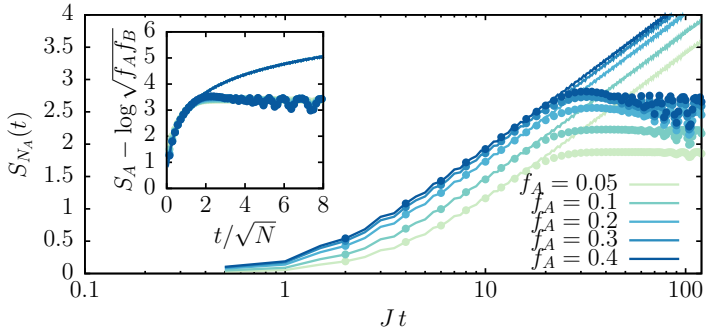

Figure 6.7: Entanglement entropy dynamics $S_{N_A}(t)$ after a quench dynamics from $h_0 = 0$ to $h_f = 2J$, for various bipartitions with fractions of spins $f_A = N_A/N = 0.05 \div 0.4$ and fixed size $N = 200$. Analytical results from Eq. (6.19) (full lines) are compared with exact numerical results (dots). In the inset, $S_{N_A} - 1/2 \log f_A f_B$ is plotted as a function of the rescaled time $t/\sqrt{N}$, in order to highlight the validity of the expansion in Eq. (6.20b).

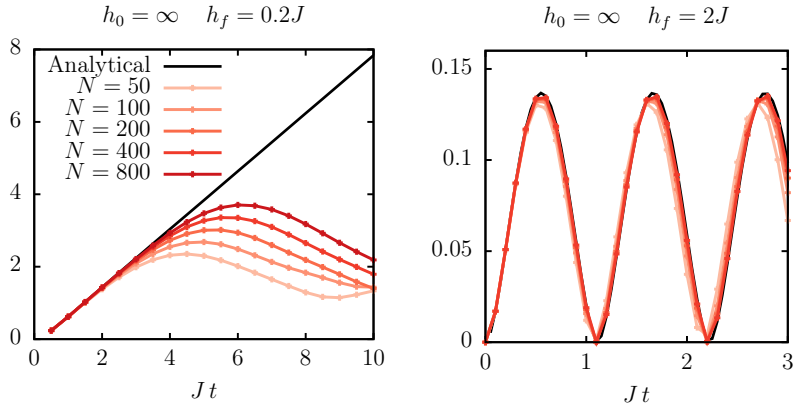

Figure 6.8: Half-system entanglement entropy dynamics after a quench from the paramagnetic ground state $|\phi_0\rangle$. Analytical results from Eq. (6.19) (black lines) are compared with exact numerical results (colors) at finite $N = 50 \div 800$. (Left) $h_f = 0.2J$ linear growth of $S_A \sim \lambda_{h_f} t$ with λ_{h_f} given in Eq. (6.50). (Right) $h_f = 2J$ periodic oscillations of $S_A(t)$ resulting from the periodic dynamics of the quantum collective fluctuations.

of local observables in Sec. 4.3.

As shown in Fig. 6.4(c),(d), the logarithmically growing entanglement entropy associated with collective spin squeezing represents the leading contribution for all considered values of α. Indeed, the small additional entanglement which appears upon increasing α can be understood as the contribution of the long-wavelength spin waves with $|\mathbf{k}| \propto 1/L$, which are not suppressed, see Eq. (6.45) and Fig. F.1.

We finally emphasize that all the phenomenology exemplified in Figs. 6.5, 6.6 and 6.7, as well as the quality of the agreement between the exact numerics and our analytical results, do not depend on the specific choice of the quantum Ising model (6.46), nor on the specific choice of pre- and post-quench parameters.

It is noteworthy to remark that the rigorous understanding of the slow entanglement growth presented in this Chapter sets the basis of the effectiveness of matrix-product-state techniques for simulating the nonequilibrium dynamics of long-range interacting systems, as these techniques rely precisely on low amounts of entanglement. The results above may be extended to a wider class of long-range models beyond spin systems, for which a general semiclassical description based on permutational symmetry is available, as discussed in Chap. 2, including models characterized by multiple collective degrees of freedom, such as the Dicke model for atomic ensembles collectively interacting with cavity light, see App. E. Such a model has been recently implemented in experiments with ionic crystals confined in a Penning trap [353] [cf. Sec. 1.2.1.] In this system, hyperfine levels of the ions are described by quantum spins, and the effective interactions between them are mediated by the center-of-mass vibrational mode of the crystal, realizing a well-isolated spin-boson Hamiltonian of Dicke form. We present the adaptation of formalism above to this model in App. E. It should be noted that, in this case, the "natural" bipartition is between the spins and the phonons. Due to the creation of entanglement between spins and phonons, the collective spin *uncertainty* grows in time. (This should be contrasted to isolated

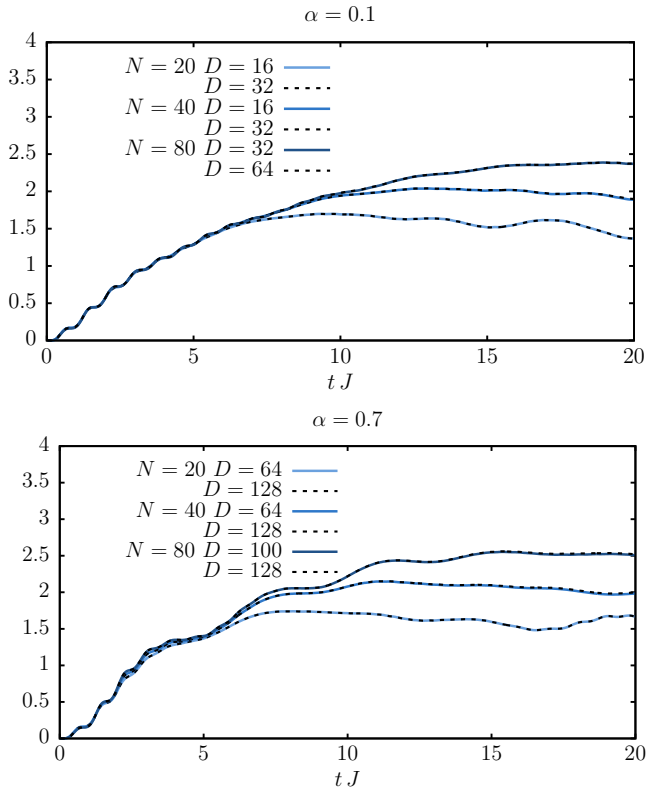

Figure 6.9: Convergence of the MPS-TDVP results with respect to increasing the bond dimension D, for $\alpha = 0.1$ (left panel) and $\alpha = 0.7$ (right panel) for a quench from $h_0 = 0$ to $h_f = 2$. Data for system size $N = 20 \div 80$ in full line are compared with dashed lines with larger bond dimension D.

spin systems, in which interactions make spin fluctuations *squeeze* without affecting the quantum uncertainty.) This uncertainty is readily accessible with standard tools of atomic physics, and offers a direct readout of the amount of entanglement entropy before the Ehrenfest time, as can be derived within the theory presented in this Chapter.

Part II

Slow dynamics by quantum confinement of excitations

Chapter 7

Effective confining potentials in one-dimensional quantum systems

In Sec. 1.2.2 of the Introduction, we have anticipated that a peculiar form of *effective* long-range interactions between elementary excitations may arise in quantum systems with local interactions. Unlike the previously discussed algebraically-decaying interactions, such emergent interactions increase with the spatial separation, which results in spatial confinement of elementary excitations. In this Chapter, we shall review the physics of confinement in one-dimensional quantum systems and its spectral and equilibrium signatures, on which most of the theoretical and experimental work has focussed so far.

As recalled in the Introduction, the nonequilibrium physics in the presence of confinement witnessed a renewed interest stimulated by the quest for atomistic quantum simulations of lattice gauge theories, and has started to be investigated in the context of condensed-matter models, as well. This research direction features a wealth of interesting open problems, and we shall address and discuss some of them in the next Chapter.

In the following, for the sake of definiteness, we shall discuss the Schwinger model of quantum electrodynamics in $1+1$-dimensional spacetime (Sec. 7.1). We shall recall how effective linearly-growing (Coulomb) potentials arise between charges (Sec. 7.1.3). This involves the elimination of the gauge field degrees of freedom, achieved by solving the Gauss law. Hence, we shall show how one may solve the gauge-symmetry constraint in the reverse way to eliminate matter degrees of freedom (Sec. 7.1.4). This procedure leads to an alternative formulation of the model in terms of *local* self-interactions of the gauge field only. Such a mechanism allows us to precisely establish a bridge between the occurrence of quantum confinement of excitations due to gauge invariance and that in condensed-matter models (Sec. 7.2). We shall finally discuss how qualitatively similar phenomena may occur in systems with algebraically-decaying interactions, such as those discussed in the Part I of the thesis, which lie beyond the paradigm of gauge-invariance (Sec. 7.3).

Due to the relative lack of discussion in the literature concerning the relation between confinement in condensed-matter theory and in particle physics, we decided to devote the present Chapter to review the relevant aspects of this subject. The exact mapping discussed in Sec. 7.2.3 represents the core of this presentation and is currently unpublished.

7.1 One-dimensional lattice gauge theories

The Schwinger model has been formulated by J. Schwinger in 1962 as an analytically tractable toy model to study nonperturbative properties of interacting quantum field theories [204]. The model represents a version of standard quantum electrodynamics in $1+1$ spacetime dimensions. Due to the triviality of the spatial part of the Lorentz group, particles and antiparticles are spinless fermions, and the electromagnetic field consists of a single-component electric field only. Fermions have mass m and electric charge $\pm e$ and interact via the mediation of the electric field. The model is defined by the Lagrangian density

$$\mathcal{L} = -\frac{1}{4} F_{\mu\nu} F^{\mu\nu} + \bar{\psi}\left(i\partial\!\!\!/ - eA\!\!\!/ - m\right)\psi, \tag{7.1}$$

where A_μ is the electromagnetic potential, $F_{\mu\nu} = \partial_\mu A_\nu - \partial_\mu A_\nu$ is the field strength tensor, and ψ is the two-component charged fermionic field. The indices $\mu, \nu = 0, 1$ indicate respectively the time and space directions, and the slash notation indicates contraction with the Dirac matrices γ^μ, which may be represented by the Pauli matrices as $\gamma^0 = \sigma^z$ and $\gamma^1 = i\sigma^y$.

Gauge symmetry is the statement that the action $S = \int d^2x\, \mathcal{L}$ is invariant under simultaneous transformations of the gauge and the matter field

$$\psi(x) \mapsto e^{-ie\chi(x)}\psi(x), \qquad A_\mu(x) \mapsto A_\mu(x) + \partial_\mu \chi(x). \tag{7.2}$$

In order to formulate a Hamiltonian quantization of the theory, one must fix a gauge choice. A typical choice is the temporal gauge $A_0 = 0$. In this case, one defines the single-component "vector" potential $A \equiv A_1$, whose canonically conjugate variable is the electric field $E = \dot{A}$. The quantum Hamiltonian reads

$$\hat{H} = \int dx \left[-i\hat{\bar{\psi}}\gamma^1\left(\partial_1 + ie\hat{A}\right)\hat{\psi} + m\hat{\bar{\psi}}\hat{\psi} + \frac{\hat{E}^2}{2} \right]. \tag{7.3}$$

7.1.1 Lattice formulation of the Schwinger model

The lattice regularization of gauge theories has been first introduced by K. Wilson [203,354]. Here, we shall briefly recall this construction for the Schwinger model. We define a one-dimensional lattice with sites at positions ja, where $j \in \mathbb{Z}$ and a is the physical lattice spacing. We adopt the Kogut-Susskind construction of staggered fermions [355], which consists in splitting the two components of the Dirac field into even and odd sites of the lattice. In this case, one has a single (spinless) fermionic field $\hat{c}_j$, formally defined on even and odd

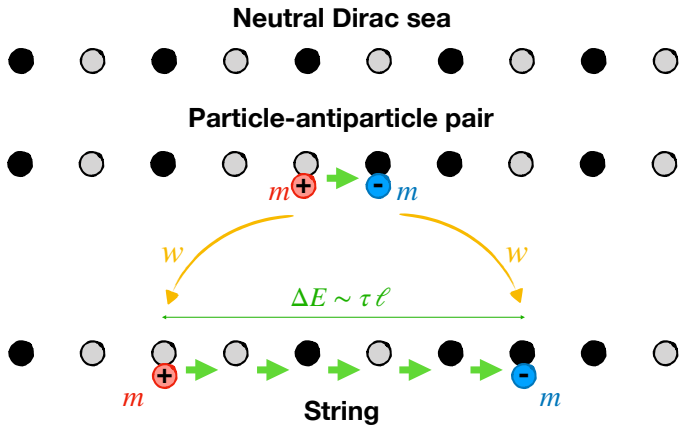

Figure 7.1: Cartoon illustration of classical configurations of charges and fields in the lattice Schwinger model in Eq. (7.10). Grey and black dots represent the configuration of Kogut-Susskind fermions $\hat{n}_j = \hat{c}_j^\dagger \hat{c}_j = 0, 1$ respectively. Green arrows represent a nonvanishing electric flux on the chain bonds, $\hat{L}_j = +1$ in this example. Top chain: ground state of the noninteracting model with $w = 0$ (Dirac sea). The electric field is vanishing everywhere, and no charges are present. Middle: A particle-antiparticle pair is created out of the vacuum by moving a Kogut-Susskind fermion. Concurrently, the value of the electric field in between changes in such a way that the Gauss law is respected. Bottom: the pair is pulled apart at a distance ℓ. The string of electric field between the charges generates the effective linear attraction potential. The conservation of the total number of Kogut-Susskind fermions corresponds to the conservation of the total physical charge.

sites as

$$\hat{\psi}_{\text{upper}}(x = 2la) \equiv \frac{\hat{c}_{2l}}{\sqrt{a}}, \qquad \hat{\psi}_{\text{lower}}(x = 2la) \equiv \frac{\hat{c}_{2l+1}}{\sqrt{a}}, \tag{7.4}$$

for $l \in \mathbb{Z}$. The lattice fermionic operators satisfy the standard anticommutation relations

$$\left[\hat{c}_i, \hat{c}_j^\dagger\right] = i\delta_{i,j}. \tag{7.5}$$

A hole in an odd site represents an antiparticle $\bar{q}$, while a fermion in an even site represents a particle q. Thus, a half-filled lattice in a staggered fermionic configuration, with odd sites occupied and even sites empty, represents the neutral Dirac sea. This is illustrated in Fig. 7.1.

The lattice regularization of the spatial derivative in the kinetic term of Dirac field involves fermionic field operators at distinct, adjacent lattice sites. Upon minimally coupling this matter field with the gauge field, the requirement of gauge invariance of the lattice Hamiltonian naturally leads to introduce the so-called parallel transporter $\hat{U}_{j,j+1}$,

$$e^{-ie\int_{ja}^{(j+1)a} \hat{A}(x)\,dx} \approx e^{-iaeA(x=ja)} \equiv \hat{U}_{j,j+1}, \tag{7.6}$$

associated with the dual lattice (i.e., with the chain bonds). Within the Hamiltonian formulation, the electric field $\hat{E}$ is the conjugate variable to the vector potential $\hat{A}$. For their lattice versions, it is convenient to define the dimensionless

quantities

$$ea\hat{A}(x = ja) \equiv \hat{\theta}_j, \qquad \frac{1}{e}\hat{E}(x = ja) \equiv \hat{L}_j, \tag{7.7}$$

which satisfy

$$\left[\hat{L}_i, \hat{\theta}_j\right] = -i\delta_{i,j}. \tag{7.8}$$

By construction, the gauge-invariant lattice regularization of the original continuum gauge theory involves a compact representation of the gauge field. In fact, the variables $\hat{\theta}_j$ are 2π-periodic, because the lattice-regularized Hamiltonian depends on it only through the parallel transporters. As a consequence, the conjugate variables $\hat{L}_j$ have integer spectrum. In terms of the parallel transporter $\hat{U}_{j,j+1} = e^{-i\hat{\theta}_j}$, the previous equation translates into

$$\left[\hat{L}_i, \hat{U}_{j,j+1}\right] = -i\delta_{i,j}\hat{U}_{j,j+1}. \tag{7.9}$$

The variables $\hat{\theta}_j$ and $\hat{L}_j$ may be interpreted as the angular configuration and the angular momentum, respectively, of a particle on a ring, i.e., as the canonical variables of a quantum rotor.

As results from the above discussion, the lattice version of the Schwinger model may be written as

$$\hat{H} = -w\sum_j \left(\hat{c}_j^\dagger \hat{U}_{j,j+1}\hat{c}_{j+1} + \text{h.c.}\right) + m\sum_j (-1)^j \hat{c}_j^\dagger \hat{c}_j + \tau\sum_j \left(\hat{L}_j - \frac{\theta}{2\pi}\right)^2. \tag{7.10}$$

As in the continuum Hamiltonian (7.3), the first term provides the minimal coupling between gauge and matter fields, the second term is the fermion mass, and the last term is the electric field energy. The extra classical parameter appearing in the last term, named θ-term or "topological angle",[1] represents a classical uniform background electric field, and has been introduced here for later purposes. As observed by Coleman [356], in $1+1$ dimensions θ is an independent parameter which nontrivially affects the physics, and the equilibrium properties of the system are 2π-periodic as a function of θ. The continuum limit is formally obtained by writing the couplings as

$$w = \frac{1}{2a}, \qquad \tau = \frac{e^2 a}{2}, \tag{7.11}$$

switching to the continuum normalization of the fields as in the definitions (7.4) and (7.7), and hence taking the limit of vanishing lattice spacing $a \to 0$.

As a consequence of staggerization, the conserved total fermion number corresponds to the total physical charge, see Fig. 7.1. Starting from the bare vacuum at $w = 0$ (Dirac sea), interactions may move fermions around, which corresponds to dynamical creation of particle-antiparticle pairs, accompanied by a corresponding change in the electric field value in between, such that the discrete Gauss law is satisfied. In fact, the local generators of the $U(1)$ gauge

[1] not to be confused with the gauge field quantum operator $\hat{\theta}_j$

symmetry of the model are

$$\hat{G}_j = \hat{L}_{j,j+1} - \hat{L}_{j-1,j} - \hat{Q}_j, \qquad \text{with } \hat{Q}_j \equiv \hat{c}_j^\dagger \hat{c}_j + \frac{1-(-1)^j}{2}, \tag{7.12}$$

and satisfy $\left[\hat{H}, \hat{G}_j\right] = 0$. A general gauge transformation is implemented by a unitary operator of the form

$$\hat{V}(\chi) = e^{-ie\sum_j \chi_j \hat{G}_j}, \tag{7.13}$$

and represents the lattice version of Eq. (7.2). The quantity $\hat{Q}_j$ in Eq. (7.12) represents the (dimensionless) charge content of site j. The physical states $|\Psi\rangle$ in Hilbert space satisfy the discrete version of the Gauss law

$$\hat{G}_j |\Psi\rangle = 0 \tag{7.14}$$

for all sites j.

7.1.2 $U(1)$-quantum link models

We observe that different formulations of $U(1)$ LGTs are obtained for different representations of the gauge degrees of freedom $\hat{L}_j$, $\hat{U}_{j,j+1}$ which satisfy the same commutation relations $\left[\hat{L}_i, \hat{U}_{j,j+1}\right] = -i\delta_{i,j}\hat{U}_{j,j+1}$. While in the standard Wilsonian formulation they span infinite-dimensional Hilbert spaces, one may also consider the so-called $U(1)$ quantum link models (QLM) [357,358], where they are represented by finite-dimensional quantum spin variables, i.e., $\hat{L}_j = \hat{s}_j^z$ and $\hat{U}_{j,j+1} = \hat{s}_j^+$, where $\hat{s}^\alpha$ are quantum spin-s operators. As noted in Ref. [218], this formulation is particularly suited for quantum simulation purposes. Note that the parallel transporter is no longer unitary in these models.

For later purposes, we comment here on the spin-1/2 version of the $U(1)$ quantum link model. This peculiar realization of quantum electrodynamics is equivalent to the lattice Schwinger model in the presence of a θ-angle close to $\theta = \pi$ and of a strong coupling τ [7]. To see this, with reference to the lattice Schwinger model in Eq. (7.10) above, let us introduce the parameter $\epsilon = \theta/\pi - 1$ which quantifies the deviation of the vacuum angle from π. For $|\epsilon| \ll 1$, the two lowest energy states of the electric field have $L_j = 0, +1$ on each bond. One requires the energy gap $2J(1+\epsilon) \equiv \Delta$ of the next excited state (either $L_j = 2$ or $L_j = -1$ depending on the sign of ϵ) to be much larger than that separating the first two, i.e., $\tau\epsilon \equiv \alpha$. Accordingly, the lattice Schwinger model with strong $\tau \gg w, m$ and with a topological angle

$$\theta = \pi\left(1 + \frac{\alpha}{\tau}\right) \tag{7.15}$$

is efficiently approximated by the $s = 1/2$ QLM with an additional linear term

in the electric field proportional to α, i.e.,

$$\hat{H} = -w \sum_j \left(\hat{c}_j^\dagger \hat{s}_j^+ \hat{c}_{j+1} + \text{h.c.} \right) + m \sum_j (-1)^j \hat{c}_j^\dagger \hat{c}_j - \alpha \sum_j \hat{s}_j^z, \tag{7.16}$$

where we have taken the quantum spin-1/2 (Pauli-matrix) representation of the gauge field.

7.1.3 Elimination of gauge degrees of freedom

By virtue of the Gauss law (7.14), the allowed configurations of charged matter and gauge fields are tightly related. In order to visualize this, we may consider a basis in Hilbert space which simultaneously diagonalizes all local fermionic occupation numbers $\hat{n}_j = \hat{c}_j^\dagger \hat{c}_j$ and all electric field operators $\hat{L}_j$. We shall refer to such a basis as the "basis of classical configurations" of the system: Indeed, the Hamiltonian is diagonal in this basis when quantum fluctuations are absent, i.e., in the limit $w \to 0$. See Fig. 7.1 for illustration.

A basis of the physical subspace is provided by the subset of classical configurations which satisfy the Gauss law at all lattice sites. The crucial observation is that either type of degrees of freedom (matter or gauge fields) is redundant within the physical subspace. In fact, if a classical configuration of the gauge fields is assigned, then the configuration of the charges at all sites is uniquely fixed by the Gauss law. Conversely, if a classical configuration of the charges is assigned, then the configuration of the gauge fields at all bonds is uniquely fixed by the Gauss law up to an overall additive constant, which is selected by the boundary condition. Consequently, the physical classical configurations in Hilbert space may be labelled either in terms of gauge fields only, or in terms of charges only. The Hamiltonian can be then recast in a form which involve gauge fields only, or charges only. In this Section, we explore the latter possibility, and show that the Schwinger model is equivalent to a model of electrons and positrons interacting via long-distance Coulomb forces. In the next Section, we shall instead discuss the opposite mapping, which will turn out to be extremely far-reaching.

The lattice Schwinger model in Eq. 7.10 in the gauge-invariant subspace spanned by wavefunctions $|\psi\rangle$ which satisfy the Gauss law $\hat{G}_j |\psi\rangle = 0$, can be exactly mapped onto an unconstrained chain of spin-1/2 degrees of freedom [359]. These spins are obtained from the fermionic operators via a modified Jordan-Wigner transformation expressed as

$$\hat{c}_j = \prod_{l=-\infty}^{j-1} \left(\hat{\sigma}_l^z \hat{U}_{l,l+1}^\dagger \right) \hat{\sigma}_j^- . \tag{7.17}$$

This transformation decouples matter and gauge degrees of freedom, and thus

the Hamiltonian 7.10 takes the form

$$\hat{H} = -w \sum_j (\hat{\sigma}_j^+ \hat{\sigma}_{j+1}^- + \text{h.c.}) + \frac{m}{2} \sum_j (-1)^j \hat{\sigma}_j^z + \tau \sum_j \left(\hat{L}_j - \frac{\theta}{2\pi} \right)^2 . \tag{7.18}$$

By means of the Gauss law, the electric field can be rewritten in terms of the spin operators,

$$\hat{L}_j = \sum_{l=-\infty}^{j} \hat{Q}_j = \sum_{l=-\infty}^{j} \frac{\hat{\sigma}_l^z + (-1)^l}{2} . \tag{7.19}$$

Inserting Eq. (7.19) into Eq. (7.18), and expanding the square, we obtain three additional terms. The constant proportional to θ^2 is the electrostatic background energy. The linear term in θ is the electrostatic energy of dynamical charges $\hat{Q}_j$ in the background field. Finally, the quadratic term in the dynamical charges is a long-range interaction which may be interpreted as a Coulomb force between charges. We recall that in one spatial dimension the elementary Coulomb potentials generated by isolated charges $\pm e$ at points $x = x_0$ are linear confining potentials $V(x) = \mp e|x - x_0|$, as results from the Laplace equation $\partial_x^2 V(x) = \pm e \delta(x - x_0)$. In fact, in the neutral charge sector where $\sum_{j=-\infty}^{\infty} \hat{Q}_j = 0$, the gauge field part of the Hamiltonian may be written as

$$\hat{H}_{\text{gauge}} = -\tau \sum_{k<j} (k - j)\, \hat{Q}_j \hat{Q}_k + \tau \frac{\theta}{\pi} \sum_j j\, \hat{Q}_j + \text{ vacuum energy.} \tag{7.20}$$

By comparing with the original Hamiltonian, we see that the long-range interactions arise because a string of electric field connects a separated charge-anticharge pair, such that the local electric energy density between them is different from that outside this region. The total energy cost of pulling the pair apart is thus proportional to their spatial separation, see Fig. 7.1.

As first recognized by Coleman [356], charged excitations in the Schwinger model are deconfined at the degenerate point $\theta = \pi$. In fact, every configurations with alternating positive and negative charges have constant electrostatic energy, independently of the relative position of the charges, due to the degeneracy of the local energy $[L - (\theta/2\pi)]^2$ for $L = 0, 1$. Therefore, charges may freely move around in this case. Such a particular condition is naturally realized in the quantum link model in Eq. (7.16) when $\alpha = 0$, as explained in the previous Section. However, confinement is restored as soon as $\alpha \neq 0$. This occurrence can be rendered explicit by eliminating gauge degrees of freedom with an analogous procedure to that presented above.

In $1+1$-dimensional gauge theories, the elimination of gauge degrees of freedom may be carried out directly in the continuum limit, see Ref. [356]. It is worth to observe that such theories are rather special, because the Coulomb *forces* in one dimension are independent of the distance. For this reason, there are no retardation effects due to a finite velocity of propagation, and hence no pure-gauge dynamical effects analogous to radiation/photons in standard electrodynamics. On the contrary, the possibility to obtain an effective Hamiltonian

for matter degrees of freedom only is generally precluded in higher-dimensional gauge theories, where interactions are nonlocal in time due to retardation effects.

7.1.4 Elimination of matter degrees of freedom

In the previous Section, we have seen how the elimination of gauge degrees of freedom results in a model of matter particles only, interacting via long-range Coulomb forces. As anticipated therein, the local dynamical constraint provided by the Gauss may be also exploited in the opposite way, i.e., to eliminate the matter degrees of freedom. In the continuum Schwinger model, this procedure corresponds to the well-known description of the theory in terms of a bosonic field (*bosonization*), see the classic reference [356]. It is important to remark that the resulting effective theory is *local* in this case, and describes a self-interacting gauge field. This occurrence should be contrasted to the nonlocal effective Hamiltonian for matter degrees of freedom described in the previous Section.

We shall outline a practical route to eliminate matter degrees of freedom and derive the effective Hamiltonian for the gauge field in lattice formulations. One labels all physical classical configuration in terms of the gauge field configuration only, and hence writes down all matrix elements of the Hamiltonian in this basis. This is equivalent to solving the Gauss law explicitly to express the charges in terms of the surrounding gauge fields at all lattice sites. In so doing, the mass term of matter particles translates into an energy cost for domain-walls in the gauge field classical configurations, and transitions induced by the interaction term have to respect local constraints corresponding to the allowed configurations of the charges. Specifically, in $\mathrm{U}(1)$ LGTs with fermionic matter as considered in previous Sections, the electric field may either remain unchanged or increase (decrease) by one unit across odd (even) sites, due to fermion staggerization. In this case, the resulting effective Hamiltonian may be interpreted as an extended Bose-Hubbard model with additional local constraints. Such constraints are not present if a bosonic scalar (Higgs) matter field is considered in place of fermionic particles [209, 360, 361].

The theoretical construction for the elimination of matter degrees of freedom described above has been recently put forward in Ref. [7] in connection with quantum simulations of lattice gauge theories with experimental platforms based on ultracold atoms. It has been recognized in that work, that the locality properties remarked above make this construction particularly suited for that purpose. Previously, related ideas for Higgs-$\mathrm{U}(1)$-LGTs had been proposed by Y. Kuno et al. [360, 362]. In a subsequent work by E. Zohar and J. I. Cirac [363], a completely general construction has been presented for lattice gauge theories with arbitrary gauge group and dimensionality.

In particular, in Ref. [7], it has been demonstrated that quantum simulations of interesting dynamical phenomena of a spin-1/2 $\mathrm{U}(1)$ quantum link model have already been performed in experiments with Rydberg-atom arrays trapped in optical tweezers in the group of M. Lukin [181]. This remarkable connection relies on the fact that the matter-eliminated Hamiltonian of the QLM maps exactly onto the effective Hamiltonian which governs the Rydberg-blockaded

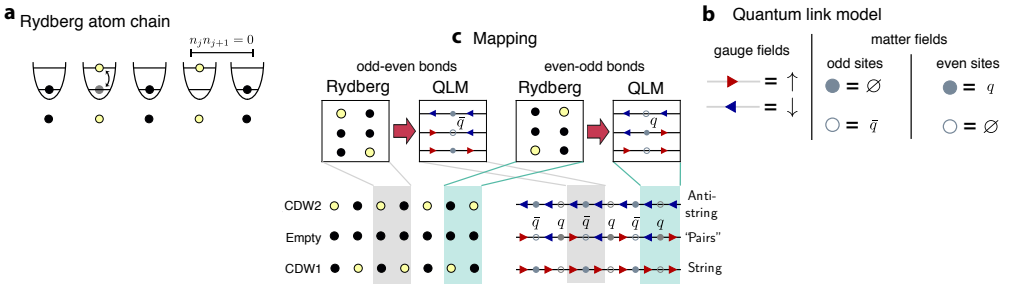

Figure 7.2: Gauge-theory interpretation of Rydberg-atom quantum simulations. **a**: Schematics of a Rydberg atom chain. Each potential well of the optical lattice hosts a single atom, which can be either in the ground (black) or excited Rydberg (yellow) state. The two levels are coupled by a laser field. The Rydberg blockade prevents the simultaneous excitations of neighboring atoms (cf. Sec. 1.2.1 in the Introduction). **b**: Degrees of freedom of a U(1) LGT in the spin-1/2 quantum link model (QLM) formulation. Gauge fields are represented by spin variables residing on links. Matter fields are represented by Kogut-Susskind fermions: an occupied site corresponds to the vacuum on odd sites, and to a quark q on even sites. An empty site, instead, to the vacuum on even sites and to an anti-quark $\bar{q}$ on odd sites. **c**: Mapping between Rydberg-blockaded states and configurations of the electric field constrained by the Gauss law in the QLM. Due to the staggered electric charge, the allowed configurations of the electric field depend on the link, as illustrated. The two so-called charge-density wave configurations "CDW1" and "CDW2" of the Rydberg-atom arrays are mapped onto the "string" and "anti-string" states, respectively, characterized by uniform rightward or leftward electric fluxes. The empty configuration with all Rydberg atoms in their ground state is mapped to a state filled by adjacent particle-antiparticle pairs.

chain in the experiment.

The Hilbert space structure following Gauss law is particularly simple in this LGT [218]. As depicted in Fig. 7.2**c**, for each block along the chain consisting of two electric fields neighbouring a matter field at site j, there are only three possible states, depending on the parity of j. The Hamiltonian for the electric field after matter-elimination can be exactly mapped onto [cf. Eq. (1.21) in the Introduction]

$$\hat{H} = \sum_{j=1}^{L} \left(\Omega \, \hat{P}^{\downarrow}_{j-1} \hat{\sigma}^{x}_{j} \hat{P}^{\downarrow}_{j+1} + \delta \, \hat{\sigma}^{z}_{j} \right) - \alpha \sum_{j=1}^{L} (-1)^{j} \hat{\sigma}^{z}_{j}, \tag{7.21}$$

where $\hat{\sigma}^{\alpha}_{j}$ are Pauli matrices at site j. The projections $\hat{P}^{\downarrow}$ onto the "down" state ensure that the spin-flip dynamics generated by $\Omega \neq 0$ is constrained within the Hilbert subspace without nearest-neighbor excited sites, as illustrated in Fig. 7.2**a**. Such a model with $\alpha = 0$ was introduced in Ref. [201] to model the dynamics of resonant excitations in a tilted one-dimensional Mott insulator, and further theoretically investigated in Ref. [364]. The same Hamiltonian also describes the aforementioned chain of trapped Rydberg atoms interacting via strong dipolar forces: When the spacing between the atoms is sufficiently tight, the system enters the so-called regime of Rydberg-blockade, in which dipolar interactions between neighboring excited atoms are so intense that all states with pairs of excited neighbors are energetically inaccessible and hence effectively projected out. For more details, see Sec. 1.2.1.

The constrained Hilbert space of Rydberg-atom chains (or of resonant tilted 1d Mott insulators) and that of a spin-1/2 $U(1)$ quantum link model are isomorphic.[2] A one-to-one correspondence between two bases of states can be established by identifying, alternately on odd and even lattice sites, the configurations of the atoms (ground-state or excited) allowed by the Rydberg blockade, with the classical configurations of the electric field allowed by the Gauss law (see Fig. 7.2**c**). In terms of the two Hamiltonians (7.21) and (7.16), this unitary transformation consists in identifying the operators $\hat{\sigma}_j^x \leftrightarrow 2\hat{s}_{j-1,j}^x$, $\hat{\sigma}_j^{y,z} \leftrightarrow (-1)^j 2\hat{s}_{j-1,j}^{y,z}$ and the parameters $2\Omega = -w$, $2\delta = -m$.

As anticipated above, this mapping overcomes the most challenging task in quantum simulating gauge theories, by restricting the dynamics directly within the gauge-invariant Hilbert space, and provides an immediate connection between Rydberg-atom experiments [181] and particle physics phenomena, as detailed in Ref. [7]. Thereby, matter-integration represents now one of the most promising routes to quantum simulations of gauge theories. In the next Section, we shall show that matter-integration represents the key to bridge gauge theories with confinement physics in condensed matter systems, as well.

7.2 Confinement in one-dimensional condensed-matter systems

As we have seen in previous Sections, particle confinement is a characteristic occurrence in interacting gauge theories in $1+1$ dimensional spacetime. Besides the example of $U(1)$ gauge theories detailed above (the Schwinger model of quantum electrodynamics), confinement may also occur in other Abelian [e.g., $\mathbb{Z}_n$] as well as nonAbelian [e.g., $SU(3)$] gauge theories.

As anticipated in the Introduction, an analogous effect is actually also ubiquitous in one-dimensional condensed matter systems. In this case, confinement typically arises in the ordered phases of systems with a spontaneously broken discrete symmetry, whose elementary particle/antiparticle excitations consist of kink/antikink configurations locally connecting different degenerate ground states (vacua). Upon explicitly breaking the symmetry by external fields or local interactions, the different vacua acquire a macroscopically different energy, making a pair of kink and antikink experience an interaction potential proportional to their spatial separation. As a consequence, the excitation spectrum undergoes a nonperturbative change, from a finite continuous band of "deconfined" free particles to a discrete tower of bound states of confined particles.

The phenomenon anticipated above, pertains to general one-dimensional quantum systems across a first-order quantum phase transition. Its occurrence has been first discussed by McCoy and Wu [223] in a paradigmatic statistical physics model, namely the quantum Ising chain in a tilted magnetic field, and stimulated much subsequent work based on field-theoretical descriptions [224–228]. Recently, experiments with inelastic neutron scattering

[2] In fact, it may be shown that both have dimension $\mathcal{F}_{L+2} \sim \text{const} \times \phi^L$, where $\mathcal{F}_\ell$ is the ℓ-th Fibonacci number, $\phi \approx 1.618$ is the golden ratio and L is the number of sites in the chain.

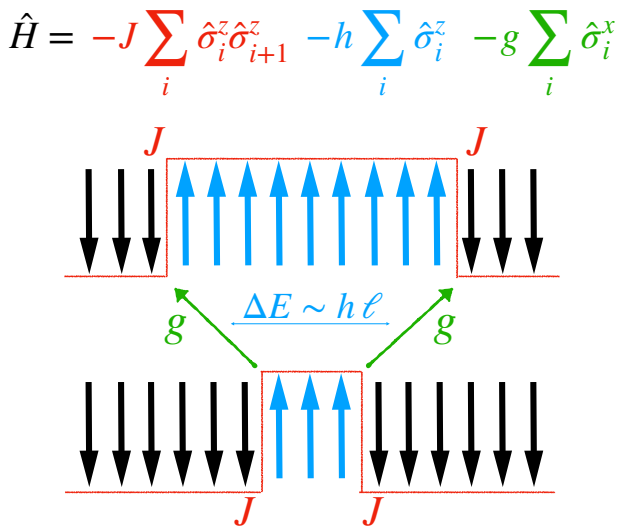

Figure 7.3: Schematic illustration of confinement of domain-wall excitations in a ferromagnetic quantum Ising chain. Black (blue) arrows represent spins polarized in the positive (negative) z directions. The energy of such configurations is equal to the energy cost of domain-walls ($\propto J$, red) plus the energy cost of the reversed domain ($\propto h$, blue), giving rise to an effective potential for domain-walls proportional to their spatial separation. A weak transverse field ($|g| \ll J$, green) generates an effective hopping of domain-walls. By virtue of the confining potential, domain-walls form bound states referred to as "mesons" in analogy with particle physics.

on quasi1d magnetic insulators have beautifully detected signatures of confinement [233, 234], and theoretical investigations have started to address lattice effects on confinement physics away from the critical scaling region in a number of quantum spin chains and ladders [229–232].

7.2.1 Confinement in the quantum Ising chain

We review the physics of confined excitations in condensed-matter systems, focusing on the quantum Ising chain for the sake of illustration. The model is defined by the Hamiltonian

$$\hat{H} = -J \sum_j \hat{\sigma}_j^z \hat{\sigma}_{j+1}^z - h \sum_j \hat{\sigma}_j^z - g \sum_j \hat{\sigma}_j^x, \tag{7.22}$$

where $\hat{\sigma}_j^\alpha$, with $\alpha = x, y, z$, are Pauli matrices acting on site $j \in \mathbb{Z}$. We use here the opposite convention $x \leftrightarrow z$ with respect to Eq. (1.1) in the Introduction. The Ising coupling $J > 0$ represents ferromagnetic nearest-neighbor interactions, and the external magnetic field has a longitudinal (h) and a transverse (g) component.

The quantum Ising chain in Eq. (7.22) is exactly solvable in the two limits $g \to 0$ and $h \to 0$. In the former case, the Hamiltonian is trivially diagonal in the $\hat{\sigma}^z$ basis. In the latter case, the model acquires a $\mathbb{Z}_2$ symmetry with respect to inverting the z-axis, and can be mapped to a quadratic fermionic Hamiltonian [41]. A quantum phase transition at $g = \pm J$ separates a symmetric,

paramagnetic phase ($|g| > J$) from a broken-symmetry, ferromagnetic phase ($|g| < J$) characterized by two degenerate and oppositely magnetized ground states $|\pm\rangle$ with $\langle\hat{\sigma}_j^z\rangle_\pm = \pm\sigma \neq 0$. The order parameter σ vanishes abruptly at the quantum critical point $g = \pm J$ with a critical behavior $\sigma \sim (1 - g/J)^{1/8}$ characteristic of the 2d classical Ising universality class. In the ferromagnetic phase, the free fermionic quasiparticles physically correspond to freely moving domain-walls (or kinks) connecting the two oppositely magnetized ground states.

Within the ferromagnetic phase, a finite longitudinal field $h \neq 0$ causes a nonperturbative modification of the spectrum of the elementary excitations. In fact, the perturbation selects as a ground state the one with $\langle\hat{\sigma}_j^z\rangle$ along h, and raises the energy of the opposite one by a macroscopic amount. Similarly, the longitudinal field raises the energy of configurations with domains of reversed spins by an amount proportional to the spatial extension of these domains. This corresponds to a linear, V-shaped interaction potential between two consecutive domain-walls delimiting a domain. The elementary quasiparticle excitations therefore become *confined* into composite objects called *mesons*, in analogy with the low-energy limit of gauge theories, as discussed above in Sec. 7.1. See Fig. 7.3 for an illustration. This phenomenon has been first recognized and studied in the Ising field theory, which describes the vicinity of the critical point $|g| \lesssim J$. More recently, it has been studied also away from criticality, where lattice effect cannot be neglected, still in the weak confinement regime $|h| \ll |g|$. (See the beginning of the Chapter for references.)

7.2.2 Spectrum of mesonic excitations

The mass spectrum of elementary mesonic excitations in the weak confinement regime has been studied analitycally by P. Fonseca and A. Zamolodchikov [227] and by S. B. Rutkevich [228]. The strategy followed by these authors consists in solving analytically the Schrödinger problem in the two-kink sector, and then perturbatively accounting for the corrections induced by transitions to sectors with four, six, ... kinks. In particular, due to the confining nature of the potential, the energy eigenstates of the two-kink problem form an infinite tower of bound states. Denoting by $m = 2\big(J - |g|\big)$ the rest energy ("mass") of kink excitations in the transverse field quantum Ising chain, the discrete mass spectrum $\{M_n\}_{n=1,2,...}$ of mesons lies in the interval $[2m, \infty)$ and reduces to a dense continuum for $h \to 0$. Above the threshold $M_n > 4m$, mesons become kinematically unstable, as they are expected to decay into two lighter mesons. Their lifetime near criticality has been determined by S. B. Rutkevich with semiclassical techniques [228]. Away from criticality, it has been recognized by the same author, that the decay of heavy mesons [230] is much slower and must have a nonperturbative origin.

The emergence of domain-wall confinement may actually be better visualized by resorting to the opposite limit of vanishing transverse field $g \to 0$, in which quantum fluctuations are suppressed and the Hamiltonian is diagonal in the basis of classical spin configurations in the z-direction in Hilbert space. The

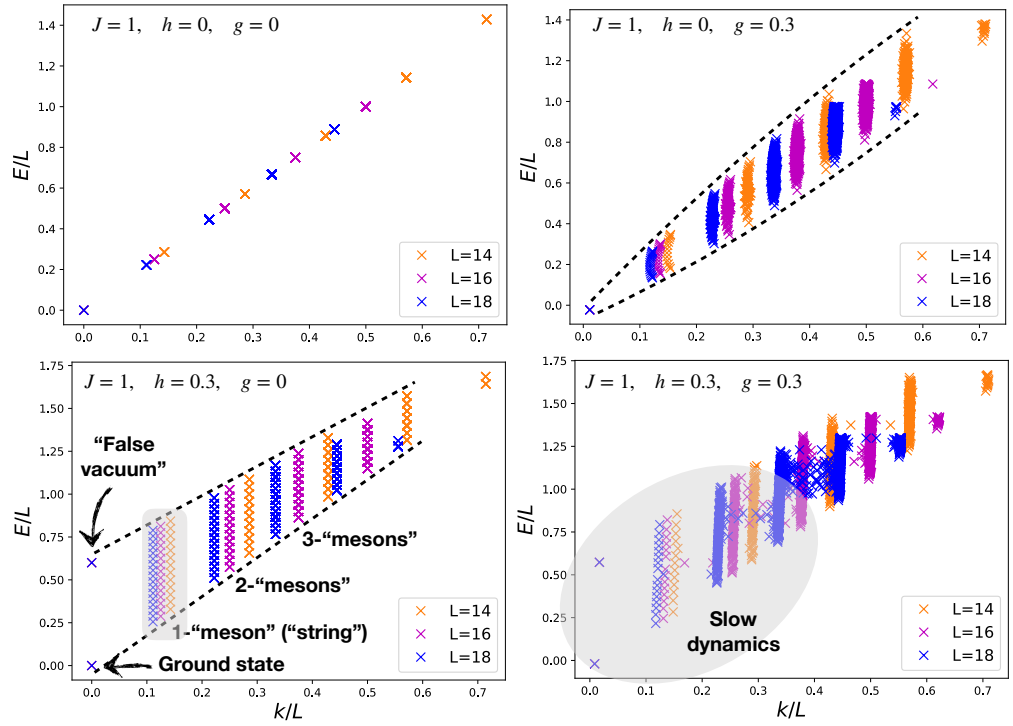

Figure 7.4: Spectrum of the quantum Ising chain in Eq. (7.22), obtained by numerical diagonalization of the Hamiltonian. The scatter plots show the excitation energy density $E/L = [\langle E|\hat{H}|E\rangle - E_{vac}]/L$ and the (average) density of kinks $k/L = [1 - \langle E|\sum_j \hat{\sigma}^z_j \hat{\sigma}^z_{j+1}|E\rangle/L]/2$ [cf. Eq. (7.23)] in each of the first 1.58^L excited eigenstates $|E\rangle$, denoted by crosses, for increasing chain length $L = 14, 16, 18$ (associated with colors), and for four different choices of the magnetic field h, g (associated with panels). In the thermodynamic limit $L \to \infty$, the spectrum densely fills the regions delimited by the black dashed lines, which serve as a guide to the eye. Top left: Classical Ising chain with a vanishing field $h = g = 0$. The ground state is twice degenerate, and the excitation energy is proportional to the number of kinks, $E_k - E_{vac} = 2Jk$. Top right: Quantum Ising chain in a transverse field ($h = 0$, $g \neq 0$). The latter respects the $\mathbb{Z}_2$ symmetry, and hence it does not lift the ground-state degeneracy. The energy density of excited states increases proportionally to the density of kink quasiparticles, which acquire a finite bandwidth in momentum space. (In this case, due to integrability with $h = 0$, the number of kinks survives for $g \neq 0$ as an exact quantum number across the whole spectrum, but this is not generic.) Bottom left: Classical Ising chain in a longitudinal field ($h \neq 0$, $g = 0$). The spectrum is given by Eq. (7.23). The longitudinal field breaks the $\mathbb{Z}_2$ symmetry. Consequently, one of the two original ground states for $h = 0$ — denoted "false vacuum" — acquires a finite excitation energy density when $h \neq 0$. Similarly, states with a low density of kinks form discrete towers (denoted "mesons") with extensive energy, labelled by the extra quantum number n in Eq. (7.23). The grey shading highlight the tower of two-kink bound states ($k = 2$). Bottom right: Quantum Ising chain in a skew magnetic field ($h \neq 0$, $g \neq 0$). The model is nonintegrable, and all excited states with equal energy density are expected to mix and become thermal in the thermodynamic limit $L \to \infty$ (in the sense of the eigenstate thermalization hypothesis, cf. Sec. 1.1.1). However, we shall show in Chap. 8 that the thermalization dynamics of states with a low density of kinks is extremely slow. This portion of the Hilbert space is highlighted by the grey shading. See also Refs. [365, 366].

spectrum of $\hat{H}$ in this limit is illustrated in the left panels of Fig. 7.4. All energy levels

$$E_{k,n} = E_{vac} + 2Jk + 2hn, \tag{7.23}$$

with $E_{vac} = -(J+h)L$, may be classified by two quantum numbers, namely the number of kinks k and the number of reversed spins n, and form a 2-dimensional "ladder". The following observation is crucial. For $h \to 0$, the number of kinks is a measure of the energy of the system, and states with few kinks have a finite energy. This property is preserved by arbitrary perturbations which respect the $\mathbb{Z}_2$ symmetry of the model. In this case, kinks may acquire a finite continuous dispersion bandwidth, as shown in the top right panel of Fig. 7.4. However, as soon as the symmetry is broken by a small longitudinal field component $h \neq 0$ (or other symmetry-breaking perturbations), states with a small number k of kinks may become macroscopically excited, because the excitation energy due to the longitudinal field is proportional to the extension of magnetic domains between consecutive kinks. States with a fixed k thus form unbounded discrete towers of states, labelled by the quantum number n. See Fig. 7.3.

By analogy with confinement in gauge theories, one refers to isolated kinks as "quarks", and to bound states of two kinks as "mesons". The dramatic change in the structure of the energy spectrum illustrated in Fig. 7.4, is the mathematical counterpart of the physics of confinement. In fact, asymptotic states with isolated traveling kinks cease to exist as soon as an infinitesimal symmetry-breaking perturbation is present.

In this picture, one may easily visualize the expected instability of heavy mesons for $|h| \ll J$: Large two-kink bound states (i.e., single mesons) with $k = 2$ and $n > 2J/h + 1 \gg 1$ have equal or larger energy with respect to four-kink states (i.e., two mesons), which are much more numerous. It is thus expected that the quantum fluctuations caused by a nonvanishing transverse field $|g| \ll J$ will stimulate the decay of a single meson ($k = 2$) into multiple mesons ($k = 4, 6, \dots$) in the long run. This will be discussed in the next Chapter.

7.2.3 Equivalence to $1+1$-d lattice gauge theories

In this Section, we shall show that one-dimensional quantum many-body lattice systems exhibiting confinement of excitations can be reformulated as confining lattice gauge theories (LGTs). This is achieved via the introduction of fictitious matter degrees of freedom on the dual chain, together with local dynamical constraints playing the role of the Gauss law.

In order to illustrate this equivalence, we shall focus on the quantum Ising chain introduced in Eq. (7.22), and show that this model can be exactly mapped to a $U(1)$ LGT. The correspondence is best understood by considering the basis of classical spin configurations introduced in the previous Section and illustrated in Fig. 7.5. The key point is to interpret the longitudinal projection of Ising spins $\hat{s}^z_j = \hat{\sigma}^z_j/2$ as the local "electric field", such that a kink (antikink) in the spin configuration is associated with the presence of a positron (electron) on the corresponding bond. By the Gauss law, the value of the electric field jumps

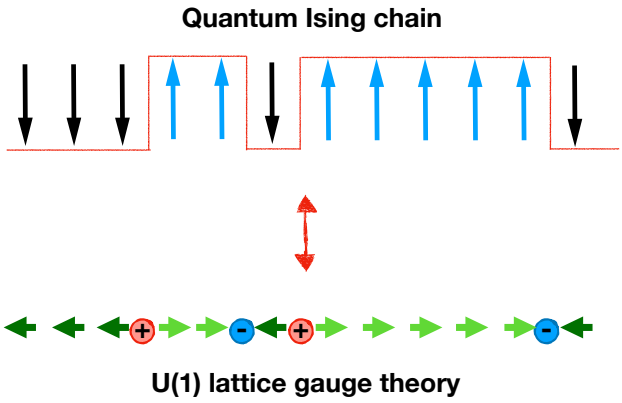

Figure 7.5: Illustration of the exact mapping between the quantum Ising chain in Eq. (7.22) and a $\mathrm{U}(1)$ lattice gauge theory described by Eq. (7.24), akin to the quantum link model introduced in Sec. 7.1.2, see the text. At the level of classical configurations, the mapping is realized by identifying the configuration of Ising spins (top) with that of the electric field (bottom, green arrows). By virtue of the Gauss law, the configuration of the latter determines also the configuration of the charges, provided a strong on-site "Hubbard" repulsion is considered which prevents charges and anticharges from sitting on the same site (see the text). The presence of a charge (anticharge) accompanies each jump upwards (donwards) of the electric field value along the chain, i.e., to a kink (antikink) in the Ising chain. At the level of the Hamiltonian, the Ising couplings represents an energy cost for kinks and antikinks, and maps to the mass of the particles. The longitudinal field maps to the string tension in the gauge theory. Finally, each of the terms in Eq. (7.24) is associated with a possible spin-flip transition in the Ising model, induced by the transverse field. This mapping is exact, and illustrates how confinement of excitations in condensed-matter models is equivalent to that in gauge theories as far as one-dimensional systems are concerned.

up (down) by one charge unit as the particle (antiparticle) is met along the chain, and bonds with no variation of the spin configuration contain no matter particles.

Interestingly, the possibility of mapping to a LGT may be implemented in different ways based, exploiting the same idea above. In particular, it is possible to formulate mappings to models with different gauge symmetry groups, such as $\mathbb{Z}_2$ or $U(1)$. In order to establish a closer analogy with the discussion on quantum electrodynamics in previous Sections, we shall detail the latter below. (The former has been established in unpublished work, and is not reported here.)

The mapping to a $U(1)$ LGT is illustrated in Fig. 7.5. One introduces two species of fermions ("+" and "−") residing on the dual chain, i.e., on the bonds of the original chain.[3] The corresponding creation operators $(\hat{c}_j^+)^\dagger$ and $(\hat{c}_j^-)^\dagger$ create a positron or an electron, respectively, at site j of the dual chain, corresponding to the bond $(j, j+1)$ of the original chain. Denoting the occupancy numbers $n_j^\pm = (\hat{c}_j^\pm)^\dagger \hat{c}_j^\pm$, we can write

$$\hat{H}_{U(1)} = \hat{H}_{\text{matter}} + \hat{H}_{\text{gauge}} + \hat{H}_{\text{int}}, \tag{7.24}$$

where

$$\hat{H}_{\text{matter}} = m \sum_j (\hat{n}_j^+ + \hat{n}_j^-) + U \sum_j \hat{n}_j^+ \hat{n}_j^-, \tag{7.25}$$

$$\hat{H}_{\text{gauge}} = \tau \sum_j \hat{s}_j^z, \tag{7.26}$$

$$\hat{H}_{\text{int}} = w \sum_j \Big[(\hat{c}_{j-1}^+)^\dagger \hat{s}_j^- \hat{c}_j^+ + \text{ h.c. } + \tag{7.27}$$

$$(\hat{c}_{j-1}^-)^\dagger \hat{s}_j^+ \hat{c}_j^- + \text{ h.c. } + \tag{7.28}$$

$$(\hat{c}_{j-1}^+)^\dagger \hat{s}_j^+ (\hat{c}_j^-)^\dagger + \text{ h.c. } + \tag{7.29}$$

$$(\hat{c}_{j-1}^-)^\dagger \hat{s}_j^- (\hat{c}_j^+)^\dagger + \text{ h.c. } \Big] . \tag{7.30}$$

In order to obtain an exact correspondence with the Ising chain, it is necessary to prevent particles and antiparticles to occupy the same place, which can be enforced with a strong Hubbard interaction $U \to \infty$.

Gauge-invariance of interactions is expressed by the local conservation laws

$$\left[\hat{H}, \hat{G}_j\right] = 0, \tag{7.31}$$

with

$$\hat{G}_j = \hat{s}_{j+1}^z - \hat{s}_j^z - (\hat{n}_j^+ - \hat{n}_j^-) m, \tag{7.32}$$

which give rise to the Gauss law constraints within the neutral gauge sector $\hat{G}_j \equiv 0$. In fact, the Gauss law asserts that the variation (discrete divergence)

[3] Note that our convenient choice is opposite to Wilson prescription for lattice regularization of gauge theories, whereby matter and gauge degrees of freedom are placed on lattice sites and bonds respectively. In one-dimensional chains, though, sites and bonds are actually interchangeable.

of the gauge field strength $\hat{\sigma}^z$ across a bond $(j, j+1)$ equals the charge content $\hat{Q}_{j,j+1}$ of the bond. In the neutral gauge sector, the charge is given by the dynamical fermions, i.e., $\hat{Q}_{j,j+1} = \hat{n}_j^+ - \hat{n}_j^-$ on the bond.

In view of the discussion in Sec. 7.1.4, it is clear that a given classical configuration of the gauge field fully specifies the configuration of the matter particles via the Gauss law. The redundant matter degrees of freedom may be thereby eliminated. One can check that all matrix elements of the Hamiltonian (7.24) between two classical gauge field configurations, coincide with the corresponding matrix elements of the quantum Ising chain in Eq. (7.22), upon identifying the electric field $\hat{s}_j^z$ with the Ising spins $\hat{\sigma}_j^z/2$ and the parameters $m = 2J$, $\tau = 2h$, $w = 2g$.

The exact mapping between $\hat{H}_{U(1)}$ and the quantum Ising chain is similar to that between the $s = 1/2$ $U(1)$-quantum link model in Eq. (7.16) and the Rydberg-blockaded chain in Eq. (7.21). The major difference regards fermions, which are of "Hubbard-type" in Eq. (7.24) whereas staggered (Kogut-Susskind) fermions enter the QLM in Eq. (7.16). Analogous mappings may be constructed for any one-dimensional quantum chain. The presence of confinement between domain-wall excitations can thus be recast in the form of Coulomb potentials between matter particles in a gauge-invariant interacting theory.

7.3 "Confinement" in systems with long-range interactions

In this final Section, we show that confinement of excitations may arise in systems with long-range interactions, such as those considered in Part I of the thesis. This aspect has been put forward in a recent work by F. Liu and coworkers, Ref. [267]. In this case, the effective confining potential between excitations is *nonlinear*, which precludes interpretations via underlying gauge symmetries. However, as we shall see, the resulting phenomenology bears important similarities with the systems studied in Sec. 7.2.

As discussed in the Introduction, long-range interactions may stabilize ordering at finite temperature in one-dimensional chains. Correspondingly, a pair of adjacent domain-wall excitations may not be able to travel far apart from each other indefinitely, even in the absence of a symmetry-breaking field. This hints at the existence of an effective confining potential between domain-walls.

7.3.1 Nonlinear confining potential between domain-walls

In order to bring the discussion to a formal level, we consider the long-range ferromagnetic quantum Ising chain, already presented in the Introduction and studied in Chaps. 5 and 6. The Hamiltonian of the system is reported here for convenience,

$$\hat{H} = -\frac{J}{\mathcal{N}_{\alpha,L}} \sum_{1 \leqslant i \neq j \leqslant L} \frac{\hat{\sigma}_i^x \hat{\sigma}_j^x}{\|i-j\|^\alpha} - g \sum_{i=1}^{L} \hat{\sigma}_i^z. \tag{7.33}$$

In this equation, $\hat{\sigma}_i^{x,y,z}$ are Pauli matrices, L is the number of spins along the chain, g is a transverse magnetic field, and the exponent $\alpha \geqslant 0$ characterizes the

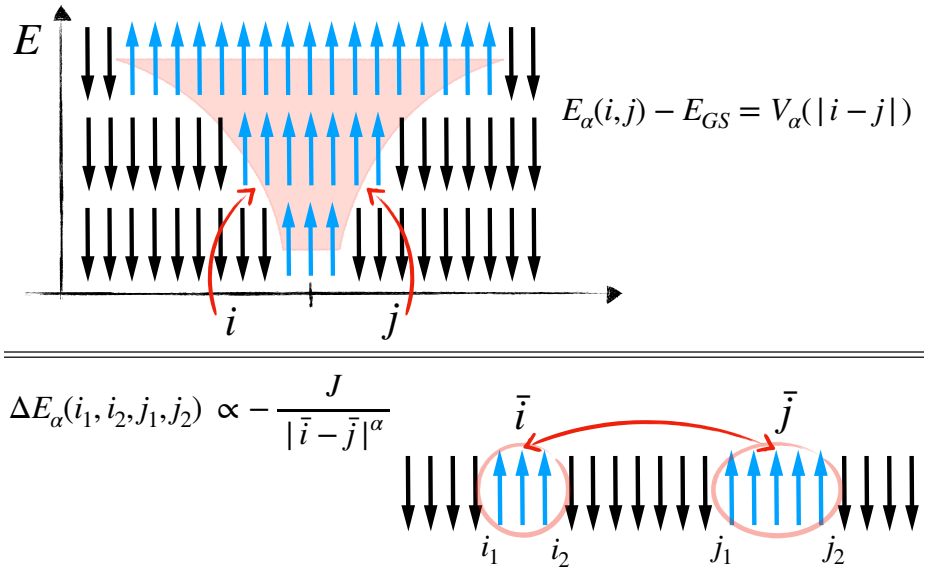

Figure 7.6: Illustration of the effective attraction between domain-walls in the long-range quantum Ising chain in Eq. (8.34). Top: As domain-walls as pulled apart, the configurational energy increases as described by the effective potential V_α computed in the text. Botton: Bound domain-walls form mesons. Such composite objects feel a residual attraction due to the long-range nature of the interactions, as discussed in Sec. 7.3.2.

range of the ferromagnetic spin-spin interaction. Periodic boundary conditions are assumed, with the distance defined as the minimal distance along the ring $||i-j|| \equiv \text{Min}\left(|i-j|, L-|i-j|\right)$. The Kač rescaling factor $\mathcal{N}_{\alpha,L} = \sum_{1\leqslant i\neq j\leqslant L}||i-j||^{-\alpha}/(L-1)$ ensures that taking the local energy scale $J>0$ independent of α and of the system size results in a proper thermodynamic limit [324] [cf. Eqs. (5.4) and (6.39)].

Confinement of domain-wall excitations occurs in the ordered (ferromagnetic) phase $|g| < g_{cr}(\alpha)$ of this model, for $\alpha \leqslant 2$. To see this, let us determine the spectrum of excitations in the limiting case $g \to 0$, in which the Hamiltonian is diagonal in the $\hat{\sigma}^x$ basis. The two degenerate ground states are fully and oppositely magnetized along the x direction. The whole spectrum may be classified in terms of the number of domain-walls and of their distances along the chain.

A first tower of excitations is constituted by states with two kinks separated by a distance $n = 1, 2, \ldots$ as illustrated in Fig. 7.6. The excitation energy of such states above the ground state is

$$V_{\alpha,L}(n) = \frac{2J}{\mathcal{N}_{\alpha,L}} \sum_{1\leqslant i\leqslant n} \sum_{n+1\leqslant j\leqslant L} \frac{1}{||i-j||^\alpha}, \tag{7.34}$$

and may be interpreted as a configurational energy cost for creating and pulling a pair of kink-antikink excitations to a distance of n lattice sites apart. The occurrence of confinement depends crucially on the large-distance properties of this effective potential. For large n and L, the leading term of this expression may be obtained by estimating the sums in Eq. (7.34) via the corresponding

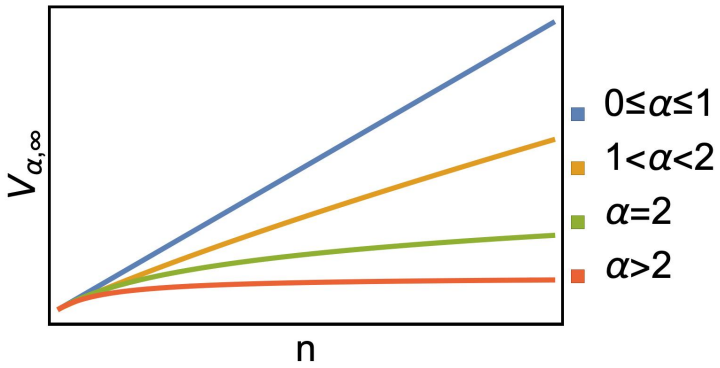

Figure 7.7: Plot of the effective attraction potential between domain-walls in the long-range quantum Ising chain, expressed by Eq. (7.35).

integrals. One finds

$$V_{\alpha,L}(n) \underset{\substack{L\to\infty \\ n\gg 1}}{\sim} 4J \times \begin{cases} n & \text{for } 0 \leqslant \alpha \leqslant 1 \\ c_\alpha\, n^{2-\alpha} & \text{for } 1 < \alpha < 2, \\ \dfrac{6}{\pi^2}\, \log n & \text{for } \alpha = 2, \\ 1 - c_\alpha \left(2^{2-\alpha} - \dfrac{1}{n^{\alpha-2}}\right) & \text{for } \alpha > 2, \end{cases} \tag{7.35}$$

with $c_\alpha = 1/[(2-\alpha)(\alpha-1)\zeta(\alpha)]$, ζ is the Riemann zeta-function. The behavior of the effective potential as determined by Eq. (7.35) is shown in Fig. 7.7.

Upon considering a small transverse field $|g| \ll J$, the structure of the two-kink spectrum may be understood by projecting the Hamiltonian onto the two-kink subspace. The resulting two-body problem in the center-of-mass frame is described by an effective Hamiltonian H_{eff}, with matrix elements

$$\left[H_{\text{eff}}\right]_{n,m} = V_{\alpha,L}(n)\,\delta_{n,m} - 2g\left(\delta_{n,m+1} + \delta_{n,m-1}\right). \tag{7.36}$$

In this expression, $V_{\alpha,L}(n)$ is the ladder of unperturbed energy levels computed above, and the transverse field g provides a nearest-neighbor hopping amplitude for kinks by flipping spins at the edges of the domain with reversed magnetization.

The resulting spectrum is determined primarily by the shape of the potential $V_{\alpha,L}(n)$, which we display in Fig. 8.9 for some representative values of α. By Eqs. (7.35), for $\alpha > 2$ the potential is asymptotically flat in the thermodynamic limit, i.e., it approaches a finite limiting value $V(\infty)$ as $n \to \infty$. Therefore, the potential well hosts a finite number of bound states, which increases from zero for $\alpha \to \infty$ to infinity for $\alpha \searrow 2$. In particular, all eigenstates with a sufficiently large quantum number $n > n^*(\alpha)$ are scattering states, i.e., spatially-extended waves characterized by their quasimomentum, and form a finite continuous band in the thermodynamic limit. The quantity $V(\infty) - V(1)$ represents the "ionization energy" of the bound state, i.e., the energy cost for deconfining a pair of domain-walls.

However, the structure of the two-kink spectrum undergoes a discontinuous change as α is decreased below 2. In this case, the effective potential $V(n)$ between consecutive domain-walls becomes confining at large distances, i.e., it grows unbounded as $n \to \infty$. As a consequence, all two-kink states are bound, and the spectrum remains an infinite discrete ladder in the thermodynamic limit. By analogy with confinement in gauge theories, we shall refer to bound states of domain-walls as "mesons".

To summarize, one has the following structure of the spectrum of excitations on varying the range of interactions. For long-range interactions with $\alpha \leqslant 1$, one recovers the mean-field result in the thermodynamic limit, with equally spaced excitations (cf. Chap. 2 and App. F). In the regime with an intermediate range $1 < \alpha \leqslant 2$ of interactions, one has a nonlinear effective confining potential for adjacent domain-walls. Finally, for $\alpha > 2$ one has a finite energy gap for topological excitations, i.e., isolated domain-walls which destabilize ferromagnetic long-range order. We see that "confinement" of domain-walls in one-dimensional quantum systems with a discrete symmetry, is the counterpart of the stabilization of long-range order.

Similarly to the short-range quantum Ising chain in a tilted field discussed above in Sec. 7.2, a nonvanishing transverse field $|g| \ll J$ is expected to induce an instability of heavy mesons with $n \gg 1$. In fact, these states are quasiresonant in energy with states with multiple lighter mesons characterized by a smaller quantum number n. Since such states are much more numerous, one expects that quantum fluctuations will lead to decay processes in the long run. We shall address such dynamical problems in the next chapters.

7.3.2 Residual attraction between "mesons"

The confining forces which bind together domain-walls may be seen as the analog of the strong interactions that bind together quarks in protons and neutrons. However, at low energies, such composite particles may bind together into atomic nuclei via residual, weaker "molecular" interactions. Such an effect exists also in the systems under considerations, due to the long range of interactions, whereby mesons may bind together.

A simple estimate of this effect can be given as follow. Suppose we have two mesons, [1] and [2], characterized by quantum numbers n and m related to their extent, respectively, and placed around sites $\bar{i}$ and $\bar{j}$ along the chain of length $L \gg r$, as shown in the bottom of Fig. 7.6. The excitation potential energies of each isolated meson, $V_\alpha(n)$ and $V_\alpha(m)$, have been computed above and depend on the value of α. The total configurational energy of the system can be expressed as

$$E_{tot} \equiv E_{GS} + V_\alpha(n) + V_\alpha(m) - \Delta E_\alpha(r). \tag{7.37}$$

This equation defines quantity ΔE_α, which represents the *binding energy* of the two mesons. In the limit $g \to 0$ of vanishing quantum fluctuations, its exact

expression is

$$\Delta E_\alpha(r) = \frac{2J}{\mathcal{N}_{\alpha,L}} \sum_{i\in[1]} \sum_{j\in[2]} \frac{1}{|i-j|^\alpha}. \tag{7.38}$$

If $\bar{i}$ and $\bar{j}$ are the positions of the centers of the two mesons, we may give a simple estimate valid for $|\bar{i}-\bar{j}| \gg n, m$:

$$\Delta E_\alpha\big(|\bar{i}-\bar{j}|\big) \;\sim\; \frac{2J}{\mathcal{N}_{\alpha,L}} \frac{1}{\big|\bar{i}-\bar{j}\big|^\alpha}. \tag{7.39}$$

As expected, for $\alpha \leqslant 1$ the binding energy vanishes in the thermodynamic limit ($\mathcal{N}_{\alpha,L} \sim L^{1-\alpha}$), because individual spins only feel each other via a mean field, and thus the two mesons have a vanishing additional binding energy. However, for $\alpha > 1$, one finds that mesons attract each other with the bare long-range forces of the system, proportional to $r^{-\alpha}$. This should be contrasted to the behavior of domain-walls, which attract each other with the confining potential proportional to $r^{2-\alpha}$ and $\log r$ for $\alpha = 2$. In a simple analogy, kinks represent charged particles which attract each other with a potential $V_\alpha(r)$, and mesons represent neutral dipoles, which attract each other with a potential $\sim \partial^2 V_\alpha/\partial r^2$. See the bottom of Fig. 7.6 for an illustration.

Chapter 8

Dynamical signatures of confinement

The equilibrium physics associated with confinement has been intensely investigated in the last decades, mostly via imaginary-time path-integral MonteCarlo simulations [367–370]. However, such a method usually suffers from severe sign problems in real-time computations [371]. This obstacle precludes the numerical investigation of dynamical phenomena involved in many important setups, such as heavy-ion collisions and early-Universe evolution [215]. As recalled in Sec. 1.2.2 of the Introduction and in Chap. 7, the recent efforts in developing quantum simulation platforms have stimulated a renewed interest in real-time confinement physics [215–217, 372]. This field is still in its infancy, and the results currently in sight concern simple (Abelian) lattice gauge theories in $1+1$ spacetime dimensions, rather than $\mathrm{SU}(3)$ quantum chromodynamics in a $3+1$ dimensional spacetime, which would be the ultimate goal from the particle-physics perspective. In spite of significant simplifications, the former theories share with the latter many nontrivial properties, such as confinement and chiral symmetry breaking [215].

In the light of the above discussion, it is natural to address the nonequilibrium evolution of quantum chains with confinement of excitations. As we have demonstrated in Sec. 7.2.3, such models may always be interpreted as confining lattice gauge theories. Besides the goal of quantum simulating particle-physics phenomena, the perspective of statistical physics and condensed matter theory also offer a wealth of natural questions. For instance, it is a priori unclear whether gauge-invariance and confinement can give rise to interesting nonequilibrium behavior, such as, e.g., slow thermalization, glassy dynamics, ergodicity breaking, nonthermal stationary states, ... Such questions could be relevant not only for matter in extreme conditions, but also for a number of interesting condensed-matter systems which possess an effective low-energy description in terms of an emergent lattice gauge theory, such as frustrated quantum antiferromagnets or spin liquids — see references quoted in the review in Ref. [215]. Moreover, this problem is directly relevant for (quasi)one-dimensional quantum systems with confined excitations, such as those discussed in Sec. 7.2 — see the references therein. In this respect, these phenomena may be investigated, ob-

served and measured with ultracold atoms trapped in low-dimensional optical lattices.

Several recent numerical studies have addressed the consequences of confinement on the real-time nonequilibrium dynamics of highly-excited states. In many circumstances, it appears that confinement is associated with anomalous dynamical behavior and spectral properties even at finite energy density above the ground state, where conventional thermalization would be a priori expected. The major signatures of this occurrence are manifest after a global quench, whereby one finds extraordinarily long-lived coherent oscillations of local observables, suppression of light-cone spreading of quantum correlations and transport, and bounded dynamical entanglement entropy. These striking phenomena should be contrasted to the "common-wisdom" behavior of quantum many-body systems, reviewed in Sec. 1.1 of the Introduction.

In the following, we shall first review in Sec. 8.1 the existing numerical evidence of the above signatures in the literature. Hence, we present in Secs. 8.2 and 8.3 a theoretical discussion on the origin of such anomalous dynamical behavior. The last Sec. 8.5 is devoted to numerical simulations which confirm the theory expectations in a variety of relevant models. The theoretical understanding presented in Secs. 8.2 and 8.3 is in large part the subject of ongoing (unpublished) work, whereas the numerical simulations of Sec. 8.5 have been reported in the publications in Refs. [5–7].

8.1 Confinement and slowdown of thermalization

Most investigations on the nonequilibrium dynamics of systems with confined excitations concern two classes of initial states, namely the "bare vacuum" states with no particles, and "bare strings" with a particle-antiparticle pair separated at a certain distance, cf. Figs. 7.1 and 7.3. Such states are eigenstates of the noninteracting Hamiltonian with vanishing gauge-invariant matter-field coupling. Then, a quantum quench to a nonvanishing value of this coupling gives rise to nonequilibrium time-evolution. The interacting Hamiltonian has no extra local conservation laws, and the considered initial states are highly-excited atypical states at finite energy density. According to conventional statistical mechanics, the system is thus expected to locally equilibrate to the thermal ensemble at a temperature set by its energy density, cf. the discussion in Sec. 1.2.2 of the Introduction.

It has been observed that in many circumstances where confinement is present, such expectation is actually not fulfilled. In particular, time-evolution after a global homogeneous quench may show surprising long-lived coherent oscillations in local observables [208, 373], for weak quenches [212, 289] at low energy density above the interacting ground state, see Fig. 8.1. Concurrently, the spatial spreading of equal-time quantum correlations between local observables (see Sec. 1.1.1) is anomalously weak beyond a characteristic length scale, and the dynamical growth of entanglement entropy (see Sec. 1.1.5) is also remarkably suppressed, as reported in Ref. [289] and illustrated in Fig. 8.2. This occurrence

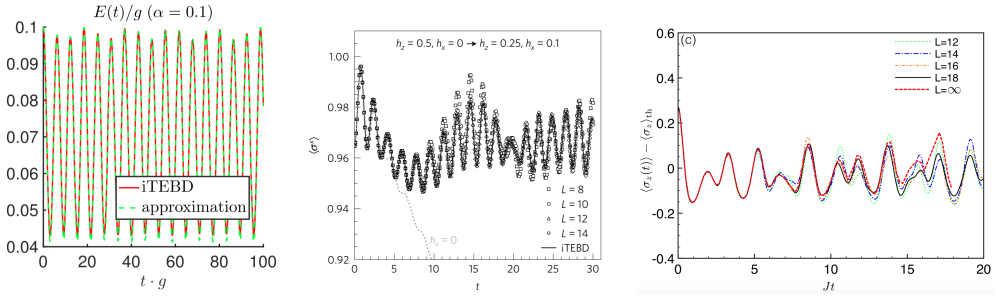

Figure 8.1: Instances of extraordinarily long-lived coherent oscillations of local observables after a global quench in systems with confined excitations, from Refs. [212] (left) [289] (middle), [375] (right panel). Left: dynamics of the electric field after a quench of the background field in the Schwinger model. Middle: dynamics of the longitudinal magnetization in a ferromagnetic quantum Ising chain after a quench of the tilted field, in the regime of weak confinement. Right: same as in the middle panel, but for a deep quench away from the perturbative regime. Both models have confined excitations, and coherent oscillations may be interpreted as the excitation of a dilute condensate of zero-momentum mesons [212, 289, 375].

has been connected with confinement of quasiparticles into stable mesons, cf. Chap. 7 [289, 365, 366]. The weak thermalization scenario proposed by M. C. Bañuls et al. in Ref. [374] can also be related to the condensation of stable "mesonic" quasiparticles, building on the results by C. J. Lin and O. I. Motrunich [375].

It is interesting to further observe that the long-lived coherent oscillations discovered in the experiment with a Rydberg-blockaded chain reported in Ref. [181] (cf. Sec. 1.2.1) have also been connected with the nonequilibrium dynamics of a lattice gauge theory via the exact mapping presented in Sec. 7.1.4. In this last case, long-time coherence seems to have a different origin, connected with a subset of nonthermal eigenstates dubbed "many-body quantum scars" [376] or closeness to integrability [377] in the continuum limit [7]; this subject is currently under active debate and will not be discussed here.

The lack of equilibration discussed above is even more striking in inhomogeneous conditions such as in string dynamics. Here, a variety of numerical simulations in several $1+1$-dimensional lattice gauge theories as well as with several techniques, have reported a remarkable stability of string inhomogeneity, even in the conditions particle production by string breaking would be energetically accessible and entropically favorable [207, 209, 213, 214, 221, 365, 366, 378]. In Fig. 8.3, we report a remarkable instance of this phenomenon in the spin-1 U(1)-quantum link model from Ref. [213]. Using the language of Sec. 7.2 above, the suppression of string breaking may be viewed as the long-time stability of kinematically unstable heavy mesons.

Our purpose in this Chapter is to rationalize such diverse findings reviewed above and provide theoretical understanding for the seemingly ubiquitous slowdown of nonequilibrium dynamics and thermalization in systems with confinement of excitations. The exact mappings discussed in Chap. 7 provide a rigorous bridge between condensed-matter systems and lattice gauge theories via the elimination of matter degrees of freedom. Below, we shall show that

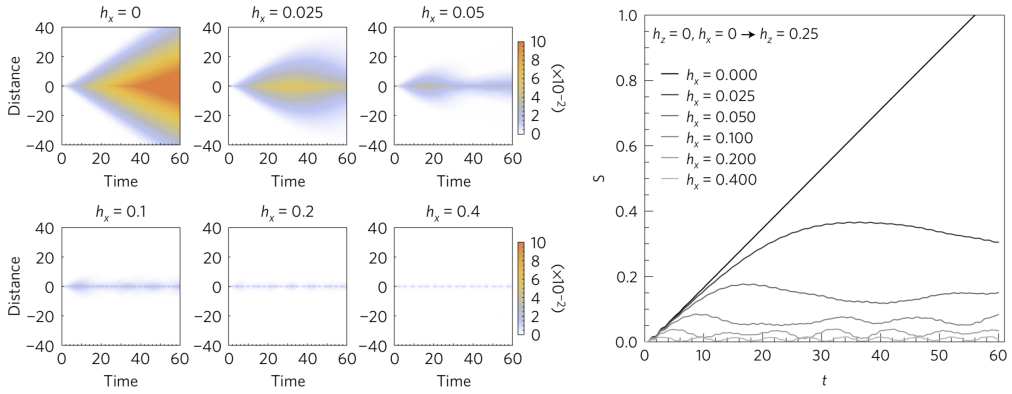

Figure 8.2: Instances of the suppressed spreading of quantum correlations (left) and of the suppressed growth of half-chain entanglement entropy growth (right) after a global quench in a ferromagnetic quantum Ising chain in the regime of weak confinement, from Ref. [289]. The initial state is the fully polarized ferromagnetic state, which evolves in the presence of a transverse (h_z) and longitudinal (h_x) field. Data show the results for a fixed post-quench transverse field and a range of values of the longitudinal field. As soon as the latter is activated, spreading of quantum information information is severely slowed down. In the quoted article, this phenomenon has been recognized to be due to excited quasiparticles pairs binding into zero-momentum mesons. This occurrence signals a nonperturbative dynamical effect of confinement of excitations.

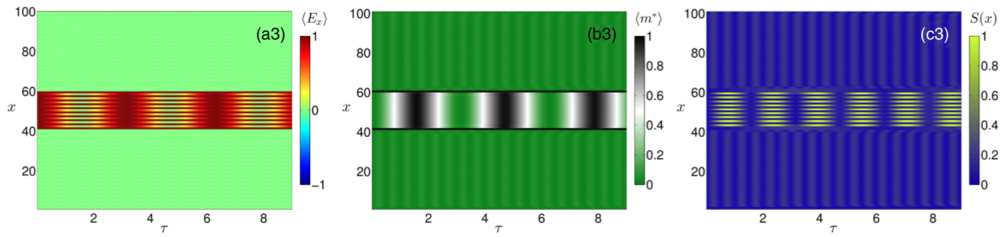

Figure 8.3: Instances of suppressed string breaking in the real-time evolution of a the $U(1)$ quantum link model with $s = 1$, a confining lattice gauge theory akin to the Schwinger model (see Sec. 7.1.2 for details), in the regime of weak matter-field coupling, from Ref. [213]. The initial state is an eigenstate of the noninteracting Hamiltonian with vanishing matter-field coupling, and has a particle and an antiparticle sitting in the bare vacuum of the theory and separated by an electric flux string of 20 lattice sites. The system evolves with the interacting Hamiltonian, and the time-evolution (horizontal direction, rightwards) of several quantities as a function of the spatial position (vertical axis) are monitored: the local electric field intensity (left), the local density of particles (middle), and the entanglement entropy associated with a bipartition defined by the bond between x and $x+1$ along the chain (right).

anomalous dynamics in highly excited states has to be "universally" expected whenever confinement is present.

It is worth to observe that a superficially related occurrence of slow dynamics and nonthermal behavior in lattice gauge theories has been recently put forward in Refs. [165–167, 379]. This phenomenon has been dubbed *disorder-free localization*, as it concerns generic translation-invariant quantum states evolving with gauge-invariant Hamiltonians. The underlying mechanism of disorder-free localization is actually very similar to that of standard disorder-induced many-body Anderson localization [157, 169–173]. The role of gauge-invariance is to provide exact local conservation laws $\left[\hat{G}_j, \hat{H}\right] = 0$ (Gauss law) that "freeze" the distribution of local degrees of freedom $\langle \hat{G}_j(t) \rangle = q_j$, which act thereby as an external disorder to be averaged upon.

The essence of disorder-free localization can be understood in the following terms [379]. Differently from the spirit and the approach of the studies under consideration above, as well as of the work reviewed in this thesis, the states considered in disorder-free localization are not restricted to a single gauge-sector such as the neutral gauge sector $\hat{G}_j \equiv 0$. On the contrary, they have large weight in all possible gauge sectors. Since the Hamiltonian is block-diagonal in gauge-sectors, there is no quantum interference between the relative wavefunction components. Therefore, as long as gauge-invariant observables are considered, the wavefunction may be thought as a *classical* superposition of the wavefunction components in the various gauge sectors. The gauge sectors are labelled by the collection $\{\hat{G}_j = q_j\}_j$ of the eigenvalues of the local generators of gauge symmetry, which have the meaning of external charges. By gauge symmetry, the spatial distribution of static charges represents a fixed, static background for dynamical degrees of freedom. Therefore, a classical average over this distribution, as prescribed by the quantum superposition of gauge-sectors in the initial state, is equivalent to averaging over quenched disorder which takes discrete values. Consequently, disorder-free localization in gauge-invariant systems is conceptually a different phenomenon from slow dynamics due to confinement, which takes place in the single sector of physical states with $q_j = 0$ for all lattice sites j.

8.2 Suppression of string breaking and lifetime of unstable mesons

We aim at providing a theoretical framework to understand the occurrence of slow dynamics in systems with confinement of excitations. For the purpose of simplicity and comparison with previous theoretical work, we shall mainly focus on the quantum Ising chain in Eq. (7.22). We adopt throughout the suggestive terminology of gauge theories to indicate relevant classical configurations and their domain-walls: *bare vacuum, particles, strings, false vacuum*.

We first focus on the suppression of string breaking. Its essential underlying mechanism may be understood in elementary terms as a tunneling process across a high energy barrier. The total energy content of a gauge field string is

proportional to its length, and hence it can be in principle arbitrarily high. The process that converts the large amount of potential energy contained in a string into masses of particle-antiparticle pairs is entropically favorable, as a string state is very atypical compared to many-particle states at a given energy. Thus, string breaking is expected to occur if the dynamics are ergodic. However, for this process to conserve energy, particle and antiparticle must be separated at a distance ℓ^* such that the subtracted energy from the broken string portion equal their mass, $\tau\ell^* \sim 2m$. If the string tension τ is much smaller than the particle mass m, locally created pairs have to tunnel through a distance ℓ^* in order for the string to decay. This occurs through high-order processes in perturbation theory, and hence is very slow.

The above phenomenology and considerations may be made rigorous by systematically constructing the effective Hamiltonian in perturbation theory in the inverse particle mass. This allows one to estimate the slowness of the asymptotic thermalization. We formally split the Hamiltonian into an "unperturbed" part $\hat{H}_0$ possessing a highly-degenerate block structure, and a "perturbation" $\hat{V}$. We work in the regime where the dominant term $\hat{H}_0$ in the Hamiltonian is the particle mass: This defines sectors of the Hilbert space labelled by the number of particles and well separated in energy. The interactions in $\hat{V}$ may contain block-diagonal matrix elements $\hat{V}_{\text{diag}} \equiv \hat{H}_1$, corresponding to particle or antiparticle motion, and block-off-diagonal ones $\hat{V}_{\text{offdiag}} \equiv \hat{R}_1$, corresponding to particle-antiparticle pair creation or annihilation. The latter processes may be eliminated by performing a unitary transformation $e^{\hat{S}_1}$ such that the transformed Hamiltonian

$$\hat{H}' = e^{\hat{S}_1}\hat{H}e^{-\hat{S}_1} = \hat{H}_0 + \hat{H}_1 + \hat{R}_1 + \left[\hat{S}_1, \hat{H}_0\right] + \text{second order} \tag{8.1}$$

is purely diagonal up to second order. This amounts to choosing the anti-hermitian generator $\hat{S}_1$ in such a way that $\hat{V}_{\text{offdiag}} + \left[\hat{S}_1, \hat{H}_0\right] = 0$, which fully determines $\hat{S}_1$ as a block-off-diagonal operator. The resulting effective Hamiltonian $\hat{H}^{(1)}_{\text{eff}} = \hat{H}_0 + \hat{H}_1$ accurately describes the nonequilibrium dynamics upon transforming back to the original basis via the inverse transformation $e^{-\hat{S}_1}$, up to a quadratic time scale in the inverse perturbation strength.

This standard Schrieffer-Wolff procedure [380] can be carried out to all orders in perturbation theory: The unitary transformation $e^{\hat{S}_{\leqslant n}}$, with $\hat{S}_{\leqslant n} = -\hat{S}^\dagger_{\leqslant n} = \hat{S}_1 + \hat{S}_2 + \cdots + \hat{S}_n$, can be chosen in such a way that the transformed Hamiltonian

$$\hat{H}' = e^{\hat{S}_{\leqslant n}}\hat{H}e^{-\hat{S}_{\leqslant n}} = \hat{H}_0 + \hat{H}_1 + \cdots + \hat{H}_n + \hat{V}_{>n} \equiv \hat{H}^{(n)}_{\text{eff}} + \hat{V}_{>n} \tag{8.2}$$

commutes with $\hat{H}_0$ up to any given order n, i.e., $\left[\hat{H}_j, \hat{H}_0\right] = 0$. In other words, the effective Hamiltonian $\hat{H}^{(n)}_{\text{eff}}$ preserves the block-diagonal structure of $\hat{H}_0$ and accounts for all transitions within each sector of $\hat{H}_0$ occurring through up to n block-off-diagonal transitions.

Explicitly, the effective Hamiltonian terms and the generator of the unitary transformation are defined order by order via the following recursive algorithm.

We define $\hat{V}_1 \equiv \hat{V}$ and for $n \geqslant 2$

$$\hat{V}_n = \sum_{(k_1,\ldots,k_p)\in[n]'} \frac{1}{p!}\big[\hat{S}_{k_1},\big[\hat{S}_{k_2},\ldots,\big[\hat{S}_{k_p},\hat{H}_0\big]\ldots\big]\big] + \sum_{(k_1,\ldots,k_p)\in[n-1]} \frac{1}{p!}\big[\hat{S}_{k_1},\big[\hat{S}_{k_2},\ldots,\big[\hat{S}_{k_p},\hat{V}\big]\ldots\big]\big]\,, \quad (8.3)$$

where the summations run over the set $[m]$ of the ordered partitions $(k_1,\ldots,k_p)$ of an integer m, i.e., $k_i \geqslant 1$ and $\sum_{i=1}^{p} k_i = m$, and the prime $[m]'$ excludes the trivial partition $(k_1 = m)$ with $p = 1$. The operator $\hat{V}_n$ represents the effective perturbation at order n, i.e., the term of order n in the transformed Hamiltonian after eliminating all block-off-diagonal transitions up to order $n-1$, i.e., $\hat{H}' = \hat{H}_0 + \cdots + \hat{H}_{n-1} + \hat{V}_n + \hat{V}_{>n}$. Similarly to the first step above, we split the effective perturbation into a block-diagonal and a block-off-diagonal term, $\hat{V}_n \equiv \hat{H}_n + \hat{R}_n$. The former constitutes the n-th order correction to the effective Schrieffer-Wolff Hamiltonian $\hat{H}_{\text{eff}}$, while the latter can be eliminated by choosing $\hat{S}_n$ in such a way that $\big[\hat{S}_n,\hat{H}_0\big] + \hat{R}_n = 0$.

This construction is algorithmic and may be carried out directly in the thermodynamic limit, as it involves the commutation of local operators only. However, manual computations are limited to the first few orders because the combinatorial complexity increases rapidly with the perturbative order n. In order to show what the effective Hamiltonian looks like, we report its expression up to second order for the quantum Ising chain:

$$\hat{H}_0 = -J\sum_j \hat{\sigma}^z_j\hat{\sigma}^z_{j+1}, \quad (8.4)$$

$$\hat{H}_1 = -h\sum_j \sigma^z_j - g\sum_j \hat{P}^{\uparrow}_{j-1}\hat{\sigma}^x_j\hat{P}^{\downarrow}_{j+1} + \hat{P}^{\downarrow}_{j-1}\hat{\sigma}^x_j\hat{P}^{\uparrow}_{j+1}, \quad (8.5)$$

$$\hat{H}_2 = \frac{g^2}{4J}\sum_j \Big[+ \hat{P}^{\uparrow}_{j-1}(\hat{\sigma}^-_j\hat{\sigma}^+_{j+1} + \hat{\sigma}^+_j\hat{\sigma}^-_{j+1})\hat{P}^{\uparrow}_{j+2} \quad (8.6)$$

$$+ \hat{P}^{\downarrow}_{j-1}(\hat{\sigma}^-_j\hat{\sigma}^+_{j+1} + \hat{\sigma}^+_j\hat{\sigma}^-_{j+1})\hat{P}^{\downarrow}_{j+2} \quad (8.7)$$

$$- \hat{P}^{\uparrow}_{j-1}(\hat{\sigma}^+_j\hat{\sigma}^+_{j+1} + \hat{\sigma}^-_j\hat{\sigma}^-_{j+1})\hat{P}^{\downarrow}_{j+2} \quad (8.8)$$

$$- \hat{P}^{\downarrow}_{j-1}(\hat{\sigma}^+_j\hat{\sigma}^+_{j+1} + \hat{\sigma}^-_j\hat{\sigma}^-_{j+1})\hat{P}^{\uparrow}_{j+2} \quad (8.9)$$

$$- \hat{\sigma}^z_j\hat{\sigma}^z_{j+1}\Big]. \quad (8.10)$$

$$(8.11)$$

The general convergence properties of such a construction have been discussed by D. Abanin et al. in Ref. [73] and later by C. J. Lin and O. I Motrunich in Ref. [74] and by D. V. Else et al. in Ref. [75]. It is found therein that the magnitude of the term $\hat{H}_n$ is bounded by $n!$. Consequently, the perturbative series is expected to be divergent for arbitrarily small perturbations. While the divergence of the perturbative series points to an asymptotic mixing of the eigenstates among sectors and thermalization, truncation of the series to the

optimal order n^* equal to the inverse perturbation strength leads to an exponential bound for the thermalization time. Our construction is similar to that of Ref. [375] for the quantum Ising chain. However, while these authors were interested in the homogeneous dynamics of elementary quasiparticle excitations above the ground state, we are here interested in the effective dynamics of dilute domain-walls (particles), which represent high-energy excitations of the model.

The rest $\hat{V}_{>n}$ of the truncated Schrieffer-Wolff transformation at the optimal order n^* is exponentially small in the perturbation strength, and its effect can be correspondingly neglected for exponentially long times,

$$T_{sb} \sim g^{-1} \exp\left(J/\sqrt{h^2+g^2}\right). \tag{8.12}$$

Denoting $\hat{H}_{eff}^{(n^*)} \equiv \hat{H}_{eff}$ and $\hat{S}_{\leqslant n^*} \equiv \hat{S}$, the nonequilibrium evolution of the system is thus very accurately reproduced by

$$\left|\Psi(t)\right\rangle \approx \left|\widetilde{\Psi}(t)\right\rangle = e^{-\hat{S}}\, e^{-it\hat{H}_{eff}}\, e^{\hat{S}} \left|\Psi(t=0)\right\rangle, \tag{8.13}$$

whereby the number of particles is exactly conserved, and the particle motion is dressed by complicated perturbative processes.

The above argument provides us with a lower bound for the lifetime of mesonic excitations with mass $M_n > 2M_1$ above the threshold which allows for decay into multiple mesons, cf. Sec. 7.2.2. In fact, such a process involves the creation of extra particle-antiparticle pairs, which has been shown to be exponentially slow. Hence, in this regime, the quantized spectrum of excitations discussed in Sec. 7.2.2 is thus meaningful even beyond the kinematic threshold for decay processes.

We finally comment on the analogous problem of heavy-meson decay in the presence of long-range interactions, introduced in Sec. 7.3. In that case, the spectrum of the unperturbed Hamiltonian $\hat{H}_0$ in Eq. (8.34) with vanishing transverse field $g = 0$, is much less degenerate than that analyzed in the present Section, due to the spatial dependence of interactions. In particular, there are no widely spaced bands which allow us to apply the same formal scheme as discussed above. However, it is still the case that the production of isolated pairs of kinks-antikinks far away from other excitations is strongly energetically suppressed. Therefore, we expect that some form of slowness of decay and thermalization processes should apply in this case, as well. This represents an interesting open problem, whose analysis is left for future studies. In Sec. 8.5.2 below, we shall show that numerical simulations are consistent with the above expectation.

8.3 Slow diffusion of mesons

As explained above, pair production is exponentially slow in the regime of weak confinement. During this long transient regime, the effective dynamics of particles and their bound states is governed by the effective Hamiltonian $\hat{H}_{eff}$, which accounts for resonant perturbative processes.

In order to disentangle the effect of having a finite particle mass from the intrinsic slow dynamics of $\hat{H}_{\text{eff}}$, it is convenient to consider the formal limit of infinite mass, i.e., $J \to \infty$ in the quantum Ising chain. The corresponding lowest-order effective Hamiltonian $\hat{H}_0 + \hat{H}_1$ describes the dynamics of hardcore particles hopping along the chain and subject to linear interaction potentials. Higher-order terms in $\hat{H}_{\text{eff}}$ do not alter the physics qualitatively, as they just renormalize the hopping amplitude and range of particles, and introduce hopping of light mesons. As follows from the discussion in the previous Section, the spatial range of a given perturbative transition in $\hat{H}_{\text{eff}}$ is bounded above by the order in perturbation theory at which it appears.

Here, we aim at studying the effective dynamics of isolated mesons. For this purpose, we consider the two-body problem, i.e., a particle (kink) at site n_1 and an antiparticle (antikink) at site $n_2 > n_1$. The lowest order effective Hamiltonian in the two-particle sector $H_{[2]}$ may be split as $H_{\text{conf}} + H_{\text{hop}}$, whose matrix elements read

$$\left[H_{\text{conf}}\right]_{n_1 n_2, m_1 m_2} = 2h\left(n_2 - n_1\right) \delta_{n_1, m_1} \delta_{n_2, m_2}, \tag{8.14}$$

and

$$\begin{aligned}\left[H_{\text{hop}}\right]_{n_1 n_2, m_1 m_2} = g \big(&\delta_{n_1+1, m_1} \delta_{n_2, m_2} + \delta_{n_1-1, m_1} \delta_{n_2, m_2} \\ &+ \delta_{n_1, m_1} \delta_{n_2+1, m_2} + \delta_{n_1, m_1} \delta_{n_2-1, m_2}\big).\end{aligned} \tag{8.15}$$

Since the interaction part depends on the positive distance $n_2 - n_1$ only, it is convenient to switch to the center-of-mass and relative coordinates $n_\pm = n_1 \pm n_2$. We plug the ansatz $\Psi_{n_+, n_-}(K) = e^{iKn_+} \psi_{n_-}(K)$ into the Schrödinger equation $H_{[2]}\Psi = E\Psi$. The center-of-mass plane wave e^{iKn_+} factors out, and the problem reduces to the single-particle Wannier-Stark ladder problem,

$$2hn_- \psi_{n_-} + 2g \cos K \left(\psi_{n_- - 1} + \psi_{n_- + 1}\right) = E \psi_{n_-}, \tag{8.16}$$

subject to a hard wall at the origin $n_- > 0$, i.e., to the boundary condition $\psi_{n_- = 0} \equiv 0$.

In the absence of a boundary, the problem may be exactly solved via elementary techniques, see App. G. The energy eigenvalues $E_n = 2hn$, with $n \in \mathbb{Z}$, are independent of the off-diagonal hopping amplitude g. The eigenfunctions can be expressed as

$$\Psi_j^{(n)} = \mathcal{J}_{n-j}\left(g \cos K / h\right), \tag{8.17}$$

where $\mathcal{J}_\nu$ is the standard Bessel function of order ν. These Wannier-Stark orbitals are related to each other via lattice translations, $\Psi_j^{(n)} = \Psi_{j-r}^{(n+r)}$, and are exponentially localized around the respective sites n of the chain. The mechanism of localization is a quite intuitive lattice effect, well known as Wannier-Stark localization or Bloch oscillations. The kinetic energy of domain-walls is finite and of order $2g$. Due to energy conservation, a particle can slide along a linear potential of slope $2h$ at most by a distance g/h before bouncing

back and oscillating. Such an effect is robust, and does not depend on taking the infinite-mass limit $J \to \infty$.

Wavefunctions localized far from the boundary $n_- \gg 2g/h$ are hardly affected by the boundary itself, and hence their energy $E_n(K) = hn$ is independent of K. In other words, heavy mesons with $n \gg g/h$ have asymptotically constant dispersion relations (flat bands). This reflects the fact that their center of mass described by the coordinate $n_+/2$ does not diffuse. The bound particle and antiparticle that compose the meson, perform independent Bloch oscillations of temporal period $2\pi/h$ at the edges of a domain of approximately n lattice sites. However, the presence of the boundary *curves* the band $E_n(K)$ of mesons with $n \lesssim \xi_{loc} = g/h$, i.e., whose spatial extent is comparable with that of Bloch oscillations. In other words, the center of mass of a sufficiently light meson, originally placed at position $n_+/2$ along the chain, slowly diffuses over an appreciable time scale. The fast relative coordinate n_- oscillates with a period $2\pi/h$.

The bandwidth of the dispersion relations of mesons, equal to their inverse diffusion time scale, may be simply estimated by the following argument. The modification produced by a hard wall at the origin to the bulk Wannier-Stark orbitals localized around sites $n \gg \xi_{loc}$, is proportional to the local amplitude of the wavefunction tail, i.e.,

$$\mathcal{J}_n\big(g\cos K/h\big) \sim \frac{1}{n!}\big(g\cos K/h\big)^{2n}. \tag{8.18}$$

Therefore, the energy difference acquired by orbitals with different $-\pi < K \leqslant \pi$, will be of this order. In other words, the bandwidth of the dispersion relation of the n-th excited mesonic state, and hence the corresponding maximal velocity of propagation, is of order

$$v_{diff} \underset{n \gg g/h}{\approx} \frac{1}{n!}\big(g/h\big)^{2n}. \tag{8.19}$$

This estimate can be easily verified by numerical diagonalization of the two-body Hamiltonian $H_{[2]}$ in Eqs. (8.14) and (8.15), and agrees with the following perturbative argument: The lowest order process in g/h which moves the center of mass of a string of length n involves the destruction and recreation of the whole string, and hence occurs at order $2n$. An exact solution of this problem in terms of Bessel functions has been found by H. C. Fogedby [381].

Isolated mesons in the quantum Ising chain may be excited by reversing finite domains of n spins in a longitudinally polarized state. According to the picture derived in this Section, as such states evolve under the effect of a weak transverse field, the meson wavefunction will slowly spread ballistically in space, with a speed v_{diff} given by Eq. (8.19). As J is decreased, such a speed is quantitatively modified (increased) by higher-order terms in the effective Hamiltonian $\hat{H}_{eff}$. Additionally, as explained in the previous Section, heavy mesons are expected to decay into multiple lighter mesons over the exponentially long time scale in Eq. (8.19).

8.4 Continuum limit and the Schwinger effect

We comment here on the continuum limit, which is a central concern if one is interested in high-energy physics [203] and field theories [223], which represent the primary fields where the phenomenon of confinement has first emerged. The limit of large particle mass discussed above is akin to the nonrelativistic limit of field theories, in which particle-antiparticle pair creation and annihilation is suppressed and the particle number is effectively conserved. In fact, an exponential law very closely reminiscent of Eq. (8.12) appears in the discussion of the so-called *Schwinger mechanism*, which concerns pair-production out of the false vacuum after a quench of a background uniform classical field [382].

We briefly recall this result by J. Schwinger. Particle production out of the vacuum by a strong background electric field $\mathcal{E}$ can be monitored through the decay of the so-called vacuum persistence amplitude, i.e.,

$$\left|\langle\psi_0|e^{-iH(\mathcal{E})t}|\psi_0\rangle\right|^2 \sim e^{-2\Gamma(\mathcal{E})Vt} \tag{8.20}$$

where V is the volume of the system. The decay rate per unit volume and time is twice the real part $\Gamma(\mathcal{E})$ of the effective action obtained by integrating out the fermionic field. This quantity can be computed with standard field-theoretical techniques, and one finds [382]

$$\Gamma(\mathcal{E}) = \frac{(e\mathcal{E})^2}{(2\pi)^3}\sum_{n=1}^{\infty}\frac{1}{n^2}\exp\left(-\frac{n\pi m^2}{|e\mathcal{E}|}\right). \tag{8.21}$$

The inverse of $2\Gamma(\mathcal{E})$ represents the typical time scale of pair production, and increases exponentially as the external field weakens. A threshold $\mathcal{E}_{cr} = \pi m^2/e$ appears, such that for $\mathcal{E} \gg \mathcal{E}_{cr}$ pair production becomes visible in accessible time scales. In standard laboratory conditions, the value of this Schwinger threshold is extremely high, i.e., $\approx 10^{18}$ Volts/meters. The essential singularity as $\mathcal{E} \to 0$ signals the nonperturbative origin of this phenomenon, which may be pictured as a quantum tunneling across a high energy barrier (cf. the discussion in Sec. 8.2).

Within the exact mapping discussed in Sec. 7.2.3, the interior of heavy mesons in the quantum Ising chain represents a string of uniform electric field. (In particular, the analogy is stronger for the "false vacuum" with all spins reversed against the longitudinal field.) The process of string breaking by pair creation is actually analogous to the Schwinger mechanism, thereby explaining the similarity of the structure of Eqs. (8.12) and (8.21). While this analogy carries over to the continuum limit as far as the decay of the false vacuum is concerned, this is not the case for heavy mesons. In fact, their long-time stability actually relies on a lattice effect, namely the Bloch oscillations of charges at the edge of the string. In the continuum limit, the electrostatic energy gain as the charges are attracted to each other by the Coulomb force, can be compensated by indefinite acceleration. During a scattering event, if the total energy is sufficiently high, the original particle-antiparticle pair may actually generate extra pairs. The rate of

such a process is much higher than that in Eq. (8.12), exponentially suppressed and akin to the Schwinger mechanism. According to the analysis of the Ising field theory by S. Rutkevich in Ref. [228], the former is proportional to the third power of the longitudinal field h^3 in the regime of weak confinement (rather than being exponential suppressed as in the lattice regime).

8.5 Quasilocalization of dilute particles

The discussion of Sec. 8.3 regarded the dynamics of isolated mesons. As we have argued, the latter may become extremely slow when confinement is present.

We find that the slow nonergodic behavior affects a much larger portion of the many-body Hilbert space, constituted by all states with dilute particles. In such states, the empty space between consecutive particles can be viewed by the mapping in Sec. 7.2.3 as electric flux strings. By the argument of Sec. 8.2, strings are stable against pair creation for exponentially long times, thus preventing the occurrence of thermalization on this time scale. The effective dynamics governed by $\hat{H}_{\text{eff}}$ is number-conserving and nonintegrable, and hence it is expected that the system *prethermalizes* to the Gibbs ensemble $e^{-\beta \hat{H}_{\text{eff}}}/Z$ at the inverse temperature β uniquely determined by the energy density of the initial state. For this to happen, it is necessary that particles can propagate. However, the combination of confinement and lattice effects cause Wannier-Stark localization of particles in their mutual linear confining potential, which suppresses spatial propagation and makes prethermalization also extremely slow. The system remains trapped in metastable fully localized states, characterized by persistent energy gradients, coherent oscillations of local observables and bounded entanglement entropy. The lifetime of such states also grows exponentially with the diluteness parameter.

The discussion above outlines the following scenario. Not only *thermalization* is extremely slow, due to the large particle mass J, but also *prethermalization* governed by $\hat{H}_{\text{eff}}$ is expected to present a growing hierarchy of time scales associated with the diluteness of domain-walls in the initial state.

In the extreme dilute limit with particles infinitely far apart from their nearest neighbors, the effective dynamics governed by $\hat{H}_{\text{eff}}$ can be determined exactly, as discussed in the Sec. 8.3 and more thoroughly in App. G. Eigenstates are product states of localized Wannier-Stark orbitals: for the quantum Ising chain in Eq. (7.22), the localized wavefunction centered around the site n reads

$$\Psi_j^{(n)} = \mathcal{J}_{n-j}(g/h), \tag{8.22}$$

where $\mathcal{J}_\nu$ is the standard Bessel function of order ν. The tails of this localized orbitals decay faster than exponentially for $|n-j| \gg g/h \equiv \xi_{\text{loc}}$. If the distance between neighboring particles is much larger than this scale, transport and thermalization are completely suppressed, and particles oscillate around their initial position forever. Delocalization sets in only when the distance be-

tween neighboring particles becomes comparable with the localization length $\xi_{\rm loc}$. Thermalization of such atypical initial states involves the conversion of electrostatic energy into masses of neutral pairs, because such processes are clearly entropically favorable. However, they occur over exponentially long times $T_{\rm sb} \sim g^{-1} \exp\left(J/\sqrt{h^2+g^2}\right)$ [cf. Eq. (8.12)].

8.5.1 Suppression of energy transport in quantum Ising chains

In order to test the above scenario, it is convenient to consider the simplest situation, namely, a single isolated domain-wall in an open chain of L spins governed by $\hat{H}$ in Eq. (7.22). Numerical simulations of this problem have been communicated in Ref. [5]. In order to (partly) conform with the notations of the original paper, we exchange the role of x and z, i.e.,

$$\hat{H} = -J \sum_j \hat{\sigma}_j^x \hat{\sigma}_{j+1}^x - h \sum_j \hat{\sigma}_j^x - g \sum_j \hat{\sigma}_j^z. \tag{8.23}$$

We consider an initial state with a single domain-wall in the middle of the chain which reads, in terms of the eigenstates $|\uparrow\rangle_j$ and $|\downarrow\rangle_j$ of $\hat{\sigma}_j^x$,

$$|\Psi_0\rangle = \bigotimes_{j=1}^{L/2} |\uparrow\rangle_j \bigotimes_{j=L/2+1}^{L} |\downarrow\rangle_j \equiv \left|\uparrow_1 \ldots \uparrow_{L/2} \downarrow_{L/2+1} \ldots \downarrow_L\right\rangle, \tag{8.24}$$

and which is also an eigenstate of the quantum Ising chain (8.23) with a vanishing transverse field $g = 0$. At time $t > 0$, a transverse field $g \neq 0$ is suddenly switched on and we study the nonequilibrium evolution of the energy density profile $\langle \hat{\mathcal{H}}_j(t) \rangle$ as a function of j, where

$$\hat{\mathcal{H}}_j = -J\hat{\sigma}_j^x \hat{\sigma}_{j+1}^x - \frac{g}{2}\left(\hat{\sigma}_j^z + \hat{\sigma}_{j+1}^z\right) - \frac{h}{2}\left(\hat{\sigma}_j^x + \hat{\sigma}_{j+1}^x\right). \tag{8.25}$$

For $h = 0$, the initial energy density $\langle \hat{\mathcal{H}}_j(t=0) \rangle$ is equal on the two sides of the junction at $j = L/2$, due to the $\mathbb{Z}_2$ symmetry. However, in the presence of a nonvanishing longitudinal field $h > 0$, the chain acquires an initial macroscopic energy imbalance between the left ("cold") part and the right ("hot") part. In particular, the latter may be viewed as a "false vacuum" whose energy lies in the middle of the many-body spectrum, and may thereby be expected to decay into a finite density of traveling excitations upon activating the transverse field $g \neq 0$, leading to a meltdown of the initial imbalance after a transient. In order to numerically explore the nonequilibrium evolution of the chain, we employ time-evolving block decimation (TEBD) simulations [383]. It turns out that the entanglement grows slowly up to moderate values of the field $g \lesssim 0.5J$, which allows us to extend the simulations to unusually long times (we chose $t_M = 10^3 J^{-1}$) with modest computational efforts, as in the case of Ref. [289]. We investigate the behavior of $\langle \hat{\mathcal{H}}_j(t) \rangle$ [see Eq. (8.25)] and of the associated current

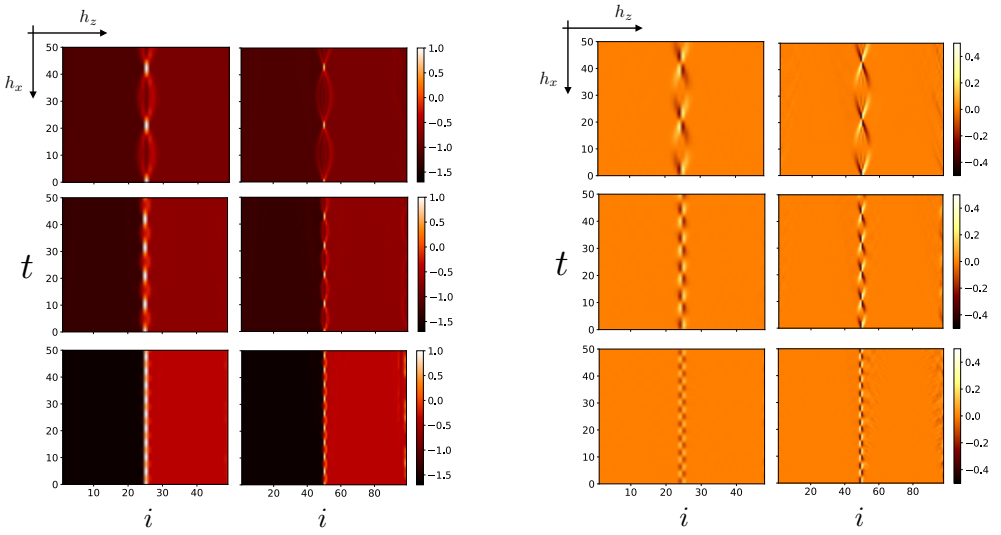

Figure 8.4: Evolution of the energy density $\langle\hat{\mathcal{H}}_i(t)\rangle$ (left panel) and of the energy current density $\langle\hat{\mathcal{J}}_i(t)\rangle$ (right panel) profiles, governed by the Hamiltonian (8.23) starting from the inhomogeneous domain-wall state (8.24), obtained from TEBD simulations, for a range of increasing field values $g = 0.2$ ($L = 50$), 0.4 ($L = 100$) and $h = 0.15, 0.3, 0.6$, varying as indicated by the axes (from Ref. [5], notation: $h_x \to h$, $h_z \to g$), and $J = 1$. The same qualitative behavior as that illustrated here persists up to long times $t_M = 10^3$. Note the oscillations of the profiles around the junction, with spatial amplitude $\propto g/h$ and frequency $\propto h$, while there is no evidence for the activation of transport.

$\langle\hat{\mathcal{J}}_j(t)\rangle$, with

$$\hat{\mathcal{J}}_j = Jg\left(\hat{\sigma}^x_{j-1}\hat{\sigma}^y_j - \hat{\sigma}^y_j\hat{\sigma}^x_{j+1}\right), \tag{8.26}$$

for various values of h and g, $|g| \ll J$. The results of the simulations are illustrated in Fig. 8.4 only up to times $t = 50J^{-1}$, as no qualitative differences are observed up to t_M. In both the "strong" ($h \gg |g|$) and "weak" ($h \lesssim |g|$) confinement regime, energy transfer between the two halves of the chain is suppressed even at late times. As shown in Fig. 8.4, the main dynamical effect of switching on g is given by pronounced oscillations of the profiles around the position $j = L/2$ of the junction, with characteristic emergent amplitudes and frequencies which depend on the values of the fields. In particular, the energy current density is vanishing everywhere except around the junction, where it oscillates between positive values (aligned with the energy gradient) and negative values (against the energy gradient). We emphasize that, within our protocol, an increase in the energy gradient between the two halves, caused by a stronger h, does not result in the activation of transport: on the contrary, it turns out that the oscillations at the junction acquire an even smaller amplitude (see Fig. 8.4 from top to bottom).

As anticipated above, the oscillations of the profiles shown in Fig. 8.4 may be interpreted as the quantum motion of the isolated kink initially localized at the junction, triggered by the transverse field $g \neq 0$. In fact, the kinetic energy associated with this motion has a finite bandwith $\sim g$ on the lattice, and therefore, because of energy conservation, the kink quasiparticle can travel, in the linear

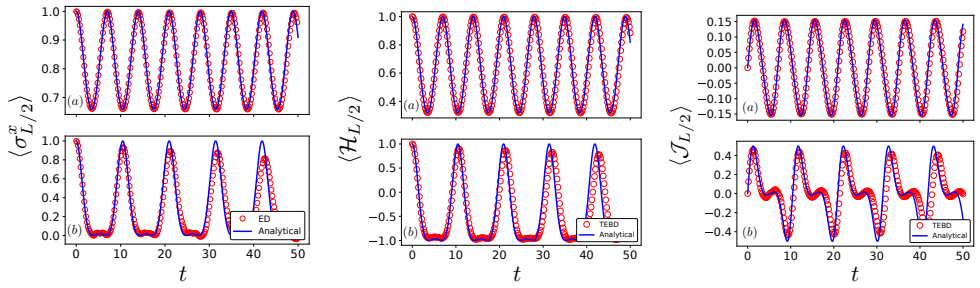

Figure 8.5: Comparison between the numerical results $\langle\hat{\sigma}^x_{L/2}(t)\rangle$, $\langle\hat{\mathcal{H}}_{L/2}(t)\rangle$, $\langle\hat{\mathcal{J}}_{L/2}(t)\rangle$ (symbols), and the analytical approximations $m_{L/2}(t)$, $e_{L/2}(t)$, $j_{L/2}(t)$ (solid lines) for the magnetization (left panel), energy density (central panel) and energy density current (right panel) respectively, at the junction $j = L/2$, as obtained from ED (with $L = 16$) or TEBD (with $L = 50$ or 100), and from the effective single-particle model, respectively. These curves refer to $h = 0.45$, $g = 0.2$ (top row), and $h = 0.3$, $g = 0.4$ (bottom row),with $J = 1$. Note that discrepancies between symbols and solid lines appear as time increases, due to the neglected multi-kink processes. The associated time scale, however, increases upon decreasing g.

confining potential $V_n \sim -2hn$, at most a distance $\xi_{loc} \sim g/h$ (confinement length scale), before bouncing back and oscillating. This phenomenon is analogous to the Wannier-Stark localization of electrons in a one-dimensional crystal subject to a constant electric field [304]. As described above, for $|g|, |h| \ll J$ we can map the motion of the isolated kink onto the problem of a single quantum particle hopping on a one-dimensional lattice, by projecting the many-body Hilbert space onto the single-kink linear subspace. This subspace is spanned by the states $|n\rangle$ with a single domain-wall located between sites n and $n+1$, with $n = 1, 2, \ldots, L-1$. The corresponding unperturbed energy eigenvalues are $E_n = 2J + 2h(L-n) + E_{GS}$, where $E_{GS} = -J(L-1) - hL$ is the unperturbed ground-state energy of the chain. The resulting matrix elements $\langle n|H|m\rangle$ of the Hamiltonian (8.23) read $E_{GS}\delta_{n,m} + [H_{eff}]_{nm}$, with

$$\big[H_{eff}\big]_{nm} = \big[2J + 2(L-n)h\big]\delta_{n,m} - g\,(\delta_{n,m+1} + \delta_{n,m-1}). \tag{8.27}$$

We note that the off-diagonal perturbation produces an effective hopping amplitude for the kink quasiparticle. Accordingly, the effective Hamiltonian H_{eff} describes the dynamics in terms of a single particle hopping in a one-dimensional lattice in the presence of a linear potential, where the state of the particle is described by a vector $\{\psi_n\}$ with $n = 1, 2, \ldots, L-1$. This problem is exactly solvable, see App. G. The absolute value squared of the n-th component of the wavefunction $\psi_n(t)$ is equal to the probability that the particle is at site n at time t. Within this picture, the initial state in Eq. (8.24) maps to $\psi_n(0) = \delta_{n,L/2}$, corresponding to a particle localized at the junction between the two chains. Similarly, the magnetization $\langle\sigma^x_j(t)\rangle$ at site j and time t can be expressed within this single-particle picture as

$$m_j(t) = 1 - 2\sum_{n=1}^{j-1} \big|\psi_n(t)\big|^2, \tag{8.28}$$

where $\psi_n(t) = \sum_m \left[(\exp(-iH_{\rm eff}t)\right]_{nm}\psi_m(0)$ is the time evolved state within the projected space.

In order to test the accuracy of our approximation, we compare the dynamics obtained from the above effective single-particle problem with the exact dynamics generated by $\hat{H}$ [see Eq. (8.23)] in the full many-body Hilbert space, starting from the domain-wall initial state $|\Psi_0\rangle$ of Eq. (8.24) as obtained via both exact diagonalization (ED) and TEBD techniques.[1] The comparison between $m_{L/2}(t)$ and $\langle\sigma^x_{L/2}(t)\rangle$ is shown in Fig. 8.5. In particular, we observe that the agreement is fairly good up to moderate values of the transverse field $g \lesssim 0.4J$. Similarly, the relevant nonequilibrium profiles of the energy and energy current densities can be studied within the above effective single-particle description. This is achieved by projecting the energy density $\hat{\mathcal{H}}_j$ at site j in Eq. (8.25) onto the single-kink subspace,

$$\left[\mathcal{H}^{\rm eff}_j\right]_{nm} = \frac{1}{2}\left[J(2\delta_{j,n}-1) - h\,\mathrm{sgn}(n-j)\right]\delta_{n,m} - \frac{g}{2}\left(\delta_{j,m+1}+\delta_{j+1,m+1}\right)\delta_{n,m+1} + (m\leftrightarrow n), \quad (8.29)$$

where the sign function $\mathrm{sgn}(x)$ equals 1 for $x>0$, -1 for $x<0$ and 0 for $x=0$. From the continuity equation

$$\frac{d\mathcal{H}^{\rm eff}_j}{dt} = i\left[H_{\rm eff}, \mathcal{H}^{\rm eff}_j\right] = \mathcal{J}^{\rm eff}_j - \mathcal{J}^{\rm eff}_{j+1}, \quad (8.30)$$

we can infer the corresponding effective expression for the energy current density operator $\hat{\mathcal{J}}_j$ at site j, i.e.,

$$\left[\mathcal{J}^{\rm eff}_j\right]_{nm} = 2iJg\delta_{n,m+1}\,\delta_{m,j-1} - \frac{i}{2}g^2\delta_{m,j-2}\,\delta_{n,m+2} - \frac{i}{2}g^2\delta_{m,j-1}\,\delta_{n,m+2} - (m\leftrightarrow n). \quad (8.31)$$

The time-dependent expectation value of the energy density at site j within this single-particle picture can therefore be written as

$$e_j(t) = \sum_{n,m}\psi^*_n(t)\left[\mathcal{H}^{\rm eff}_j\right]_{nm}\psi_m(t), \quad (8.32)$$

with an analogous expression for the current $j_j(t)$, in terms of $\mathcal{J}^{\rm eff}_j$. In Fig. 8.5 we compare the time evolution of $e_{L/2}(t)$ and $j_{L/2}(t)$ with the corresponding numerically exact quantities $\langle\mathcal{H}_{L/2}(t)\rangle$ and $\langle\mathcal{J}_{L/2}(t)\rangle$ as obtained from the TEBD simulations. As shown in App. G, the spectrum of the effective Hamiltonian (8.27) consists of integer multiples of $2h$, which results in exactly periodic behavior of the blue lines in Fig. 8.5. It is remarkable that, in spite of the

[1] In this case, the simulations based on exact diagonalization of the Hamiltonian can be pushed until unexpected long times because finite-size effects such as revivals are suppressed, due to the fact that excitations are confined [289].

crudeness of the truncation of the effective Hamiltonian to lowest order, the agreement is excellent for small values $g = 0.2J$ of the transverse field, whereas for sizable values $g = 0.4J$, small quantitative discrepancies appear, still retaining a fairly good qualitative agreement.

Considering now general many-particle states with a given low density $0 < p \ll 1$ of particles and antiparticles, we expect that such states will exhibit a hierarchy of long delocalization time scales, whereby the particles at the edge of the shortest strings or antistrings will diffuse first, and so on. The associated time scales are given by the inverse energy shift due to the interaction of localized orbitals, i.e., the inverse band curvature estimated in Sec. 8.3. It follows that the typical delocalization time scale is related to the average interparticle distance $1/p$ as

$$T_{\text{diff}}(p) \;\sim\; \Gamma(1/p)\left(\frac{h}{g}\right)^{2/p}. \tag{8.33}$$

In particular, we remark that for sufficiently small p the expected time scale of string breaking becomes shorter than the particle delocalization time scale, and thus is expected to become the most relevant time scale. Figure 8.6 shows the result of preliminary numerical simulations, where the quasilocalization of particles (domain-walls) induced by confinement is apparent.

8.5.2 Domain-wall localization in long-range quantum Ising chains

In Ref. [6], the analogous problem has been studied for "confinement" induced by long-range interactions, as discussed in Sec. 7.3. We consider a ferromagnetic quantum Ising chain with algebraically-decaying couplings. We (partly) conform to the notations of Sec. 7.3 and of Ref. [6]: the Hamiltonian is

$$\hat{H} = -\frac{J}{\mathcal{N}_{\alpha,L}} \sum_{1\leqslant i\neq j\leqslant L} \frac{\hat{\sigma}_i^x \hat{\sigma}_j^x}{|i-j|^\alpha} - g\sum_{i=1}^{L} \hat{\sigma}_i^z, \tag{8.34}$$

where $\hat{\sigma}_i^{x,y,z}$ are Pauli matrices, L is the number of quantum spins-1/2 along the chain, g is a transverse magnetic field, and the exponent $\alpha \geqslant 0$ characterizes the range of the ferromagnetic spin-spin interaction. Differently from Sec. 7.3, in this case it is convenient to assume open boundary conditions. The rescaling factor $\mathcal{N}_{\alpha,L} = \sum_{1\leqslant i\neq j\leqslant L} |i-j|^{-\alpha}/(L-1)$ ensures that taking the local energy scale $J > 0$ independent of α and of the system size results in a proper thermodynamic limit [324].

We study the nonequilibrium evolution governed by $\hat{H}$ in Eq. (8.34) starting from initial states $|\Psi_0\rangle = |n\rangle$ with a *longitudinal* domain-wall between sites n and $n+1$, i.e.,

$$|n\rangle = \bigotimes_{i=1}^{n} |\uparrow\rangle_i \bigotimes_{i=n+1}^{L} |\downarrow\rangle_i \;\equiv\; \big|\uparrow_1 \dots \uparrow_n \downarrow_{n+1} \dots \downarrow_L\big\rangle, \tag{8.35}$$

where $|\uparrow,\downarrow\rangle_i$ denotes the eigenstates of $\hat{\sigma}_i^x$ with eigenvalues ± 1, respectively. More general initial states $|n_1, n_2, \dots\rangle$ with multiple domain-walls at positions

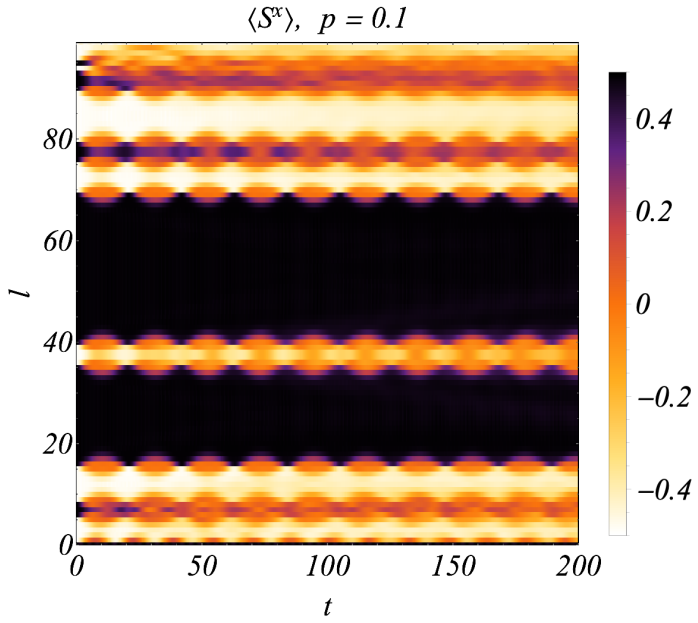

Figure 8.6: Evolution of the magnetization $\langle \hat{\sigma}^x_l(t)/2 \rangle$ versus space (vertical axis) and time (horizontal axis), governed by the quantum Ising chain in Eq. (7.22) with $J = 1$, $h = 0.15$, and $g = 0.2$, starting from a nonentangled initial product state drawn from an ensemble with a fixed density $p = 0.1$ of longitudinal domain-walls along the chain. In agreement with the theory presented in this Chapter, domain-walls remain localized for a long time by Bloch oscillations in their mutual confining potentials. Due to the occurrence of quasilocalization, entanglement entropy grows very slowly (not shown), which allows us to push TEBD computations to long times. The phenomenon discussed here is reminiscent of Stark many-body-localization, recently put forward in Refs. [384,385], in which interacting particles are localized by strong *external* electric fields in the absence of disorder, despite inter-particle interactions. However, in systems with confined excitations, effective confining fields are internally generated by translation-invariant local interactions in the system (see Sec. 7.2.3), and the occurrence of localization requires a low particle density (but not a low energy).

$n_1, n_2, \ldots$ have also been considered. All these states are eigenstates of the Hamiltonian (8.34) for $g = 0$. Upon quenching to a nonvanishing field $g \neq 0$, the system evolves out of equilibrium. The evolution can be studied by monitoring the dynamics of the spatial profiles of relevant local observables such as, e.g., the magnetization density $\langle \hat{\sigma}^x_l(t) \rangle$.

For large α, the spatially-localized domain-wall in the initial state represents a superposition of elementary excitations at all possible momenta, and, accordingly, it is expected to exhibit unbounded spreading in space. On the other hand, for $\alpha \leqslant 2$ isolated domain-walls become highly-excited states. In agreement with the theory in Sec. 7.3, we find a markedly different domain-wall dynamics characterized by spatial localization.

We perform numerical computations of the nonequilibrium evolution for a range of values of the post-quench transverse field $g/J \in [0, 0.5]$ and of the exponent $\alpha \in [0, 3]$, and for system sizes $L = 50$, 100, 200. We use the second-order integrator of the time-dependent variational principle on matrix product states (MPS-TDVP) developed in Refs. [351,386] with the time step $J\,\Delta t = 0.01$

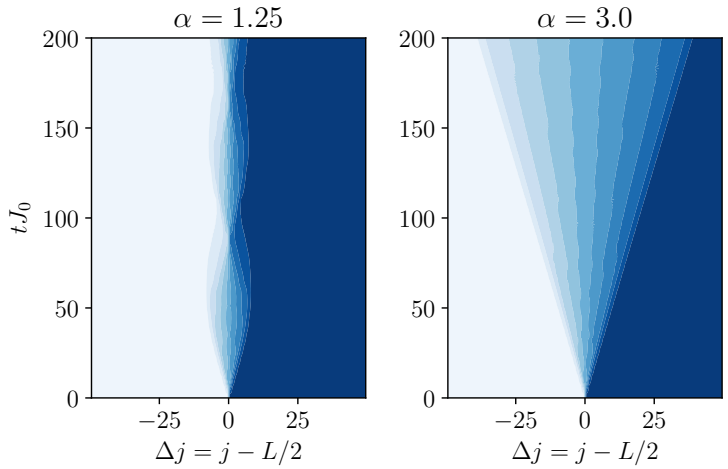

Figure 8.7: Nonequilibrium evolution of the longitudinal magnetization $\langle \sigma_j^x(t) \rangle$ [cf. Eq. (8.34)] in an open ferromagnetic quantum Ising chain of $L = 100$ spins with interactions between spins at site i and j given by $J_{i,j} \propto |i-j|^{-\alpha}$ and $\alpha = 1.25$ (left) and 3 (right) after a global quench of the transverse field h starting from a state with a single domain-wall at the center $j = L/2$ of the chain. Shown data range from -1 (darkest) to $+1$ (lightest). Similar qualitative behaviors are found for $\alpha > 2$ and $\alpha < 2$, respectively. Data are obtained via MPS-TDVP simulations converged with bond dimension $D = 64$ for the Hamiltonian (8.34) with the quench $g = 0 \to g = 0.1\,J$.

and bond dimension $D = 64$. The qualitative features of the results of the simulations appear to depend crucially on α being smaller or larger than 2. In particular, as shown in Fig. 8.7 for the local magnetization, for $\alpha > 2$ unbounded light-cone spreading of the domain-wall occurs from the region around its initial position across the entire system. However, in the presence of longer-range interactions with $\alpha \leqslant 2$, the inhomogeneity initially spreading out from the center of the chain bounces back at a particular characteristic length scale and remains subsequently trapped within this finite region. The spatial amplitude and the temporal duration of this bounce appear to depend on α, g, and, counterintuitively, on the system size L. This quasilocalization scenario for magnetic defects generalizes to initial states with more domain-walls, as long as their initial separation is larger than the amplitude of their spreading. The stability of the magnetization profiles away from the initial positions of domain-walls implies that the lumps of excess energy density, initially concentrated around those positions, remain trapped within the surrounding portions of the chain for a considerable time, highlighting the dramatic slow-down of thermalization and transport.

The mechanism underlying the quasilocalization of domain-walls in the presence of long-range interactions and the analytical description of its quantitative features rely on the discussion of Sec. 7.3. The crucial observation is that spin-flip processes occurring far away from the domain-wall location and generated by a small transverse field involve, unlike those occurring next to it, a sizable configurational energy cost as compared to the perturbation strength g. The former processes give rise to small fluctuations of the order parameter away from the domain-wall, and, crucially, the excited "mesonic" quasiparticles, made out of two tightly bound domain-walls, have vanishing center-of-mass

momentum to lowest order in perturbation theory. The latter processes, instead, generate effective dynamics of the domain-wall.

Similarly to the analysis of the quantum Ising chain in a tilted field detailed above, we capture these effective dynamics by projecting the many-body quantum Hamiltonian in Eq. (8.34) onto the subspace spanned by the states $\{|n\rangle\}$ of Eq. (8.35) with a single domain-wall located between sites n and $n+1$, with $n = 1, 2, \dots, L-1$. Within this approach, the matrix elements of the Hamiltonian (8.34) in this subspace may be written as $\langle n|\hat{H}|m\rangle = E_{GS}\delta_{n,m} + [H_{\text{eff}}]_{n,m}$, where $E_{GS} = -J(L-1)$ is the ferromagnetic ground state energy, and

$$\left[H_{\text{eff}}\right]_{n,m} = V_{\alpha,L}(n)\delta_{n,m} - g(\delta_{n,m+1} + \delta_{n,m-1}), \tag{8.36}$$

where the diagonal term $V_{\alpha,L}(n)$ is given by the ferromagnetic configurational excess energy

$$V_{\alpha,L}(n) = \frac{2}{\mathcal{N}_{\alpha,L}} \sum_{1\leqslant i\leqslant n} \sum_{n+1\leqslant j\leqslant L} \frac{J}{|i-j|^{\alpha}}. \tag{8.37}$$

The quantum evolution starting from a domain-wall $|n_0\rangle$ in Eq. (8.35) is thus approximated by the motion of a single quantum particle initially placed at the site n_0 of a one-dimensional lattice of length $L-1$, hopping to neighboring sites and subject to the potential $V_{\alpha,L}(n)$.

The resulting qualitative behavior is determined primarily by the shape of the potential $V_{\alpha,L}(n)$, which we displayed in Fig. 8.9 for some representative values of α. For large L and n, the potential $V_{\alpha,L}(n)$ can be estimated by approximating sums by integrals in the defining expression, as in Eq. (7.35). The result with open boundary conditions is

$$V_{\alpha,L}(n) \underset{\substack{L\to\infty \\ n/L=x}}{\sim} 4J \times \begin{cases} -\dfrac{1}{2}\, L\, \mathcal{V}_{\alpha}(x) & \text{for } 0 \leqslant \alpha < 1, \\ \dfrac{c_{\alpha}}{2}\, L^{2-\alpha}\, \mathcal{V}_{\alpha}(x) & \text{for } 1 < \alpha < 2, \\ 1 - \dfrac{c_{\alpha}}{2^{\alpha-1}} & \text{for } \alpha > 2, \end{cases} \tag{8.38}$$

with $c_{\alpha} = 1/[(2-\alpha)(\alpha-1)\zeta(\alpha)]$, ζ is the Riemann zeta-function, and $\mathcal{V}_{\alpha}$ is the smooth scaling function

$$\mathcal{V}_{\alpha}(x) = x^{2-\alpha} + (1-x)^{2-\alpha} - 1. \tag{8.39}$$

In the limiting case $\alpha = 2$, powers are substituted by logarithms.

One realizes that for $\alpha > 2$, the potential becomes flat (i.e., independent of n) in the limit $L \to \infty$, and hence eigenstates approach spatially-extended plane waves characterized by their momentum. Conversely, for $1 < \alpha \leqslant 2$ the spatial dependence of $V_{\alpha,L}(n)$ has a nontrivial subextensive scaling $L^{2-\alpha}$ with the system size L, described by the smooth function $\mathcal{V}_{\alpha}$. In particular, due to the concurrence of unbounded potential energy $\sim JL^{2-\alpha}$ and bounded kinetic energy $\sim g$ on the lattice, energy conservation implies that a particle initially placed at a given lattice site can travel at most a finite distance away from

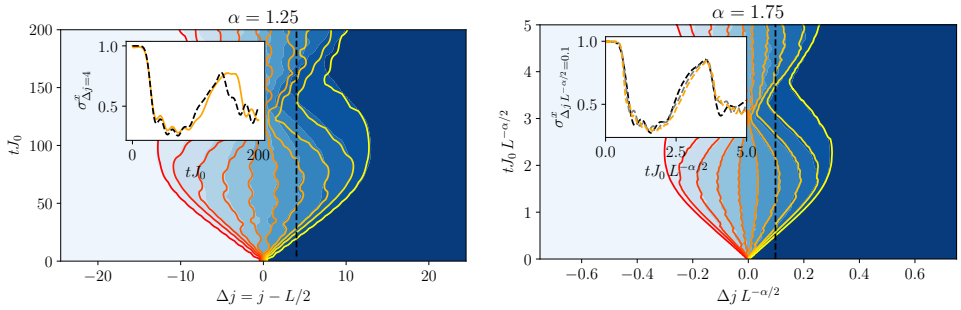

Figure 8.8: Left: Quantitative comparison between the nonequilibrium evolution of the magnetization obtained from MPS-TDVP numerical simulations (blue scale, background coloring) and those predicted by the single-domain-wall approximation in Eq. (8.40) (yellow-red scale, solid contour lines). These data refer to $\alpha = 1.25$, $\hbar/J = 0.1$, $L = 200$. Inset: time slice of the plot at the indicated position along the chain, with a comparison between the MPS-TDVP data (dashed black line) and the result of the approximation (solid orange). Right: Quantitative verification of the validity of the semiclassical scaling laws of the profiles in Eq. (8.43) with respect to the system size L. These data are obtained from MPS-TDVP simulations with $\alpha = 1.75$, $g/J = 0.1$, and $L = 100$ (blue scale, background coloring) or 200 (yellow-red scale, solid contour lines). Inset: time slice of the plot at the indicated rescaled position along the chain, with a comparison between $L = 100$ (dashed black line) and $L = 200$ (dashed orange). In both panels, data are converged with bond dimension $D = 64$.

it. Correspondingly, all eigenstates of H_{eff} are spatially localized.[2] This sharp transition in the structure of the spectrum of H_{eff} in Eq. (8.36) upon decreasing α below 2 is illustrated in Fig. 8.9 and provides a simple explanation for the onset of quasilocalization in the presence of long-range interactions, as shown in Fig. 8.7.

We note that the quasilocalization of magnetic defects discussed above, takes place only if the effective potential $V_{\alpha,L}$ is confining at large distances, i.e., for $\alpha \leqslant 2$, as discussed in Sec. 7.3. Accordingly, this phenomenon it is not directly related with the confined dynamics of correlations functions [267] and anomalous cusps in the time-evolution of the Loschmidt echo [387], which occur whenever the effective potential possesses bound states, i.e., also for $\alpha > 2$ in the present model.

For $0 \leqslant \alpha \leqslant 1$ and in the thermodynamic limit, the ferromagnetic interaction is exactly described by its mean-field approximation and thus it is equivalent to that between a spin and the self-consistent longitudinal field $\lambda_j(t) = \frac{J_0}{2\mathcal{N}_{\alpha,L}} \sum_{i(\neq j)}^{L} \frac{\langle \sigma_i^x(t) \rangle}{|i-j|^\alpha}$. This is the reason why, in the following, we focus on the more interesting case $1 < \alpha \leqslant 2$ corresponding to intermediate-range interactions.

We test the effectiveness of the above single-domain-wall approximation by quantitatively comparing its results with those of the MPS-TDVP simulations. Relevant observables are projected onto the single-domain-wall subspace, and their expectation on the evolving state $\langle \widetilde{\Psi}(t) \rangle = e^{-iH_{\text{eff}}t} |n_0\rangle$ is computed. We

[2] At finite L, due to inversion symmetry with respect to the center of the open chain, the eigenstates of H_{eff} are actually even and odd superpositions of wavefunctions localized at symmetric positions in the chain. However, such a finite-size effect is unstable to any perturbation which breaks this symmetry, such as, e.g., random boundary conditions.

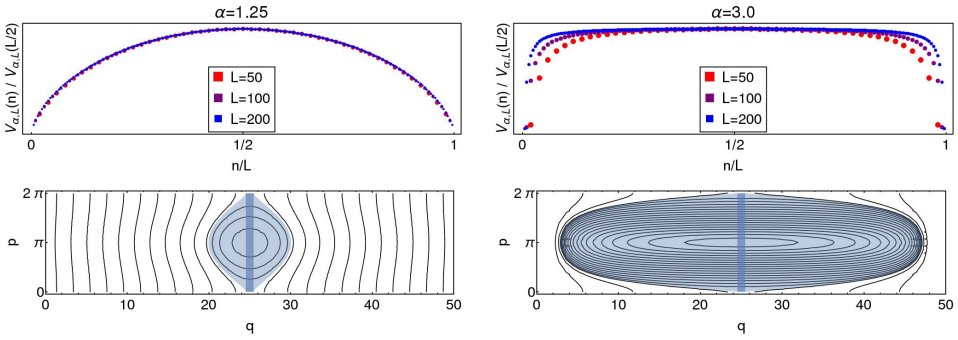

Figure 8.9: Effective description of the dynamics of a single domain-wall. First row: effective potential $V_{\alpha,L}(n)$ experienced by the domain-wall at position n along the chain, rescaled by its maximal value $V_{\alpha,L}(L/2)$, as a function of the rescaled lattice position n/L, for system sizes $L = 50, 100, 200$. Second row: sequence of trajectories defined by the classical Hamiltonian (8.41), corresponding to the classical limit of eigenstates of the single-domain-wall problem defined by the Hamiltonian in Eq. (8.36) with $g/J = 0.1$ and $L = 50$, obtained from the Bohr-Sommerfeld quantization rule (for a better visualization, one every two possible quantized trajectories is drawn). The coordinate $q \in [1, L-1]$ represents the position along the chain, and the conjugated momentum $p \in [0, 2\pi]$ represents the lattice quasimomentum. The blue shading illustrates the semiclassical motion of the domain-wall: the initial dark-shaded wavepacket, spatially localized at position $L/2$ and widespread along the momentum axis, traverses the light-shaded region of phase space during its time-evolution.

primarily focus on the local magnetization $m_j(t) = \langle\widetilde{\Psi}(t)|\sigma_j^x|\widetilde{\Psi}(t)\rangle$, which reads

$$m_j(t) = 1 - 2\sum_{1\leqslant n<j} \big|\langle n|\widetilde{\Psi}(t)\rangle\big|^2. \tag{8.40}$$

The quantitative comparison between this profile and the corresponding one obtained from MPS-TDVP simulations is shown in the left panel of Fig. 8.8 with solid contour lines and background coloring, respectively, and in the relative inset for the time-evolving magnetization at a fixed position along the chain indicated by the vertical black dashed line. The agreement turns out to be excellent for small g and up to considerably long times. It appears to slowly deteriorate at long times, with an associated time scale that decreases upon increasing g. However, in all cases, the qualitative agreement remains fairly good for all accessible times.

The above single-domain-wall approach allows one to derive the quantitative features of the quasilocalization of domain-walls and, in particular, to elucidate the role of long-range interactions in determining its strong sensitivity to the system size. This is conveniently achieved through a semiclassical treatment of the single-particle quantum-mechanical problem defined by the Hamiltonian in Eq. (8.36), which describes its solution with increasing accuracy as $L \to \infty$ (see App. G).

Taking the classical limit in Eqs. (8.36), defined on the phase space $(q, p) \in [1, L-1] \times [0, 2\pi]$ with periodic boundary conditions on the momentum p, one finds for $\alpha > 1$

$$\mathcal{H}_{cl}(q, p) = -2g\cos p + c_\alpha J\Big[q^{2-\alpha} + (L-q)^{2-\alpha} - L^{2-\alpha}\Big]. \tag{8.41}$$

The semiclassical trajectories are defined by Hamilton's equations $\dot{q} = \partial_p \mathcal{H}_{cl}$ and $\dot{p} = -\partial_q \mathcal{H}_{cl}$. Fig. 8.9 shows the structure of the semiclassical eigenstates for $1 < \alpha \leqslant 2$ (left) and $\alpha > 2$ (right), obtained by quantizing the phase space area encircled by classical trajectories, illustrating the quasilocalization transition.

Scaling laws for the motion of quasilocalized domain-walls as a function of the parameters and of the system size can be derived within this semiclassical treatment. In particular, by evaluating the extension and frequency of the classical trajectories crossing a position n_0 along the chain (see Fig. 8.9 for an illustration), one readily derives an estimate of the spatial width Δj and of the temporal period Δt of the spatiotemporal profiles, given by

$$\Delta j \propto g L^{\alpha-1} , \qquad \Delta t \propto L^{\alpha-1} , \tag{8.42}$$

respectively, for domain-walls far away from the center of the chain, i.e., with $n_0 \ll L/2$ or $n_0 \gg L/2$, and

$$\Delta j \propto \sqrt{g L^{\alpha}} , \qquad \Delta t \propto \sqrt{L^{\alpha}/g} , \tag{8.43}$$

respectively, for domain-walls near the center of the chain, i.e., with $n_0 \approx L/2$. These predicted scaling laws are confirmed by the nonequilibrium profiles obtained via MPS-TDVP to a high degree of accuracy, as shown, e.g., in the right panel of Fig. 8.8 with rescaled numerical data for various system sizes L superimposed. Thus, the counterintuitive dependence of the local dynamical behavior of confined domain-walls on the chain length L, observed in the numerical simulations, is actually determined by the system-size scaling of the configurational energy $V_{\alpha,L}(n)$ approximately governing the evolution of isolated domain-walls, which is, in turn, a manifestation of the long-range nature of the interactions.

8.5.3 Particle localization in the lattice Schwinger model

As is clear by considering the exact mappings described in Secs. 7.1.4 and 7.2.3, an analogous phenomenon of particle localization induced by lattice effects in string dynamics may be found in actual confining lattice gauge theories.

In Fig. 8.10 we show this occurrence in the $U(1)$ quantum link model with $s = 1/2$, Eq. (7.16), which is equivalent to the Schwinger model with a topological angle θ close to π (cf. the discussion in Sec. 7.1.2). The strength of confinement may be tuned by varying the latter parameter, which plays a similar role to the longitudinal field in the quantum Ising chain. The Hamiltonian is reported here for convenience:

$$\hat{H} = -w \sum_j \left(\hat{c}_j^\dagger \hat{s}_j^+ \hat{c}_{j+1} + \text{h.c.} \right) + m \sum_j (-1)^j \hat{c}_j^\dagger \hat{c}_j - \alpha \sum_j \hat{s}_j^z . \tag{8.44}$$

The left panels show the dynamical evolution of a finite electric string generated by a particle-antiparticle pair, at the deconfined point $\theta = \pi$ (top) and in the confined phase with $\theta \neq \pi$ (bottom). The right panels show the same evolution

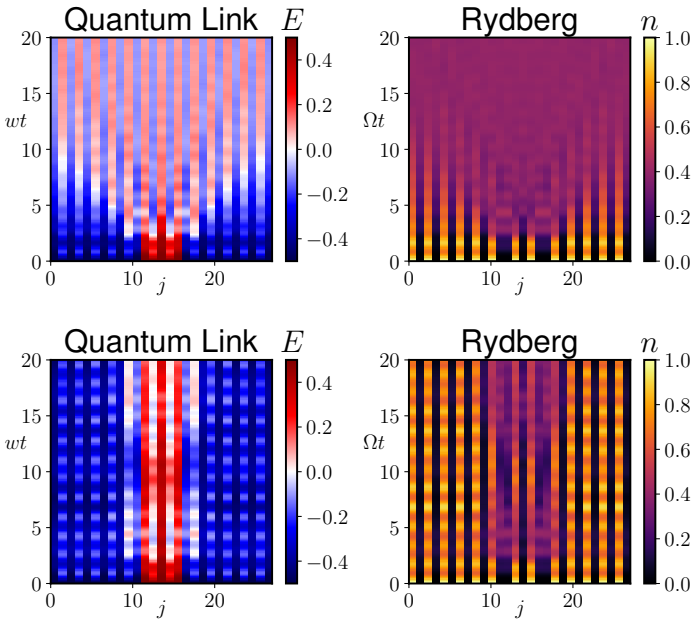

Figure 8.10: Confinement induced by the θ−angle and string dynamics in the $s = 1/2$ U(1)-quantum link model (QLM) [cf. Eq. (8.44)]. Evolution of a particle-antiparticle pair is displayed in terms of space- and time-dependent electric field in the QLM (left panels) and of the density of excited atoms in the Rydberg array (right panels), with $m = -\delta = 1.5\Omega$ and $L = 28$. Simulations in the top row have $\alpha = 0$, corresponding to the deconfined field theory with $\theta = \pi$. Effects of confinement emerge in the second row, where a nonvanishing $\sigma = 0.3\Omega$ stabilizes the electric string.

as it would appear in terms of measurements of Rydberg atom excitations in a quantum simulation, exploiting the exact mapping of Sec. 7.1.4. While for $\alpha = 0$ nothing prevents the initially localized particles from propagating along the chain (top panels), the presence of a linear confining potential proportional to α between them stabilizes the electric string, leading to effective Bloch oscillations of the edges and to a long lifetime, (bottom panels) which can be explained via the theory of Sec. 8.3.

The suppression of string breaking discussed above in the context of the $s = 1/2$ QLM can be immediately generalized to Wilson LGTs. We study the evolution of a bare string of finite length generated by a particle antiparticle pair in the bare vacuum in the lattice Schwinger model, defined by Eq. (7.10) and reported here for convenience

$$\hat{H} = -w \sum_j \left(\hat{c}_j^\dagger \hat{U}_{j,j+1} \hat{c}_{j+1} + \text{h.c.} \right) + m \sum_j (-1)^j \hat{c}_j^\dagger \hat{c}_j + \tau \sum_j \left(\hat{L}_j - \frac{\theta}{2\pi} \right)^2 . \quad (8.45)$$

In the absence of background fields ($\theta = 0$), the theory is confining and features slow relaxation, as shown in Fig. 8.11. Remarkably, string breaking is strongly suppressed even in the regime $\tau \simeq m \simeq w$ in which all terms in $\hat{H}$ compete in magnitude.

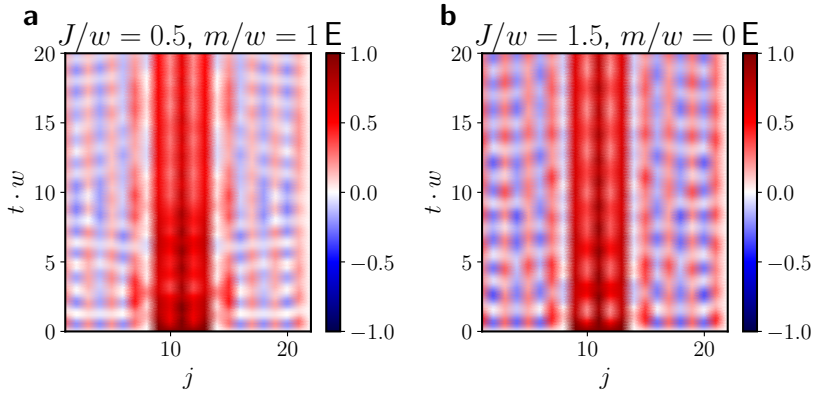

Figure 8.11: Suppression of string breaking in the lattice Schwinger model [cf. Eq. (8.45)], from Ref. [7] (notation: $J \to \tau$). Evolution of the electric flux spatial profile starting from a finite string generated by a particle-antiparticle pair in the bare vacuum. Open boundary conditions are assumed. The plots show that string breaking is strongly suppressed even when the electrostatic string tension τ is comparable in magnitude with the rest mass m and the kinetic energy w of fermionic particles.

Appendix A

Broken permutational invariance

In this Appendix, we briefly discuss simple generalizations of the ideas of Ref. [83], reviewed in Sec. 2.1.1.

A first generalization is represented by nonsymmetric states which evolve with a permutationally invariant Hamiltonian. Such states may be ground states which spontaneously break permutational invariance, or more simply they may be generated by bringing together a number of initially separated subsystems and let them evolve with fully permutationally-invariant interactions (a so-called *inhomogeneous quench*). In this case, the full permutational symmetry breaks down into the product of smaller permutational-symmetry groups acting on each subsystem. While the full system evolves outside of its totally symmetric subspace (TSS), the restricted symmetry allows a description of the dynamics within the product of the TSSs of individual subsystems. Semiclassical theory can thereby be applied in the thermodynamic limit, provided each subsystem is extensive.

Specifically, we may consider any product state of the form $|\alpha_1, \alpha_2, \ldots, \alpha_N\rangle$, in which $N^{(j)}$ particular units are in the individual state $|j\rangle$, for $j = 1, \ldots, q$. Some of the $N^{(j)}$'s may be vanishing, so one has in general $n \leqslant q$ subsets. The global state is not symmetrized, and hence permutational invariance is broken for $n > 1$. However, the system is still invariant upon permuting the $N^{(1)}$ units in state $|1\rangle$ among themselves, the $N^{(2)}$ units in state $|2\rangle$ among themselves, and so on. More generally, each subset of $N^{(j)}$ units may be prepared in a totally symmetric state, i.e., in its TSS. In this last case, as in Sec. 2.1.1, the state of the j-th subsystem is fully specified by the set of occupation numbers $\{N_\alpha^{(j)}\}_{\alpha=1,\ldots,q}$, and the restriction $n \leqslant q$ is removed.

We claim that the nonequilibrium dynamics starting from such a state as described above, reduces to the dynamics of $n \times (q-1)$ semiclassical degrees of freedom, defined by the fractions

$$\left\{ x_\alpha^{(j)} \equiv \frac{N_\alpha^{(j)}}{N^{(j)}} \right\}_{\substack{j=1,\ldots,n \\ \alpha=1,\ldots,q}} \tag{A.1}$$

of units in state $|\alpha\rangle$ within the j-th subsystem, and taking into account the n

exact constraints $\sum_{\alpha=1}^{q} x_\alpha^{(j)} \equiv 1$ for $j = 1, \ldots, n$. In fact, one immediately realizes that terms in the Hamiltonian which simultaneously involve operators belonging to different subsystems, may still be written in the form of local jumps as in Eq. (2.6). Therefore, one ends up with an effective Hamiltonian which is formally identical with Eq. (2.8), whence one derives one analogous to Eq. (2.10), in terms of an enhanced semiclassical phase space corresponding to the product of the individual ones of each subsystem.

A second, closely related generalization, consists of two or more systems, possibly composed of different kinds of degrees of freedom, which are individually invariant under permutations. In this case, permutations of degrees of freedom belonging to different subsystems cannot be defined. However, the Hamiltonian does possess a restricted permutational invariance within each separate subsystem, exactly as in the previous case. Therefore, this case may be treated along the same lines as above, upon possibly introducing a different q for each subsystem. The interactions only couple different subsystems via their collective operators, which behave semiclassically for large subsystem sizes. Such a description is relevant, e.g., for the dynamics of internal degrees of freedom in coupled spinor Bose-Einstein condensates.

Appendix B

Gaussian states

In this Appendix, we briefly review the mathematical properties of bosonic Gaussian *pure* states, their various parameterizations, and their time-evolution.

A Gaussian pure state of a quantum bosonic degree of freedom, described by canonical variables $\hat{q}$, $\hat{p}$, with $[\hat{q},\hat{p}] = i$, is defined by a complex Gaussian wavefunction

$$\psi(x) = \frac{1}{\sqrt{Z}} e^{-\frac{(x-x_0)^2}{2\xi}}, \tag{B.1}$$

with $x_0 \in \mathbb{R}$, and

$$\xi \equiv |\xi| e^{i\alpha} \in \mathbb{C} \qquad \text{with } -\pi/2 < \alpha < \pi/2. \tag{B.2}$$

Normalization requires $Z = \sqrt{\pi|\xi|/\cos\alpha}$. Upon applying a rigid translation, we can set $x_0 = 0$.

With this parameterization, one can compute the "moments",

$$\begin{cases} \Delta^{qq} \equiv \langle \hat{q}^2 \rangle = \int dx\, x^2 |\psi(x)|^2 = \dfrac{|\xi|}{2\cos\alpha}, \\ \Delta^{pp} \equiv \langle \hat{p}^2 \rangle = \int dx \left| \dfrac{d\psi(x)}{dx} \right|^2 = \dfrac{1}{2|\xi|\cos\alpha}, \\ \Delta^{qp} \equiv \dfrac{1}{2}\langle \hat{q}\hat{p} + \hat{p}\hat{q} \rangle = \int dx\, \psi^*(x) \left(-ix\dfrac{d}{dx} - i\dfrac{d}{dx}x \right) \psi(x) = \dfrac{\tan\alpha}{2}. \end{cases} \tag{B.3}$$

In particular, the minimal-uncertainty relation is satisfied for all Gaussian states,

$$\Delta^{qq}\Delta^{pp} = \frac{1}{4} + (\Delta^{qp})^2. \tag{B.4}$$

(It can be shown that for general states the left-hand side is greater or equal than the right-hand side, and equality holds for Gaussian states only [388].) The three variables Δ subject to the minimal-uncertainty constraint constitute an alternative parameterization of general Gaussian states.

The above relation can be formulated in a compact matrix form. Let us denote

$$\hat{\mathbf{x}} = \begin{bmatrix} \hat{q} \\ \hat{p} \end{bmatrix}. \tag{B.5}$$

Let us define the matrix of correlations

$$\Delta_{ij} = \left\langle \frac{\hat{x}_i \hat{x}_j + \hat{x}_j \hat{x}_i}{2} \right\rangle, \tag{B.6}$$

such that

$$\Delta \equiv \begin{pmatrix} \Delta^{qq} & \Delta^{qp} \\ \Delta^{qp} & \Delta^{pp} \end{pmatrix}. \tag{B.7}$$

The minimal-uncertainty relation (B.4) may thus be reformulated as

$$\det \Delta = \frac{1}{4}. \tag{B.8}$$

This relation possesses a simple geometrical interpretation in classical phase space. In fact, the Wigner function $W(q,p)$ (see, e.g., Refs. [308,310]) associated with the Gaussian wavefunction $\psi(x)$ is a positive Gaussian distribution in phase space,

$$W(q,p) = \frac{1}{\sqrt{2\pi\Delta}} \exp\left[-\frac{1}{2} \begin{pmatrix} q & p \end{pmatrix} \cdot \Delta^{-1} \cdot \begin{pmatrix} q \\ p \end{pmatrix}. \right] \tag{B.9}$$

The moments Δ define the "shape" of this distribution. We can thus uniquely associate each Gaussian wavefunction with an ellipse in classical phase space, defined by a contour line of the Wigner function which encloses a given weight. The minimal-uncertainty relation asserts that the area of the ellipse is independent of the parameters (i.e., of ξ). This is directly related to the quantization of phase space area in units of the Planck constant (recall that $\hbar \equiv 1$ in our units). The standard form of Heisenberg Heisenberg relation $\Delta^{qq}\Delta^{pp} \geqslant 1/4$ follows from Eq. (B.4) and is saturated only for $\alpha = 0$. For a general Gaussian pure state, minimal uncertainty variables may be obtained by rotating $\hat{q}$ and $\hat{p}$ to align with the ellipse's axes.

A related parameterization can be formulated in terms of the classical action-angle variables. We define the standard annihilation and creation operators as $\hat{b} = (\hat{q} - i\hat{p})/\sqrt{2}$ and $\hat{b}^\dagger$. We define

$$n = \langle \hat{n} \rangle = \langle \hat{b}^\dagger \hat{b} \rangle = \frac{\Delta^{qq} + \Delta^{pp} - 1}{2}. \tag{B.10}$$

From the uncertainty relation (B.4), we get

$$\left(\frac{\Delta^{qq} - \Delta^{pp}}{2} \right)^2 + (\Delta^{qp})^2 = \frac{\Delta^{qq} + \Delta^{pp} - 1}{2} \left(\frac{\Delta^{qq} + \Delta^{pp} - 1}{2} + 1 \right) = n(n+1). \tag{B.11}$$

Hence, we can write the parameterization

$$\begin{cases} \dfrac{\Delta^{qq} + \Delta^{pp} - 1}{2} \equiv n, \\ \dfrac{\Delta^{qq} - \Delta^{pp}}{2} \equiv \sqrt{n(n+1)} \cos\phi, \\ \Delta^{qp} \equiv \sqrt{n(n+1)} \sin\phi. \end{cases} \tag{B.12}$$

The parameters n and ϕ parameterize the whole family of Gaussian pure states. Note that these variables are singular at $n = 0$, corresponding to the state $|0\rangle$ defined by $\xi = 1$.

Gaussian pure states may be generated by linear canonical transformation starting from the reference state $|0\rangle$, which we shall call the fundamental coherent state. Such a state is the null vector of the standard annihilation operator $\hat{b}$. Let us define the squeezing and rotation operators,

$$\hat{U}_s(\lambda) = \exp\left(-i\lambda\frac{\hat{q}\hat{p}+\hat{p}\hat{q}}{2}\right), \qquad \hat{U}_r(\theta) = \exp\left(-i\theta\frac{\hat{q}^2+\hat{p}^2-1}{2}\right). \tag{B.13}$$

Hence, we define the family of states

$$|\psi(\lambda,\theta)\rangle \equiv U_r(\theta)\hat{U}_s(\lambda)\,|0\rangle\,. \tag{B.14}$$

Unitary transformations generated by quadratic hermitian operators preserve the space of Gaussian states. On varying the parameters θ and λ, one spans all Gaussian wavefunctions. Therefore, these two parameters constitute a further independent parameterization of Gaussian pure states. The geometrical interpretation of these variables in classical phase space can be given along the lines above: one starts with the fundamental coherent state, represented by a unit circle centered at the origin, then squeezes (stretches) it by a factor $e^{\pm\lambda}$ along the two Cartesian axes, and hence rotates it around the origin by an angle θ. In this way one generates all possible ellipses in phase space, which are in one-to-one correspondence with Gaussian states as from the mapping above. The (λ,θ)-parameterization can be related to the previous ones via the following formulas:

$$\begin{cases} \Delta^{qq} = \frac{1}{2}\left(\cos^2\theta e^{2\lambda} + \sin^2\theta e^{-2\lambda}\right), \\ \Delta^{pp} = \frac{1}{2}\left(\sin^2\theta e^{2\lambda} + \cos^2\theta e^{-2\lambda}\right), \\ \Delta^{qp} = \frac{1}{2}\cos\theta\sin\theta\left(e^{2\lambda} - e^{-2\lambda}\right), \end{cases} \tag{B.15}$$

and

$$|\xi|^2 = \frac{\Delta^{qq}}{\Delta^{pp}} = \frac{1+\cos 2\theta\tanh 2\lambda}{1-\cos 2\theta\tanh 2\lambda}, \qquad \tan\alpha = 2\Delta^{qp} = \sin 2\theta\sinh 2\lambda. \tag{B.16}$$

Gaussian pure states may also be obtained as ground states of definite quadratic Hamiltonians of the form

$$\hat{H} = a\frac{\hat{p}^2}{2} + b\frac{\hat{q}^2}{2} + c\frac{\hat{q}\hat{p}+\hat{p}\hat{q}}{2} \tag{B.17}$$

with $ab - c^2 > 0$. This can be achieved in two steps. First, a quadratic form can be diagonalized by means of an orthogonal transformation, i.e., a rotation, implemented by $\hat{U}_r(\theta)$ for some θ. This transformation brings the Hamiltonian

into a diagonal form

$$\hat{U}_r(\theta)\,\hat{H}\,\hat{U}_r^\dagger(\theta) = \hat{H}' = a'\frac{\hat{p}^2}{2} + b'\frac{\hat{q}^2}{2}. \tag{B.18}$$

Hence, a squeezing transformation, implemented by $\hat{U}_s(\lambda)$ for some λ, brings the Hamiltonian into the fundamental form

$$\hat{U}_s(\lambda)\,\hat{H}'\,\hat{U}_s^\dagger(\lambda) = \hat{H}'' = \omega\left(\frac{\hat{p}^2}{2} + \frac{\hat{q}^2}{2}\right) = \omega\left(\hat{b}^\dagger\hat{b} + \frac{1}{2}\right). \tag{B.19}$$

The ground state of $\hat{H}''$ is the fundamental coherent state $|0\rangle$. The ground state of the original Hamiltonian $\hat{H}$ is obtained by transforming back to original variables, i.e.,

$$\hat{U}_r(\theta)\hat{U}_s(\lambda)\,|0\rangle \equiv |\psi(\lambda,\theta\rangle\,. \tag{B.20}$$

The overall magnitude of the Hamiltonian parameters a, b, c just fix the spectrum ω, whereas their two independent ratios consititute a further parameterization of Gaussian states. Diagonalization of a quadratic bosonic Hamiltonian is discussed also in Sec. 6.1.2.

Gaussian pure states are parameterized by two numbers, plus an irrelevant phase factor. Quadratic Hamiltonians generate unitary transformations which map Gaussian states into Gaussian states. Time-evolution of Gaussian states governed by (generally time-dependent) quadratic Hamiltonians plays a crucial role in semiclassical physics, as explained in several circumstances in Part I of the thesis. This evolution can be described by two coupled ordinary differential equations. More generally, one has one pair of ODEs per degree of freedom.

Let us introduce a compact notation for a system of n degrees of freedom as

$$\hat{\mathbf{x}} = \begin{pmatrix} \hat{q}_1 \\ \vdots \\ \hat{q}_n \\ \hat{p}_1 \\ \vdots \\ \hat{p}_n \end{pmatrix}, \tag{B.21}$$

and a quadratic Hamiltonian

$$\hat{H}(t) = \frac{1}{2}\hat{\mathbf{x}}^T \cdot \mathcal{H}(t) \cdot \hat{\mathbf{x}}, \tag{B.22}$$

where $\mathcal{H}(t)$ is the $2n \times 2n$ symmetric matrix of real coefficients. Denoting the simplectic unit matrix as

$$\mathbb{J} = \begin{pmatrix} \mathbb{O} & \mathbb{I} \\ -\mathbb{I} & \mathbb{O} \end{pmatrix}. \tag{B.23}$$

One has the Heisenberg equations of motion

$$\dot{\hat{\mathbf{x}}} = \mathbb{J}\mathcal{H}(t) \cdot \hat{\mathbf{x}} \equiv A(t) \cdot \hat{\mathbf{x}}\,. \tag{B.24}$$

Let us define the matrix of correlations

$$\Delta = \frac{1}{2}\left\langle \hat{\mathbf{x}} \cdot \hat{\mathbf{x}}^{\mathsf{T}} + \text{ transpose} \right\rangle, \qquad \text{i.e.,} \qquad \Delta_{ij} = \left\langle \frac{\hat{x}_i \hat{x}_j + \hat{x}_j \hat{x}_i}{2} \right\rangle . \tag{B.25}$$

The evolution equation of the correlations can be expressed as

$$\dot{\Delta} = A(t) \cdot \Delta + \Delta \cdot A(t)^{\mathsf{T}}. \tag{B.26}$$

By means of the transformation formulas above, one may rewrite the evolution of Gaussian pure states in any of the parameterizations. In this thesis, we always use the latter form (B.26) for analytical and numerical calculations.

Appendix C

Floquet Hamiltonian and high-frequency expansion

Whenever the time-dependent Hamiltonian of a system has a period T, i.e., $\hat{H}(t+T) = \hat{H}(t)$, the resulting time-evolution operator $U(t_2, t_1)$ satisfies

$$\hat{U}(t_0 + nT, t_0) = \left[\hat{U}(t_0 + T, t_0)\right]^n \tag{C.1}$$

for any integer n. Accordingly, it is convenient to define an effective static Hamiltonian $\hat{H}_{\text{eff}}$ [110, 302],

$$\hat{U}(t_0 + T, t_0) = \mathcal{T} e^{-i\int_{t_0}^{t_0+T} d\tau\, \hat{H}(\tau)} \equiv e^{-iT\hat{H}_{\text{eff}}}, \tag{C.2}$$

usually referred to as the *Floquet Hamiltonian*. Its spectrum is defined up to integer multiples of the frequency $2\pi/T$ and it is independent of the choice of the reference time t_0. The state of the system at stroboscopic times $t_n = t_0 + nT$ is therefore entirely and unambiguously determined by the Floquet Hamiltonian $\hat{H}_{\text{eff}}$. A series expansion of $\hat{H}_{\text{eff}}$ in powers of the period T, known as the *Magnus expansion*, can be written as

$$\hat{H}_{\text{eff}} = \sum_{n=0}^{\infty} \hat{H}_{\text{eff}}^{(n)}, \tag{C.3}$$

with $\hat{H}_{\text{eff}}^{(n)}$ proportional to T^n. Explicitly, the first terms read

$$\hat{H}_{\text{eff}}^{(0)} = \int_{t_0}^{t_0+T} \frac{d\tau_1}{T}\, \hat{H}(\tau_1), \tag{C.4}$$

$$\hat{H}_{\text{eff}}^{(1)} = \frac{T}{2} \int_{t_0}^{t_0+T} \frac{d\tau_1}{T} \int_{t_0}^{t_0+\tau_1} \frac{d\tau_2}{T} \left[\hat{H}(\tau_1), \hat{H}(\tau_2)\right], \tag{C.5}$$

with the higher order terms involving a increasing number of nested commutators of $\hat{H}$ at different times. This expansion is convergent when T is smaller than the inverse maximal extension of the spectrum of $\hat{H}(t)$ [302].

Appendix D

Nonequilibrium spin-wave theory with weak disorder

In this Appendix, we explore applications of spin-wave theory in weakly disordered magnetic systems. The material below is unpublished.

We consider the following two models:

$$\hat{H}_{GM} = -\frac{\lambda}{N}\sum_{i,j=1}^{N}\hat{\boldsymbol{\sigma}}_i\cdot\hat{\boldsymbol{\sigma}}_j - \sum_{i=1}^{N} h_i\hat{\sigma}_i^z, \tag{D.1}$$

$$\hat{H}_{LMG} = -\frac{\lambda}{N}\sum_{i,j=1}^{N}\hat{\sigma}_i^x\hat{\sigma}_j^x - \sum_{i=1}^{N} h_i\hat{\sigma}_i^z, \tag{D.2}$$

where σ's are Pauli matrices. The former model (D.1) represents the so-called Gaudin magnet. When the external field is uniform ($h_i \equiv h$), the model is trivially solvable, because the two terms of $\hat{H}$ commute. For an arbitrary set of local fields $\{h_i\}_i$, the model is nontrivially Bethe-ansatz solvable, and possesses a complete set of N commuting integrals of motion [303]. The latter model (D.2) represents a fully-connected Ising ferromagnet, which is an anisotropic version of the former [it has $\mathbb{Z}_2 \equiv O(1)$ rather than $O(3)$ symmetry]. When the external field is uniform ($h_i \equiv h$), it maps to the Lipkin-Meshkov-Glick model. Such a model has been discussed at length in Chap. 2. Unlike the isotropic case, this model has a "quantum" ($T = 0$) ferromagnet/paramagnet transition on varying the strength of the external field. As soon as an inhomogeneity in the local fields is present, both the Bethe-ansatz and the mean-field solvability break down, and the analysis must resort to some approximation.

We consider a weak disorder, i.e., local fields with small random fluctuations around an average value. This may be studied by expanding in small fluctuations around spin-coherence. For the Gaudin magnet, the approximation can in principle be checked against an exact treatment. (This model has been studied in relation to many-body localization in Ref. [389].) On the other hand, the Ising phenomenology is richer in the clean case, since the model undergoes equilibrium and dynamical transitions, as discussed in Chap. 2. Finite-range

interactions may also be considered along the lines of Chap. 3. We are interested in investigating the interplay of weak disorder and interactions, and the impact of the former on the nonequilibrium phenomena discussed in Part I of the thesis. However, it should be noted that spin-wave theory is not expected to succeed in capturing a disorder-dominated phase, e.g., a many-body localized phase.

We sketch below how the nonequilibrium spin-wave theory expounded in Chap. 3 can be extended to deal with inhomogeneous local fields. We rewrite both models (D.1) and (D.2) in Fourier components of the spins. We use the following notation: $\tilde{\sigma}_k \equiv \sum_j e^{-ikj}\sigma_j$, but $\tilde{h}_k \equiv (1/N)\sum_j e^{-ikj}h_j$:

$$\hat{H}_{GM} = -\frac{\lambda}{N}\left|\tilde{\vec{\sigma}}_{k=0}\right|^2 - \sum_k \tilde{h}_{-k}\tilde{\sigma}^z_k; \tag{D.3}$$

$$\hat{H}_{LMG} = -\frac{\lambda}{N}\left(\tilde{\sigma}^x_{k=0}\right)^2 - \sum_k \tilde{h}_{-k}\tilde{\sigma}^z_k. \tag{D.4}$$

Now we define

$$h_i \equiv h + \Delta h \cdot \mathcal{X}_i, \tag{D.5}$$

and

$$\tilde{\mathcal{X}}_k \equiv \frac{1}{\sqrt{N}}\sum_j e^{-ikj}\mathcal{X}_j. \tag{D.6}$$

Substituting,

$$\tilde{h}_0 = h + \frac{\Delta h \cdot \tilde{\mathcal{X}}_0}{\sqrt{N}}, \qquad \tilde{h}_k \equiv \tilde{h}^*_{-k} = \frac{\Delta h \cdot \tilde{\mathcal{X}}_k}{\sqrt{N}} \quad \text{for } k \neq 0. \tag{D.7}$$

Setting $\bar{h} \equiv \tilde{h}_0$, we can separate the Hamiltonian into a clean and a disordered part:

$$\hat{H}_{GM} = -\frac{\lambda}{N}\left|\tilde{\vec{\sigma}}_{k=0}\right|^2 - \bar{h}\,\tilde{\sigma}^z_{k=0} - \Delta h \sum_{k\neq 0}\tilde{\mathcal{X}}_{-k}\frac{\tilde{\sigma}^z_k}{\sqrt{N}}; \tag{D.8}$$

$$\hat{H}_{LMG} = -\frac{\lambda}{N}\left(\tilde{\sigma}^x_{k=0}\right)^2 - \bar{h}\,\tilde{\sigma}^z_{k=0} - \Delta h \sum_{k\neq 0}\tilde{\mathcal{X}}_{-k}\frac{\tilde{\sigma}^z_k}{\sqrt{N}}. \tag{D.9}$$

If we take the local fields h_i as independent Gaussian random variables (RVs) with common mean h and common dispersion around the mean equal to Δh, then the Fourier components of the disorder are also independent Gaussian RVs. Given the above definitions, the variables $\mathcal{X}_j$ are standard Gaussian variables, as well as their Fourier components $\tilde{\mathcal{X}}_{,k}$

$$\begin{aligned} \langle \mathcal{X}_j \rangle &= 0, \qquad \langle \mathcal{X}_j^2 \rangle = 1, \\ \langle \tilde{\mathcal{X}}_k \rangle &= 0, \qquad \langle \tilde{\mathcal{X}}_k^2 \rangle = 1. \end{aligned} \tag{D.10}$$

For different choices we may have nonGaussian and/or correlated $\{\tilde{\mathcal{X}}_k\}$. In equations (D.8) and (D.9), we have $\bar{h} \to h$ in the thermodynamic limit (no disorder dressing of the average field), and $\tilde{\mathcal{X}}$'s are random numbers of order 1. The first two terms represent the clean part of $\hat{H}$, and the last term accounts for

the disorder. The global amount of disorder is controlled by the parameter Δh.

The analysis now proceeds as in the clean case in Chap. 3. We decompose the spins in a rotated frame aligned with the instantaneous (equilibrium or out-of-equilibrium) average total spin, acting as the reference spin-coherent vacuum on top of which spin-wave excitations are built. The spins are then transformed to canonical (Holstein-Primakoff) coordinates $\tilde{q}_k, \tilde{p}_k$, obtaining an expansion of $\hat{H}$ which depends parametrically on the classical reference configuration of the system. In the clean case, both the equilibrium equation of state and the nonequilibrium equations of motion are found by requiring the linear terms in $\tilde{q}_{k=0}, \tilde{p}_{k=0}$ in the Hamiltonian $\hat{H}$ to vanish, which fixes the state or the evolution of the reference frame, and then writing the evolution of fluctuations around the time-dependent spin-coherent reference state at Gaussian level.

However, in the presence of disorder, this is no longer the case. The Hamiltonians (D.8) and (D.9) have linear terms in $\tilde{q}_k, \tilde{p}_k$. This results from the equations

$$\tilde{\sigma}^z_k = \Big(\mathbf{X}\cdot\mathbf{z}\Big)\tilde{\sigma}^X_k + \Big(\mathbf{Y}\cdot\mathbf{z}\Big)\tilde{\sigma}^Y_k + \Big(\mathbf{Z}\cdot\mathbf{z}\Big)\tilde{\sigma}^Z_k \tag{D.11}$$

and

$$\begin{aligned}
\frac{\tilde{\sigma}^X_k}{\sqrt{N}} &= (1/\sqrt{s})\ \tilde{q}_k + \dots \\
\frac{\tilde{\sigma}^Y_k}{\sqrt{N}} &= (1/\sqrt{s})\ \tilde{p}_k + \dots \\
\frac{\tilde{\sigma}^Z_k}{\sqrt{N}} &= -(1/\sqrt{s})\ \sum_{k'} \frac{\tilde{q}_{k'}\tilde{q}_{k-k'} + \tilde{p}_{k'}\tilde{p}_{k-k'}}{2\sqrt{Ns}}.
\end{aligned} \tag{D.12}$$

Such linear terms are proportional to the disorder strength Δh in the Hamiltonian. Therefore, disorder induces weak distortions of the spin-coherence, of order $\mathcal{O}(\Delta h)$.

In this case, in equilibrium one has

$$\langle \tilde{q}_k \rangle \propto \langle \tilde{p}_k \rangle \propto \Delta h \cdot \tilde{\chi}_{-k} + \dots \tag{D.13}$$

and out of equilibrium we need to take into account not only the evolution of the quantum correlations $\Delta^{qq}_k, \Delta^{qp}_k, \Delta^{pp}_k$ defined in Eqs. (3.34), but also the evolution of the expectation values $\langle \tilde{q}_k(t) \rangle, \langle \tilde{p}_k(t) \rangle$. The approximate equations of motion can be obtained from the Hamiltonian expanded to quadratic order

in the fluctuations $\tilde{q}_k, \tilde{p}_k$. We get

$$\begin{aligned}\hat{H}_{GM} =&\{\text{classical average}\}+\\ &-\frac{\sqrt{N}}{\sqrt{s}}\bar{h}\Big(\big(\mathbf{X}\cdot\mathbf{z}\big)\,\tilde{q}_0+\big(\mathbf{Y}\cdot\mathbf{z}\big)\,\tilde{p}_0\Big)\\ &+\frac{1}{s}\Big(2\lambda+\bar{h}\big(\mathbf{Z}\cdot\mathbf{z}\big)\Big)\sum_{k\neq 0}\frac{\tilde{q}_k\tilde{q}_{-k}+\tilde{p}_k\tilde{p}_{-k}-1}{2}\\ &-\frac{\Delta h}{\sqrt{s}}\sum_{k\neq 0}\tilde{\mathfrak{X}}_{-k}\Big(\big(\mathbf{X}\cdot\mathbf{z}\big)\tilde{q}_k+\big(\mathbf{Y}\cdot\mathbf{z}\big)\tilde{p}_k\Big)\\ &+\frac{1}{\sqrt{N}}\frac{\Delta h}{s}\big(\mathbf{Z}\cdot\mathbf{z}\big)\sum_{k\neq 0,k'}\tilde{\mathfrak{X}}_{-k}\,\frac{\tilde{q}_{k'}\tilde{q}_{k-k'}+\tilde{p}_{k'}\tilde{p}_{k-k'}}{2},\end{aligned}\tag{D.14}$$

and

$$\begin{aligned}\hat{H}_{LMG} =&\{\text{classical average}\}+\\ &-\frac{\sqrt{N}}{\sqrt{s}}\Big(2\lambda\,(1-\epsilon)\,(\mathbf{Z}\cdot\mathbf{x})\,(\mathbf{X}\cdot\mathbf{x})+\bar{h}\,(\mathbf{X}\cdot\mathbf{z})\Big)\tilde{q}_0\\ &-\frac{\sqrt{N}}{\sqrt{s}}\Big(2\lambda\,(1-\epsilon)\,(\mathbf{Z}\cdot\mathbf{x})\,(\mathbf{Y}\cdot\mathbf{x})+\bar{h}\,(\mathbf{Y}\cdot\mathbf{z})\Big)\tilde{p}_0\\ &+\frac{1}{s}\Big(2\lambda\big(\mathbf{Z}\cdot\mathbf{x}\big)^2+\bar{h}\big(\mathbf{Z}\cdot\mathbf{z}\big)\Big)\sum_{k}\frac{\tilde{q}_k\tilde{q}_{-k}+\tilde{p}_k\tilde{p}_{-k}-1}{2}\\ &-\frac{\Delta h}{\sqrt{s}}\sum_{k\neq 0}\tilde{\mathfrak{X}}_{-k}\Big(\big(\mathbf{X}\cdot\mathbf{z}\big)\tilde{q}_k+\big(\mathbf{Y}\cdot\mathbf{z}\big)\tilde{p}_k\Big)\\ &+\frac{1}{\sqrt{N}}\frac{\Delta h}{s}\big(\mathbf{Z}\cdot\mathbf{z}\big)\sum_{k\neq 0,k'}\tilde{\mathfrak{X}}_{-k}\,\frac{\tilde{q}_{k'}\tilde{q}_{k-k'}+\tilde{p}_{k'}\tilde{p}_{k-k'}}{2}.\end{aligned}\tag{D.15}$$

In the nonequilibrium setting, one needs to add to $\hat{H}$ an extra Larmor term $-2\boldsymbol{\omega}(t)\cdot\tilde{\boldsymbol{\sigma}}_{k=0}$, which accounts for the noninertial frame, cf. Sec. 3.2.

The equilibrium equation of state or the nonequilibrium equations of motion are obtained in a straightforward way from the above Hamiltonians. Self-consistency requires that $\langle\tilde{q}_0\rangle\equiv\langle\tilde{q}_0\rangle\equiv 0$, which fixes the configuration or the evolution of the frame $(\mathbf{X},\mathbf{Y},\mathbf{Z})$. In the presence of disorder, the solution is perturbatively modified in powers of $\Delta h\neq 0$. Linear terms in the spin-wave variables determine nonvanishing ground-state expectation values:

$$\omega\,\langle\tilde{q}_k\rangle+\big(\mathbf{Z}\cdot\mathbf{z}\big)\frac{\Delta h}{\sqrt{N}}\sum_{k'\neq 0}\tilde{\mathfrak{X}}_{k'}\langle\tilde{q}_{k-k'}\rangle\stackrel{!}{=}\sqrt{s}\,\big(\mathbf{X}\cdot\mathbf{z}\big)\Delta h\cdot\tilde{\mathfrak{X}}_{-k}\tag{D.16}$$

where the common frequency of the spin waves ω is equal to $2\lambda+\bar{h}\big(\mathbf{Z}\cdot\mathbf{z}\big)$ in the Gaudin case or $2\lambda\big(\mathbf{Z}\cdot\mathbf{x}\big)^2+\bar{h}\big(\mathbf{Z}\cdot\mathbf{z}\big)$ in the Lipkin case. The solution of (D.16) to first order in Δh is obtained by disregarding the second term. An analogous equation fixes the equilibrium value of $\langle\tilde{p}_k\rangle$.

The interpretation of the above result is simple in the real-space description, where one has

$$\langle \hat{q}_j \rangle, \langle \hat{p}_j \rangle \propto \Delta h \cdot \chi_j. \tag{D.17}$$

The local field h_j generates a local distortion of the spin at site j away from the mean-field configuration that results from the competition of ferromagnetic infinite-range interaction and the uniform field. Correspondingly, the spin-wave density will be $\epsilon = \mathcal{O}\Big((\Delta h)^2\Big)$. This statement is *exact* in the thermodynamic limit.

Within the formalism, we can account for quantum fluctuations around the configuration distorted by weak disorder. Setting

$$\tilde{q}_k \equiv \langle \tilde{q}_k \rangle + \delta \tilde{q}_k, \qquad \tilde{p}_k \equiv \langle \tilde{p}_k \rangle + \delta \tilde{p}_k, \tag{D.18}$$

and substituting into the Hamiltonians, the linear terms in δq's, δp's cancel by construction, and one ends up with the quadratic truncation of the Hamiltonian in the fluctuations. Due to infinite-range interactions, the lattice sites only feel each other via the self-consistent value of the effective field (or mean field) which determines their configuration. Therefore, one ends up with a set of decoupled oscillators in real space with disordered frequencies. In particular, disorder localizes spin excitations within single sites.

On the other hand, finite-range interactions such as those analyzed in Part I of the thesis tend to delocalize spin excitations, and compete with disorder. The effect of this interplay on the nonequilibrium dynamics is not a priori clear, and constitutes a subject of interest for theory and experiments. The expansion above together with that presented in Chap. 3 for finite-range interactions provide a a starting point to investigate these problems.

Appendix E

Semiclassical expansion for the dynamics of the Dicke model

We consider the Dicke model,

$$\hat{H} = \omega_0 \sum_{j=1}^{N} \hat{s}_j^z + \omega \hat{b}^\dagger \hat{b} + \frac{\gamma}{\sqrt{N}} \frac{\hat{b}^\dagger + \hat{b}}{\sqrt{2}} \sum_{j=1}^{N} \hat{s}_j^x, \tag{E.1}$$

where $\hat{s}^\alpha$, with $\alpha = x, y, z$, are spin-1/2 operators and $\hat{b}$, $\hat{b}^\dagger$ are bosonic operators. The quantum spins describe an ensemble of atomic two-level systems collectively interacting with a quantized radiation field, represented by the single bosonic mode $\hat{b}$.

The model may be formulated in terms of a collective spin $\hat{S}^\alpha = \sum_j \hat{s}_j^\alpha$ and the bosonic mode $\hat{b}$. Both these degrees of freedom approach their classical limit for $N \to \infty$, described by the classical Hamiltonian $\hat{H}/N \to \mathcal{H}_{cl}$

$$\mathcal{H}_{cl} = \omega_0 S^z + \omega \frac{Q^2 + P^2}{2} + \gamma Q S^x \tag{E.2}$$

Quantum fluctuations around the classical limit may be studied in terms of a semiclassical $1/N$ expansion. They are relevant to describe the long-time nonequilibrium behavior of collective quantities as well as the entanglement properties of the system.

Quantum fluctuations of the collective spin may be described via a Holstein-Primakoff expansion around the time-dependent direction of the average orientation, as in Chap. 3. Quantum fluctuations of the radiation field are simply represented by deviations away from the macroscopic expectation values. In

formulas:

$$\hat{S}^{\alpha} \approx \mathbf{X}(t)\cdot\boldsymbol{\alpha}\,\sqrt{N/2}\,\hat{q} + \mathbf{Y}(t)\cdot\boldsymbol{\alpha}\,\sqrt{N/2}\,\hat{p} + \mathbf{Z}(t)\cdot\boldsymbol{\alpha}\,\left(\frac{N}{2} - \frac{\hat{q}^2+\hat{p}^2-1}{2}\right), \tag{E.3}$$

$$\hat{Q} = \sqrt{N}\mathcal{Q}(t) + \delta\hat{Q}, \tag{E.4}$$

$$\hat{P} = \sqrt{N}\mathcal{P}(t) + \delta\hat{P}, \tag{E.5}$$

with $\alpha = x, y, z$. The classical functions $\mathcal{Q}(t)$, $\mathcal{P}(t)$ and $\mathbf{Z}(t)$ are chosen in such a way that they account for the classical dynamics of the system. As a consequence, the two quantum bosonic operators $(\hat{q}, \hat{p})$ and $(\hat{Q}, \hat{P})$ have vanishing expectation values and describe quantum fluctuations around the classical dynamics. The $\sqrt{N}$ scaling of classical variables may be understood as the occurrence that all terms in the Hamiltonian are extensive and balance each other in equilibrium. Conversely, typical quantum fluctuations in equilibrium, quantified by the expectation values of quadratic bosonic operators, are of order $\mathcal{O}(1)$, i.e., subextensive. This corresponds to having an effective Planck constant $\hbar_{\text{eff}} = \hbar/N$.

The semiclassical time-evolution of the system can be obtained by substituting the time-dependent expansion above into the Hamiltonian and truncating to quadratic order. Dynamics of quantum fluctuations are generated by the modified Hamiltonian $\widetilde{H} = \hat{H} - i\dot{\hat{V}}(t)\hat{V}^{\dagger}(t)$ which includes the inertial terms, due to the time-dependence of the transformation. In order for the approximation to be self-consistent, one must appropriately choose the classical functions $\mathcal{Q}(t)$, $\mathcal{P}(t)$ and $\mathbf{Z}(t)$ in such a way that linear terms in the bosonic variables vanishing. This results in the classical dynamics of the collective spin and the radiation field:

$$\begin{cases} \dot{\mathcal{Q}} = \omega\mathcal{P}, \\ \dot{\mathcal{P}} = -\omega\mathcal{Q} - \dfrac{\gamma}{2}\mathbf{Z}\cdot\mathbf{x}, \\ \dot{\mathbf{Y}}\cdot\mathbf{Z} = \omega_0\,\mathbf{X}\cdot\mathbf{z} + \gamma\mathcal{Q}\,\mathbf{X}\cdot\mathbf{x}, \\ \dot{\mathbf{Z}}\cdot\mathbf{X} = \omega_0\,\mathbf{Y}\cdot\mathbf{z} + \gamma\mathcal{Q}\,\mathbf{Y}\cdot\mathbf{x}. \end{cases} \tag{E.6}$$

The dynamics of quantum fluctuations is regulated by the equations of motion

$$\begin{cases} \dot{\delta\hat{Q}} = +\omega\delta\hat{P}, \\ \dot{\delta\hat{P}} = -\omega\delta\hat{Q} - \dfrac{\gamma}{\sqrt{2}}(\mathbf{X}\cdot\mathbf{x}\,\hat{q} + \mathbf{Y}\cdot\mathbf{x}\,\hat{p}), \\ \dot{\hat{q}} = -(\omega_0\,\mathbf{Z}\cdot\mathbf{z} + \gamma\mathcal{Q}\,\mathbf{Z}\cdot\mathbf{x} - \dot{\mathbf{X}}\cdot\mathbf{Y})\hat{p} + \dfrac{\gamma}{\sqrt{2}}\,\mathbf{Y}\cdot\mathbf{x}\,\delta\hat{Q}, \\ \dot{\hat{p}} = +(\omega_0\,\mathbf{Z}\cdot\mathbf{z} + \gamma\mathcal{Q}\,\mathbf{Z}\cdot\mathbf{x} - \dot{\mathbf{X}}\cdot\mathbf{Y})\hat{q} - \dfrac{\gamma}{\sqrt{2}}\,\mathbf{X}\cdot\mathbf{x}\,\delta\hat{Q}. \end{cases} \tag{E.7}$$

With the standard choice of parameterization of the rotating frame

$$\mathbf{X} \equiv \begin{pmatrix} \cos\theta\cos\phi \\ \cos\theta\sin\phi \\ -\sin\theta \end{pmatrix}, \quad \mathbf{Y} \equiv \begin{pmatrix} -\sin\phi \\ \cos\phi \\ 0 \end{pmatrix}, \quad \mathbf{Z} \equiv \begin{pmatrix} \sin\theta\cos\phi \\ \sin\theta\sin\phi \\ \cos\theta \end{pmatrix}. \tag{E.8}$$

one has

$$\dot{\mathbf{Y}} \cdot \mathbf{Z} = \cos\theta\dot{\phi}, \qquad \dot{\mathbf{Z}} \cdot \mathbf{X} = \dot{\theta}, \qquad \dot{\mathbf{X}} \cdot \mathbf{Y} = -\sin\theta\dot{\phi}. \tag{E.9}$$

From these equations, one derives the evolution equations of quantum correlation functions. We will do this in a compact form. Let us denote

$$\hat{\mathbf{x}} = \begin{pmatrix} \delta\hat{Q} \\ \delta\hat{P} \\ \hat{q} \\ \hat{p} \end{pmatrix}, \tag{E.10}$$

and let us rewrite Eqs. (E.7) compactly as

$$\dot{\hat{\mathbf{x}}} = A(t) \cdot \hat{\mathbf{x}}, \tag{E.11}$$

where $A(t)$ is a time-dependent 4×4 matrix defined by Eqs. (E.7). Now let us define the matrix of correlations

$$\Delta_{ij} = \left\langle \frac{\hat{x}_i \hat{x}_j + \hat{x}_j \hat{x}_i}{2}. \right\rangle \tag{E.12}$$

As in App. B, one finds the evolution equation of the correlations

$$\dot{\Delta} = A(t) \cdot \Delta + \Delta \cdot A(t)^T. \tag{E.13}$$

These equations form the basis to address entanglement dynamics between atoms and the cavity field in the Dicke model, along the lines of Chap. 6. In particular, entanglement entropy may be accessed by collective measurements on the atoms, with an established set of techniques in experimental AMO physics.

Appendix F

Fourier transform of $1/r^\alpha$

In studying long-range interactions, one often needs the Fourier transform of $1/r^\alpha$ on a periodic d-dimensional lattice of $N = L^d$ sites. In this Appendix, we discuss the behavior of this function. For simplicity we focus on hypercubic lattices with unit spacing, i.e, the j-th lattice site has integer spatial coordinates $\mathbf{r}_j = (r_j^1, \dots, r_j^d)$ with $r_j^\mu = 1, 2, \dots, L$, and we define the distance as the minimal (Euclidean) distance on the discrete d-dimensional torus, i.e.,

$$\|\mathbf{r}_j - \mathbf{r}_i\| \equiv \sqrt{\sum_{\mu=1}^{d} \left[\mathrm{Min}\left(|r_i^\mu - r_j^\mu|, L - |r_i^\mu - r_j^\mu| \right) \right]^2}. \tag{F.1}$$

The properties derived below rely only on the $1/r^\alpha$ decay, and not on the specific lattice nor on the choice of periodization of the distance.

The Fourier transform is defined as

$$f_{\alpha,\mathbf{k}} = \frac{1}{\mathcal{N}_{\alpha,N}} \sum_{j(\neq i)}^{N} \frac{e^{-i\mathbf{k}\cdot(\mathbf{r}_j - \mathbf{r}_i)}}{\|\mathbf{r}_j - \mathbf{r}_i\|^\alpha}, \tag{F.2}$$

where the quasimomentum takes values $\mathbf{k} = 2\pi\mathbf{n}/N$ in the Brillouin zone, with $\mathbf{n} = (n_1, \dots, n_d)$ and $n_\mu = 0, 1, \dots, L-1$. The Kac normalization factor $1/\mathcal{N}_{\alpha,N}$ is chosen in such a way that for all α, d and N one has

$$f_{\alpha,\mathbf{k}=\mathbf{0}} \equiv 1. \tag{F.3}$$

In particular,

$$\mathcal{N}_{\alpha,N} \equiv \sum_{j(\neq i)}^{N} \frac{1}{\|\mathbf{r}_j - \mathbf{r}_i\|^\alpha} \underset{N\to\infty}{\sim} \begin{cases} N^{d-\alpha} & \text{for } \alpha < d, \\ \log N & \text{for } \alpha = d, \\ \text{const} & \text{for } \alpha > d. \end{cases} \tag{F.4}$$

Note that $\sum_{\mathbf{k}} f_{\alpha,\mathbf{k}} \equiv 0$ for all α, d and N.

For $\alpha = 0$, one has a delta function

$$f_{\alpha=0,\mathbf{k}} \equiv \delta_{\mathbf{k},\mathbf{0}}. \tag{F.5}$$

For long-range interactions with $0 < \alpha < d$, one can safely approximate sums with integrals in their defining expression (F.2), which captures the leading order. Hence, one can switch to spherical coordinates and integrate over all the angles, obtaining

$$f_{\alpha,\mathbf{k}\neq\mathbf{0}} \sim \frac{1}{L^{d-\alpha}} \int_1^L d\rho\, \rho^{d-1-\alpha}\, \frac{\mathcal{J}_{d/2-1}(|\mathbf{k}|\rho)}{(|\mathbf{k}|\rho)^{d/2-1}}, \tag{F.6}$$

where $\mathcal{J}_\nu(x)$ is the standard Bessel function of order ν. While for small ρ the integral is never singular (due to the assumption of long-range interactions, $\alpha < d$), for large ρ the integrand is asymptotically oscillating with period $2\pi/|\mathbf{k}|$ and amplitude decaying as $\rho^{(d-1)/2-\alpha}$, which yields convergence only for $\alpha > (d-1)/2$. In this case, by rescaling $|\mathbf{k}|\rho = \eta$ to obtain a dimensionless integrand and denoting by $F(\eta)$ its primitive which satisfies $F(\infty) = 0$ and is uniformly bounded, one obtains the asymptotic estimate

$$f_{\alpha,\mathbf{k}\neq\mathbf{0}} \underset{L\to\infty}{\sim} -\frac{F(|\mathbf{k}|)}{(|\mathbf{k}|L)^{d-\alpha}}. \tag{F.7}$$

In the limiting case $\alpha = d$, one can similarly compute

$$f_{\alpha,\mathbf{k}\neq\mathbf{0}} \underset{L\to\infty}{\sim} -\frac{\log|\mathbf{k}| + \tilde{F}(|\mathbf{k}|)}{\log L}, \tag{F.8}$$

where $\tilde{F}$ is the nonsingular (bounded) part of the primitive F. On the other hand, for $\alpha \leqslant (d-1)/2$, by isolating the purely oscillatory terms and repeatedly integrating by parts, we can obtain an expansion of the primitive of the form

$$f_{\alpha,\mathbf{k}\neq\mathbf{0}} \sim \frac{1}{(|\mathbf{k}|L)^{d-\alpha}} \left(c_1 (|\mathbf{k}|L)^{\frac{d-1}{2}-\alpha} + c_2 (|\mathbf{k}|L)^{\frac{d-1}{2}-\alpha-1} + \dots \right), \tag{F.9}$$

with $c_{1,2,\dots}$ numerical constants. To sum up, the following estimates have been established,

$$\left|f_{\alpha,\mathbf{k}\neq\mathbf{0}}\right| \leqslant \begin{cases} \text{const} \times \dfrac{1}{(|\mathbf{k}|L)^{\frac{d+1}{2}}} & \text{for } \alpha \leqslant \dfrac{d-1}{2}, \\ \text{const} \times \dfrac{1}{(|\mathbf{k}|L)^{d-\alpha}} & \text{for } \dfrac{d-1}{2} < \alpha < d, \\ \text{const} \times \dfrac{\left|\log|\mathbf{k}| + \tilde{F}(|\mathbf{k}|)\right|}{\log L} & \text{for } \alpha = d. \end{cases} \tag{F.10}$$

These bounds imply that for all fixed $\mathbf{k} \neq \mathbf{0}$, the perturbing coupling $f_{\alpha,\mathbf{k}}$ is vanishingly small in thermodynamic limit $L \to \infty$ whenever $\alpha \leqslant d$.

For $\alpha > d$, the function $f_{\alpha,\mathbf{k}}$ attains everywhere a finite limit as $L \to \infty$. However, it has a singular behavior for small wavevectors $\mathbf{k}$ due to the slow decay of $|\mathbf{r}|^{-\alpha}$. The leading terms are

$$f_{\alpha,\mathbf{k}} \underset{k\to 0}{\sim} 1 - c(\alpha)|\mathbf{k}|^{\alpha-d} - \kappa(\alpha)|\mathbf{k}|^2. \tag{F.11}$$

In particular, for $d < \alpha < d+1$ the function has a cusp. In long-range interacting physical systems, where $f_{\alpha,\mathbf{k}}$ usually enters the dispersion relations of quasiparticles, the cusp singularity is at the root of an unbounded maximal velocity of propagation of long-wavelength excitations. However, for shorter-range interactions with $\alpha \geqslant d+1$, a finite maximal velocity appears, reproducing the relativistic behavior characteristic of locally-interacting field theories. In the limit $\alpha = \infty$, one finally recovers the familiar result with nearest-neighbor interactions, i.e.,

$$f_{\infty,\mathbf{k}} = \frac{1}{d} \sum_{\mu=1}^{d} \cos(k_\mu). \tag{F.12}$$

By numerically computing the function f for some values of α and d, one can check all the properties derived above. In particular, the bounds (F.10) are actually accurate. This is illustrated in Fig. F.1.

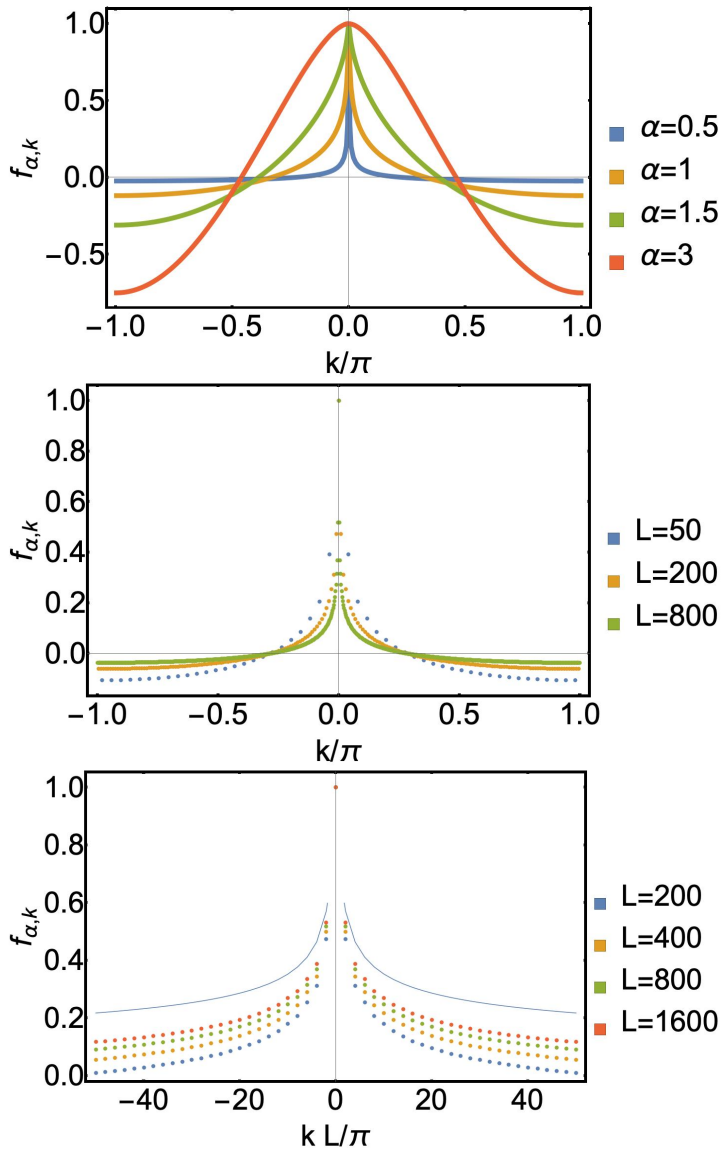

Figure F.1: Plots of the function $f_{\alpha,k}$ for $d = 1$. Top panel: $f_{\alpha,k}$ is shown for several values of α, for $N = L = 400$. One recognizes a function squeezed towards $k = 0$ ($0 \leqslant \alpha \leqslant 1$), a finite function with a cusp behavior for small k ($1 < \alpha < 2$), and a cosine-like function ($\alpha \gg 2$). Middle panel: $f_{\alpha,k}$ is shown for $\alpha = 0.7$ and increasing values of $N = L$. A qualitatively similar behavior occurs for $0 \leqslant \alpha \leqslant 1$. Squeezing towards a delta function as $L \to \infty$ occurs with a speed $N^{-(1-\alpha)}$ for $\alpha < 1$ and $\log N$ for $\alpha = 1$. Bottom panel: a zoom of the plot in the middle panel is shown, for larger values of $N = L$. The rescaled function in the vicinity of $k = 0$ appears to converge to a finite limiting curve as $L \to \infty$. The blue solid line illustrates the bound obtained in Eq. (F.10).

Appendix G

Bloch oscillations

In this Appendix, we briefly review the exact solution of the one-dimensional Wannier-Stark problem, and discuss its relevant generalizations needed in Part II of this thesis.

Spectrum. — We are interested in the problem of a single quantum particle hopping on a chain and subject to a linear potential. The Schrödinger equation reads

$$j\psi_j + \kappa(\psi_{j+1} + \psi_{j-1}) = -i\partial_t\psi_j, \qquad j \in \mathbb{Z}. \tag{G.1}$$

This problem emerges primarily in the context of electrons subject to a constant electric field. In Chaps. 7 and 8, it models the dynamics of an isolated domain-wall in a quantum Ising chain subject to a tilted magnetic field. (Actually, the latter is equivalent to the former via the exact mapping presented in Sec. 7.2.3.) See also Ref. [390] for a further experimental phenomenon described by this model.

The static problem can be solved in Fourier space. The transformed wavefunction reads

$$\tilde{\psi}(k) = \sum_j \frac{e^{ikj}}{\sqrt{2\pi}}\psi_j. \tag{G.2}$$

We plug the ansatz $\psi_j(t) = e^{-iEt}\psi_j$ into Eq. (G.1) and take its Fourier transform, obtaining

$$\Big(-i\partial_k + 2\kappa\cos k\Big)\tilde{\psi}(k) = E\tilde{\psi}(k). \tag{G.3}$$

This differential equation can be solved with elementary methods. Upon transforming back to the lattice representation, we find

$$\psi_j \propto \int_{-\pi}^{\pi} \frac{dk}{2\pi}\, e^{i[(E-j)k - 2\kappa\sin k]} \equiv \mathcal{J}_{E-j}(2\kappa), \tag{G.4}$$

where $\mathcal{J}_\nu$ is the standard Bessel function of order ν. This wavefunction is normalizable only for integer values of $E-j$. Hence, the spectrum of the Hamiltonian is an infinite equispaced ladder

$$E_n = n, \qquad n \in \mathbb{Z}, \tag{G.5}$$

independent of κ. This could be deduced a priori from the transformation properties of the Schrödinger equation under lattice translations. For the same reason, the eigenfunctions

$$\psi_j^{(n)} \propto \mathcal{J}_{n-j}(2\kappa) \tag{G.6}$$

can be obtained from a single one, e.g., $\psi_j^{(0)}$, by a rigid shift, i.e.,

$$\psi_j^{(n)} \equiv \psi_{j-n}^{(0)}. \tag{G.7}$$

These Wannier-Stark orbitals are localized around their reference lattice site, and their tails decay faster than exponentially outside the classically accessible region $|j-n| \lesssim 2\kappa$ (see below).

Time-evolution. — By virtue of the regular spacing of the spectrum, time-evolution is strictly periodic in time. It can be obtained with a physically insightful strategy. By means of a gauge transformation, we can trade the linear electrostatic potential in Eq. (G.1) with a uniform, linear-in-time vector potential. For this one-dimensional lattice problem, a vector potential corresponds to a complex phase in the hopping amplitude $\kappa \to \kappa e^{it}$. In this gauge, the problem is translation-invariant (though time-dependent), and hence it can be diagonalized in Fourier space.

The gauge transformation above is implemented by the time-dependent unitary transformation $\hat{V}(t)$

$$\psi_j(t) = \Big[\hat{V}(t)\psi'(t)\Big]_j \equiv e^{-itj}\psi'_j(t). \tag{G.8}$$

This 2π-periodic transformation eliminates the static linear potential in the modified Hamiltonian $\widetilde{H}(t) = \hat{V}\hat{H}\hat{V}^\dagger + i\dot{\hat{V}}\hat{V}^\dagger$, and changes $\kappa \to \kappa e^{it}$. In Fourier space, the transformed Eq. (G.1) reads

$$\Big[2\kappa\cos(k-t)\Big]\,\tilde{\psi}'(k,t) = -i\partial_t\tilde{\psi}'(k,t). \tag{G.9}$$

The time-evolved wavefunction $\psi_j(t)$ can be found by solving the above elementary differential equation, taking the Fourier antitransform and going back to the original gauge description. For the initial condition $\psi_j(t=0) = \delta_{j,n}$, we find

$$\begin{aligned}\psi_j(t) = e^{itj}\int_{-\pi}^{\pi}\frac{dk}{2\pi}\,e^{ik(j-n)}\,e^{i4\kappa\sin(t/2)\,\cos(k-t/2)} \\ \equiv (-i)^{j-n}e^{-it(j+n)/2}\,\mathcal{J}_{j-n}\Big(4\kappa\sin(t/2)\Big)\end{aligned} \tag{G.10}$$

where $\mathcal{J}_\nu$ is again the standard Bessel function of order ν. Time-evolution consists in periodic oscillations (*Bloch oscillations*) around the initial position.

Longer-range hopping. — In Sec. 8.2, we have found that the effective dynamics of domain-walls is dressed order by order in perturbation theory by processes which conserve their number, i.e., hopping transitions. In particular, at n^*-th order, there appear hopping processes of range up to n^* — see, e.g., Eq. (8.4).

The Schrödinger equation (G.1) with longer-range hopping terms can be solved with the same steps. In the general case, one obtains a similar solution to Eq. (G.4) in which $\sin k$ in the exponent is replaced with a periodic function with higher harmonics, i.e., the dispersion relation of the hopping particle in the absence of the constant field. The energy spectrum is the same Wannier-Stark ladder as in Eq. (G.5), whereas the eigenfunctions in Eq. (G.6) are modified, still retaining their localized nature.

Semiclassical evolution. — Similarly to the effective problem in Sec. 2.1.1, we embed the lattice $j \in \mathbb{Z}$ in a continuous space $x \in \mathbb{R}$, and introduce the conjugate operators

$$\hat{Q} \mapsto x, \qquad \hat{P} \mapsto -i\partial_x. \tag{G.11}$$

which satisfy $[\hat{Q}, \hat{P}] = i$. the former describes the position of the particle along the chain, and the latter represents its quasimomentum. The Hamiltonian of the Wannier-Stark ladder can be expressed in terms of these variables as

$$\hat{H} = \hat{Q} + 2\kappa \cos \hat{P}. \tag{G.12}$$

The Heisenberg equations of motion

$$\frac{d}{dt}\hat{Q} = -2\kappa \sin \hat{P}, \qquad \frac{d}{dt}\hat{P} = -1, \tag{G.13}$$

can be solved in closed form:

$$\hat{Q}(t) = \hat{Q}(0) - 2\kappa\Big[\cos t \, \cos\big(\hat{P}(0)\big) + \sin t \, \sin\big(\hat{P}(0)\big)\Big], \qquad \hat{P}(t) = \hat{P}(0) - t. \tag{G.14}$$

The time-evolving expectation values of $\hat{Q}$ and $\hat{P}$ can then be determined explicitly for any given initial state. In particular, we retrieve the exact properties of 2π-periodicity (recall that $\hat{P}$ is an angular variable) and localization ($|\hat{Q}(t) - \hat{Q}(0)|$ is bounded for all times).

The dynamics attain a semiclassical limit when $\kappa \gg 1$. In order to see this, we define the rescaled variables

$$\hat{q} = \hat{Q}/\kappa \mapsto \xi, \qquad \hat{p} = \hat{P} \mapsto -(i/\kappa)\partial_\xi, \tag{G.15}$$

which satisfy $[\hat{q}, \hat{p}] = i/\kappa$. In terms of these variables, the Schrödinger equation reads

$$\big(\hat{q} + 2\cos\hat{p}\big)\psi = -(i/\kappa)\partial_t\psi. \tag{G.16}$$

Thus, one has a quantum problem with an effective Planck constant $\hbar_{\text{eff}} = 1/\kappa$.

Hard boundaries. — The solution to the Wannier-Stark problem in the presence of a boundary (i.e., on a semi-infinite chain) plays a crucial role in the physics discussed in Sec. 8.3, as it describes the two-domain-wall problem in the center-of-mass frame. As discussed therein, the qualitative effect of the boundary is to modify the orbitals that significantly overlap with it, i.e., those localized at a distance d of the order of the Wannier-Stark localization length κ. In a semiclassical picture, these are the trajectories that hit the hard wall, whereas

oscillations around distant positions from the wall are unaffected by its presence. An exact solution to this generalized problem in terms of Bessel functions has been found by H. C. Fogedby in Ref. [381].

Inhomogeneous ladders. — We finally discuss another generalization of the Wannier-Stark ladder, namely a nonuniform field $n \mapsto V(n)$ in Eq. (G.1). Such problem is relevant for confinement in systems with long-range interactions, as detailed in Secs. 7.3 and 8.5.2, where for an exponent α of the algebraically-decaying interactions in the range $(1, 2)$, one has the scaling form

$$V_\alpha(n) = n^{2-\alpha} + (L-n)^{2-\alpha} - L^{2-\alpha} \equiv L^{2-\alpha}\, v_\alpha(n/L) \tag{G.17}$$

for a finite open chain of L sites, i.e., $1 \leqslant n \leqslant L$ [cf. Eq. (8.39)]. In this case, with the same definitions of $\hat{Q}$ and $\hat{P}$ as above, one has

$$\hat{H} = V(\hat{Q}) + 2\kappa \cos \hat{P}. \tag{G.18}$$

By virtue of the scaling of the potential with L, we can define the rescaled variables

$$\hat{q} = \hat{Q}/L \mapsto \xi, \qquad \hat{p} = \hat{P} \mapsto -(i/L)\partial_\xi, \tag{G.19}$$

which satisfy $[\hat{q}, \hat{p}] = i/L$. In terms of these variables, the Schrödinger equation reads

$$\Big(L^{2-\alpha}\, v(\hat{q}) + 2\kappa \cos \hat{p}\Big)\psi = -i\partial_t \psi. \tag{G.20}$$

A semiclassical limit with an effective Planck constant $\hbar_{\text{eff}} = 1/L$ is defined for $\kappa \sim L^{2-\alpha}$ and by rescaling time by an extra factor $L^{\alpha-1}$. These operations reproduce the scaling laws in Eqs. (8.42).

Bibliography

[1] A. Lerose, J. Marino, B. Žunkovič, A. Gambassi and A. Silva, *Chaotic Dynamical Ferromagnetic Phase Induced by Nonequilibrium Quantum Fluctuations*, *Phys. Rev. Lett.* **120** (2018) 130603.

[2] A. Lerose, B. Žunkovič, J. Marino, A. Gambassi and A. Silva, *Impact of nonequilibrium fluctuations on prethermal dynamical phase transitions in long-range interacting spin chains*, *Phys. Rev. B* **99** (2019) 045128.

[3] A. Lerose, J. Marino, A. Gambassi and A. Silva, *Prethermal quantum many-body Kapitza phases of periodically driven spin systems*, *Phys. Rev. B* **100** (2019) 104306.

[4] A. Lerose and S. Pappalardi, *Origin of the slow growth of entanglement entropy in long-range interacting systems*, *arXiv:1811.05505* (2018).

[5] P. P. Mazza, G. Perfetto, A. Lerose, M. Collura and A. Gambassi, *Suppression of transport in nondisordered quantum spin chains due to confined excitations*, *Phys. Rev. B* **99** (2019) 180302.

[6] A. Lerose, B. Žunkovič, A. Silva and A. Gambassi, *Quasilocalized excitations induced by long-range interactions in translationally invariant quantum spin chains*, *Phys. Rev. B* **99** (2019) 121112.

[7] F. M. Surace, P. P. Mazza, G. Giudici, A. Lerose, A. Gambassi and M. Dalmonte, *Lattice gauge theories and string dynamics in Rydberg atom quantum simulators*, *arXiv:1902.09551* (2019).

[8] V. K. Varma, A. Lerose, F. Pietracaprina, J. Goold and A. Scardicchio, *Energy diffusion in the ergodic phase of a many body localizable spin chain*, *Journal of Statistical Mechanics: Theory and Experiment* **2017** (2017) 053101.

[9] S. Sachdev, *Quantum Phase Transitions*. Cambridge University Press, 2011.

[10] P. Di Francesco, P. Mathieu and Senechal, *Conformal Field Theory*. Springer, 1999.

[11] P. Calabrese, F. H. L. Essler and M. Fagotti, *Quantum Quench in the Transverse-Field Ising Chain*, *Phys. Rev. Lett.* **106** (2011) 227203.

[12] J. v. Neumann, *Beweis des Ergodensatzes und des H-Theorems in der neuen Mechanik*, *Zeitschrift für Physik* **57** (1929) 30.

[13] G. Gallavotti, *Statistical Mechanics: A short treatise*. Springer, 1999.

[14] M. Greiner, O. Mandel, T. W. Hansch and I. Bloch, *Collapse and revival of the matter wave field of a Bose-Einstein condensate*, *Nature* **419** (2002) 51.

[15] M. Greiner, O. Mandel, T. Esslinger, T. W. Hänsch and I. Bloch, *Quantum phase transition from a superfluid to a Mott insulator in a gas of ultracold atoms*, *Nature* **415** (2002) 39.

[16] I. Bloch, J. Dalibard and W. Zwerger, *Many-body physics with ultracold gases*, *Rev. Mod. Phys.* **80** (2008) 885.

[17] S. Trotzky, P. Cheinet, S. Fölling, M. Feld, U. Schnorrberger, A. M. Rey et al., *Time-Resolved Observation and Control of Superexchange Interactions with Ultracold Atoms in Optical Lattices*, *Science* **319** (2008) 295.

[18] M. Cheneau, P. Barmettler, D. Poletti, M. Endres, P. Schausz, T. Fukuhara et al., *Light-cone-like spreading of correlations in a quantum many-body system*, *Nature* **481** (2012) 484.

[19] A. M. Kaufman, M. E. Tai, A. Lukin, M. Rispoli, R. Schittko, P. M. Preiss et al., *Quantum thermalization through entanglement in an isolated many-body system*, *Science* **353** (2016) 794.

[20] T. Schweigler, V. Kasper, S. Erne, I. Mazets, B. Rauer, F. Cataldini et al., *Experimental characterization of a quantum many-body system via higher-order correlations*, *Nature* **545** (2017) 323.

[21] B. Rauer, S. Erne, T. Schweigler, F. Cataldini, M. Tajik and J. Schmiedmayer, *Recurrences in an isolated quantum many-body system*, *Science* **360** (2018) 307.

[22] P. R. Halmos, *Lectures on Ergodic Theory*. Martino Fine Books, 2013.

[23] M. C. Gutzwiller, *Chaos in classical and quantum mechanics*. Springer, 1990.

[24] R. V. Jensen and R. Shankar, *Statistical Behavior in Deterministic Quantum Systems with Few Degrees of Freedom*, *Phys. Rev. Lett.* **54** (1985) 1879.

[25] M. Rigol, V. Dunjko and M. Olshanii, *Thermalization and its mechanism for generic isolated quantum systems*, *Nature* **452** (2008) 854.

[26] J. Eisert, M. Friesdorf and C. Gogolin, *Quantum many-body systems out of equilibrium*, *Nature Physics* **11** (2015) 124.

[27] S. Goldstein, D. A. Huse, J. L. Lebowitz and R. Tumulka, *Thermal Equilibrium of a Macroscopic Quantum System in a Pure State*, *Phys. Rev. Lett.* **115** (2015) 100402.

[28] T. Mori, T. N. Ikeda, E. Kaminishi and M. Ueda, *Thermalization and prethermalization in isolated quantum systems: a theoretical overview*, *Journal of Physics B: Atomic, Molecular and Optical Physics* **51** (2018) 112001.

[29] J. M. Deutsch, *Quantum statistical mechanics in a closed system*, *Phys. Rev. A* **43** (1991) 2046.

[30] M. Srednicki, *Chaos and quantum thermalization*, *Phys. Rev. E* **50** (1994) 888.

[31] L. D'Alessio, Y. Kafri, A. Polkovnikov and M. Rigol, *From quantum chaos and eigenstate thermalization to statistical mechanics and thermodynamics*, *Advances in Physics* **65** (2016) 239.

[32] S. Weinberg, *The Quantum Theory of Fields, Volume 1: Foundations*. Cambridge University Press, 2005.

[33] P. Bocchieri and A. Loinger, *Quantum Recurrence Theorem*, *Phys. Rev.* **107** (1957) 337.

[34] F. H. L. Essler and M. Fagotti, *Quench dynamics and relaxation in isolated integrable quantum spin chains*, *Journal of Statistical Mechanics: Theory and Experiment* **2016** (2016) 064002.

[35] P. Calabrese and J. Cardy, *Time Dependence of Correlation Functions Following a Quantum Quench*, *Phys. Rev. Lett.* **96** (2006) 136801.

[36] E. H. Lieb and D. W. Robinson, *The finite group velocity of quantum spin systems*, *Comm. Math. Phys.* **28** (1972) 251.

[37] D. A. Roberts and B. Swingle, *Lieb-Robinson Bound and the Butterfly Effect in Quantum Field Theories*, *Phys. Rev. Lett.* **117** (2016) 091602.

[38] V. Khemani, D. A. Huse and A. Nahum, *Velocity-dependent Lyapunov exponents in many-body quantum, semiclassical, and classical chaos*, *Phys. Rev. B* **98** (2018) 144304.

[39] X. Han and S. A. Hartnoll, *Quantum Scrambling and State Dependence of the Butterfly Velocity*, *arXiv:1812.07598v3* (2019).

[40] J.-S. Caux and J. Mossel, *Remarks on the notion of quantum integrability*, *Journal of Statistical Mechanics: Theory and Experiment* **2011** (2011) P02023.

[41] E. Lieb, T. Schultz and D. Mattis, *Two soluble models of an antiferromagnetic chain*, *Annals of Physics* **16** (1961) 407.

[42] B. Sutherland, *Beautiful models*. Singapore: World Scientific, 2004.

[43] T. Kinoshita, T. Wenger and D. S. Weiss, *A quantum Newton's cradle*, *Nature* **440** (2006) 900.

[44] M. A. Cazalilla, *Effect of Suddenly Turning on Interactions in the Luttinger Model*, *Phys. Rev. Lett.* **97** (2006) 156403.

[45] M. Rigol, V. Dunjko, V. Yurovsky and M. Olshanii, *Relaxation in a Completely Integrable Many-Body Quantum System: An Ab Initio Study of the Dynamics of the Highly Excited States of 1D Lattice Hard-Core Bosons*, *Phys. Rev. Lett.* **98** (2007) 050405.

[46] M. Cramer, C. M. Dawson, J. Eisert and T. J. Osborne, *Exact Relaxation in a Class of Nonequilibrium Quantum Lattice Systems*, *Phys. Rev. Lett.* **100** (2008) 030602.

[47] T. Barthel and U. Schollwöck, *Dephasing and the Steady State in Quantum Many-Particle Systems*, *Phys. Rev. Lett.* **100** (2008) 100601.

[48] D. Fioretto and G. Mussardo, *Quantum quenches in integrable field theories*, *New Journal of Physics* **12** (2010) 055015.

[49] J.-S. Caux and R. M. Konik, *Constructing the Generalized Gibbs Ensemble after a Quantum Quench*, *Phys. Rev. Lett.* **109** (2012) 175301.

[50] P. Calabrese, F. H. L. Essler and M. Fagotti, *Quantum quenches in the transverse field Ising chain: II. Stationary state properties*, *Journal of Statistical Mechanics: Theory and Experiment* **2012** (2012) P07022.

[51] T. Langen, S. Erne, R. Geiger, B. Rauer, T. Schweigler, M. Kuhnert et al., *Experimental observation of a generalized Gibbs ensemble*, *Science* **348** (2015) 207.

[52] F. H. L. Essler and M. Fagotti, *Quench dynamics and relaxation in isolated integrable quantum spin chains*, *Journal of Statistical Mechanics: Theory and Experiment* **2016** (2016) 064002.

[53] P. Calabrese and J. Cardy, *Quantum quenches in extended systems*, *Journal of Statistical Mechanics: Theory and Experiment* **2007** (2007) P06008.

[54] M. Kollar, F. A. Wolf and M. Eckstein, *Generalized Gibbs ensemble prediction of prethermalization plateaus and their relation to nonthermal steady states in integrable systems*, *Phys. Rev. B* **84** (2011) 054304.

[55] M. Stark and M. Kollar, *Kinetic description of thermalization dynamics in weakly interacting quantum systems*, *arXiv:1308.1610* (2013).

[56] J. Berges, S. Borsányi and C. Wetterich, *Prethermalization*, *Phys. Rev. Lett.* **93** (2004) 142002.

[57] J. Berges, *Introduction to Nonequilibrium Quantum Field Theory*, *AIP Conf. Proc.* **739** (2004) 3.

[58] C. Kollath, A. M. Läuchli and E. Altman, *Quench Dynamics and Nonequilibrium Phase Diagram of the Bose-Hubbard Model*, *Phys. Rev. Lett.* **98** (2007) 180601.

[59] M. Moeckel and S. Kehrein, *Interaction Quench in the Hubbard Model*, *Phys. Rev. Lett.* **100** (2008) 175702.

[60] A. Rosch, D. Rasch, B. Binz and M. Vojta, *Metastable Superfluidity of Repulsive Fermionic Atoms in Optical Lattices*, *Phys. Rev. Lett.* **101** (2008) 265301.

[61] M. Moeckel and S. Kehrein, *Real-time evolution for weak interaction quenches in quantum systems*, *Annals of Physics* **324** (2009) 2146.

[62] M. Gring, M. Kuhnert, T. Langen, T. Kitagawa, B. Rauer, M. Schreitl et al., *Relaxation and Prethermalization in an Isolated Quantum System*, *Science* **337** (2012) 1318.

[63] J. Marino and A. Silva, *Nonequilibrium dynamics of a noisy quantum Ising chain: Statistics of work and prethermalization after a sudden quench of the transverse field*, *Phys. Rev. B* **89** (2014) 024303.

[64] T. Langen, R. Geiger, M. Kuhnert, B. Rauer and J. Schmiedmayer, *Local emergence of thermal correlations in an isolated quantum many-body system*, *Nature Physics* **9** (2013) 640.

[65] N. Nessi, A. Iucci and M. A. Cazalilla, *Quantum Quench and Prethermalization Dynamics in a Two-Dimensional Fermi Gas with Long-Range Interactions*, *Phys. Rev. Lett.* **113** (2014) 210402.

[66] T. Langen, T. Gasenzer and J. Schmiedmayer, *Prethermalization and universal dynamics in near-integrable quantum systems*, *Journal of Statistical Mechanics: Theory and Experiment* **2016** (2016) 064009.

[67] F. H. L. Essler, S. Kehrein, S. R. Manmana and N. J. Robinson, *Quench dynamics in a model with tuneable integrability breaking*, *Phys. Rev. B* **89** (2014) 165104.

[68] B. Bertini, F. H. L. Essler, S. Groha and N. J. Robinson, *Prethermalization and Thermalization in Models with Weak Integrability Breaking*, *Phys. Rev. Lett.* **115** (2015) 180601.

[69] B. Bertini, F. H. L. Essler, S. Groha and N. J. Robinson, *Thermalization and light cones in a model with weak integrability breaking*, *Phys. Rev. B* **94** (2016) 245117.

[70] M. Marcuzzi, J. Marino, A. Gambassi and A. Silva, *Prethermalization in a Nonintegrable Quantum Spin Chain after a Quench*, *Phys. Rev. Lett.* **111** (2013) 197203.

[71] M. Babadi, E. Demler and M. Knap, *Far-from-Equilibrium Field Theory of Many-Body Quantum Spin Systems: Prethermalization and Relaxation of Spin Spiral States in Three Dimensions*, *Phys. Rev. X* **5** (2015) 041005.

[72] M. Marcuzzi, J. Marino, A. Gambassi and A. Silva, *Prethermalization from a low-density Holstein-Primakoff expansion*, *Phys. Rev. B* **94** (2016) 214304.

[73] D. Abanin, W. De Roeck, W. W. Ho and F. Huveneers, *A Rigorous Theory of Many-Body Prethermalization for Periodically Driven and Closed Quantum Systems*, *Communications in Mathematical Physics* **354** (2017) 809.

[74] C.-J. Lin and O. I. Motrunich, *Explicit construction of quasiconserved local operator of translationally invariant nonintegrable quantum spin chain in prethermalization*, *Phys. Rev. B* **96** (2017) 214301.

[75] D. V. Else, B. Bauer and C. Nayak, *Prethermal Phases of Matter Protected by Time-Translation Symmetry*, *Phys. Rev. X* **7** (2017) 011026.

[76] R. A. Barankov, L. S. Levitov and B. Z. Spivak, *Collective Rabi Oscillations and Solitons in a Time-Dependent BCS Pairing Problem*, *Phys. Rev. Lett.* **93** (2004) 160401.

[77] R. A. Barankov and L. S. Levitov, *Synchronization in the BCS Pairing Dynamics as a Critical Phenomenon*, *Phys. Rev. Lett.* **96** (2006) 230403.

[78] E. A. Yuzbashyan, O. Tsyplyatyev and B. L. Altshuler, *Relaxation and Persistent Oscillations of the Order Parameter in Fermionic Condensates*, *Phys. Rev. Lett.* **96** (2006) 097005.

[79] V. Gurarie, *Nonequilibrium Dynamics of Weakly and Strongly Paired Superconductors*, *Phys. Rev. Lett.* **103** (2009) 075301.

[80] M. Eckstein, M. Kollar and P. Werner, *Thermalization after an Interaction Quench in the Hubbard Model*, *Phys. Rev. Lett.* **103** (2009) 056403.

[81] M. Schiró and M. Fabrizio, *Time-Dependent Mean Field Theory for Quench Dynamics in Correlated Electron Systems*, *Phys. Rev. Lett.* **105** (2010) 076401.

[82] B. Sciolla and G. Biroli, *Quantum Quenches and Off-Equilibrium Dynamical Transition in the Infinite-Dimensional Bose-Hubbard Model*, *Phys. Rev. Lett.* **105** (2010) 220401.

[83] B. Sciolla and G. Biroli, *Dynamical transitions and quantum quenches in mean-field models*, *Journal of Statistical Mechanics: Theory and Experiment* **2011** (2011) P11003.

[84] A. Gambassi and P. Calabrese, *Quantum quenches as classical critical films*, *EPL (Europhysics Letters)* **95** (2011) 66007.

[85] M. Schiró and M. Fabrizio, *Quantum quenches in the Hubbard model: Time-dependent mean-field theory and the role of quantum fluctuations*, *Phys. Rev. B* **83** (2011) 165105.

[86] M. Sandri, M. Schiró and M. Fabrizio, *Linear ramps of interaction in the fermionic Hubbard model*, *Phys. Rev. B* **86** (2012) 075122.

[87] B. Sciolla and G. Biroli, *Quantum quenches, dynamical transitions, and off-equilibrium quantum criticality*, *Phys. Rev. B* **88** (2013) 201110.

[88] M. S. Foster, M. Dzero, V. Gurarie and E. A. Yuzbashyan, *Quantum quench in a* $\mathrm{p}+\mathrm{i}\mathrm{p}$ *superfluid: Winding numbers and topological states far from equilibrium*, *Phys. Rev. B* **88** (2013) 104511.

[89] M. S. Foster, V. Gurarie, M. Dzero and E. A. Yuzbashyan, *Quench-Induced Floquet Topological* p*-Wave Superfluids*, *Phys. Rev. Lett.* **113** (2014) 076403.

[90] P. Smacchia, M. Knap, E. Demler and A. Silva, *Exploring dynamical phase transitions and prethermalization with quantum noise of excitations*, *Phys. Rev. B* **91** (2015) 205136.

[91] F. Peronaci, M. Schiró and M. Capone, *Transient Dynamics of* d*-Wave Superconductors after a Sudden Excitation*, *Phys. Rev. Lett.* **115** (2015) 257001.

[92] E. A. Yuzbashyan, M. Dzero, V. Gurarie and M. S. Foster, *Quantum quench phase diagrams of an* s*-wave BCS-BEC condensate*, *Phys. Rev. A* **91** (2015) 033628.

[93] J. C. Halimeh, V. Zauner-Stauber, I. P. McCulloch, I. de Vega, U. Schollwöck and M. Kastner, *Prethermalization and persistent order in the absence of a thermal phase transition*, *Phys. Rev. B* **95** (2017) 024302.

[94] I. Homrighausen, N. O. Abeling, V. Zauner-Stauber and J. C. Halimeh, *Anomalous dynamical phase in quantum spin chains with long-range interactions*, *Phys. Rev. B* **96** (2017) 104436.

[95] H.-K. Janssen, B. Schaub and B. Schmittmann, *New universal short-time scaling behaviour of critical relaxation processes*, *Z. Phys. B Cond. Mat.* **73** (1989) 539.

[96] P. Calabrese and A. Gambassi, *Ageing properties of critical systems*, *Journal of Physics A: Mathematical and General* **38** (2005) R133.

[97] A. Chandran, A. Nanduri, S. S. Gubser and S. L. Sondhi, *Equilibration and coarsening in the quantum* O(N) *model at infinite* N, *Phys. Rev. B* **88** (2013) 024306.

[98] A. Maraga, A. Chiocchetta, A. Mitra and A. Gambassi, *Aging and coarsening in isolated quantum systems after a quench: Exact results for the quantum* $O(\mathrm{N})$ *model with* $\mathrm{N} \to \infty$, *Phys. Rev. E* **92** (2015) 042151.

[99] A. Chiocchetta, M. Tavora, A. Gambassi and A. Mitra, *Short-time universal scaling in an isolated quantum system after a quench*, *Phys. Rev. B* **91** (2015) 220302.

[100] A. Chiocchetta, A. Gambassi, S. Diehl and J. Marino, *Dynamical Crossovers in Prethermal Critical States*, *Phys. Rev. Lett.* **118** (2017) 135701.

[101] J. Zhang, G. Pagano, P. W. Hess, A. Kyprianidis, P. Becker, H. Kaplan et al., *Observation of a many-body dynamical phase transition with a 53-qubit quantum simulator*, *Nature* **551** (2017) 601.

[102] M. Heyl, A. Polkovnikov and S. Kehrein, *Dynamical Quantum Phase Transitions in the Transverse-Field Ising Model*, *Phys. Rev. Lett.* **110** (2013) 135704.

[103] P. Jurcevic, H. Shen, P. Hauke, C. Maier, T. Brydges, C. Hempel et al., *Direct Observation of Dynamical Quantum Phase Transitions in an Interacting Many-Body System*, *Phys. Rev. Lett.* **119** (2017) 080501.

[104] M. Heyl, *Dynamical quantum phase transitions: a review*, *Reports on Progress in Physics* **81** (2018) 054001.

[105] C. Karrasch and D. Schuricht, *Dynamical phase transitions after quenches in nonintegrable models*, *Phys. Rev. B* **87** (2013) 195104.

[106] B. Žunkovič, M. Heyl, M. Knap and A. Silva, *Dynamical Quantum Phase Transitions in Spin Chains with Long-Range Interactions: Merging Different Concepts of Nonequilibrium Criticality*, *Phys. Rev. Lett.* **120** (2018) 130601.

[107] S. A. Weidinger, M. Heyl, A. Silva and M. Knap, *Dynamical quantum phase transitions in systems with continuous symmetry breaking*, *Phys. Rev. B* **96** (2017) 134313.

[108] J. Lang, B. Frank and J. C. Halimeh, *Dynamical Quantum Phase Transitions: A Geometric Picture*, *Phys. Rev. Lett.* **121** (2018) 130603.

[109] M. Grifoni and P. Hänggi, *Driven quantum tunneling*, *Physics Reports* **304** (1998) 229.

[110] M. Bukov, L. D'Alessio and A. Polkovnikov, *Universal high-frequency behavior of periodically driven systems: from dynamical stabilization to Floquet engineering*, *Advances in Physics* **64** (2015) 139.

[111] M. Holthaus, *Floquet engineering with quasienergy bands of periodically driven optical lattices*, *Journal of Physics B: Atomic, Molecular and Optical Physics* **49** (2015) 013001.

[112] N. Goldman and J. Dalibard, *Periodically Driven Quantum Systems: Effective Hamiltonians and Engineered Gauge Fields*, *Phys. Rev. X* **4** (2014) 031027.

[113] M. Heyl, P. Hauke and P. Zoller, *Quantum localization bounds Trotter errors in digital quantum simulation*, *Science Advances* **5** (2019) .

[114] T. Kitagawa, E. Berg, M. Rudner and E. Demler, *Topological characterization of periodically driven quantum systems*, *Phys. Rev. B* **82** (2010) 235114.

[115] N. H. Lindner, G. Refael and V. Galitski, *Floquet topological insulator in semiconductor quantum wells*, *Nature Physics* **7** (2011) 490.

[116] F. Wilczek, *Superfluidity and Space-Time Translation Symmetry Breaking*, *Phys. Rev. Lett.* **111** (2013) 250402.

[117] H. Watanabe and M. Oshikawa, *Absence of Quantum Time Crystals*, *Phys. Rev. Lett.* **114** (2015) 251603.

[118] N. Y. Yao, A. C. Potter, I.-D. Potirniche and A. Vishwanath, *Discrete Time Crystals: Rigidity, Criticality, and Realizations*, *Phys. Rev. Lett.* **118** (2017) 030401.

[119] S. Choi, J. Choi, R. Landig, G. Kucsko, H. Zhou, J. Isoya et al., *Observation of discrete time-crystalline order in a disordered dipolar many-body system*, *Nature* **543** (2017) 221.

[120] J. Zhang, P. Hess, A. Kyprianidis, P. Becker, A. Lee, J. Smith et al., *Observation of a discrete time crystal*, *Nature* **543** (2017) 217.

[121] D. H. Dunlap and V. M. Kenkre, *Dynamic localization of a charged particle moving under the influence of an electric field*, *Phys. Rev. B* **34** (1986) 3625.

[122] D. H. Dunlap and V. M. Kenkre, *Effect of scattering on the dynamic localization of a particle in a time-dependent electric field*, *Phys. Rev. B* **37** (1988) 6622.

[123] A. Eckardt, C. Weiss and M. Holthaus, *Superfluid-Insulator Transition in a Periodically Driven Optical Lattice*, *Phys. Rev. Lett.* **95** (2005) 260404.

[124] A. Zenesini, H. Lignier, D. Ciampini, O. Morsch and E. Arimondo, *Coherent Control of Dressed Matter Waves*, *Phys. Rev. Lett.* **102** (2009) 100403.

[125] P. L. Kapitza, *Dynamical Stability of a pendulum when its point of suspension vibrates, and pendulum with a vibrating suspension*, *Collected Papers of P.L. Kapitza* **2** (1965) 714.

[126] E. D. Courant, M. S. Livingston and H. S. Snyder, *The Strong-Focusing Synchroton—A New High Energy Accelerator*, *Phys. Rev.* **88** (1952) 1190.

[127] G. Z. K. Horvath, R. C. Thompson and P. L. Knight, *Fundamental physics with trapped ions*, *Contemporary Physics* **38** (1997) 25.

[128] H. Saito and M. Ueda, *Dynamically Stabilized Bright Solitons in a Two-Dimensional Bose-Einstein Condensate*, *Phys. Rev. Lett.* **90** (2003) 040403.

[129] F. K. Abdullaev, J. G. Caputo, R. A. Kraenkel and B. A. Malomed, *Controlling collapse in Bose-Einstein condensates by temporal modulation of the scattering length*, *Phys. Rev. A* **67** (2003) 013605.

[130] W. Zhang, B. Sun, M. S. Chapman and L. You, *Localization of spin mixing dynamics in a spin-1 Bose-Einstein condensate*, *Phys. Rev. A* **81** (2010) 033602.

[131] T. M. Hoang, C. S. Gerving, B. J. Land, M. Anquez, C. D. Hamley and M. S. Chapman, *Dynamic Stabilization of a Quantum Many-Body Spin System*, *Phys. Rev. Lett.* **111** (2013) 090403.

[132] F. Abdullaev and R. Kraenkel, *Macroscopic quantum tunneling and resonances in coupled Bose–Einstein condensates with oscillating atomic scattering length*, *Physics Letters A* **272** (2000) 395.

[133] E. Boukobza, M. G. Moore, D. Cohen and A. Vardi, *Nonlinear Phase Dynamics in a Driven Bosonic Josephson Junction*, *Phys. Rev. Lett.* **104** (2010) 240402.

[134] A. Russomanno, A. Silva and G. E. Santoro, *Periodic Steady Regime and Interference in a Periodically Driven Quantum System*, *Phys. Rev. Lett.* **109** (2012) 257201.

[135] V. M. Bastidas, C. Emary, G. Schaller and T. Brandes, *Nonequilibrium quantum phase transitions in the Ising model*, *Phys. Rev. A* **86** (2012) 063627.

[136] M. Benito, A. Gómez-León, V. M. Bastidas, T. Brandes and G. Platero, *Floquet engineering of long-range* p*-wave superconductivity*, *Phys. Rev. B* **90** (2014) 205127.

[137] L. D'Alessio and M. Rigol, *Long-time Behavior of Isolated Periodically Driven Interacting Lattice Systems*, *Phys. Rev. X* **4** (2014) 041048.

[138] L. D'Alessio and A. Polkovnikov, *Many-body energy localization transition in periodically driven systems*, *Annals of Physics* **333** (2013) 19.

[139] D. A. Abanin, W. De Roeck and F. Huveneers, *Exponentially Slow Heating in Periodically Driven Many-Body Systems*, *Phys. Rev. Lett.* **115** (2015) 256803.

[140] D. A. Abanin, W. De Roeck, W. W. Ho and F. Huveneers, *Effective Hamiltonians, prethermalization, and slow energy absorption in periodically driven many-body systems*, *Phys. Rev. B* **95** (2017) 014112.

[141] T. Mori, T. Kuwahara and K. Saito, *Rigorous Bound on Energy Absorption and Generic Relaxation in Periodically Driven Quantum Systems*, *Phys. Rev. Lett.* **116** (2016) 120401.

[142] F. Machado, G. D. Meyer, D. V. Else, C. Nayak and N. Y. Yao, *Exponentially Slow Heating in Short and Long-range Interacting Floquet Systems*, *arXiv:1708.01620* (2017).

[143] L. Amico, R. Fazio, A. Osterloh and V. Vedral, *Entanglement in many-body systems*, *Rev. Mod. Phys.* **80** (2008) 517.

[144] P. Calabrese and J. Cardy, *Entanglement entropy and quantum field theory*, *Journal of Statistical Mechanics: Theory and Experiment* **2004** (2004) P06002.

[145] P. Calabrese and J. Cardy, *Evolution of entanglement entropy in one-dimensional systems*, *Journal of Statistical Mechanics: Theory and Experiment* **2005** (2005) P04010.

[146] V. Alba and P. Calabrese, *Entanglement dynamics after quantum quenches in generic integrable systems*, *SciPost Phys.* **4** (2018) 17.

[147] V. Alba and P. Calabrese, *Entanglement and thermodynamics after a quantum quench in integrable systems*, *Proceedings of the National Academy of Sciences* **114** (2017) 7947.

[148] M. Serbyn, Z. Papić and D. A. Abanin, *Universal Slow Growth of Entanglement in Interacting Strongly Disordered Systems*, *Phys. Rev. Lett.* **110** (2013) 260601.

[149] D. A. Huse, R. Nandkishore and V. Oganesyan, *Phenomenology of fully many-body-localized systems*, *Phys. Rev. B* **90** (2014) 174202.

[150] G. Vidal, *Efficient Classical Simulation of Slightly Entangled Quantum Computations*, *Phys. Rev. Lett.* **91** (2003) 147902.

[151] U. Schollwöck and S. R. White, *Methods for time dependence in DMRG*, *AIP Conference Proceedings* **816** (2006) 155.

[152] F. Verstraete, V. Murg and J. I. Cirac, *Matrix product states, projected entangled pair states, and variational renormalization group methods for quantum spin systems*, *Advances in Physics* **57** (2008) 143.

[153] M. C. Bañuls, M. B. Hastings, F. Verstraete and J. I. Cirac, *Matrix Product States for Dynamical Simulation of Infinite Chains*, *Phys. Rev. Lett.* **102** (2009) 240603.

[154] R. Horodecki, P. Horodecki, M. Horodecki and K. Horodecki, *Quantum entanglement*, *Rev. Mod. Phys.* **81** (2009) 865.

[155] P. Calabrese and J. Cardy, *Evolution of entanglement entropy in one-dimensional systems*, *Journal of Statistical Mechanics: Theory and Experiment* **2005** (2005) P04010.

[156] J. H. Bardarson, F. Pollmann and J. E. Moore, *Unbounded Growth of Entanglement in Models of Many-Body Localization*, *Phys. Rev. Lett.* **109** (2012) 017202.

[157] P. W. Anderson, *Absence of Diffusion in Certain Random Lattices*, *Phys. Rev.* **109** (1958) 1492.

[158] H. Kim and D. A. Huse, *Ballistic Spreading of Entanglement in a Diffusive Nonintegrable System*, *Phys. Rev. Lett.* **111** (2013) 127205.

[159] A. Nahum, J. Ruhman, S. Vijay and J. Haah, *Quantum Entanglement Growth under Random Unitary Dynamics*, *Phys. Rev. X* **7** (2017) 031016.

[160] M. Fagotti and P. Calabrese, *Evolution of entanglement entropy following a quantum quench: Analytic results for the* XY *chain in a transverse magnetic field*, *Phys. Rev. A* **78** (2008) 010306.

[161] M. Žnidarič, T. Prosen and P. Prelovšek, *Many-body localization in the Heisenberg* XXZ *magnet in a random field*, *Phys. Rev. B* **77** (2008) 064426.

[162] J. H. Bardarson, F. Pollmann and J. E. Moore, *Unbounded Growth of Entanglement in Models of Many-Body Localization*, *Phys. Rev. Lett.* **109** (2012) 017202.

[163] N. Y. Yao, C. R. Laumann, J. I. Cirac, M. D. Lukin and J. E. Moore, *Quasi-Many-Body Localization in Translation-Invariant Systems*, *Phys. Rev. Lett.* **117** (2016) 240601.

[164] A. A. Michailidis, M. Žnidarič, M. Medvedyeva, D. A. Abanin, T. Prosen and Z. Papić, *Slow dynamics in translation-invariant quantum lattice models*, *Phys. Rev. B* **97** (2018) 104307.

[165] A. Smith, J. Knolle, D. L. Kovrizhin and R. Moessner, *Disorder-Free Localization*, *Phys. Rev. Lett.* **118** (2017) 266601.

[166] A. Smith, J. Knolle, R. Moessner and D. L. Kovrizhin, *Absence of Ergodicity without Quenched Disorder: From Quantum Disentangled Liquids to Many-Body Localization*, *Phys. Rev. Lett.* **119** (2017) 176601.

[167] A. Smith, J. Knolle, R. Moessner and D. L. Kovrizhin, *Dynamical localization in $\mathbb{Z}_2$ lattice gauge theories*, *Phys. Rev. B* **97** (2018) 245137.

[168] M. Brenes, M. Dalmonte, M. Heyl and A. Scardicchio, *Many-Body Localization Dynamics from Gauge Invariance*, *Phys. Rev. Lett.* **120** (2018) 030601.

[169] D. Basko, I. Aleiner and B. Altshuler, *Metal–insulator transition in a weakly interacting many-electron system with localized single-particle states*, *Annals of Physics* **321** (2006) 1126.

[170] V. Oganesyan and D. A. Huse, *Localization of interacting fermions at high temperature*, *Phys. Rev. B* **75** (2007) 155111.

[171] D. A. Huse, R. Nandkishore and V. Oganesyan, *Phenomenology of fully many-body-localized systems*, *Phys. Rev. B* **90** (2014) 174202.

[172] J. Z. Imbrie, V. Ros and A. Scardicchio, *Local integrals of motion in many-body localized systems*, *Annalen der Physik* **529** (2017) 1600278.

[173] M. Serbyn, Z. Papić and D. A. Abanin, *Criterion for Many-Body Localization-Delocalization Phase Transition*, *Phys. Rev. X* **5** (2015) 041047.

[174] G. Bertin, *Dynamics of Galaxies*. Cambridge University Press, 2000.

[175] R. J. Goldston and P. Rutherford, *Introduction to Plasma Physics*. Routledges, 1995.

[176] M. Born, and K. Huang, *Dynamical theory of crystal lattices*. Clarendon Oxford, 1954.

[177] D. Ruelle, *Statistical mechanics of a one-dimensional lattice gas*, *Comm. Math. Phys.* **9** (1968) 267.

[178] A. Campa, T. Dauxois, D. Fanelli and S. Ruffo, *Physics of long-range interacting systems*. Oxford University Press, 2015.

[179] L. Béguin, A. Vernier, R. Chicireanu, T. Lahaye and A. Browaeys, *Direct Measurement of the van der Waals Interaction between Two Rydberg Atoms*, *Phys. Rev. Lett.* **110** (2013) 263201.

[180] A. Browaeys, D. Barredo and T. Lahaye, *Experimental investigations of dipole–dipole interactions between a few Rydberg atoms*, *Journal of Physics B: Atomic, Molecular and Optical Physics* **49** (2016) 152001.

[181] H. Bernien, S. Schwartz, A. Keesling, H. Levine, A. Omran, H. Pichler et al., *Probing many-body dynamics on a 51-atom quantum simulator*, *Nature* **551** (2017) 579.

[182] M. Albiez, R. Gati, J. Fölling, S. Hunsmann, M. Cristiani and M. K. Oberthaler, *Direct Observation of Tunneling and Nonlinear Self-Trapping in a Single Bosonic Josephson Junction*, *Phys. Rev. Lett.* **95** (2005) 010402.

[183] H. Häffner, C. F. Roos and R. Blatt, *Quantum computing with trapped ions*, *Physics reports* **469** (2008) 155.

[184] P. Jurcevic, H. Shen, P. Hauke, C. Maier, T. Brydges, C. Hempel et al., *Direct Observation of Dynamical Quantum Phase Transitions in an Interacting Many-Body System*, *Phys. Rev. Lett.* **119** (2017) 080501.

[185] R. Blatt and C. F. Roos, *Quantum simulations with trapped ions*, *Nature Physics* **8** (2012) 277.

[186] B. Neyenhuis, J. Zhang, P. W. Hess, J. Smith, A. C. Lee, P. Richerme et al., *Observation of prethermalization in long-range interacting spin chains*, *Science advances* **3** (2017) e1700672.

[187] J. W. Britton, B. C. Sawyer, A. C. Keith, C.-C. J. Wang, J. K. Freericks, H. Uys et al., *Engineered two-dimensional Ising interactions in a trapped-ion quantum simulator with hundreds of spins*, *Nature* **484** (2012) 489.

[188] P. Richerme, Z.-X. Gong, A. Lee, C. Senko, J. Smith, M. Foss-Feig et al., *Non-local propagation of correlations in quantum systems with long-range interactions*, *Nature* **511** (2014) 198.

[189] P. Jurcevic, B. P. Lanyon, P. Hauke, C. Hempel, P. Zoller, R. Blatt et al., *Quasiparticle engineering and entanglement propagation in a quantum many-body system*, *Nature* **511** (2014) 202.

[190] J. Zhang, G. Pagano, P. W. Hess, A. Kyprianidis, P. Becker, H. Kaplan et al., *Observation of a many-body dynamical phase transition with a 53-qubit quantum simulator*, *Nature* **551** (2017) 601.

[191] G. Pagano, P. W. Hess, H. B. Kaplan, W. L. Tan, P. Richerme, P. Becker et al., *Cryogenic trapped-ion system for large scale quantum simulation*, *Quantum Science and Technology* **4** (2018) 014004.

[192] K.-K. Ni, S. Ospelkaus, M. H. G. de Miranda, A. Pe'er, B. Neyenhuis, J. J. Zirbel et al., *A High Phase-Space-Density Gas of Polar Molecules*, *Science* **322** (2008) 231.

[193] S. A. Moses, J. P. Covey, M. T. Miecnikowski, D. S. Jin and J. Ye, *New frontiers for quantum gases of polar molecules*, *Nature Physics* **13** (2016) 13.

[194] G. Balasubramanian et al., *Ultralong spin coherence time in isotopically engineered diamond*, *Nature Materials* **8** (2009) 383.

[195] A. de Paz, A. Sharma, A. Chotia, E. Maréchal, J. H. Huckans, P. Pedri et al., *Nonequilibrium Quantum Magnetism in a Dipolar Lattice Gas*, *Phys. Rev. Lett.* **111** (2013) 185305.

[196] H. Labuhn, D. Barredo, S. Ravets, S. De Léséleuc, T. Macrì, T. Lahaye et al., *Tunable two-dimensional arrays of single Rydberg atoms for realizing quantum Ising models*, *Nature* **534** (2016) 667.

[197] I. Bloch, J. Dalibard and S. Nascimbène, *Quantum simulations with ultracold quantum gases*, *Nat. Phys.* **8** (2012) 267.

[198] I. Lesanovsky and H. Katsura, *Interacting Fibonacci anyons in a Rydberg gas*, *Phys. Rev. A* **86** (2012) 041601.

[199] D. Barredo, V. Lienhard, S. de Léséleuc, T. Lahaye and A. Browaeys, *Synthetic three-dimensional atomic structures assembled atom by atom*, *Nature* **561** (2018) 79.

[200] J. Zeiher, J.-y. Choi, A. Rubio-Abadal, T. Pohl, R. van Bijnen, I. Bloch et al., *Coherent Many-Body Spin Dynamics in a Long-Range Interacting Ising Chain*, *Phys. Rev. X* **7** (2017) 041063.

[201] S. Sachdev, K. Sengupta and S. M. Girvin, *Mott insulators in strong electric fields*, *Phys. Rev. B* **66** (2002) 075128.

[202] S. Weinberg, *The Quantum Theory of Fields, Volume 2: Modern Applications*. Cambridge University Press, 2005.

[203] J. B. Kogut, *An introduction to lattice gauge theory and spin systems*, *Rev. Mod. Phys.* **51** (1979) 659.

[204] J. Schwinger, *Gauge Invariance and Mass. II*, *Phys. Rev.* **128** (1962) 2425.

[205] C. Hamer, *Lattice model calculations for* $\mathrm{SU}(2)$ *Yang-Mills theory in* $1+1$ *dimensions*, *Nuclear Physics B* **121** (1977) 159.

[206] C. J. Hamer, Z. Weihong and J. Oitmaa, *Series expansions for the massive Schwinger model in Hamiltonian lattice theory*, *Phys. Rev. D* **56** (1997) 55.

[207] F. Hebenstreit, J. Berges and D. Gelfand, *Real-Time Dynamics of String Breaking*, *Phys. Rev. Lett.* **111** (2013) 201601.

[208] F. Hebenstreit, J. Berges and D. Gelfand, *Simulating fermion production in* 1+1 *dimensional QED*, *Phys. Rev. D* **87** (2013) 105006.

[209] Y. Kuno, S. Sakane, K. Kasamatsu, I. Ichinose and T. Matsui, *Quantum simulation of* $(1+1)$*-dimensional* $\mathrm{U}(1)$ *gauge-Higgs model on a lattice by cold Bose gases*, *Phys. Rev. D* **95** (2017) 094507.

[210] B. Buyens, J. Haegeman, K. Van Acoleyen, H. Verschelde and F. Verstraete, *Matrix Product States for Gauge Field Theories*, *Phys. Rev. Lett.* **113** (2014) 091601.

[211] B. Buyens, J. Haegeman, H. Verschelde, F. Verstraete and K. Van Acoleyen, *Confinement and String Breaking for* QED_2 *in the Hamiltonian Picture*, *Phys. Rev. X* **6** (2016) 041040.

[212] B. Buyens, J. Haegeman, F. Hebenstreit, F. Verstraete and K. Van Acoleyen, *Real-time simulation of the Schwinger effect with matrix product states*, *Phys. Rev. D* **96** (2017) 114501.

[213] T. Pichler, M. Dalmonte, E. Rico, P. Zoller and S. Montangero, *Real-Time Dynamics in* $\mathrm{U}(1)$ *Lattice Gauge Theories with Tensor Networks*, *Phys. Rev. X* **6** (2016) 011023.

[214] P. Sala, T. Shi, S. Kühn, M. C. Bañuls, E. Demler and J. I. Cirac, *Variational study of* $\mathrm{U}(1)$ *and* $\mathrm{SU}(2)$ *lattice gauge theories with Gaussian states in* $1+1$ *dimensions*, *Phys. Rev. D* **98** (2018) 034505.

[215] U. J. Wiese, *Ultracold quantum gases and lattice systems: quantum simulation of lattice gauge theories*, *Ann. Phys.* **525** (2013) 777.

[216] E. Zohar, J. I. Cirac and B. Reznik, *Quantum simulations of lattice gauge theories using ultracold atoms in optical lattices*, *Reports on Progress in Physics* **79** (2015) 014401.

[217] M. Dalmonte and S. Montangero, *Lattice gauge theory simulations in the quantum information era*, *Contemporary Physics* **57** (2016) 388.

[218] D. Banerjee, M. Dalmonte, M. Müller, E. Rico, P. Stebler, U.-J. Wiese et al., *Atomic Quantum Simulation of Dynamical Gauge Fields Coupled to Fermionic Matter: From String Breaking to Evolution after a Quench*, *Phys. Rev. Lett.* **109** (2012) 175302.

[219] C. Schweizer, F. Grusdt, M. Berngruber, L. Barbiero, E. Demler, N. Goldman et al., *Floquet approach to* $\mathbb{Z}_2$ *lattice gauge theories with ultracold atoms in optical lattices*, *arxiv:1901.07103* (2019).

[220] A. Celi, B. Vermersch, O. Viyuela, H. Pichler, M. Lukin and P. Zoller, *Emerging* 2D *Gauge theories in Rydberg configurable arrays*, *arxiv:1907.03311* (2019).

[221] S. Notarnicola, M. Collura and S. Montangero, *Real time dynamics quantum simulation of* $(1+1)-\mathrm{D}$ *lattice QED with Rydberg atoms*, *arxiv:1907.12579* (2019).

[222] E. A. Martinez, C. A. Muschik, P. Schindler, D. Nigg, A. Erhard, M. Heyl et al., *Real-time dynamics of lattice gauge theories with a few-qubit quantum computer*, *Nature* **534** (2016) 516.

[223] B. M. McCoy and T. T. Wu, *Two-dimensional Ising field theory in a magnetic field: Breakup of the cut in the two-point function*, *Phys. Rev. D* **18** (1978) 1259.

[224] R. Shankar and G. Murthy, *Deconfinement in* $\mathrm{d}=1$*: Asymptotic and half-asymptotic particles*, *Phys. Rev. B* **72** (2005) 224414.

[225] S. B. Rutkevich, *Decay of the metastable phase in* $\mathrm{d}=1$ *and* $\mathrm{d}=2$ *Ising models*, *Phys. Rev. B* **60** (1999) 14525.

[226] G. Delfino, P. Grinza and G. Mussardo, *Decay of particles above threshold in the Ising field theory with magnetic field*, *Nuclear Physics B* **737** (2006) 291.

[227] P. Fonseca and A. Zamolodchikov, *Ising Spectroscopy I: Mesons at* $T < T_c$, *arxiv:hep-th/0612304* (2006).

[228] S. B. Rutkevich, *Large-*$\mathfrak{n}$ *Excitations in the Ferromagnetic Ising Field Theory in a Weak Magnetic Field: Mass Spectrum and Decay Widths*, *Phys. Rev. Lett.* **95** (2005) 250601.

[229] Z. Cai, C. Wu and U. Schollwöck, *Confinement: A real-time visualization*, *Phys. Rev. B* **85** (2012) 075102.

[230] S. B. Rutkevich, *Energy Spectrum of Bound-Spinons in the Quantum Ising Spin-Chain Ferromagnet*, *Journal of Statistical Physics* **131** (2008) 917.

[231] S. B. Rutkevich, *Kink confinement in the antiferromagnetic XXZ spin-(1/2) chain in a weak staggered magnetic field*, *EPL (Europhysics Letters)* **121** (2018) 37001.

[232] T. Suzuki and S.-i. Suga, *Quantized excitation spectra by magnon confinement in quasi-one-dimensional* $S=1$ *spin systems*, *Phys. Rev. B* **98** (2018) 180406.

[233] Z. Wang, M. Schmidt, A. K. Bera, A. T. M. N. Islam, B. Lake, A. Loidl et al., *Spinon confinement in the one-dimensional Ising-like antiferromagnet* $SrCo_2V_2O_8$, *Phys. Rev. B* **91** (2015) 140404.

[234] A. K. Bera, B. Lake, F. H. L. Essler, L. Vanderstraeten, C. Hubig, U. Schollwöck et al., *Spinon confinement in a quasi-one-dimensional anisotropic Heisenberg magnet*, *Phys. Rev. B* **96** (2017) 054423.

[235] Z.-X. Gong, M. Foss-Feig, F. G. S. L. Brandão and A. V. Gorshkov, *Entanglement Area Laws for Long-Range Interacting Systems*, *Phys. Rev. Lett.* **119** (2017) 050501.

[236] T. Koffel, M. Lewenstein and L. Tagliacozzo, *Entanglement Entropy for the Long-Range Ising Chain in a Transverse Field*, *Phys. Rev. Lett.* **109** (2012) 267203.

[237] D. Vodola, L. Lepori, E. Ercolessi, A. V. Gorshkov and G. Pupillo, *Kitaev Chains with Long-Range Pairing*, *Phys. Rev. Lett.* **113** (2014) 156402.

[238] I. Frérot, P. Naldesi and T. Roscilde, *Entanglement and fluctuations in the XXZ model with power-law interactions*, *Phys. Rev. B* **95** (2017) 245111.

[239] M. L. Wall, A. Safavi-Naini and A. M. Rey, *Boson-mediated quantum spin simulators in transverse fields: XY model and spin-boson entanglement*, *Phys. Rev. A* **95** (2017) 013602.

[240] D. Dylewsky, J. K. Freericks, M. L. Wall, A. M. Rey and M. Foss-Feig, *Nonperturbative calculation of phonon effects on spin squeezing*, *Phys. Rev. A* **93** (2016) 013415.

[241] N. Defenu, A. Trombettoni and S. Ruffo, *Criticality and phase diagram of quantum long-range O(*N*) models*, *Phys. Rev. B* **96** (2017) 104432.

[242] S. Fey and K. P. Schmidt, *Critical behavior of quantum magnets with long-range interactions in the thermodynamic limit*, *Phys. Rev. B* **94** (2016) 075156.

[243] D. Jaschke, K. Maeda, J. D. Whalen, M. L. Wall and L. D. Carr, *Critical phenomena and Kibble–Zurek scaling in the long-range quantum Ising chain*, *New Journal of Physics* **19** (2017) 033032.

[244] L. Vanderstraeten, M. Van Damme, H. P. Büchler and F. Verstraete, *Quasiparticles in Quantum Spin Chains with Long-Range Interactions*, *Phys. Rev. Lett.* **121** (2018) 090603.

[245] N. Defenu, T. Enss, M. Kastner and G. Morigi, *Dynamical Critical Scaling of Long-Range Interacting Quantum Magnets*, *Phys. Rev. Lett.* **121** (2018) 240403.

[246] N. Shammah, S. Ahmed, N. Lambert, S. De Liberato and F. Nori, *Open quantum systems with local and collective incoherent processes: Efficient numerical simulations using permutational invariance*, *Phys. Rev. A* **98** (2018) 063815.

[247] D. V. Else, F. Machado, C. Nayak and N. Y. Yao, *An improved Lieb-Robinson bound for many-body Hamiltonians with power-law interactions*, *arXiv:1809.06369* (2018).

[248] K. R. Fratus and M. Srednicki, *Eigenstate Thermalization and Spontaneous Symmetry Breaking in the One-Dimensional Transverse-Field Ising Model with Power-Law Interactions*, *arXiv:1611.03992* (2016).

[249] O. Viyuela, L. Fu and M. A. Martin-Delgado, *Chiral Topological Superconductors Enhanced by Long-Range Interactions*, *Phys. Rev. Lett.* **120** (2018) 017001.

[250] N. Y. Yao, C. R. Laumann, S. Gopalakrishnan, M. Knap, M. Müller, E. A. Demler et al., *Many-Body Localization in Dipolar Systems*, *Phys. Rev. Lett.* **113** (2014) 243002.

[251] R. Singh, R. Moessner and D. Roy, *Effect of long-range hopping and interactions on entanglement dynamics and many-body localization*, *Phys. Rev. B* **95** (2017) 094205.

[252] P. Hauke and M. Heyl, *Many-body localization and quantum ergodicity in disordered long-range Ising models*, *Phys. Rev. B* **92** (2015) 134204.

[253] A. L. Burin, *Localization in a random XY model with long-range interactions: Intermediate case between single-particle and many-body problems*, *Phys. Rev. B* **92** (2015) 104428.

[254] G. L. Celardo, R. Kaiser and F. Borgonovi, *Shielding and localization in the presence of long-range hopping*, *Phys. Rev. B* **94** (2016) 144206.

[255] K. S. Tikhonov and A. D. Mirlin, *Many-body localization transition with power-law interactions: Statistics of eigenstates*, *Phys. Rev. B* **97** (2018) 214205.

[256] P. Sierant, K. Biedroń, G. Morigi and J. Zakrzewski, *Many-body localization in presence of cavity mediated long-range interactions*, *arXiv:1902.00357* (2019).

[257] S. Roy and D. E. Logan, *Self-consistent theory of many-body localisation in a quantum spin chain with long-range interactions*, *arXiv:1903.04851* (2019).

[258] S. Nag and A. Garg, *Many-body localization in the presence of long-range interactions and long-range hopping*, *Phys. Rev. B* **99** (2019) 224203.

[259] R. Modak and T. Nag, *Many-body dynamics in long-range hopping model in the presence of correlated and uncorrelated disorder*, *arXiv:1903.05099* (2019).

[260] A. O. Maksymov and A. L. Burin, *Many-body localization in spin chains with the long-range transverse interactions: scaling of critical disorder with the system size*, *arXiv:1905.02286* (2019).

[261] R. M. Nandkishore and S. L. Sondhi, *Many-Body Localization with Long-Range Interactions*, *Phys. Rev. X* **7** (2017) 041021.

[262] A. Russomanno, F. Iemini, M. Dalmonte and R. Fazio, *Floquet time crystal in the Lipkin-Meshkov-Glick model*, *Phys. Rev. B* **95** (2017) 214307.

[263] I. Homrighausen, N. O. Abeling, V. Zauner-Stauber and J. C. Halimeh, *Anomalous dynamical phase in quantum spin chains with long-range interactions*, *Phys. Rev. B* **96** (2017) 104436.

[264] J. C. Halimeh and V. Zauner-Stauber, *Dynamical phase diagram of quantum spin chains with long-range interactions*, *Phys. Rev. B* **96** (2017) 134427.

[265] M. G. Nezhadhaghighi and M. A. Rajabpour, *Entanglement dynamics in short- and long-range harmonic oscillators*, *Phys. Rev. B* **90** (2014) 205438.

[266] L. F. Santos, F. Borgonovi and G. L. Celardo, *Cooperative Shielding in Many-Body Systems with Long-Range Interaction*, *Phys. Rev. Lett.* **116** (2016) 250402.

[267] F. Liu, R. Lundgren, P. Titum, G. Pagano, J. Zhang, C. Monroe et al., *Confined Quasiparticle Dynamics in Long-Range Interacting Quantum Spin Chains*, *Phys. Rev. Lett.* **122** (2019) 150601.

[268] M. E. Fisher, S.-k. Ma and B. G. Nickel, *Critical Exponents for Long-Range Interactions*, *Phys. Rev. Lett.* **29** (1972) 917.

[269] J. Sak, *Recursion Relations and Fixed Points for Ferromagnets with Long-Range Interactions*, *Phys. Rev. B* **8** (1973) 281.

[270] N. Defenu, A. Codello, S. Ruffo and A. Trombettoni, *Criticality of Spin Systems with Weak Long-Range Interactions*, *arxiv:1908.05158* (2019).

[271] C. Itzykson and J.-M. Drouffe, *Statistical Field Theory*. Cambridge University Press, 1991.

[272] F. J. Dyson, *Existence of a phase-transition in a one-dimensional Ising ferromagnet*, *Communications in Mathematical Physics* **12** (1969) 91.

[273] D. J. Thouless, *Long-Range Order in One-Dimensional Ising Systems*, *Phys. Rev.* **187** (1969) 732.

[274] A. Dutta and J. K. Bhattacharjee, *Phase transitions in the quantum Ising and rotor models with a long-range interaction*, *Phys. Rev. B* **64** (2001) 184106.

[275] F. Machado, D. V. Else, G. D. Kahanamoku-Meyer, C. Nayak and N. Y. Yao, *Prethermal Phases of Non-equilibrium Matter in Long-range Interacting Systems*, *arxiv:1908.07530* (2019).

[276] M. C. Tran, A. Ehrenberg, A. Y. Guo, P. Titum, D. A. Abanin and A. V. Gorshkov, *Locality and Heating in Periodically Driven, Power-law Interacting Systems*, *arxiv:1908.02773* (2019).

[277] M. Foss-Feig, Z.-X. Gong, C. W. Clark and A. V. Gorshkov, *Nearly Linear Light Cones in Long-Range Interacting Quantum Systems*, *Phys. Rev. Lett.* **114** (2015) 157201.

[278] Z.-X. Gong, M. Foss-Feig, S. Michalakis and A. V. Gorshkov, *Persistence of Locality in Systems with Power-Law Interactions*, *Phys. Rev. Lett.* **113** (2014) 030602.

[279] P. Hauke and L. Tagliacozzo, *Spread of Correlations in Long-Range Interacting Quantum Systems*, *Phys. Rev. Lett.* **111** (2013) 207202.

[280] J. Eisert, M. van den Worm, S. R. Manmana and M. Kastner, *Breakdown of Quasilocality in Long-Range Quantum Lattice Models*, *Phys. Rev. Lett.* **111** (2013) 260401.

[281] L. Lepori, A. Trombettoni and D. Vodola, *Singular dynamics and emergence of nonlocality in long-range quantum models*, *Journal of Statistical Mechanics: Theory and Experiment* **2017** (2017) 033102.

[282] L. Cevolani, G. Carleo and L. Sanchez-Palencia, *Protected quasilocality in quantum systems with long-range interactions*, *Phys. Rev. A* **92** (2015) 041603.

[283] L. Cevolani, G. Carleo and L. Sanchez-Palencia, *Spreading of correlations in exactly solvable quantum models with long-range interactions in arbitrary dimensions*, *New Journal of Physics* **18** (2016) 093002.

[284] M. Van Regemortel, D. Sels and M. Wouters, *Information propagation and equilibration in long-range Kitaev chains*, *Phys. Rev. A* **93** (2016) 032311.

[285] I. Frérot, P. Naldesi and T. Roscilde, *Multispeed Prethermalization in Quantum Spin Models with Power-Law Decaying Interactions*, *Phys. Rev. Lett.* **120** (2018) 050401.

[286] J. Schachenmayer, B. P. Lanyon, C. F. Roos and A. J. Daley, *Entanglement Growth in Quench Dynamics with Variable Range Interactions*, *Phys. Rev. X* **3** (2013) 031015.

[287] A. S. Buyskikh, M. Fagotti, J. Schachenmayer, F. Essler and A. J. Daley, *Entanglement growth and correlation spreading with variable-range interactions in spin and fermionic tunneling models*, *Phys. Rev. A* **93** (2016) 053620.

[288] S. Pappalardi, A. Russomanno, B. Žunkovič, F. Iemini, A. Silva and R. Fazio, *Scrambling and entanglement spreading in long-range spin chains*, *Phys. Rev. B* **98** (2018) 134303.

[289] M. Kormos, M. Collura, G. Takács and P. Calabrese, *Real-time confinement following a quantum quench to a non-integrable model*, *Nature Physics* **13** (2016) 246.

[290] J. Vidal, R. Mosseri and J. Dukelsky, *Entanglement in a first-order quantum phase transition*, *Phys. Rev. A* **69** (2004) 054101.

[291] T. Mori, *Classical ergodicity and quantum eigenstate thermalization: Analysis in fully connected Ising ferromagnets*, *Phys. Rev. E* **96** (2017) 012134.

[292] A. Lamacraft, *Spin-1 microcondensate in a magnetic field*, *Phys. Rev. A* **83** (2011) 033605.

[293] H. Lipkin, N. Meshkov and A. Glick, *Validity of many-body approximation methods for a solvable model: (I). Exact solutions and perturbation theory*, *Nuclear Physics* **62** (1965) 188.

[294] A. Das, K. Sengupta, D. Sen and B. K. Chakrabarti, *Infinite-range Ising ferromagnet in a time-dependent transverse magnetic field: Quench and ac dynamics near the quantum critical point*, *Phys. Rev. B* **74** (2006) 144423.

[295] B. Žunkovič, A. Silva and M. Fabrizio, *Dynamical phase transitions and Loschmidt echo in the infinite-range XY model*, *Phil. Trans. R. Soc.* **A 374** (2016) 20150160.

[296] L. D. Landau and E. M. Lifsits, *Mechanics*. Butterworth-Heinemann, 1976.

[297] A. Russomanno, R. Fazio and G. E. Santoro, *Thermalization in a periodically driven fully connected quantum Ising ferromagnet*, *EPL (Europhysics Letters)* **110** (2015) 37005.

[298] A. Das, K. Sengupta, D. Sen and B. K. Chakrabarti, *Infinite-range Ising ferromagnet in a time-dependent transverse magnetic field: Quench and ac dynamics near the quantum critical point*, *Phys. Rev. B* **74** (2006) 144423.

[299] J. Pöschel, *A lecture on the classical KAM theorem*, *arXiv:0908.2234* (2009).

[300] J. Tomkovič, W. Muessel, H. Strobel, S. Löck, P. Schlagheck, R. Ketzmerick et al., *Experimental observation of the Poincaré-Birkhoff scenario in a driven many-body quantum system*, *Phys. Rev. A* **95** (2017) 011602.

[301] L. D. Landau and E. M. Lifshitz, *Mechanics*. Butterworth-Heinemann, 1976.

[302] S. Blanes, F. Casas, J. Oteo and J. Ros, *The Magnus expansion and some of its applications*, *Physics Reports* **470** (2009) 151.

[303] G. Ortiz, R. Somma, J. Dukelsky and S. Rombouts, *Exactly solvable models derived from a generalized Gaudin algebra*, *Nucl. Phys. B* **707** (2005) 421.

[304] G. H. Wannier, *Statistical Physics*. Dover, 1966.

[305] S. Dusuel and J. Vidal, *Continuous unitary transformations and finite-size scaling exponents in the Lipkin-Meshkov-Glick model*, *Phys. Rev. B* **71** (2005) 224420.

[306] L. D. Landau and E. M. Lifsits, *Quantum Mechanics: Non-Relativistic Theory*. Butterworth-Heinemann, 1981.

[307] M. Caprio, P. Cejnar and F. Iachello, *Excited state quantum phase transitions in many-body systems*, *Annals of Physics* **323** (2008) 1106.

[308] R. G. Littlejohn, *The semiclassical evolution of wave packets*, *Physics Reports* **138** (1986) 193.

[309] M. Brack and R. K. Bhaduri, *Semiclassical Physics*. Addison-Wesley, 1997.

[310] A. Polkovnikov, *Phase space representation of quantum dynamics*, *Annals of Physics* **325** (2010) 1790.

[311] E. H. Lieb, J. P. Solovej, R. Seiringer and J. Yngvason, *The Mathematics of the Bose Gas and its Condensation*. Birkhäuser Basel, 2005.

[312] M. Correggi, A. Giuliani and R. Seiringer, *Validity of the Spin-Wave Approximation for the Free Energy of the Heisenberg Ferromagnet*, *Communications in Mathematical Physics* **339** (2015) 279.

[313] L. D. Landau and E. M. Lifshitz, *Classical Theory of Fields*. Butterworth-Heinemann, 1980.

[314] R. Feynman and F. Vernon, *The theory of a general quantum system interacting with a linear dissipative system*, *Annals of Physics* **24** (1963) 118.

[315] A. O. Caldeira and A. J. Leggett, *Influence of Dissipation on Quantum Tunneling in Macroscopic Systems*, *Phys. Rev. Lett.* **46** (1981) 211.

[316] J. Strzalko, J. Grabski, A. Stefanski, P. Perlikowski and T. Kapitaniak, *Understanding Coin-Tossing*, *The Mathematical Intelligencer* **32** (2010) 54.

[317] G. Piccitto, B. Žunkovič and A. Silva, *Dynamical Phase Diagram of a Quantum Ising Chain with Long Range Interactions*, *arXiv:1906.00691* (2019).

[318] A. Giuliani, J. L. Lebowitz and E. H. Lieb, *Ising models with long-range antiferromagnetic and short-range ferromagnetic interactions*, *Phys. Rev. B* **74** (2006) 064420.

[319] J. Haegeman, C. Lubich, I. Oseledets, B. Vandereycken and F. Verstraete, *Unifying time evolution and optimization with matrix product states*, *Phys. Rev. B* **94** (2016) 165116.

[320] C. Lubich, I. Oseledets and B. Vandereycken, *Time Integration of Tensor Trains*, *SIAM Journal on Numerical Analysis* **53** (2015) 917.

[321] A. Russomanno, A. Silva and G. E. Santoro, *Periodic Steady Regime and Interference in a Periodically Driven Quantum System*, *Phys. Rev. Lett.* **109** (2012) 257201.

[322] A. Lazarides, A. Das and R. Moessner, *Periodic Thermodynamics of Isolated Quantum Systems*, *Phys. Rev. Lett.* **112** (2014) 150401.

[323] P. Calabrese, F. H. L. Essler and M. Fagotti, *Quantum quench in the transverse field Ising chain: I. Time evolution of order parameter correlators*, *Journal of Statistical Mechanics: Theory and Experiment* **2012** (2012) P07016.

[324] M. Kac and C. J. Thompson, *Critical Behavior of Several Lattice Models with Long-Range Interaction*, *Journal of Mathematical Physics* **10** (1969) 1373.

[325] C. Senko, P. Richerme, J. Smith, A. Lee, I. Cohen, A. Retzker et al., *Realization of a Quantum Integer-Spin Chain with Controllable Interactions*, *Phys. Rev. X* **5** (2015) 021026.

[326] L. Vanderstraeten, M. Van Damme, H. P. Büchler and F. Verstraete, *Quasiparticles in Quantum Spin Chains with Long-Range Interactions*, *Phys. Rev. Lett.* **121** (2018) 090603.

[327] T. Shirai, J. Thingna, T. Mori, S. Denisov, P. Hänggi and S. Miyashita, *Effective Floquet–Gibbs states for dissipative quantum systems*, *New Journal of Physics* **18** (2016) 053008.

[328] A. Lazarides, A. Das and R. Moessner, *Periodic Thermodynamics of Isolated Quantum Systems*, *Phys. Rev. Lett.* **112** (2014) 150401.

[329] E. Canovi, M. Kollar and M. Eckstein, *Stroboscopic prethermalization in weakly interacting periodically driven systems*, *Phys. Rev. E* **93** (2016) 012130.

[330] A. Chandran and S. L. Sondhi, *Interaction-stabilized steady states in the driven* O(N) *model*, *Phys. Rev. B* **93** (2016) 174305.

[331] M. Bukov, S. Gopalakrishnan, M. Knap and E. Demler, *Prethermal Floquet Steady States and Instabilities in the Periodically Driven, Weakly Interacting Bose-Hubbard Model*, *Phys. Rev. Lett.* **115** (2015) 205301.

[332] S. A. Weidinger and M. Knap, *Floquet prethermalization and regimes of heating in a periodically driven, interacting quantum system*, *Scientific reports* **7** (2017) 45382.

[333] R. Citro, E. G. D. Torre, L. D'Alessio, A. Polkovnikov, M. Babadi, T. Oka et al., *Dynamical stability of a many-body Kapitza pendulum*, *Annals of Physics* **360** (2015) 694.

[334] M. Kitagawa and M. Ueda, *Squeezed spin states*, *Phys. Rev. A* **47** (1993) 5138.

[335] A. S. Sørensen and K. Mølmer, *Entanglement and Extreme Spin Squeezing*, *Phys. Rev. Lett.* **86** (2001) 4431.

[336] A. Sørensen, L.-M. Duan, J. Cirac and P. Zoller, *Many-particle entanglement with Bose–Einstein condensates*, *Nature* **409** (2001) 63.

[337] G. Tóth, C. Knapp, O. Gühne and H. J. Briegel, *Optimal Spin Squeezing Inequalities Detect Bound Entanglement in Spin Models*, *Phys. Rev. Lett.* **99** (2007) 250405.

[338] K. R. A. Hazzard, M. van den Worm, M. Foss-Feig, S. R. Manmana, E. G. Dalla Torre, T. Pfau et al., *Quantum correlations and entanglement in far-from-equilibrium spin systems*, *Phys. Rev. A* **90** (2014) 063622.

[339] M. Foss-Feig, Z.-X. Gong, A. V. Gorshkov and C. W. Clark, *Entanglement and spin-squeezing without infinite-range interactions*, *arXiv:1612.07805* (2016).

[340] L. Pezzé and A. Smerzi, *Entanglement, Nonlinear Dynamics, and the Heisenberg Limit*, *Phys. Rev. Lett.* **102** (2009) 100401.

[341] J. Vidal, S. Dusuel and T. Barthel, *Entanglement entropy in collective models*, *Journal of Statistical Mechanics: Theory and Experiment* **2007** (2007) P01015.

[342] T. Barthel, S. Dusuel and J. Vidal, *Entanglement Entropy beyond the Free Case*, *Phys. Rev. Lett.* **97** (2006) 220402.

[343] M. A. Metlitski and T. Grover, *Entanglement Entropy of Systems with Spontaneously Broken Continuous Symmetry*, *arXiv:1112.5166* (2011).

[344] T. Barthel, M.-C. Chung and U. Schollwöck, *Entanglement scaling in critical two-dimensional fermionic and bosonic systems*, *Phys. Rev. A* **74** (2006) 022329.

[345] T. Hiroshima, *Decoherence and entanglement in two-mode squeezed vacuum states*, *Phys. Rev. A* **63** (2001) 022305.

[346] D. J. Wineland, J. J. Bollinger, W. M. Itano, F. L. Moore and D. J. Heinzen, *Spin squeezing and reduced quantum noise in spectroscopy*, *Phys. Rev. A* **46** (1992) R6797.

[347] J. Ma, X. Wang, C. Sun and F. Nori, *Quantum spin squeezing*, *Physics Reports* **509** (2011) 89.

[348] W. H. Zurek and J. P. Paz, *Quantum chaos: a decoherent definition*, *Physica D: Nonlinear Phenomena* **83** (1995) 300 .

[349] R. Schubert, R. O. Vallejos and F. Toscano, *How do wave packets spread? Time evolution on Ehrenfest time scales*, *Journal of Physics A: Mathematical and Theoretical* **45** (2012) 215307.

[350] J. Haegeman, C. Lubich, I. Oseledets, B. Vandereycken and F. Verstraete, *Unifying time evolution and optimization with matrix product states*, *Phys. Rev. B* **94** (2016) 165116.

[351] J. Haegeman, J. I. Cirac, T. J. Osborne, I. Pižorn, H. Verschelde and F. Verstraete, *Time-Dependent Variational Principle for Quantum Lattices*, *Phys. Rev. Lett.* **107** (2011) 070601.

[352] B. Pirvu, V. Murg, J. I. Cirac and F. Verstraete, *Matrix product operator representations*, *New Journal of Physics* **12** (2010) 025012.

[353] A. Safavi-Naini, R. Lewis-Swan, J. Bohnet, M. Garttner, K. Gilmore, E. Jordan et al., *Exploring adiabatic quantum dynamics of the Dicke model in a trapped ion quantum simulator*, *arXiv:1711.07392* (2017).

[354] K. G. Wilson, *Confinement of quarks*, *Phys. Rev. D* **10** (1974) 2445.

[355] J. Kogut and L. Susskind, *Hamiltonian formulation of Wilson's lattice gauge theories*, *Phys. Rev. D* **11** (1975) 395.

[356] S. Coleman, *More about the massive Schwinger model*, *Annals of Physics* **101** (1976) 239.

[357] S. Chandrasekharan and U.-J. Wiese, *Quantum link models: A discrete approach to gauge theories*, *Nuclear Physics B* **492** (1997) 455.

[358] D. Horn, *Finite matrix models with continuous local gauge invariance*, *Physics Letters B* **100** (1981) 149 .

[359] T. Banks, L. Susskind and J. Kogut, *Strong-coupling calculations of lattice gauge theories: (1 + 1)-dimensional exercises*, *Phys. Rev. D* **13** (1976) 1043.

[360] K. Kasamatsu, I. Ichinose and T. Matsui, *Atomic Quantum Simulation of the Lattice Gauge-Higgs Model: Higgs Couplings and Emergence of Exact Local Gauge Symmetry*, *Phys. Rev. Lett.* **111** (2013) 115303.

[361] Y. Kuno, S. Sakane, K. Kasamatsu, I. Ichinose and T. Matsui, *Atomic quantum simulation of a three-dimensional* $\mathrm{U}(1)$ *gauge-Higgs model*, *Phys. Rev. A* **94** (2016) 063641.

[362] Y. Kuno, K. Kasamatsu, Y. Takahashi, I. Ichinose and T. Matsui, *Real-time dynamics and proposal for feasible experiments of lattice gauge–Higgs model simulated by cold atoms*, *New Journal of Physics* **17** (2015) 063005.

[363] E. Zohar and J. I. Cirac, *Removing staggered fermionic matter in* $\mathrm{U}(\mathrm{N})$ *and* $\mathrm{SU}(\mathrm{N})$ *lattice gauge theories*, *Phys. Rev. D* **99** (2019) 114511.

[364] P. Fendley, K. Sengupta and S. Sachdev, *Competing density-wave orders in a one-dimensional hard-boson model*, *Phys. Rev. B* **69** (2004) 075106.

[365] A. J. A. James, R. M. Konik and N. J. Robinson, *Nonthermal States Arising from Confinement in One and Two Dimensions*, *Phys. Rev. Lett.* **122** (2019) 130603.

[366] N. J. Robinson, A. J. A. James and R. M. Konik, *Signatures of rare states and thermalization in a theory with confinement*, *Phys. Rev. B* **99** (2019) 195108.

[367] I. Montvay and G. Muenster, *Quantum Fields on a lattice*. Cambridge Univ. Press, Cambridge, 1994.

[368] Z. Fodor and C. Hoelbling, *Light hadron masses from lattice QCD*, *Rev. Mod. Phys.* **84** (2012) 449.

[369] K. Fukushima and T. Hatsuda, *The phase diagram of dense QCD*, *Rep. Progr. Phys.* **74** (2010) 014001.

[370] R. Soltz, C. DeTar, F. Karsch, S. Mukherjee and P. Vranas, *Lattice QCD Thermodynamics with Physical Quark Masses*, *Annual Review of Nuclear and Particle Science* **65** (2015) 379.

[371] E. A. Calzetta and B. L. Hu, *Nonequilibrium Quantum Field Theory*. Cambridge Univ. Press, Cambridge, 2008.

[372] J. Preskill, *Simulating quantum field theory with a quantum computer*, *arXiv.1811.10085* (2018).

[373] K. Rajagopal and F. Wilczek, *Emergence of coherent long wavelength oscillations after a quench: application to QCD*, *Nuclear Physics B* **404** (1993) 577.

[374] M. C. Bañuls, J. I. Cirac and M. B. Hastings, *Strong and Weak Thermalization of Infinite Nonintegrable Quantum Systems*, *Phys. Rev. Lett.* **106** (2011) 050405.

[375] C.-J. Lin and O. I. Motrunich, *Quasiparticle explanation of the weak-thermalization regime under quench in a nonintegrable quantum spin chain*, *Phys. Rev. A* **95** (2017) 023621.

[376] C. Turner, A. Michailidis, D. Abanin, M. Serbyn and Z. Papić, *Weak ergodicity breaking from quantum many-body scars*, *Nature Physics* **14** (2018) 745.

[377] V. Khemani, C. R. Laumann and A. Chandran, *Signatures of integrability in the dynamics of Rydberg-blockaded chains*, *Phys. Rev. B* **99** (2019) 161101.

[378] J. Park, Y. Kuno and I. Ichinose, *Glassy dynamics from quark confinement: Atomic quantum simulation of the gauge-Higgs model on a lattice*, *Phys. Rev. A* **100** (2019) 013629.

[379] M. Brenes, M. Dalmonte, M. Heyl and A. Scardicchio, *Many-Body Localization Dynamics from Gauge Invariance*, *Phys. Rev. Lett.* **120** (2018) 030601.

[380] A. H. MacDonald, S. M. Girvin and D. Yoshioka, $\frac{t}{U}$ *expansion for the Hubbard model*, *Phys. Rev. B* **37** (1988) 9753.

[381] H. C. Fogedby, *The Ising chain in a skew magnetic field*, *Journal of Physics C: Solid State Physics* **11** (1978) 2801.

[382] J. Schwinger, *On Gauge Invariance and Vacuum Polarization*, *Phys. Rev.* **82** (1951) 664.

[383] G. Vidal, *Classical Simulation of Infinite-Size Quantum Lattice Systems in One Spatial Dimension*, *Phys. Rev. Lett.* **98** (2007) 070201.

[384] E. van Nieuwenburg, Y. Baum and G. Refael, *From Bloch oscillations to many-body localization in clean interacting systems*, *Proceedings of the National Academy of Sciences* **116** (2019) 9269.

[385] M. Schulz, C. A. Hooley, R. Moessner and F. Pollmann, *Stark Many-Body Localization*, *Phys. Rev. Lett.* **122** (2019) 040606.

[386] J. Haegeman, C. Lubich, I. Oseledets, B. Vandereycken and F. Verstraete, *Unifying time evolution and optimization with matrix product states*, *Phys. Rev. B* **94** (2016) 165116.

[387] J. C. Halimeh, M. Van Damme, V. Zauner-Stauber and L. Vanderstraeten, *Quasiparticle Origin of Dynamical Quantum Phase Transitions*, *arxiv:1810.07187* (2018).

[388] H. P. Robertson, *The Uncertainty Principle*, *Phys. Rev.* **34** (1929) 163.

[389] F. Buccheri, A. De Luca and A. Scardicchio, *Structure of typical states of a disordered Richardson model and many-body localization*, *Phys. Rev. B* **84** (2011) 094203.

[390] K. Iwano, *Bloch Oscillations Due to Quantum Domain Breathing in One-Dimensional Electronic Photoinduced Phase Transitions*, *Applied Sciences* **9** (2019) 2461.